Journal of Biomedical Photonics & Engineering

by Samara State Aerospace University (SSAU)

Volume 1, Issue 1 (*March 2015*)

Editorial Board

Editor-In-Chief

Valery V. Tuchin - Saratov State University, Russia; Institute of Precision Mechanics and Control RAS, Russia; University of Oulu, Finland; Samara State Aerospace University, Russia

Deputy Editor-In-Chief

Valery P. Zakharov - Samara State Aerospace University, Russia

Editorial Board

Stefan Andersson-Engels (Lund University, Sweden), **Alexey N. Bashkatov** (Saratov State University, Russia), **Ekaterina Borisova** (Academician Emil Djakov Institute of Electronics, Bulgarian Academy of Sciences, Bulgaria), **Wei Chen** (University of Central Oklahoma, USA), **Arthur Chiou** (National Yang-Mind University, Taiwan), **Elina A. Genina** (Saratov State University, Russia), **Min Gu** (Swinburne University, Australia), **Nikolay G. Khlebtsov** (Institute of Biochemistry and Physiology of Plants and Microorganisms RAS, Russia), **Juergen Lademann** (Charite University Clinic, Germany), **Kirill V. Larin** (University of Houston, USA), **Martin Leahy** (University of Galway, Ireland), **Qingming Luo** (Huazhong University of Science and Technology, China), **Stephen J Matcher** (University of Sheffield, Great Britain), **Igor Meglinski** (University of Oulu, Finland), **Vladimir S. Pavelyev** (Image Processing Systems Institute RAS, Russia), **Francesco Pavone** (University of Florence, Italy), **Roberto Pini** (Institute of Applied Physics, Italy), **Igor A. Platonov** (Samara State Aerospace University, Russia), **Juergen Popp** (Institute of Photonic Technology, Germany), **Alexander V. Priezzhev** (Moscow State University, Russia), **David Sampson** (The University of Western Australia, Australia), **Alexander Savitsky** (Institute of Biochemistry RAS, Russia), **Alexander P. Shkurinov** (Moscow State University, Russia), **Peter So** (Massachusetts Institute of Technologies, USA), **Janis Spigulis** (University of Latvia, Latvia), **Ilya V.Turchin** (Institute of Applied Physics RAS, Russia), **Vladimir G. Volostnikov** (N.P.Lebedev Physical Institute, Russia), **Lihong V. Wang** (Washington University, USA), **Ruikang Wang** (University of Washington, USA), **Xunbin Wei** (Shanghai Jiao Tong University, China), **Dan Zhu** (Britton Chance Center for Biomedical Photonics, Huazhong University of Science and Technology, China).

Postal address:

39B Lukacheva st., room #301

Samara 443086, Russian Federation

© 2015 SSAU

Contents

Review papers

Tissue Optics and Photonics: Biological Tissue Structures 3
by V.V. Tuchin

Optical clearing of biological tissues: prospects of application in medical diagnostics and phototherapy 22
by E.A. Genina, A.N. Bashkatov, Yu.P. Sinichkin, I.Yu. Yanina, and V.V. Tuchin

Regular papers

Change of optical properties of hair cells during malignant tumor development 59
by V.S. Maryakhina, L.S. Scheglova, and K. Anenkova

Line optical traps formed by LC SLM 64
by A. Korobtsov, S. Kotova, N. Losevsky, A. Mayorova, and S. Samagin

Lung neoplasm diagnostics using Raman spectroscopy and autofluorescence analysis 70
by V.P. Zakharov, I.A. Bratchenko, D.N. Artemyev, O.O. Myakinin, D.V. Kornilin, S.V. Kozlov, and A.A. Moryatov

OCT/LCT monitoring the drug effect on the human cornea structure *in vivo* 77
by E.A. Genina, A.N. Bashkatov, I.D. Kamenskikh, I.O. Kolbenev, T.G. Kamenskikh, and V.V. Tuchin

A pulsed photoacoustic technique for studying red blood cell sedimentation 81
by M. Kinnunen

Quantification of Mouse Embryonic Eye Development with Optical Coherence Tomography *In Utero* 90
by N. Sudheendran, M. Mashiatulla, R. Raghunathan, S.H. Syed, M.E. Dickinson, I.V. Larina, and K.V. Larin

 © 2015 SSAU

Tissue Optics and Photonics: Biological Tissue Structures

V.V. Tuchin
Saratov State University, 83 Astrakhanskaya str., Saratov 410012, Russia
Institute of Precision Mechanics and Control RAS, 24 Rabochaya str., Saratov 410028, Russia
Samara State Aerospace University (SSAU), 34 Moskovskoye Shosse, Samara 443086, Russia

e-mail: tuchinvv@mail.ru

Abstract. This is the first section of the review-tutorial paper describing fundamentals of tissue optics and photonics mostly devoted to biological tissue structures and their specificity related to light interactions at its propagation in tissues. The next sections of the paper will describe light-tissue interactions caused by tissue dispersion, scattering, and absorption properties, including light reflection and refraction, absorption, elastic quasi-elastic and inelastic scattering. The major tissue absorbers and types of elastic scattering, including Rayleigh and Mie scattering, will be presented. © 2015 Samara State Aerospace University (SSAU).

Keywords: biophotonics; tissue optics; tissue structures.

Paper #1991 received 2014.12.25; accepted for publication 2015.02.01; published online 2015.03.28.

References

1. R. R. Anderson, and J. A. Parrish, Optical properties of human skin in The Science of Photomedicine, eds. J. D. Regan, and J. A. Parrish, Plenum Press, NY, 147–194 (1982).
2. G. J. Müller, and D. H. Sliney (eds.) Dosimetry of Laser Radiation in Medicine and Biology, SPIE Inst. Adv. Opt. Techn. IS5, SPIE Press, Bellingham, WA. (1989),
3. A. V. Priezzhev, V. V. Tuchin, and L. P. Shubochkin, Laser Diagnostics in Biology and Medicine, Nauka, Moscow (1989).
4. K. Frank, and M. Kessler (eds.), Quantitative Spectroscopy in Tissue, pmi Verlag, Frankfurt am Main (1992).
5. A. J. Welch, and van M. J. C. Gemert (eds.), Tissue Optics, Academic, NY (1992).
6. S. L. Jacques, "Monte Carlo modeling of light transport in tissues," in Tissue Optics, A. J. Welch, and van M. C. J. Gemert (eds.), Academic, NY (1992).
7. G. Müller, B. Chance, R. Alfano, et al. (eds.), Medical Optical Tomography: Functional Imaging and Monitoring, SPIE Inst. Adv. Opt. Techn. IS11, SPIE Press, Bellingham, WA (1993).
8. V. V. Tuchin, Lasers light scattering in biomedical diagnostics and therapy, J. Laser Appl. 5 (2, 3), 43–60 (1993).
9. V. V. Tuchin (ed.), Selected Papers on Tissue Optics: Applications in Medical Diagnostics and Therapy, MS102, SPIE Press, Bellingham, WA (1994).
10. M. S. Patterson, "Noninvasive measurement of tissue optical properties: current status and future prospects" in Comments Mol. Cell. Biophys. 8, Gordon and Breach Sci. Publ. Inc., 387–417 (1995).
11. B. Chance, M. Cope, E. Gratton, N. Ramanujam, and B. Tromberg, Phase measurement of light absorption and scatter in human tissue, Rev. Sci. Instrum. 69(10), 3457–3481 (1998).
12. V. V. Tuchin, Light scattering study of tissues, Physics – Uspekhi 40 (5), 495–515 (1997).
13. O. Minet, G. Müller, and J. Beuthan (eds.), Selected Papers on Optical Tomography, Fundamentals and Applications in Medicine, MS147, SPIE Press, Bellingham, WA (1998).
14. V. V. Tuchin, Tissue Optics: Light Scattering Methods and Instruments for Medical Diagnosis, SPIE Tutorial Texts in Optical Engineering TT38, SPIE Press, Bellingham, WA (2000).
15. V. V. Tuchin (ed.), Handbook of Optical Biomedical Diagnostics, PM107, SPIE Press, Bellingham, WA (2002) (translated to Russian, Fizmatlit, Moscow, 2007, 2 vols.).
16. H.-P. Berlien, and G. J. Müller (eds.), Applied Laser Medicine, Springer-Verlag, Berlin (2003).
17. T. Vo-Dinh (ed.), Biomedical Photonics Handbook, CRC Press, Boca Raton (2003).
18. V. V. Tuchin (ed.), Coherent-Domain Optical Methods for Biomedical Diagnostics, Environmental and Material Science, vols. 1 & 2, Kluwer Academic Publishers, Boston, Dordrecht, L. (2004).

19. B. Wilson, V. Tuchin, and S. Tanev (eds.), Advances in Biophotonics, NATO Science Series I. Life and Behavioural Sciences, 369, IOS Press, Amsterdam (2005).
20. V. V. Tuchin, L. V. Wang, and D. A. Zimnyakov, Optical Polarization in Biomedical Applications, Springer, NY (2006).
21. V. V. Tuchin, Optical Clearing of Tissues and Blood, PM 154, SPIE Press, Bellingham, WA (2006).
22. A. Kishen, and A. Asundi (eds.), Photonics in Dentistry. Series of Biomaterials and Bioengineering, Imperial College Press, London (2006).
23. V. V. Tuchin, Tissue Optics: Light Scattering Methods and Instruments for Medical Diagnosis, 2nd ed., PM 166, SPIE Press, Bellingham, WA (2007) (translated to Russian, Fizmatlit, Moscow, 2012).
24. L. V. Wang, and H.-I. Wu, Biomedical Optics: Principles and Imaging, Wiley-Intersience, Hoboken, NJ (2007).
25. V. V. Tuchin, A clear vision for laser diagnostics, IEEE J. Select. Tops. Quant. Electr. 13(6), 1621–1628 (2007).
26. R. Splinter, and B. A. Hooper, An Introduction to Biomedical Optics, CRC Press, Taylor & Francis Group, NY, London (2007).
27. V. V. Tuchin (ed.), Handbook of Optical Sensing of Glucose in Biological Fluids and Tissues, CRC Press, Taylor & Francis Group, London (2009).
28. M. F. Yang, V. V. Tuchin, and A. N. Yaroslavsky, "Principles of light skin interactions" in Light-Based Therapies for Skin of Color, E. D. Baron (ed.), Springer, London, 1–45 (2009).
29. G. B. Altshuler, and V. V. Tuchin, "Physics behind the light-based technology: Skin and hair follicle interactions with light" in Cosmetic Applications of Laser & Light-Based Systems, G. Ahluwalia (ed.), William Andrew, Inc., Norwich, NY, 49–109 (2009).
30. V. V. Tuchin, "Optical spectroscopy of biological materials," Chapter 16 in Encyclopedia of Applied Spectroscopy, D. L. Andrews (ed.), Wiley-VCH Verlag GmbH & Co. KGaA, Weinheim, 555–626 (2009).
31. E. D. Baron (ed.), Light-Based Therapies for Skin of Color, Springer, London (2009).
32. G. Ahluwalia (ed.), Light Based Systems for Cosmetic Application, William Andrew, Norwich (2009).
33. K.-E. Peiponen, R. Myllylä, and A. V. Priezzhev, Optical Measurement Techniques, Innovations for Industry and the Life Science, Springer-Verlag, Berlin, Heidelberg (2009).
34. P. Zakharov, and F. Scheffold, Advances in dynamic light scattering techniques, in Light Scattering Reviews 4: Single Light Scattering and Radiative Transfer, A. A. Kokhanovsky (ed.), Springer, Heidelberg, 433–468 (2009).
35. A. Wax, and V. Backman (eds.), Biomedical Applications of Light Scattering, McGraw-Hill, NY (2010).
36. V. V. Tuchin (ed.), Handbook of Photonics for Biomedical Science, CRC Press, Taylor & Francis Group, London (2010).
37. M. M. Nazarov, A. P. Shkurinov, V. V. Tuchin, and X.-C. Zhang, Terahertz tissue spectroscopy and imaging, Chapter 23 in Handbook of Photonics for Biomedical Science, V. V. Tuchin (ed.), CRC Press, Taylor & Francis Group, London, 591–617 (2010).
38. F. S. Pavone (ed.), Laser Imaging and Manipulation in Cell Biology, Wiley-VCH Verlag GmbH & Co. KGaA, Weinheim (2010).
39. E. A. Genina, A. N. Bashkatov, and V. V. Tuchin, Tissue optical immersion clearing, Expert Rev. Med. Devices 7(6), 825–842 (2010).
40. V. V. Tuchin, Lasers and Fibre Optics in Biomedical Science, 2nd ed., Fizmatlit, Moscow (2010).
41. A. P. Dhawan, B. D'Alessandro, and X. Fu, "Optical Imaging Modalities for Biomedical Applications," IEEE Reviews in Biomedical Engineering 3, 69−92 (2010).
42. X.-C. Zhang, and J. Xu, Introduction to THz Wave Photonics, Springer, NY (2010).
43. E. A. Genina, A. N. Bashkatov, K. V. Larin, and V. V. Tuchin, "Light–tissue interaction at optical clearing," in Laser Imaging and Manipulation in Cell Biology, F. S. Pavone (ed.) (Wiley-VCH Verlag GmbH & Co. KGaA, Weinheim), 115–164 (2010).
44. A. N. Bashkatov, E. A. Genina, and V. V. Tuchin, Optical properties of skin, subcutaneous, and muscle tissues: a review, J. Innov. Opt. Health Sci. 4(1), 9–38 (2011).
45. D. A. Boas, C. Pitris, and N. Ramanujam (eds.), Handbook of Biomedical Optics, CRC Press, Taylor & Francis Group, London (2011).
46. V. V. Tuchin (ed.), Advanced Optical Cytometry: Methods and Disease Diagnoses, Wiley-VCH Verlag GmbH & Co. KGaA, Weinheim (2011).
47. V. V. Tuchin, Dictionary of Biomedical Optics and Biophotonics, SPIE Press, Bellingham, WA (2012).
48. K. V. Larin, M. G. Ghosn, A. N. Bashkatov, E. A. Genina, N. A. Trunina, and V. V. Tuchin, "Optical clearing for OCT image enhancement and in-depth monitoring of molecular diffusion," IEEE J. Select. Tops. Quant. Electr. 18 (3) 1244–1259 (2012).
49. V. V. Tuchin (ed.), Coherent-Domain Optical Methods: Biomedical Diagnostics, Environmental Monitoring and Material Science, Berlin, Heidelberg, N. Y., Springer-Verlag, 2nd ed., 2 vols (2013).

50. R. K. Wang, and V. V. Tuchin, "Optical coherence tomography: light scattering and imaging enhancement," in Coherent-Domain Optical Methods: Biomedical Diagnostics, Environmental Monitoring and Material Science. V. 1, 2nd edition, V. V. Tuchin (ed.), Springer-Verlag, Berlin, Heidelberg, NY, 665–742 (2013).
51. A. Douplik, G. Saiko, I. Schelkanova, and V. V. Tuchin, "The response of tissue to laser light," in Lasers for Medical Applications: Diagnostics, Therapy and Surgery, H. Jelinkova (ed.), Woodhead Publishing, Ltd., Cambridge, pp.47–109 (2013).
52. D. Zhu, K. V. Larin, Q. Luo, and V. V. Tuchin, "Recent progress in tissue optical clearing," Laser Photonics Rev. 7(5), 732–757 (2013).
53. D. Zhu, Q. Luo, and V. V. Tuchin, "Tissue Optical Clearing," in Advanced Biophotonics: Tissue Optical Sectioning, R. K. Wang, and V. V. Tuchin (eds.), CRC Press, Taylor & Francis Group, Boca Raton, London, NY, 621–672 (2013).
54. J. Wang, Y. Zhang, P. Li, Q. Luo, and D. Zhu, "Review: Tissue Optical Clearing Window for Blood Flow Monitoring (Invited Paper)," IEEE J. Select. Tops Quant. Electr. 20 (2), 6801112-1–12 (2014).
55. O. Nadiarnykh, and P. J. Campagnola, "SHG and optical clearing," in Second Harmonic Generation Imaging, F. S. Pavone, and P. J. Campagnola (eds.), CRC Press, Taylor & Francis Group, Boca Raton, London, NY, 169−189 (2014).
56. F. S. Pavone, and P. J. Campagnola (eds.), Second Harmonic Generation Imaging, CRC Press, Taylor & Francis Group, Boca Raton, London, NY (2014).
57. T. Vo-Dinh (ed.), Biomedical Photonics Handbook, 2nd ed., CRC Press, Boca Raton (2014).
58. V. V. Tuchin, Tissue Optics: Light Scattering Methods and Instruments for Medical Diagnosis, SPIE Press, PM 254, 3rd ed., SPIE Press, Bellingham, WA (2015).
59. P. Prasad, Introduction to Biophotonics. Wiley-Interscience, Hoboken, NJ (2003).
60. L. Pavesi, Ph. M. Fauchet (eds.), Biophotonics (Biological and Medical Physics, Biomedical Engineering), Springer Verlag, Berlin, Heidelberg (2008).
61. J. Popp, V. Tuchin, A. Chiou, and S. H. Heinemann (eds.), Handbook of Biophotonics: Basics and Techniques, vol.1, Wiley-VCH Verlag GmbH & Co. KGaA, Weinheim (2011).
62. J. Popp, V. V. Tuchin, A. Chiou, and S. H. Heinemann (eds.), Handbook of Biophotonics: Photonics for Health Care, vol. 2, WILEY-VCH Verlag GmbH & Co. KGaA, Weinheim (2011).
63. J. Popp, V. V. Tuchin, A. Chiou, and S. H. Heinemann (eds.), Handbook of Biophotonics: Photonics in Pharmaceutics, Bioanalysis and Environmental Research, vol. 3, WILEY-VCH Verlag GmbH & Co. KGaA, Weinheim (2012).
64. R. K. Wang, and V. V. Tuchin, Advanced Biophotonics: Tissue Optical Sectioning, CRC Press, Taylor & Francis Group, London (2013).
65. A. Yariv, Quantum Electronics, John Wiley & Sons, NY (1989).
66. F. H. Silver, Biological Materials: Structure, Mechanical Properties, and Modelling of Soft Tissues, New York Univ. Press, NY (1987).
67. F. A. Duck, Physical Properties of Tissue: A Comprehensive Reference Book, Academic, L. (1990).
68. T. B. Fitzpatrick, A. Z. Eisen, K. Wolff, I. M. Freedberg, and K. F. Austen (eds.), Dermatology in General Medicine, McGraw-Hill, NY (1993).
69. J. D. Bancroft, and A. Stevens (eds.), Theory and Practice of Histological Techniques, Churchill Livingstone, Edinburgh, NY (1990).
70. R. G. Kessel, Basic Medical Histology: The Biology of Cells, Tissues, and Organs, Oxford Univ. Press, NY (1998).
71. P. Agache, and P. Humbert (eds.), Measuring the Skin, Springer, Berlin, Heidelberg (2004).
72. T. A. Waigh, Applied Biophysics: Molecular Approach for Physical Scientists, John Wiley & Sons Ltd, Chichester (2007).
73. I. P. Herman, Physics of the Human Body, Springer, Berlin, Heidelberg, NY (2007).
74. D. M. Maurice, "The cornea and sclera" in The Eye, H. Davson (ed.), 3rd ed., 1B, Academic Press, Orlando, 1–158 (1984).
75. F. A. Bettelheim, "Physical basis of lens transparency" in The Ocular Lens: Structure, Function and Pathology, H. Maisel (ed.), Marcel-Dekker, NY, 265–300 (1985).
76. M. J. Hogan, J. A. Alvardo, and J. Weddel, Histology of the Human Eye, W. B. Sanders Co., Philadelphia (1971).
77. X. Wang, T. E. Milner, M. C. Chang, and J. S. Nelson, "Group refractive index measurement of dry and hydrated type I collagen films using optical low-coherence reflectometry," J. Biomed. Opt. 1(2), 212–216 (1996).
78. L. Moss-Salentijn, and M. Hendricks-Klyvert, Dental and Oral Tissues, An Introduction, 3rd edition, Lea & Febiger, Philadelphia, L. (1990).
79. R. L. McCally, and R. A. Farrell, "Light scattering from cornea and corneal transparency," in Noninvasive Diagnostic Techniques in Ophthalmology, B. R. Master (ed.), Springer-Verlag, NY, 189–210 (1990).

80. R. A. Farrell, D. E. Freund, and R. L. McCally, "Research on corneal structure" in Johns Hopkins APL Techn. Digest 11, 191–199 (1990).
81. R. A. Farrell, and R. L. McCally, "Corneal transparency" in Principles and Practice of Ophthalmology, D. A. Albert, and F. A. Jakobiec (eds.), W. B. Saunders, Philadelphia, PA, 629–643 (2000).
82. Y. Kamai, and T. Ushiki, The three-dimensional organization of collagen fibrils in the human cornea and sclera, Invest. Ophthalmol. & Visual Sci. 32, 2244–2258 (1991).
83. Y. Huang, and K. M. Meek, Swelling studies on the cornea and sclera: the effect of pH and ionic strength, Biophys. J. 77, 1655–1665 (1999).
84. O. Kostyuk, O. Nalovina, T. M. Mubard, J. W. Regini, K. M. Meek, A. J. Quantock, G. F. Elliott, and S. A. Hodson, "Transparency of the bovine corneal stroma at physiological hydration and its dependence on concentration of the ambient anion," J. Physiol. 543, 633–642 (2002).
85. K. M. Meek, S. Dennis, and S. Khan, "Changes in the refractive index of the stroma and its extrafibrillar matrix when the cornea swells," Biophys. J. 85, 2205–2212 (2003).
86. H. Schaefer, and T. E. Redelmeier, Skin Barrier: Principles of Percutaneous Absorption, Karger, Basel (1996).
87. http://www.sportsci.org/encyc/adipose/adipose.html. December 17, 2014.
88. M. J. Costello, T. N. Oliver, and L. M. Cobo, "Cellular architecture in aged related human nuclear cataracts," Invest. Ophthal. & Vis. Sci. 3(1), 2244–2258 (1992).
89. Y. Ozaki, "Medical application of Raman spectroscopy," Appl. Spectrosc. Rev. 24(3), 259–312 (1988).
90. H. A. Linares, C. W. Kischer, M. Dobrkovsky, and D. L. Larson, "The histiotypic organization of the hypertrophic scar in humans," J. Invest. Dermatol. 59, 323–331 (1972).
91. P. Gong, R. A. McLaughlin, Y. M. Liew, P. R. T. Munro, F. M. Wood, and D. D. Sampson, "Assessment of human burn scars with optical coherence tomography by imaging the attenuation coefficient of tissue after vascular masking," J. Biomed. Opt. 19(2), 021111-1–10 (2014).
92. N. Ugryumova, S. J. Matcher, and D. P. Attenburrow, "Measurement of bone mineral density via light scattering," Phys. Med. Biol. 49(3), 469–483 (2004).
93. S. Kaiplavil, A. Mandelis, and B. T. Amaechi, "Truncated-correlation photothermal coherence tomography of artificially demineralized animal bones: two- and three-dimensional markers for mineral loss monitoring," J. Biomed. Opt. 19(2), 026015-1–14 (2014).
94. G. Li, J. Yin, J. Gao, T. S. Cheng, N. J. Pavlos, C. Zhang, and M. H. Zheng, "Subchondral bone in osteoarthritis: insight into risk factors and microstructural changes Arthritis. Res. Ther. 15(6), 223-1–12 (2013).
95. S. J. Matcher, "A review of some recent developments in polarization-sensitive optical imaging techniques for the study of articular cartilage," J. Appl. Phys. 105, 102041 (2009).
96. M. Sivakumar, V. Oliveira, S. Oliveira, J. Leitão, and R. Vilar, "Influence of tubule orientation on cone-shaped texture development in laser-ablated dentin," Lasers Med. Sci. 21, 160–164 (2006).
97. V. V. Tuchin, and G. B. Altshuler, "Dental and oral tissue optics" in Photonics in Dentistry. Series of Biomaterials and Bioengineering, A. Kishen and A. Asundi (eds.) Imperial College Press, L., 245–300 (2006).
98. B. M. Eley, and J. D. Manson, Periodontics, 5th ed. Elsevier Ltd., Philadelphia (2004).
99. N. A. Trunina, V. V. Lychagov, and V. V. Tuchin, "Study of water diffusion in human dentin by optical coherent tomography," Opt. Spectrosc. 109(2), 162–168 (2010).
100. P. O. Bagnaninchi, Y. Yang, M. Bonesi, G. Maffulli, C. Plelan, I. Meglinski, et al., "In-depth imaging and quantification of degenerative changes associated with Achilles ruptured tendons by polarizationsenstive optical coherence tomography," Phys. Med. Biol. 55, 3777–3787 (2010).
101. M. H. Steinberg, B. G. Forget, D. R. Higgs, and D. J. Weatherall (eds.), Disorders of Hemoglobin: Genetics, Pathophysiology, and Clinical Management, 2nd ed., Cambridge, Cambridge University Press (2009).
102. M. Fabry, and J. M. Old, "Laboratory methods for diagnosis and evaluation of hemoglobin disorders," Chapter 28 in Disorders of Hemoglobin: Genetics, Pathophysiology, and Clinical Management, M. H. Steinberg, B. G. Forget, D. R. Higgs, and D. J. Weatherall (eds.), Cambridge, Cambridge University Press, 656–686 (2009).
103. V. V. Tuchin, In vivo optical flow cytometry and cell imaging, Rivista Del Nuovo Cimento, 37(7), 375–416 (2014).
104. E. I. Galanzha, M. S. Kokoska, E. V. Shashkov, J.-W. Kim, V. V. Tuchin, and V. P. Zharov, "In vivo fiber photoacoustic detection and photothermal purging of metastasis targeted by nanoparticles in sentinel lymph nodes at single cell level," J. Biophoton. 2, 528–539 (2009).
105. S. A. Asher, and J. T. Baca, "Tear fluid photonic crystal contact lens noninvasive glucose sensors" in Handbook of Optical Sensing of Glucose in Biological Fluids and Tissues, V. V. Tuchin (ed.), Taylor & Francis Group LLC, CRC Press, 267–297 (2009).

Contents

1 Introduction
2 Biological tissue structures
2.1 General definitions and characteristics
2.2 Soft tissues
2.3 Hard tissues
2.4Tissue structural anisotropy
2.5 Blood, lymph and other bioliquids
2.6 Conclusion

1 Introduction

In this review paper, fundamentals of tissue optics and photonics are discussed. Basic principles of light-tissue interaction and light beam propagation in weakly and strongly scattering tissues are considered. The discussion of different optical phenomena in tissues in one paper could be helpful for understanding of interrelations between different optical modalities beneficial for biomedical diagnostics and treatment. Currently there are available a plenty of literature describing tissue optics and biomedical applications of optical technologies, which can be recommended for further reading [1-58]. Biophotonics as a science and technology use tissue optics as basics for designing innovative optical diagnostical and treatment technologies [59-64].

The electromagnetic wave spectrum presented schematically in Fig. 1 shows wavelength range from the very short ones of gamma rays to the very long of radio waves, where only very small interval belongs to visible light from 400 to 780 nm. Physicians who apply light in phototherapy or vision science classify the light spectrum (i.e., from 100 nm to 1000 μm) basing on the major mechanism of light interaction with biological cells or tissues. In particular, spectral ranges are classified as *ultraviolet* (UV) light (UVC, 100–280 nm; UVB, 280–315 nm; and UVA, 315–400 nm); *visible* (400–780 nm); and *infrared* (IR) ligh (IRA, 780–1400 nm; IRB, 1400–3000 nm; and IRC, 3–1000 μm). However, physicists who consider light's interaction with and propagation in abiological media (atmosphere, ocean, etc.) classify light spectrum as UV (100–400 nm), visible (400–800 nm), near IR (NIR) (800–2500 nm), middle IR (MIR) (2.5–50 μm), and far IR (FIR) (50–2000 μm). Presently, as light is more and more widely and effectively used in medicine, both classifications and terminologies are on use in the biomedical optics and biophotonics.

For example, due to great importance of the near infrared range for tissue spectroscopy and imaging, the abbreviation NIR is often used now by medical doctors. A current interest and future perspective of the terahertz range of electromagnetic radiation for biomedical applications spread the light wavelength range classification used in medicine to the 2000 μm that used by physicists.

To characterize the efficiency of light interaction with biological tissue (inducing a photochemical reaction, temperature increase, evaporation, thermal mechanical breaking, etc.) besides choosing the wavelength of light, its energetic parameters are also important. Two major parameters are typically used: energy and power. Energy is the ability of light to produce some work; energy E is measured in joules (J). Power is the rate of delivery of energy; it is normally measured in watts (W) (i.e., joules per second (J/s)).

At light interaction with tissues, produced photophysical, photochemical, or photobiological effects depend on energy density and/or power density that are provided within the target area. Energy density or fluence is the energy of the light wave that propagates through a unit area which is perpendicular to the direction of propagation of the light wave. Fluence is measured in J/m^2 or J/cm^2 and power density or intensity is measured in W/m^2 or W/cm^2. The relationship between fluence (F) and intensity (I) is given by:

$$F = I \times \tau_p, \quad (1)$$

where τ_p is the length of pulse (pulsewidth) or exposure time.

In inhomogeneous light scattering media to which tissues belong, the following parameter is often used: fluence rate (or total radiant energy fluence rate), that is, the sum of the radiance over all angles at a point $\bar{r}$; the quantity that is typically measured in irradiated tissues (W/m^2 or W/cm^2) and commonly called "intensity" or "quantum flux."

In general, a light beam is a slender stream of light. Often the user needs a collimated beam—a beam of light in which all rays are parallel to each other and the wavefront is a plane. Such a beam, in some cases, can be provided automatically by using an appropriate laser or can be formed by special optics (with possible significant loss of light energy) using conventional light sources such as lamps.

Typically, laser beam has a Gaussian shape for the transverse intensity profile. If the intensity at the centre of the beam is $I(0, z)$ for a distance z apart the position of the laser beam "waist" (the narrowest part of a beam), the formula for a Gaussian beam is [65]

$$I(r,z) = I(0,z)exp\left\{-2\left(\frac{r}{w_b(z)}\right)^2\right\}, \quad (2)$$

where r is the radial distance from the axis and $w_b(z)$ is the beam radius at distance z from laser counted from the position of the beam "waist". A single-mode fibre with a core diameter of several microns also creates a Gaussian beam at its output.

The initial beam divergence of the light source is important for a light beam focusing on the target and for controlling the light spot diameter. The radius of the beam in the focal plane of the lens with a focal length f is given by:

$$w = f \times \theta, \quad (3)$$

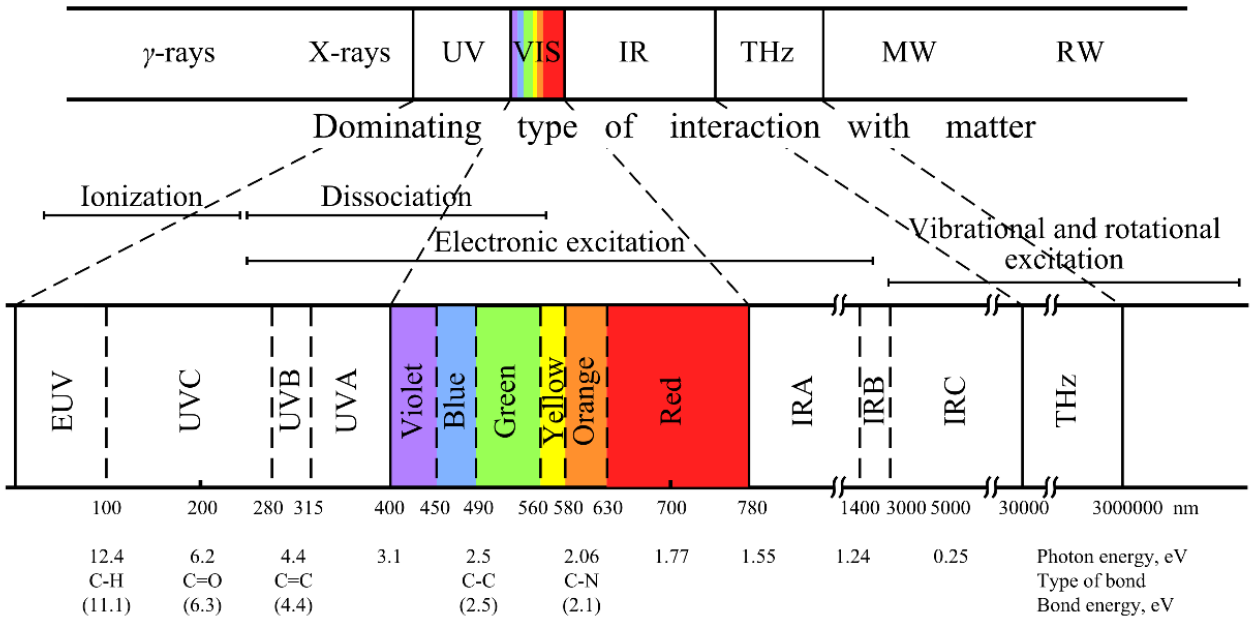


Fig. 1.1 Electromagnetic spectrum and types of interaction with matter (UV – ultraviolet, EUV – extreme UV, VIS – visible, IR – infrared, MW – microwaves, THz – terahertz, RW – radio waves). Modified from [40].

where θ is the beam divergence.

Single mode lasers or single mode fibres have a minimal beam divergence and can provide minimal light spot size; for a single mode laser (TEM_{00}-mode)

$$\theta \cong \lambda/\pi w(0), \tag{4}$$

where $w(0)$ is the laser beam radius in its "waist." Minimal light spot size in the focal plane of the aberration free optical system can be close to the wavelength λ. For enough far distance from the laser, $z >> \pi w^2(0)/\lambda$, laser beam radius is defined by a simple formula:

$$w(z) \cong z\theta. \tag{5}$$

Evidently, light-tissue interaction depends on temporal parameters of the light, whether it is continuous wave (CW) or pulse. Pulsed light can be produced as a single pulse of duration τ_p (pulsewidth), measured in seconds (s), or as successive trains of pulses with some repetition frequency (rate) f_p, measured in hertz (s^{-1}). Lamps can typically generate light pulses $\tau_p$up to nanosecond (ns) (10^{-9} s), and only lasers can generate more shorter pulses, in picosecond (ps) (10^{-12} s) or femtosecond (fs) (10^{-15} s) ranges with a high repetition rate f_p up to 100 MHz. A laser with Q-switching produces the so-called giant pulses in the nanosecond or picoseconds range, as the mode-locked laser produces ultrashort pulses in the subpicosecond or femtosecond range with a high repetition rate. In dependence of technology used, the form of pulses can be different: rectangular, triangle, or Gaussian.

To describe energetic properties of pulsed light, a few more characteristics, such as pulse energy E_p, peak power P_p (power within the individual pulse) and average power P_{ave} for a train of pulses are used:

$$P_p = E_p/\tau_p, \tag{6}$$

$$P_{ave} = E_p \times f_p. \tag{7}$$

Coherent light that is typically produced by lasers is light in which the electromagnetic waves maintain a fixed phase relationship over a period of time, and in which the phase relationship remains constant for various points in the plane that is perpendicular to the direction of propagation. Coherence length of a light source characterizes the degree of temporal coherence of the emitted light,

$$l_c = c\tau_c, \tag{8}$$

where c is the light speed and τ_c is the coherence time, which is approximately equal to the pulse duration of the pulsed light source or inversely proportional to the wavelength bandwidth $\Delta\lambda$ of a CW light source, $\tau_c \sim \lambda^2/(c\Delta\lambda)$. More precisely, for a Gaussian shape of a light source spectral band

$$l_c = \frac{2\ln(2)}{\pi} \cdot \frac{\lambda^2}{\Delta\lambda} \tag{9}$$

A single frequency CW He–Ne laser with a narrow bandwidth $\Delta\lambda = 10^{-6}$ nm and wavelength $\lambda = 632.8$ nm has a coherence length $l_c \approx 180$ m; a multimode diode laser with $\Delta\lambda = 30$ nm and $\lambda = 830$ nm has $l_c \approx 10$ μm. For a titanium-sapphire laser with $\lambda = 820$ nm, the bandwidth may be as big as 140 nm; therefore, coherence length is very short $l_c \approx 2$ μm. The shortest $l_c \approx 0.9$ μm is for a white light source ($\Delta\lambda = 400$ nm) or

even $l_c \approx 0.2$ μm for the supercontinuum radiation with $\Delta\lambda = 1500$ nm from a microstructured fibre induced by a femtosecond titanium-sapphire laser with mean wavelength of 800 nm. Coherence length is a fundamental parameter for optical coherence tomography (OCT); lower the l_c value, the better is the image resolution that can be achieved. OCT systems based on a femtosecond titanium sapphire laser or a supercontinium-based light source allows one to image skin with a subcellular resolution of 0.2–2 μm.

Polarized light is also used in tissue examination, thus its interaction specificity with tissues and cells should be accounted for [20].

2 Biological tissues

2.1 General definitions and characteristics

Biological tissue is an aggregate of similar cells and cell products (tissue fibres and gels) forming a definite kind of structural material in normal or abnormal state [47, 51, 66-76]. There are three major types of tissues, such as epithelial, connective, and glandular. More specifically tissues characterized as areolar, reticular, fibrous, tubular, and elastic. Tissues are also could be identified as belonging to a specific organ or system, i.e., mucosal, muscular, nervous, cervical, eye, skin, lymphoid, and adipose (fat), or to pathology state, i.e., scar tissue and malignant tissue.

Based on morphology, tissues can be also grouped into four basic types: epithelium, connective tissue, muscle tissue, and nervous tissue. Epithelial tissues are formed by layers of cells that cover organ surfaces such as the surface of the skin, the airways, and the inner lining of the digestive tract. Connective tissue is comprised of cells separated by nonliving material, which is called the extracellular matrix. There are the following five types of connective tissues: loose connective, dense connective, elastic, reticular, and adipose. Bone, cartilage, and blood belong to category of "specialized connective tissue." Muscle tissues are active contractile tissues of the body formed by muscle cells and separated into three distinct categories: smooth muscle, which is found in the inner linings of organs; skeletal muscle, which is found attached to bone providing for gross movement; and cardiac muscle that is found in the heart, allowing it to contract and pump blood throughout an organism. Cells comprising the central nervous system and peripheral nervous system are classified as neural tissue.

In general, tissue fibres are long strands of scleroprotein, which are either collagen-forming white fibres or elastin-forming yellow fibres, or reticulin-forming reticular fibres. Tissue fibres, formed and maintained by fibroblasts, form part of a noncellular matrix around and among cells. A matrix may consist of an amorphous, jellylike polysaccharide together with these three types of fibre. Cells and a matrix form a connective tissue. Different forms of connective tissue possess varying proportions of the constituents of the matrix.

Areolar tissue is a soft, sometimes spongelike connective tissue that consists of an amorphous polysaccharide-containing and jellylike ground matrix with the embedded a loose network of white, yellow, and reticulin fibres. In this tissue, fibroblasts form and maintain the matrix. The areolar tissue is found all over the body, binding together organs (by mesenteries) and muscles (by sheaths), and occurring as subcutaneous tissue which function is to support or fill in the space between organs or between other tissues.

Reticular tissue is a tissue consisting of a network of reticular intercellular fibres around and among cells, with lymph in the intercellular spaces. They occur in many large organs, such as the liver, kidney and the larger glands, and in nerves and muscles. Reticular fibres are very thin, almost inextensible threads of reticulin – a tough fibrous protein. It is similar to collagen, but more resistant to high temperature and chemical reagents. Reticulin is forming in embryos and in wounds and often changes to collagen.

Fibrous tissue is a tissue mainly consisting of conjunctive collagen (or elastin) fibres, often packed in lamellar bundles or fascicles. In fibrous tissues or tissues containing fibre layers (cornea, sclera, *dura mater*, muscle, myocardium, tendon, cartilage, vessel wall, retinal nerve fibre layer (RNFL), etc.) and composed mostly of fibrils/subfibrils/microfibrils (or protofibrils) (Fig. 2), typical diameters of the cylindrical structural elements are 5–400 nm; their length is in a range from 10–25 μm to a few millimetres. Fibril is a fine fibre or filament, e.g., in muscles their diameters are in the range of 5–15 nm with a length of about 1–1.5 μm and in the eye cornea, their diameters are in the range of 26–30 nm with a mean length up to a few millimetres [74, 76].

Collagen is a tough, inelastic, fibrous protein. On boiling, it forms gelatine and, on adding acetic acid, it swells up and dissolves. Collagen in its turn forms white fibres in connective tissue. The tropocollagen or "collagen molecule" subunit is a rod about 300 nm long and 1.5 nm in diameter, made up of three polypeptide strands. There is some covalent crosslinking within the triple helices, and a variable amount of covalent crosslinking between tropocollagen helices, to form the different types of collagen found in different mature tissues. A distinctive feature of collagen is the regular arrangement of amino acids in each of the three chains of these collagen subunits.

There are a number of collagen types, which are different in their composition and structure, type I to type V are the most abundant; types I, II, III, V,VII and XI are capable of fibril formation; their distribution in tissues: type I – dermis, bone, cornea, tendon, cartilage, vessel wall, intestine, dentin, uterine wall, fat mashwork; type II – cartilage, notochord, vitreous humour, nucleus pulposus; type III – dermis, intestine, gingiva, heart valve, uterine wall, vessel wall; type IV and VII – basement membranes; type V – cornea,

placental membranes, bone, vessel wall, cartilage, gingiva, and type XI – cartilage, intervertebral disc, vitreous humour [47]. In optical measurements collagen index of refraction is of importance, for example, for type I it is n = 1.43 (fully hydrated) and 1.53 (dry) at 850 nm [77].

Collagen fibrils are collagen molecules packed into an organized overlapping bundle. In their turn, collagen fibrils associated in a bigger bundle form a collagen or white fibre – the main component of white fibrous tissue. For example, for tendon collagen, fibrils diameters are in the range from ~25 to 600 nm with bigger size for mature tendons, subfibrils are of ~25 nm, and protofibrils are in the range 10–15 nm (Fig. 2).

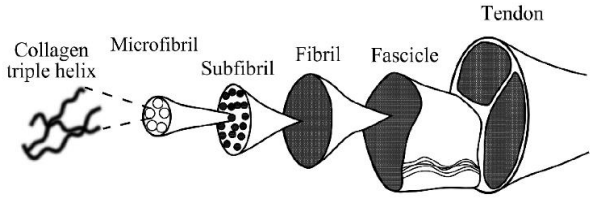


Fig. 2 Collagenous fibrillar structure in tendons: collagen triple helices are combined into microfibrils (or protofibrils), then into subfibrils, fibrils, fascicles and into tendons [72].

Yellow elastic tissue is a connective tissue that consists of a matrix of coarse yellow elastic fibres. Elastin, an elastic fibrous protein resistant to boiling and to acetic acid, is the principal constituent of this tissue formed and maintained by fibroblasts. The tissue rarely occurs pure and usually contains white fibres as well. Yellow elastic fibres are numerous in the lungs and in the walls of arteries, where elastic supporting tissues are required. Yellow elastic tissue occurs in ligaments, where an extensible tissue is required. Ligament is a band of fibrous tissue serving to connect bones, hold organs in place, etc.

Biological cell is an individual unit of protoplasm surrounded by a plasma membrane and usually containing a nucleus. A cell may exhibit all the characteristics of a living organism, or it may be highly specialized for a particular function. Cells vary considerably in size and shape, but all have the common features of metabolism. Most mammalian cells have diameters in the range of 5–75 μm. For example, in the skin epidermal layer, the cells are large (with an average cross-sectional area of about 80 μm^2) and quite uniform in size; fat cells, each containing a single lipid droplet that nearly fills the entire cell and therefore results in eccentric placement of the cytoplasm and nucleus, have a wide range of diameters from a few microns to 50–75 μm [47].

There is wide variety of structures within cells that determine tissue light scattering. Cell nuclei are on the order of 5–10 μm in diameter; mitochondria, lysosomes and peroxisoms have dimensions of 1–2 μm; ribosomes are on the order of 20 nm in diameter; and structures within various organelles, such as mitochondria, can have dimensions up to a few hundred nanometers [47, 78](Fig. 3). Usually, the particles in cells are not spherical; the models of prolate ellipsoids with a ratio of the ellipsoid axes between 2 and 10 are typical.

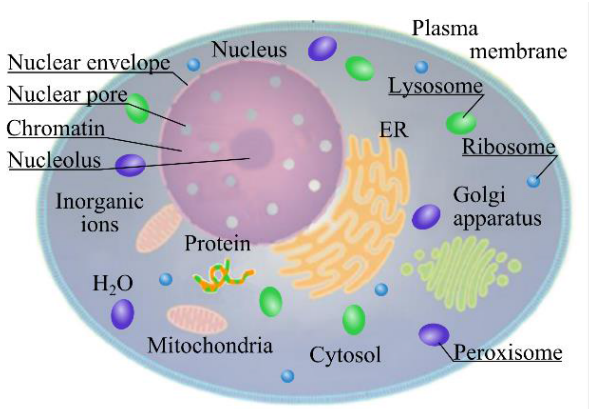


Fig. 3 Major organelles and inclusions of the cell: nucleus (chromatin, nuclear envelope, nuclear pore, nucleolus), mitochondria, lysosomes and peroxisoms, ribosomes, endoplasmic reticulum (ER), Golgi apparatus.

The hollow organs of the body are lined with a thin, highly cellular surface layer of epithelial tissue, which is supported by underlying, relatively acellular connective tissue. In healthy tissues, the epithelium often consists of a single, well–organized layer of cells with en–face diameter of 10–20 μm and height of 25 μm [47](Fig. 4). In dysplastic epithelium, cells proliferate and their nuclei enlarge and appear darker (hyperchromatic) when stained. Enlarged nuclei are primary indicators of cancer, dysplasia and cell regeneration in most human tissues.

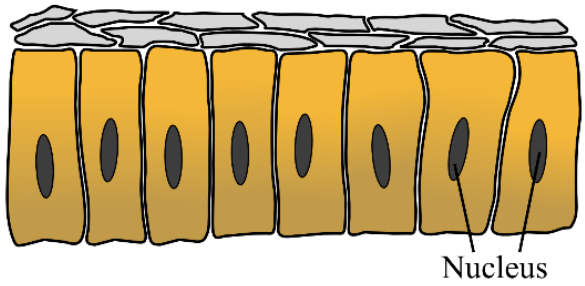


Fig. 4 One of the epithelial tissue types – a thin well–organized cellular surface layer by which the hollow organs of the body are lined.

2.2 Soft tissues

A soft (antonym to hard) tissue has its structural peculiarities and elasticity providing the specificity of light-tissue interaction. Tissue morphology, especially sizing and shaping of tissue constitutions (particles), and particle material (molecular structure) are important. For some tissues, the size distribution of the particles may be essentially monodispersive and for others it may be very broad. Two opposite examples are optically

transparent eye corneal stroma with a sharply monodispersive distribution of collagen fibre diameters, and turbid eye sclera with a rather broad distribution [74, 79-85].

Epithelial tissue is a tissue consisting of a sheet of epithelial cells held together by a minimal amount of cement-like material between the cells. It covers exposed surfaces and lines the cavities and tubes of the body. Beneath most epithelial tissue is a thin sheet of connective tissue – the basement membrane which separating epithelia from tissues below. Besides its protective function, epithelial tissue frequently has a secretory function, in which case it is known as glandular tissue. Keratinized epithelium structured to withstand abrasion. Keratin, a protein produced by mature epithelial cells called keratinocytes.

Mucous membrane (mucosa) is a membrane consisting of moist epithelium and the connective tissue immediately beneath it. It usually consists of simple epithelium, but is stratified near openings to the exterior. It is often ciliated and often contains goblet cells. Mucosa is found in the lining of the gastrointestinal and respiratory tracts, and in the urinogenital ducts. It is kept moist by glandular secretions.

Skin is the largest human organ. It covers between 1.5 and 2 m^2, comprising about one sixth of total body weight. It has barrier function against the environment and provides human body response to environment condition change [1, 68, 71, 86]. For example, skin protects us from water loss, ultraviolet rays of the sun, friction and impact wounds. It also helps in regulating body temperature and metabolism. Skin has three functional layers: epidermis, dermis, and hypodermis. The structures and component chromophores of these layers determine the attenuation of radiation in skin. In all three layers the epidermal appendages, such as nails, hair, and glands can be found. As the outermost skin layer, the epidermis forms the actual protective covering against environmental influences. It is a stratified epithelium that varies relatively little in thickness over most of the human body (between 75 and 150 μm) (Fig. 5), except on the face, where it may be as thin as 20 μm, and on the palms and soles of the feet, where its thickness may be thick as 400-5000 μm. The epidermis consists of up to 90% keratinocytes, which function as a barrier, keeping harmful substances out and preventing water and other essential substances from escaping the body. The other 10% of epidermal cells are melanocytes, which manufacture and distribute melanin, the protein that adds pigment to skin and protects the body from ultraviolet radiation. The epidermis is conventionally subdivided into *stratum basale*, a basal cell layer of keratinocytes, which is the germinative layer of the epidermis, the *stratum spinosum*, which consists of several layers of polyhedral cells lying above the germinal layer, the *stratum granulosum*, which is a layer of flattened cells containing distinctive cytoplasmic inclusions, keratohyalin granules, and the overlying *stratum corneum*, consisting of lamellae of anucleate thin, flat squames that are terminally differentiated keratinocytes. Besides body site, epidermal thickness is related to age, gender, skin type, pigmentation, and blood content. The mean thickness of the *stratum corneum* is ~18 μm at the dorsal aspect of the forearm, ~11 μm at the shoulder, and ~15 μm at the buttock. The corresponding values for the living cellular epidermis consist of *stratum granulosum*, *stratum spinosum*, and *stratum basale* (Fig. 5), are ~57 μm, 70 μm, and 81 μm, respectively. For example, for thin skin at the shoulder, its layers are typically ranged from top to down as the following: 11 μm for the *stratum corneum*, 23 μm – the *stratum granulosum*, 30 μm –the *stratum spinosum*, and 17 μm – the *stratum basale* [47].

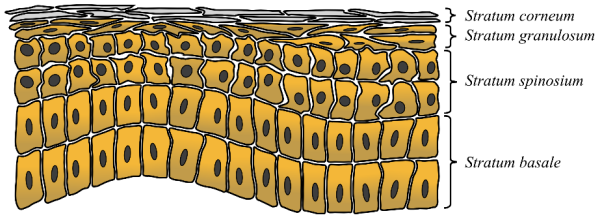


Fig. 5 Skin epidermis (epithelial layer) structure.

Due to different content of dark pigment – melanin, the tone of human skin can vary from a dark brown to a nearly colourless pigmentation, which may appear reddish due to the blood in the skin. Europeans generally have lighter skin, hair, and eyes than any other group. Africans generally have darker skin, hair, and eyes. For practical purposes, such as exposure time for sun tanning or phototherapy, six skin types are distinguished following Fitzpatrick, listed in order of decreasing lightness: I – very light, or "nordic" or "celtic" (often burns, rarely tans, tends to have freckles), II – light, or light-skinned European (usually burns, sometimes tans), III – light intermediate, or dark-skinned European (rarely burns, usually tans), IV – dark intermediate, also "Mediterranean" or "olive skin" (rarely burns, often tans), V – dark or "brown" type (naturally brown skin), and VI – very dark, or "black" type (naturally black-brown skin) [1, 68, 71, 86].

Dermis is composed of gel-like and elastic materials, water, and, primarily, collagen (Fig. 6). Collagen fibres are abundant in the dermis and run parallel to the surface of the skin, they give the skin elasticity. The dermis is much thicker than the epidermis. The upper dermis layer is a *papillary dermis*. Reticular layer of dermis (*reticular dermis*) is the lower layer of the dermis. It is made primarily of coarse collagen and elastic fibres and is denser than the upper *papillary dermis*. It strengthens the skin, providing structure and elasticity. It also supports other skin components-appendages such as sweat glands, hair follicles, and sebaceous glands. Lymph channels, blood vessels, nerve fibres, and muscle cells are also embedded in this layer.

The hypodermis consists of spongy connective tissue interspersed with energy-storing adipocytes (fat cells). Fat cells are grouped together in large cushion-like clusters held in place by collagen fibres called

connective tissue septa or sheaths. The hypodermis is heavily interlaced with blood vessels, ensuring a quick delivery of stored nutrients as needed.

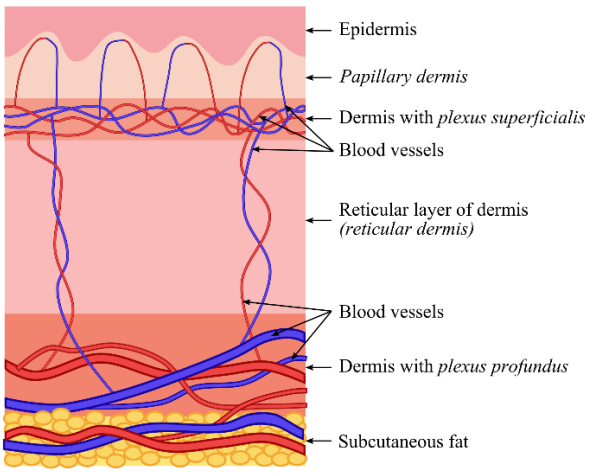


Fig. 6 Schematic representation of layered skin and subcutaneous fat.

In general, the adipose tissue is a modification of areolar tissue in which globules of oil are deposited in adipocytes. The cells occur, besides under the skin, around the abdominal organs (kidneys, liver, etc.). This tissue making in norm of 15–20% from weight of a body at men and 20–29% at women is a metabolically active "organ" supervised by neuroendocrine system. The adipose tissue of the subject consists of 60–85% of lipids, of 5–30% of water and of 2–3% of proteins [87]. Adipocyte is a cell in which a food reserve is deposited in the form of droplets of oil. The quantity of oil increases until the oil globule formed distends the cell and pushes the nucleus and cytoplasm to one side. A collection of fat cells forms adipose tissue. Fat occupies almost total volume of a fatty cell as the cell nucleus small and is located at its edge. In the different subjects the cell size is in the range 15–250 μm with mean lipid content in a cell 0.3– 1.2 mg lipid/cell, and total number of cells of $(0.2–10)\times10^{10}$. A great mass of lipids in fat tissue are neutral fats, or triglycerides (90–99%), the rest are diglycerides and monoglycerides (1-3%), phospholipids and glycolipids (0.5–3%), free fat acids and cholesterol (0.5–1.7 %). The spaces between fat cells are occupied by small capillaries and interstitial fluid.

Muscular tissue is characterized by its ability to contract on being stimulated by a motor nerve. There are three main types of muscular tissue forming three types of muscles: striped muscle, unstriped muscle, and cardiac muscle. Myocard (myocardium) is the muscular tissue of the heart. It consists mostly of cardiac muscle which is comprised of myofibrils (about 1 μm in diameter that in turn consist of cylindrical myofilaments of 6-15 nm in diameter) and aspherical mitochondria (0.1–0.2 μm in diameter). Fibres in myocardium are oriented along two different axes. It is typically birefringent since the refractive index along the axis of the muscle fibre is different from that in the transverse direction.

The dominant scatterers in an artery are the fibres, the cells, or the subcellular organelles. Muscular arteries have three main layers. The inner intimal layer consists of endothelial cells with a mean diameter of less than 10 μm. The medial layer consists mostly of closely packed smooth muscle cells with a mean diameter of 15–20 μm and small amounts of connective tissue, including elastin, collagen, and reticular fibres as well as a few fibroblasts. The outer adventitial layer consists of dense fibrous connective tissue that is largely made up of 1–12 μm in diameter collagen fibres and thinner, 2–3 μm in diameter, elastin fibres. The cylindrical collagen and elastin fibres are ordered mainly along one axis, thus causing the tissue to be birefringent.

Another type of multilayered tissue in general similar to skin is woman cervical tissue consisting of the upper epithelial layer, basal layer (basal membrane), and stromal layer. However depending on the area of the cervix, the epithelium may be in one of two forms: squamous or columnar.

The gingival tissue (gums) also consists of the mucosal tissue that laying over the jawbone [78]. The gingival tissue is naturally transparent and rendered red in colour because of the blood flowing through tissue. It connected to the teeth and bone by way of the periodontal fibres and is divided in three portions: free gingiva which forms a cuff around tooth and is not attached to bone, attached gingiva which is connected to bone, and interdental papilla which is a pointed portion of gingiva between teeth. Healthy gingiva is characterized by pale to coral pink colour with some pigmentation in darker skinned individuals.

The pulp is a soft connective tissue at centre of tooth containing fibroblasts, collagen, blood vessels, nerves and dentin forming odontoblasts. The odontoblasts make more dentin to protect tooth under conditions of pulp insult, e.g. caries. The pulp provides tooth nutrition due to rich vascular supply.

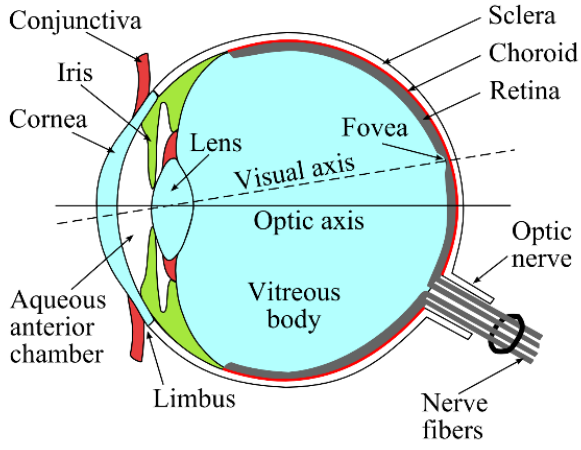


Fig. 7 Human eye structure and tissues.

Healthy tissues of the anterior human eye chamber (see Fig. 7), such as cornea and lens, are highly

transparent for visible light because of their ordered structure and the absence of strongly absorbing chromophores in this wavelength range [74-76, 79-85]. The human cornea is the frontal section of the eye's fibrous capsule with diameter of about 10 mm and averaged thickness of 0.5 mm. Its major layer constitutes 90% of the cornea's thickness is stroma, which is composed of several hundred successively stacked layers of lamellae (see Fig. 8, a-c), varied in width (0.5–250 μm) and thickness (0.2–0.5 μm) depending on the tissue region (electronic microscope images of three sequential lamellae are presented in Fig. 8, a). Within each lamella, all of the fibres are nearly in parallel with each other and with the lamella plane. Fibrils are immersed into an amorphous ground (interstitial) substance containing water, glycosaminoglycans, proteins, proteoglycans, and various salts. The glycosaminoglycans play a key role in regulating the assembly of the collagen fibrils as well as in tissue permeability to water and other molecules. A few flat cells (keratocytes) are dispersed between lamellae, cells' total volume fraction is only 3-5% of the stromal volume. The fibrils in the human cornea have a uniform diameter of about 30.8±0.8 nm with a periodicity close to two diameters, i.e., 55.3±4.0 nm, and rather high regularity in the organization of fibril axes about one another (see Fig. 8, a,c). The intermolecular spacing is of 1.63±0.10 nm [79-85]. Thus, corneal stroma has at least three levels of structural organization: the lamellae that lie parallel to the cornea′s surface, the fibrillar structure within each lamella that consists of small, parallel collagen fibrils with uniform diameters with a high degree of short-range spatial order, and the collagen molecular ultrastructure.

The sclera is a dense, white, fibrous membrane, which together with the cornea forms the external covering of the eyeball and serves as an eye protective membrane. It contains three layers: the episclera, the stroma and the lamina fusca. The stroma is the thickest layer of the sclera. In the scleral stroma, the collagen fibrils exhibit a wide range of diameters, from 25 to 230 nm [47, 82]. The average diameter of the collagen fibrils increases gradually from about 65 nm in the innermost part to about 125 nm in the outermost part of the sclera. The mean distance between fibril centres is about 285 nm. Collagen intermolecular spacing is similar to that in the cornea, in particular in bovine sclera, particularly, it is equal to 1.61±0.02 nm [83]. The fibrils are arranged in individual bundles in a parallel fashion, but more randomly than in the cornea. Within each bundle, the groups of fibres are separated from each other by large empty lacunae randomly distributed in space [82]. Collagen bundles show a wide range of widths (1 to 50 μm) and thicknesses (0.5 to 6 μm) and tend to be wider and thicker toward the inner layers. These ribbon-like structures are multiply crosslinked, their length can be a few millimetres. They cross each other in all directions, but remain parallel to the scleral surface. The episclera has a similar structure, with more randomly distributed and less compact bundles than in the stroma. The lamina fusca contains a larger amount of pigments, mainly melanin, which are generally located between the bundles.

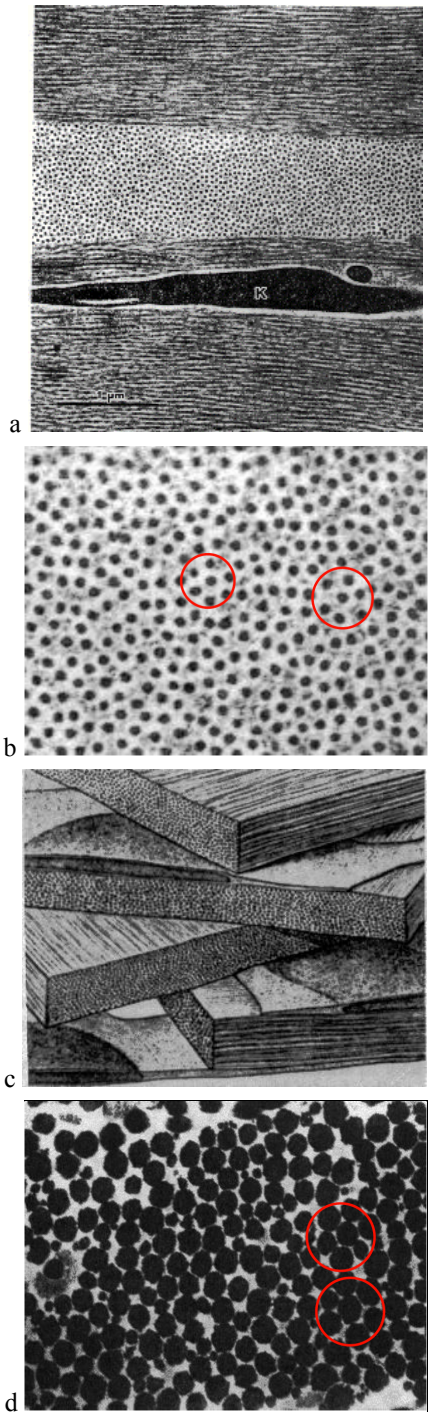


Fig. 8 The electron micrographs of the human cornea (×32,000) collagen fibrils have a uniform diameter and are arranged in the same direction within the lamellae, **K** is the keratocyte, b – presents magnified image of middle lamella of image a; c – presents the model of lamellar-fibrillar structure of the corneal stroma; d – presents scleral collagen fibrils, which display various diameters, however they are locally quasi-ordered [23, 58, 82].

The eye lens is also an example of a tissue in which the short-range spatial order is of crucial importance. Because of its high index of refraction and transparency, a lens focuses light to form an image at the retina (see Fig. 7). The eye lens material exhibits a certain viscosity that is capable of altering its radius of curvature and thus its focal length through the action of accommodating muscles. The healthy human lens is a structure containing about 60% of water and 38% of proteins. The lens consists of many fibre cells [88]. The predominant dry components of a mammalian lens are three kinds of structural proteins named α–, β–, and γ–crystallins, and their combined weight accounts for about 33% of the total weight of the lens [89]. The primary role is played by the water–soluble α–crystallin, which has a shape that is close to spherical with a diameter of about 17 nm. Age-related biochemical endogenous processes in the organism and exogenous environmental-related stresses, such as photooxidation of lens proteins at chronic UV or visible light, resulting in oxidized forms of these proteins and their crosslinking to other lens proteins, cause lens opacity due to light scattering and/or pigment formation.

The types of fibre cell disruption at cataract formation include intracellular globules, clusters of globules, vacuoles with the contents wholly or partially removed, clusters of highly curved cell membranes, and odd-shaped domains of high or low mass density. These spherical objects are variable in size (often in the range 100 to 250 nm) and occur in clusters that create potential scattering centres [88].

One more example of complex tissue structure is retinal nerve fibre layer (RNFL), which is formed by the expansion of the fibres of the optic nerve and comprises bundles of unmyelinated axons that run across the surface of the retina (see Fig. 7). Retina is the innermost coat of the posterior part of the eyeball that receives the image produced by the crystalline lens. It consists of several layers, one of which contains the rods and cones sensitive to light. The cylindrical organelles of the retinal nerve fibre layer are axonal membranes, microtubules, neurofilaments and mitochondria. Axonal membranes, like all cell membranes, are thin (6–10 nm) phospholipid bilayers that form cylindrical shells enclosing the axonal cytoplasm. Axonal microtubules are long tubular polymers of the protein tubulin with an outer diameter of ≈25 nm, an inner diameter of ≈15 nm, and a length of 10–25 μm. Neurofilaments are stable protein polymers with a diameter of ≈10 nm. Mitochondria are ellipsoidal organelles that contain densely involved membranes of lipid and protein. They are 0.1–0.2 μm thick and 1–2 μm long.

The brain and spinal cord together make up the central nervous system. Grey matter is a nervous tissue found in the central nervous system. It contains numerous cell bodies, dendrites, synapses, terminal processes of axons, blood vessels and neuroglia. Brain nuclei and nerve centres are composed of grey matter and coordination in the central nervous system is effected in grey matter. White matter is also a nervous tissue found in the central nervous system. It consists of tracts of medullated nerve fibres in the brain and spinal cord and also contains blood vessels and neuroglia. It is mainly external to grey matter, but is internal to grey matter in the cerebral hemispheres and in the cerebellum. The medullated fibres give the tissue its shiny white appearance. The spinal cord is a long, thin, tubular bundle of nervous tissue and supporting cells that extends from the brain (the medulla specifically) down to the space between the first and second lumbar vertebrae. It is around 45 cm in men and around 43 cm long in women. The brain and spinal cord is protected by three layers of tissue, called spinal *meninges*, that surround them.

The *dura mater* is the outermost layer, and it forms a tough protective coating. Between the *dura mater* and the surrounding bone of the skull or vertebrae is a space, called the epidural space, which is filled with adipose tissue, and it contains a network of blood vessels. The arachnoid is the middle protective layer, the space between the arachnoid and the underlying pia mater contains cerebrospinal fluid (CSF). The pia mater is the innermost protective layer, which is very delicate and tightly associated with the surface of the brain and spinal cord.

Dura mater is the tough and inflexible two layered tissue. A superficial layer is actually the bone inner *periosteum*, and a deep layer is the *dura mater proper*. *Dura mater proper* consists of layers of densely packed collagen fibrils having an alternating orientation (see Fig. 9).

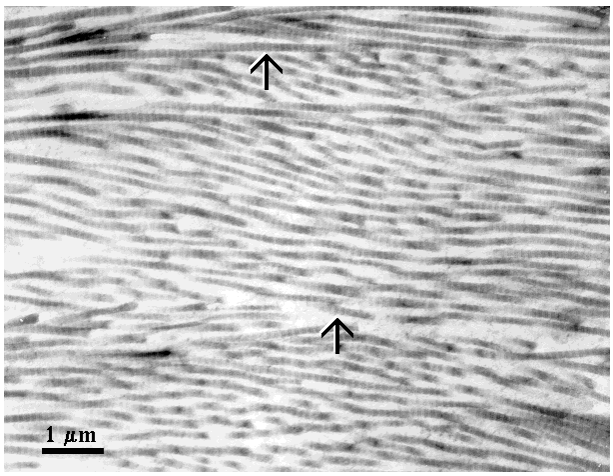


Fig. 9 Electronic micrograph of *dura mater proper* with layers of densely packed collagen fibrils having an alternating orientation and mean diameter of ~100 nm.

Tissue aging and pathology may dramatically change its structure and appearance. For example, scar tissue typically occupies areas of fibrous tissue that replace normal tissue (skin or other tissue) after injury [90, 91] (see Fig. 10). A scar results from the biologic process of wound repair. Thus, scarring is a natural part of the healing process. Other examples are benign or malignant tumours which are abnormally growing

tissues sometimes well vascularised and having the tendency to spread to other parts of the body.

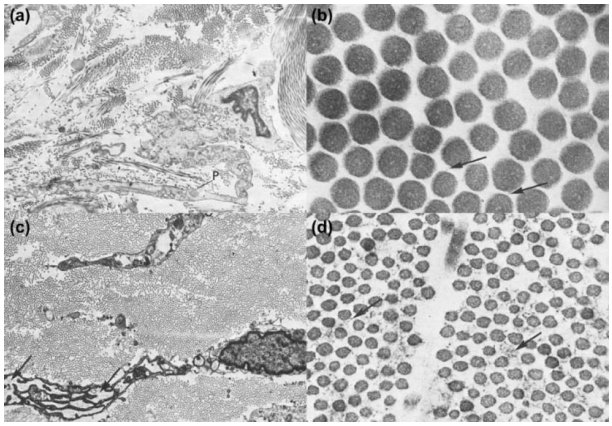


Fig. 10 Electronic micrographs of collagen fibers of normal skin (upper) [(a) and (b)] and nodule of a hypertrophic scar (down) [(c) and (d)] [magnification ×10,000 for (a) and (c) and ×105,000 for (b) and (d)] [90].

2.3 Hard tissue

The bone, tooth enamel, dentin, and cementum, as well as tendon and cartilage belong to hard tissue [22, 23, 40, 47, 58, 78, 92-99]. The bone, cartilage, and tendon are also connective tissues which typically consist of cells scattered in an amorphous mucopolysaccharide matrix in which there are varying amounts of connective tissue fibres (mainly collagen, but also elastin and reticulin).

In particular, the bone is a connective tissue forming the skeleton. It consists of cells embedded in a matrix of bone salts and collagen fibres. The bone salts (mostly calcium carbonate and phosphate, hydroxyapatite crystals) form about 60% of the mass of the bone and give it its tensile strength. Organic dry weight is 90% collagen which gives bone its elasticity and contributes to fracture resistance. In bone, entire collagen triple helices lie in a parallel, staggered array, with the 40 nm-gaps between the ends of the tropocollagen subunits, which probably serve as nucleation sites for the deposition of long, hard, fine crystals of the mineral component – hydroxyapatite with some phosphate. In this way, certain kinds of cartilage turn into bone.

The apatite or hydroxyapatite (HAP) natural crystals, $Ca_5OH(PO_4)_3$, is the major component of hard tissues. The dental enamel consists of 87–95% and bone of 50–60% of HAP crystals.

The osseous cells are interconnected by fine protoplasmic processes situated in narrow channels in the bone, and are nourished by the blood stream. This vascular nature of bone differentiates it from cartilage. The flexible tissue found in the hollow interior of bones is the bone marrow. Throughout life, all bones are in a dynamic process of growth and resorption called "remodelling." This allows the bone to adapt to changing mechanical forces and the body's need for calcium balance. The osteoblasts are mononucleate cells that are responsible for bone formation – reshaping.

The demineralization process is the loss of mineral from mineralized tissues such as bone or tooth. In tooth tissue, demineralization may lead to caries, in bone – to osteoporosis. For example, bacteria in tooth plaque use carbohydrates such as sucrose and glucose in human diet for their metabolic needs and produce lactic acid during the breakdown of these substrates. In its turn, lactic acid can demineralize the tooth hard tissue. The demineralization of outermost tooth layers – enamel and cementum is the starting point of tooth destruction. However, small amounts of tooth demineralization occur daily – remineralization can be occur as mineral is replaced with calcium and phosphate from saliva.

The osteoporosis is a disease of bone causing an increased risk of fracture due to reduction of bone mineral density, which leads to bone microarchitecture disruption, and alteration of the amount and variety of non-collagenous proteins in bone.

As an example of bone structure, an alveolar bone that is a part of upper and lower jaws, which holds roots of teeth, is shown in Fig. 11, a [47, 78]. It consists of two parts: *lamina dura* (alveolar bone proper) – dense bone lining socket with inserted periodontal fibres, and supporting bone which is a remaining part of alveolar bone composed from highly mineralized (70%) – mostly calcium phosphate (hydroxyapatite) crystals, minor amounts of magnesium, sodium and potassium, osteoblasts and osteoclasts, collagen fibres, and proteoglycans.

The periodontal ligament is a fibrous connective tissue attachment anchoring tooth to surrounding bone. The collagen fibres are embedded on tooth side in cementum and on bone side in *lamina dura*. It mainly composed of collagen with minor amounts of elastin, and ground substance – proteoglycans and water. This tissue contains such cells as fibroblasts, osteoblasts and cementoblasts, immune cells (e.g., macrophages, lymphocytes), nerves and is supplied by blood via blood vessels.

Tooth is the hard body composed of dentin surrounding a sensitive pulp and covered on the crown with enamel (see Fig. 11, a). Crown is a portion of natural tooth visible in mouth above gumline. Tissue layers from outside in are enamel, dentin, and pulp. Root is a portion of tooth under gumline, anchoring tooth in bone, layers from outside in are cementum, dentin, and pulp.

The enamel is a hardest tissue in a body, elastic, white material that contains no cells and that is an almost completely inorganic substance. The enamel covers the crown of a tooth and consists of up to 95% of natural HAP crystals and rest are water and proteins. These crystals are organized in keyhole-shaped interlocking rods/prisms. The rods are formed as enamel forming ameloblasts migrate towards outer layer of tooth, once enamel is formed, ameloblasts die, thus if enamel is destroyed, it cannot be regenerated. These rods/prisms are 4–6 μm wide and extend from the dentine-enamel-junction to the outer surface of the tooth (see Fig.11). Because of their size, number, and

refractive index, the prisms are the main light scatterers in enamel. The enamel is translucent and greyish white in colour and it has yellow hue due to underlying dentin.

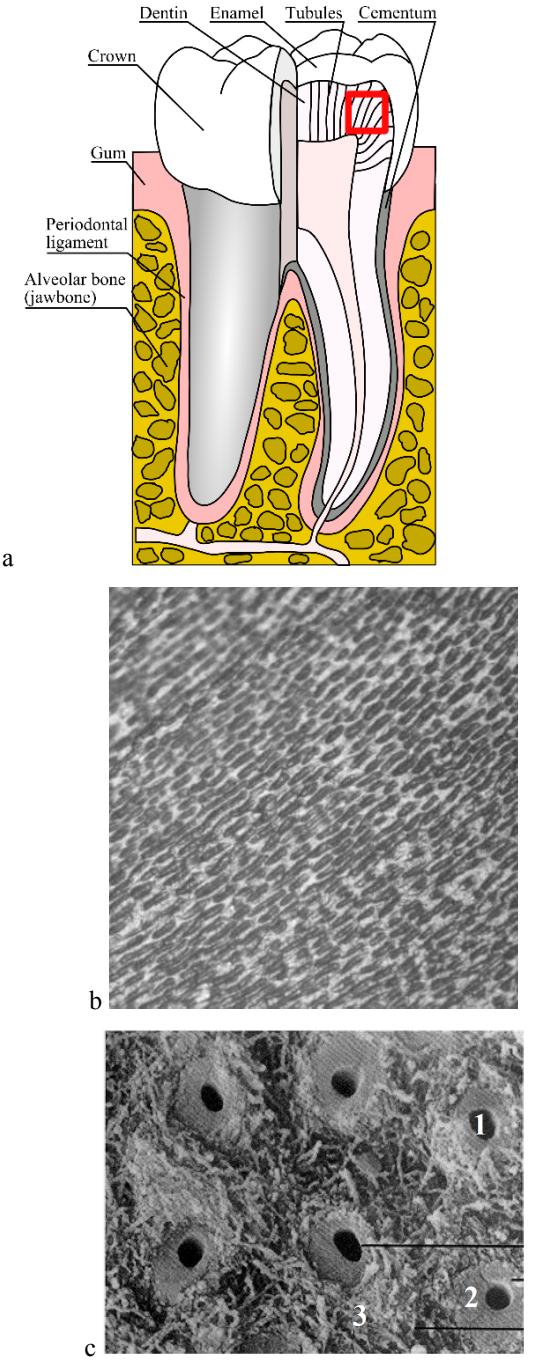


Fig. 11 Schematic representation of tooth structure, including dentinal channels – tubules (a); laser scanning microscopy image of dentinal tubules (~ 90×90 μm) (b) [97]; electron scanning micrograph of human dentin (presented by R. Vilar): (1) dentinal tubules, (2) dense and homogeneous pertubular dentin and (3) less dense and less homogeneous intertubular dentin (c).

The tooth dentin is a hard, middle calcified, elastic, yellowish material of the same substance as bone. It is the main structural part of a tooth extending from crown to root. The dentin is composed of base material that is pierced by mineralized dentinal tubules 1–5 μm in diameter which makes it porous (see Fig.11, c). The tubules' density is in the range of $(3.0–7.5)\times10^6$ cm^{-2}. They contain organic components and natural HAP crystals of 2.0–3.5 nm in diameter and up to 100 nm in length, which intensively scatter light. In average dentin contains 70% HAP crystals, 20% proteins (e.g., collagen), and 10% water. It is softer than enamel but slightly harder than bone. Unlike enamel, dentin is living tissue – cells which form dentin (odontoblasts) lie at border of dentin and pulp during the life of tooth – this gives dentin ability to grow and repair.

The tooth cementum is a thin, pale yellow, calcified bone-like layer covering root of tooth. It contains 45% HAP crystals, 55% protein (collagen) and water. It is softer than both dentin and bone. The cementum functions include coverage of the dentin tubules and insertion point of periodontal ligament fibres. It has ability to form throughout life of tooth cementoblasts which form cementum lie along root surface in periodontal ligament space.

The cartilage is a strong, resilient, skeletal tissue. There are a few types of cartilage, all of which contain chondroblasts depositing the matrix and becoming enclosed in the matrix as chondrocytes. The hyaline cartilage is the simplest and most common form that consists of a matrix of a polysaccharide-containing protein. The matrix is without structure and without blood vessels. It is more or less translucent and clear, and occurs in the cartilaginous rings of the trachea and bronchi. The yellow fibrocartilage (elastic cartilage) contains yellow fibres in the matrix. It occurs in the external ear and in the epiglottis. As well as white fibrocartilage contains white fibres in the matrix and occurs in the disks of cartilage between the vertebrae. Articular cartilage itself and cartilage-bone interface play a highly important role in normal function of joints by dissipating stresses and providing almost frictionless joint movement [94].

The tendon is a cord of white fibrous tissue. It usually attaches muscle to bones and consists mostly of parallel, densely packed collagen fibres arranged in parallel bundles interspersed with long, elliptical fibroblasts. In general, tendon fibres are cylindrical in shape with diameters ranging from 20 to 400 nm. The ordered structure of collagen fibres running parallel to a single axis makes tendon a highly optically birefringent tissue [100].

2.4 Tissue structural anisotropy

As it follows from the analysis of tissue properties, many biological tissues are structurally anisotropic. Tissue birefringence results primarily from the linear anisotropy of fibrous structures, which forms the extracellular media. The refractive index of a medium is higher (speed of light is lower) along the length of fibres than along their cross section. A specific tissue structure is a system composed of parallel cylinders that create a uniaxial birefringent medium with the optic axis parallel

to the cylinder axes. This is a so-called birefringence of form (Fig. 12). A large variety of tissues such as eye cornea, tendon, cartilage, eye sclera, *dura mater*, muscle, myocardium, artery wall, nerve, retina, bone, teeth, myelin, etc. exhibit birefringence. All these tissues contain uniaxial and/or biaxial birefringent structures. For example, myocardium contains fibres oriented along two different axes. It consists mostly of cardiac muscle fibres arranged in sheets that wind around the ventricles and atria. Since the refractive index along the axis of the cardiac muscle fibres is different from that in the transverse direction, tissue is birefringent.

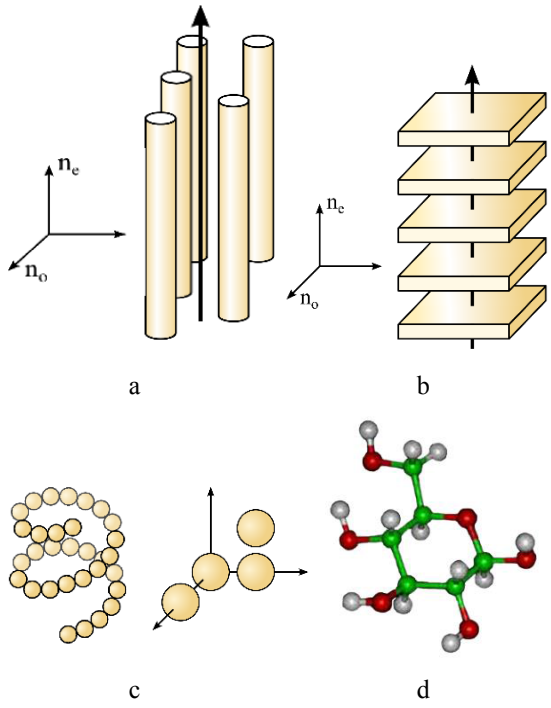


Fig. 12 Examples of structurally anisotropic models of tissues and tissue components: a – system of long dielectric cylinders; b – system of dielectric plates; c – chiral aggregates of particles; d – glucose (chiral molecule) as a tissue component [23, 58].

Form birefringence arises when the relative optical phase between the orthogonal polarization components is nonzero for forward-scattered light. For linear structures, an increase in optical field phase delay (δ_{oe}) is characterized by a difference in the effective refractive index for light polarized along, and perpendicular to, the long axis of the linear structures (Δn_{oe}). Phase retardation δ_{oe} between orthogonal polarization components, is proportional to the distance d travelled through the birefringent medium [23, 58]

$$\delta_{oe} = \frac{2\pi d \Delta n_{oe}}{\lambda_0}. \qquad (10)$$

A structure of parallel dielectric cylinders immersed in isotropic homogeneous ground substance behaves as a positive uniaxial birefringent medium ($\Delta n_{oe} = (n_e - n_o) > 0$) with its optic axis parallel to the cylinder axes (Fig. 12, a). Therefore, an incident electrical field directed parallel to the cylinder axes will be called "extraordinary ray" (e) and the incident electrical field perpendicular to the cylinder axes will be called "ordinary ray"(o). The difference (n_e - n_o) between the indices of refraction of the extraordinary and ordinary rays is a measure of the birefringence of a medium. For the Rayleigh limit (diameter of cylinders << l), the form birefringence is described as

$$\Delta n_{oe} = (n_e - n_o) = \frac{f_1 f_2 (n_1 - n_2)^2}{f_1 n_1 + f_2 n_2}, \qquad (11)$$

where f_1 is the volume fraction of the cylinders; f_2 is the volume fraction of the ground material; and n_1, n_2 are the corresponding indices. For a given difference of refraction index (n_1 – n_2), maximal birefringence is expected for approximately equal volume fractions of thin cylinders and ground material. For systems with high volume fraction of cylinders or on the contrary ground material (rare fibres), the birefringence goes down.

The experimental birefringence for muscle, coronary artery, myocardium, sclera, skin, cartilage and tendon is in the range from 1.4×10^{-3} to 4.2×10^{-3}. For these tissues, it is lowest for the muscle and highest for the tendon. For thermally treated tendon, it is twice lower than for intact tissue.

The diattenuation (linear dichroism) is the difference of attenuation of two waves with orthogonal polarizations travelling in an anisotropic medium, which is described by the difference between the imaginary (losses) parts of the effective indices of refraction for two orthogonal directions. Depending on the relationship between the sizes and the optical properties of the cylinders or plates, this difference can take positive or negative values.

The birefringence and diattenuation relate to the density and some other properties of the collagen fibres, whereas the orientation of the fast axis indicates the orientation of the collagen fibres. The densities of collagen fibres in skin and cartilage are not as uniform as in tendon, and the orientation of the collagen fibres is not distributed as orderly as in tendon. Correspondingly, the amplitude and orientation of birefringence of the skin and cartilage are not as uniformly distributed as in tendon.

In addition to linear birefringence and diattenuation, many tissue components show optical activity (circular birefringence) and circular diattenuation. In complex tissue structures, chiral aggregates of particles may be responsible for tissue optical activity (see Fig. 12, c). The molecule's chirality, which stems from its asymmetric molecular structure (see Fig. 12, d), also results in a number of effects generically called optical activity. A well-known manifestation of optical activity is the ability to rotate the plane of linearly polarized light about the axis of propagation. The amount of rotation depends on the chiral molecular concentration, the pathlength through the medium, and the light

wavelength. Interest in tissue chirality studies is driven by the potential of noninvasive *in situ* optical monitoring of the glucose in diabetic patients.

More sophisticated anisotropic tissue models can also possible. For example, the eye cornea can be represented as a system of plane anisotropic layers (plates, i.e., lamellas), each of which is composed of densely packed long cylinders (fibrils) (see Fig. 8, c) with their optical axes oriented along a spiral. This fibrilar-lamellar structure of the cornea is responsible for the linear and circular diattenuation and its dependence on the angle between the lamellas.

In bone and tooth, anisotropy is due to mineralized structures originating from hydroxyapatite crystals, which play an important role in hard tissue birefringence. In particular, dental enamel is an ordered array of such crystals surrounded by a protein/lipid/water matrix. Fairly well oriented hexagonal crystals of hydroxyapatite of approximately 30–40 nm in diameter and up to 10 μm in length are packed into an organic matrix to form enamel prisms (or rods) with an overall cross section of 4–6 μm. Enamel prisms are roughly perpendicular to the tooth surface (see Figs. 11 and 13). Tooth dentin is a complex structure, honeycombed with dentinal tubules, which are shelled organic cylinders with a highly mineralized shell.

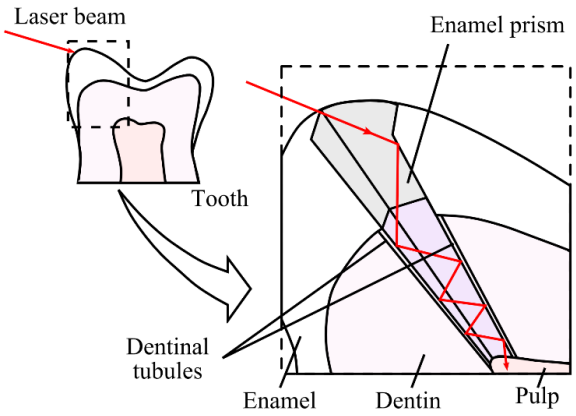


Fig. 13 Schematic representation of laser beam waveguiding in human tooth tissues [97].

Enamel and dentin waveguide properties also may have effects on anisotropy of light transportation within a tooth. The role of waveguides in enamel and dentin is played by enamel prisms and intertubular butt straps, respectively (Fig. 13). These waveguides are distinguished from conventional optical fibers by being nonuniform and containing scattering particles, such as hydroxyapatite microcrystals. However, they have waveguide properties and radiation scattered in enamel and dentin can be entrapped by these natural waveguides and transported to the pulp chamber.

2.5 Blood, lymph and other bioliquids

The blood is a fluid tissue contained in a network of vessels or sinuses in humans and animals. Blood is circulating through the network by muscular action of the vessels or the heart to transport oxygen, metabolites, and hormones. It also assists in temperature control in mammals [23, 47, 58, 101-103].

Blood contains soluble colloidal proteins (blood plasma) and blood corpuscles (blood cells) such as red blood cells (RBCs) (erythrocytes), white blood cells (WBCs) (leukocytes), and platelets (thrombocytes). Normally, blood has about 10 times as many erythrocytes as platelets and about 300 times as leukocytes. There are approximately five million per cubic millimetre RBCs in normal human blood.

A normal erythrocyte in plasma has the shape of a concave-concave disc with a diameter varying from 7.1 to 9.2 μm, a thickness of 0.9–1.2 μm in the centre and 1.7–2.4 μm on the periphery, and a volume of 90 μm^3. Platelets in the blood stream are biconvex disk-like particles with diameters ranging from 2 to 4 μm. Leukocytes are formed like spheres with a diameter of 8-22 μm.

The platelets are small, non-nucleated, round or oval disks that are fragments of cells from red bone marrow. There are approximately 200,000–400,000 per mm^3 platelets in human blood. These cells initiate blood clotting by disintegrating and releasing thrombokinase.

WBCs are nucleated, motile, colourless cells found in the blood and lymph of animals. A WBC is either a lymphocyte, a polymorph, or a monocyte. In humans, there are approximately 8000 leukocytes per cubic millimetre. A lymphocyte is a spherical WBC with one large nucleus and relatively little cytoplasm. Two types exist, small and large lymphocytes which are produced continually in lymphoid tissues, such as lymph nodes, by cell division. The cells are nonphagocytic, exhibit amoeboid movement, and produce antibodies in the blood. They constitute about 25% of all leukocytes in the human body. A monocyte is a spherical WBC with an oval nucleus. The monocytes are the largest of the WBCs. The cells are voraciously phagocytic and exhibit amoeboid movement. They are produced in lymphoid tissues and constitute about 5% of all leukocytes.

The relative volume of the RBCs in blood expressed in percentages is named hematocrit (Hct). It also can be presented as packed cell volume (PCV) or erythrocyte volume fraction (EVF). Hct is normally about 48% for men and 38% for women and independent of body size and considered as an integral part of a person's complete blood count results.

To provide the main function of RBC to carry oxygen and carbon dioxide away from and towards the lung, cell contains a respiratory pigment, haemoglobin. The cell is readily distorted, elastic, and immotile. Mammalian RBCs have no nuclei. They are formed in red bone marrow and after a relatively short life span (in average 120 days in humans) are destroyed by erythrophages. RBC index of refraction is of 1.4 in the wavelength range 600 to 1100 nm.

The haemoglobin is a red iron-containing respiratory pigment. It consists of haeme combined with globin, a blood protein and conveys oxygen to the tissues. The

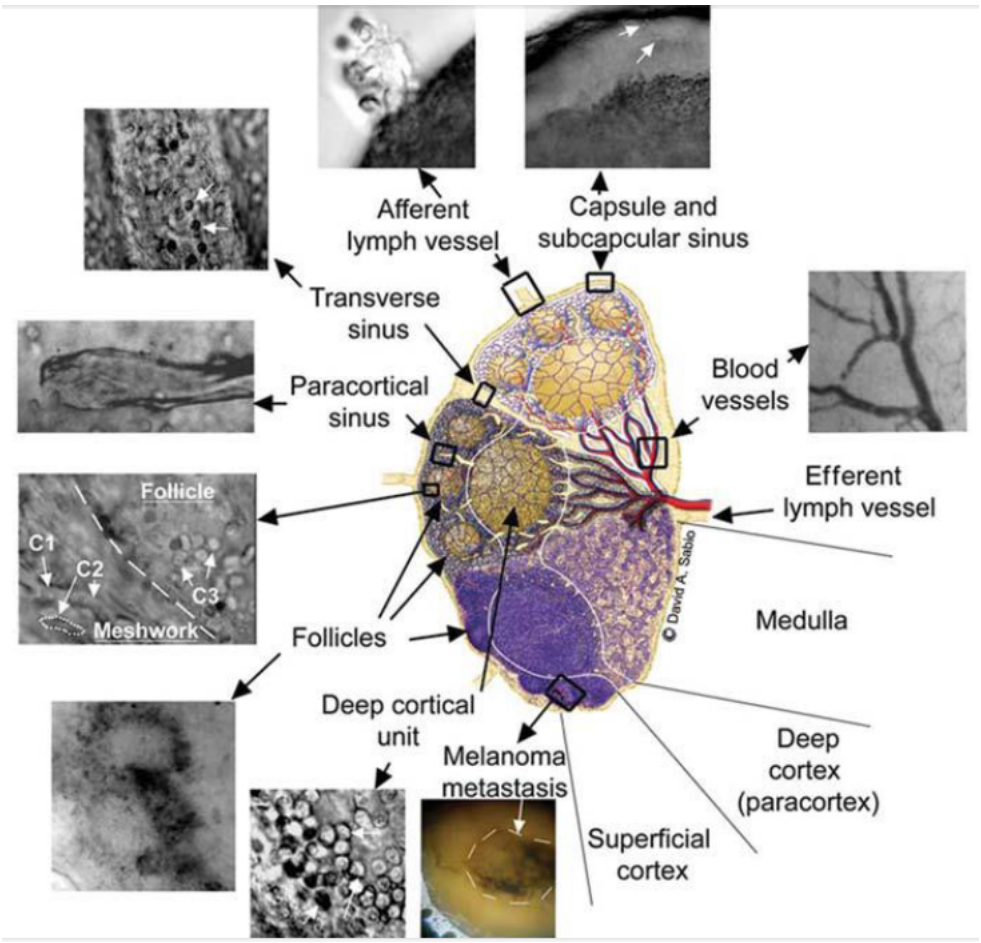


Fig. 14 The schematics of microanatomy of a lymph node designed by David Sabio presenting a midsagital section of a lymph node containing three lymphoid lobules with the basic anatomical and functional units, including superficial cortex, deep cortex and medulla, is shown (drawing in the centre). Experimental transillumination digital images of afferent lymph vessel, subcapsular, transverse, and paracortical sinuses, deep cortical unit, a reticular meshwork, follicles, and the venous vessels around central schematics are also shown: C1 presents likely basophilic lymphocytes; C2 – elongated fibroblastic reticular cells, and C3 – B lymphocytes and follicular dendritic cells; melanoma metastasis is seen in the back reflectance image [104].

haemoglobin occurs in reduced form (deoxyhaemoglobin, Hb) in venous blood and in combination with oxygen (oxyhaemoglobin, HbO_2) in arterial blood. The total haemoglobin (THb) is the sum concentration of the oxy- and deoxyhaemoglobin.

Oxyhemoglobin dissociation ability is described by dissociation curve that characterizing the relationship between oxygen partial pressure pO_2 and oxygen saturation (SaO_2). Normally about 97% of the oxygen is carried by haemoglobin whereas only 3% is carried dissolved in the blood. As the pO_2 increases, the amount of oxygen that is bound to haemoglobin, or the percent saturation of haemoglobin, also increases. The saturation of haemoglobin of about 50% and 97% is normally achieved at a pO_2 of about 26.6 mmHg and 95 mmHg, respectively, and the saturation point, SaO_2, at pO_2 = 80 mmHg. In the capillaries normally the haemoglobin is about 75% saturated and the blood delivers about 5 ml of oxygen per 100 ml of blood to the tissues. In tissues haemoglobin oxygen saturation is calculated as $SaO_2 = (HbO_2/THb)\times 100\%$.

The carboxyhemoglobin (COHb) is a stable complex of carbon monoxide and haemoglobin (bright, cherry red in colour) that forms in RBCs when carbon monoxide is inhaled or produced in normal metabolism. Because haemoglobin binds with carbon monoxide 240 times more readily than with oxygen, large quantities of it hinder delivery of oxygen to the body.

The blood plasma is the clear, waterlike, colourless liquid of blood which is formed by removing all blood corpuscles from blood.

The blood vessel is a tube through which blood flows either to or from the heart. The general terms for conducting vessels for blood are arteries, veins, arterioles, venules, and capillaries.

For *in vitro* microscopic examination of blood a well prepared blood smear is necessary. The simple wedge technique for preparation of blood smears is often applied. This simple technology is used to determine leukocyte differentials, to evaluate erythrocyte, platelet and leukocyte morphology, and, if necessary, to estimate platelet and leukocyte counts. This technique

produces a gradual decrease in thickness of the blood from thick to thin ends with the smear placed on the slide. In typical preparations, the thin section of the smear occupies approximately 1/3 of the total area and, within that area erythrocytes are distributed in a monolayer. Glass coverslips are mounted on all blood smears to prevent damage to smear during examination, cleaning, handling and storage.

The lymph in the organism is an alkaline colourless liquid obtained from blood by filtration through pores in the walls of capillaries. It contains a smaller amount of soluble blood proteins and WBCs than blood, but more lymphocytes. Normally it contains no RBCs. The lymph travels to at least one lymph node before emptying ultimately into the right or the left subclavian vein, where it mixes back with blood. The lymph that leaves a lymph node is richer in lymphocytes, as the lymph formed in the digestive system called chyle is rich in triglycerides (fat), and looks milky white. The lymph function is to bathe the cells with water and nutrients.

The lymphatic system is a network which includes the lymphoid tissue and lymphatic vessels through which the lymph travels in one-way toward the heart as well as all the structures providing the circulation and production of lymphocytes [103,104]. Lymph is formed when interstitial fluid enters the initial lymphatic vessels of the lymphatic system which transport lymph back to the blood, ultimately replacing the volume lost during the formation of the interstitial fluid. In contrast to the cardiovascular system, the lymphatic system is not closed and has no central pump. The lymph transport, therefore, is slow and sporadic, like a shuttle-stream, and occurs due to alternate contraction and relaxation of smooth muscles, valves, and compression during contraction of adjacent skeletal muscle and arterial pulsation. The study of lymphatic drainage of various organs is important in diagnosis, prognosis, and treatment of cancer. The lymphatic system, because of its physical proximity to many tissues of the body, is responsible for carrying cancerous cells between the various parts of the body in a process called metastasis. The intervening lymph nodes can trap the cancer cells (sentinel lymph node). If they are not successful in destroying the cancer cells, the nodes may become sites of secondary tumours.

The lymphoid tissue is a part of the lymphatic system and consists of connective tissue with various types of WBCs enmeshed in it, most numerous being the lymphocytes. The thymus and the bone marrow constitute the primary lymphoid tissues involved in the production and early selection of lymphocytes. The secondary lymphoid tissues are the lymph nodes, and the lymphoid follicles in tonsils, spleen, adenoids, skin, etc.

The lymphatic vessels (lymphatics) are thin-walled tubular vessels resembling veins in structure but with thinner walls and more valves. The walls are enclosed by smooth muscle and connective tissue. Lymphatic vessels drain into lymph ducts. The lymphatic vessels act as channels along which pathogens are conducted from infected areas of the body, the pathogens being unable to enter the blood capillaries. The lymph nodes are distributed along the lymphatic vessels.

The cerebrospinal fluid (CSF) is the clear liquid that fills the cavities of the brain and spinal cord and the spaces between the arachnoid and pia matter. The fluid moves in a slow current down the central canal and up the spinal meninges. It is a solution of blood solutes of low molar mass, such as glucose, but of the smaller concentration (60-80%) as in the blood. The CSF contains little or no protein and very few cells. Its function is to nourish the nervous tissue and to act as a buffer against shock to the nervous tissue. At any one time in an adult, the average volume of CSF is about 150 ml.

The saliva is a viscid, colourless, watery fluid secreted into the mouth by the salivary glands and composed from water (99%), mucin, bicarbonate, proteins, and minerals. It functioning as lubricator to protect mucosa, it assists in formation of food bolus for effective swallowing, in initial enzymatic breakdown of some food components, antimicrobial protection, buffering, and tooth enamel remineralization. There are 3 major salivary glands and hundreds of minor salivary glands in the oral cavity. The amount of saliva produced varies widely – in healthy individuals it ranges from 0.5 – 1.5L daily.

The mucus is a thin, slimy, viscous liquid secreted by epithelial cells in tissues or glands. It protects and lubricates the surface of structures, e.g., the internal surfaces of the greater part of the alimentary canal are lubricated with mucus.

The tear film on the surface of the eye also has some diagnostic potential due to correlation of tear and blood glucose concentrations [105]. It is composed of several layers. Most superficially there is a lipid layer that is less than 100 nm thick which serves several functions including preventing evaporation of the underlying aqueous layer and providing a smooth optical surface over the cornea. The lipid layer is composed of sterol esters, wax esters, and many other minor lipid components secreted from the Meibomian glands located on the margins of the eyelids. Dysfunction of these glands can lead to increased evaporation of tears from the eye, causing an increased tear osmolarity and clinical dry eye. Just below the lipid layer is a predominantly aqueous layer. Measurements of the thickness of this layer over the cornea varies from 2.7 μm to 46 μm.

2.6 Conclusion

This is the first section of the review-tutorial paper describing fundamentals of tissue optics and photonics mostly devoted to biological tissue structures and their specificity related to light interactions at its propagation in tissues. The next sections of the paper will describe light-tissue interactions caused by tissue dispersion, scattering, and absorption properties, including light reflection and refraction, absorption, elastic quasi-elastic and inelastic scattering. The major tissue

absorbers and types of elastic scattering, including Rayleigh and Mie scattering, will be presented.

Basing on the random phase screen concept, scattering of the coherent light and speckle formation principles will be discussed. Speckle interferometry and low-coherent light interferometry – optical coherence tomography (OCT), will be described.

Dynamic light scattering method as a powerful approach for functional spectroscopy and imaging of living tissues will be analysed. Fundamentals of quasi-elastic light scattering (QELS), Doppler anemometry, and dynamic speckle techniques and their applications to blood and lymph flow measurements, including full-field velocity mapping, will be discussed. Principles of diffusion wave spectroscopy and imaging, interaction of the polarized light with tissues for random and quasi-ordered tissues will be presented. Comparison of single and multiple scattering approaches, as well as description of refractive index matching concept for controlling of light interaction with tissues, will be done.

Acknowledgments

I am thankful to Valery Zakharov for his idea to write such a paper, to all my colleagues from SSU and IPMC RAS for fruitful collaboration, and to Alexander Kalyanov for help in preparation of illustrations. This work was supported by Russian Presidential grant NSh-703.2014.2, the Government of the Russian Federation grant 14.Z50.31.0004, and the Ministry of Education and Science of the Russian Federation

Optical clearing of biological tissues: prospects of application in medical diagnostics and phototherapy

E.A. Genina[1,2*], A.N. Bashkatov[1,2], Yu.P. Sinichkin[1], I.Yu. Yanina[3], V.V.Tuchin[1,2,4]

[1] N.G. Chernyshevsky Saratov State University, 83 Astrakhanskaya Str., Saratov, 410012, Russia

[2] Tomsk State University, 36 Prosp. Lenina, Tomsk, 634050, Russia

[3] V.I. Razumovsky Saratov State Medical University, 112 Bolshaya Kazachya Str., Saratov, 410012, Russia

[4] Institute of Precision Mechanics and Control, Russian Academy of Sciences, 24 Rabochaya Str., Saratov, 410028, Russia

* **e-mail:** eagenina@yandex.ru

Abstract. A review of specific features and methods of optical clearing and related interaction of light with tissues is presented. Physical and molecular mechanisms of immersion, compression, and photodynamic/photothermal optical clearing of some fibrous and cellular tissues are discussed. The possibility of efficient control of the tissue optical properties, particularly, the reduction of light scattering in tissues is demonstrated, which facilitates the increased efficiency of various optical visualisation methods (optical biopsy) used in medical purposes. © 2015 Samara State Aerospace University (SSAU).

Keywords: tissue, optical clearing, optical diagnostics, imaging.

Paper #1992 received 2014.12.26; revised manuscript received 2015.02.03; accepted for publication 2015.02.05; published online 2015.03.28.

References

1. V. V. Tuchin (Ed.), Handbook of Optical Biomedical Diagnostics, SPIE Press, PM107, Bellingham (2002).
2. T. Vo-Dinh (Ed.), Biomedical Photonics Handbook, CRC Press, Boca Raton, FL, USA (2003); second edition (2014).
3. V. V. Tuchin, Tissue Optics: Light Scattering Methods and Instruments for Medical Diagnosis, Bellingham, SPIE Press (2015).
4. D. A. Boas, "A fundamental limitation of linearized algorithms for diffuse optical tomography," Opt. Express. 1, 404-413 (1997).
5. C. L. Smithpeter, A. K. Dunn, A. J. Welch, and R. Richards-Kortum, "Penetration depth limits of *in vivo* confocal reflectance imaging," Appl. Opt. 37, 2749–2754 (1998).
6. V. V. Tuchin, L. V. Wang, and D. A. Zimnyakov, Optical Polarization in Biomedical Applications, Springer-Verlag, New York, NY, USA (2006).
7. R. Drezek, A. Dunn, and R. Richards-Kortum, "Light scattering from cells: finite-difference time-domain simulations and goniometric measurements," Appl. Opt. 38(16), 3651–3661 (1999).
8. K. Sokolov, R. Drezek, K. Gossagee, and R. Richards-Kortum, "Reflectance spectroscopy with polarized light: is it sensitive to cellular and nuclear morphology," Opt. Express 5, 302–317 (1999).
9. D. W. Leonard, and K. M. Meek, "Refractive indices of the collagen fibrils and extrafibrillar material of the corneal stroma," Biophysical J. 72, 1382–1387 (1997).
10. A. G. Borovoi, E. I. Naats, and U. G. Oppel, "Scattering of light by a red blood cell," J. Biomed. Opt. 3, 364–372 (1998).
11. A. N. Yaroslavsky, A. V. Priezzhev, J. Rodriguez, I. V. Yaroslavsky, and H. Battarbee, "Optics of blood," Chap. 2 in Handbook of Optical Biomedical Diagnostics, V. V. Tuchin, Ed., pp. 169–216, PM107 SPIE Press, Bellingham, WA, USA (2002).
12. G. Mazarevica, T. Freivalds, and A. Jurka, "Properties of erythrocyte light refraction in diabetic patients," J. Biomed. Opt. 7, 244–247 (2002).
13. M. Friebel, and M. Meinke, "Model function to calculate the refractive index of native hemoglobin in the wavelength range of 250–1100 nm dependent on concentration," Appl. Opt. 45(12), 2838–2842 (2006).

14. E. Gratton, "Deeper tissue imaging with total detection," Science 331, 1016–1017 (2011).
15. W. Denk, J. H. Strickler, and W. W. Webb, "Two-photon laser scanning fluorescence microscopy," Science, 248, 73–76 (1990).
16. C. A. Combs, A. Smirnov, D. Chess, D. B. Mcgavern, J. L. Schroeder, J. Riley, S. S. Kang, M. Lugar-Hammer, A. Gandjbakhche, J. R. Knutson, and R. S. Balaban, "Optimizing multiphoton fluorescence microscopy light collection from living tissue by noncontact total emission detection (epiTED)," J. Microsc. 241(2), 153–161 (2011).
17. C. A. Combs, A. V. Smirnov, J. D. Riley, A. H. Gandjbakhche, J. R. Knutson, and R. S. Balaban, "Optimization of multiphoton excitation microscopy by total emission detection using a parabolic light reflector," J. Microsc. 228(3), 330–337 (2007).
18. R. K. Wang, and V. V. Tuchin, "Optical coherence tomography. Light scattering and imaging enhancement," Chap. 16 in Handbook of Coherent-Domain Optical Methods. Biomedical Diagnostics, Environmental Monitoring, and Material Science, 2nd ed., V. V. Tuchin, Ed., pp. 665-742, New York, Heidelberg, Dordrecht, London: Springer (2013).
19. L. V. Wang, and S. Hu, "Photoacoustic tomography: in vivo imaging from organelles to organs," Science 335, 1458–1462 (2012).
20. Y. M. Liew, R. A. McLaughlin, F. M. Wood, and D. D. Sampson, "Reduction of image artifacts in three-dimensional optical coherence tomography of skin *in vivo*," J. Biomed. Opt. 16(11), 116018 (2011).
21. V. V. Tuchin, "A clear vision for laser diagnostics (Review)," IEEE J. Sel. Top. Quantum Electron. 13, 1621–1628 (2007).
22. V. V. Tuchin, Optical Clearing of Tissues and Blood, SPIE Press, Bellingham, WA, USA (2006).
23. R. Cicchi, F. S. Pavone, D. Massi, and D. D. Sampson, "Contrast and depth enhancement in two-photon microscopy of human skin *ex vivo* by use of optical clearing agents," Opt. Exp. 13, 2337–2344 (2005).
24. S. Plotnikov, V. Juneja, A. B. Isaacson, W. A. Mohler, and P. J. Campagnola, "Optical clearing for improved contrast in second harmonic generation imaging of skeletal muscle," Biophys. J. 90, 328–339 (2006).
25. E. A. Genina, A. N. Bashkatov, Yu. P. Sinichkin, and V. V. Tuchin, "Optical clearing of the eye sclera *in vivo* caused by glucose," Quantum Electronics 36(12), 1119-1124 (2006).
26. G. Vargas, J. K. Barton, and A. J. Welch, "Use of hyperosmotic chemical agent to improve the laser treatment of cutaneous vascular lesions," J. Biomed. Opt. 13(2), 021114 (2008).
27. M. H. Khan, S. Chess, B. Choi, K. M. Kelly, and J. S. Nelson, "Can topically applied optical clearing agents increase the epidermal damage threshold and enhance therapeutic efficacy?," Lasers Surg. Med. 35, 93–95 (2004).
28. P. D. Agrba, M. Yu. Kirillin, A. I. Abelevich, E. V. Zagaynova, and V. A. Kamensky, "Compression as a method for increasing the informativity of optical coherence tomography of biotissue," Optics and Spectroscopy 107(6), 853-858 (2009).
29. C. Drew, T. E. Milner, and C. G. Rylander, "Mechanical tissue optical clearing devices: evaluation of enhanced light penetration in skin using optical coherence tomography," J. Biomed. Opt. 14(6), 064019 (2009).
30. N. Guzelsu, J. F. Federici, H. C. Lim, H. R. Chauhdry, A. B. Ritter, and T. Findley, "Measurement of skin strech via light reflection," J. Biomed. Opt. 8, 80–86 (2003).
31. C. G. Rylander, O. F. Stumpp, T. E. Milner, N. J. Kemp, J. M. Mendenhall, K. R. Diller, and A. J. Welch, "Dehydration mechanism of optical clearing in tissue," J. Biomed. Opt. 11, 041117 (2006).
32. T. Yu, X. Wen, V. V. Tuchin, Q. Luo, and D. Zhu, "Quantitative analysis of dehydration in porcine skin for assessing mechanism of optical clearing," J. Biomed. Opt. 16, 095002 (2011).
33. W.-C. Lin, M. Motamedi, and A. J. Welch, "Dynamics of tissue optics during laser heating of turbid media," Appl. Opt. 35(19), 3413–3420 (1996).
34. D. Zhu, J. Wang, Z. Zhi, X. Wen, and Q. Luo, "Imaging dermal blood flow through the intact rat skin with an optical clearing method," J. Biomed. Opt. 15, 026008 (2010).
35. K. V. Larin, M. G. Ghosn, A. N. Bashkatov, E. A. Genina, N. A. Trunina, and V. V. Tuchin, "Optical clearing for OCT image enhancement and in-depth monitoring of molecular diffusion," IEEE J. Select. Tops. Quantum Electron. 18, 1244–1259 (2012).
36. D. Zhu, K. Larin, Q. Luo, and V. V. Tuchin, "Recent progress in tissue optical clearing," Laser & Photonics Reviews 7(5), 732-757 (2013).
37. V. A. Doubrovskii, I. Yu. Yanina, and V. V. Tuchin, "Kinetics of changes in the coefficient of transmission of the adipose tissue in vitro as a result of photodynamic action," Biophysics 57(1), 94-98 (2012).
38. I. Yu. Yanina, N. A. Trunina, and V. V. Tuchin, "Optical coherence tomography of adipose tissue at photodynamic/photothermal treatment *in vitro*," Journal of Innovative Optical Health Sciences 6(2), 1350010 (2013).
39. E. A. Genina, A. N. Bashkatov, and V. V. Tuchin, "Tissue optical immersion clearing," Expert Rev. Med. Devices 7, 825–842 (2010).

40. R. Barer, "Spectrophotometry of clarified cell suspensions," Science 121, 709–715 (1955).
41. V. V. Bakutkin, and L. P. Shubochkin, "The increase in light transmission of the sclera and the diseased cornea," Ophthalmological Journal 2, 105-107 (1991) (in Russian).
42. V. V. Tuchin, I. L. Maksimova, D. A. Zimnyakov, I. L. Kon, A. H. Mavlutov, and A. A. Mishin, "Light propagation in tissues with controlled optical properties," Proc. SPIE 2925, 118-142 (1996).
43. V. V. Tuchin, I. L. Maksimova, D. A. Zimnyakov, I. L. Kon, A. H. Mavlutov, and A. A. Mishin, "Light propagation in tissues with controlled optical properties," J. Biomed. Opt. 2, 401–417 (1997).
44. A. N. Bashkatov, E. A. Genina, V. I. Kochubey, V. V. Tuchin, and Yu. P. Sinichkin, "The influence of osmotically active chemical agents on the transport of light in the scleral tissue," Proc. SPIE 3726, 403-409 (1998).
45. V. V. Tuchin, A. N. Bashkatov, E. A. Genina, Yu. P. Sinichkin, and N. A. Lakodina, "*In vivo* investigation of the immersion-liquid-induced human skin clearing dynamics," Technical Physics Letters 27(6), 489-490 (2001).
46. E. A. Genina, Investigation of optical immersion and staining of biological tissues in vivo for optical diagnostics and laser therapy, Ph.D. thesis, Saratov State University, Saratov, Russia (2002) (in Russia).
47. A. N. Bashkatov, Control of tissue optical properties by means of osmotically active immersion liquids, Ph. D. thesis, Saratov State University, Saratov, Russia (2002) (in Russia).
48. I. V. Meglinskii, A. N. Bashkatov, E. A. Genina, D. Yu. Churmakov, and V. V. Tuchin, "Study of the possibility of increasing the probing depth by the method of reflection confocal microscopy upon immersion clearing of near-surface human skin layers," Quantum Electronics 32(10), 875-882 (2002).
49. I. V. Meglinski, A. N. Bashkatov, E. A. Genina, D. Y. Churmakov, and V. V. Tuchin, "The enhancement of confocal images of tissues at bulk optical immersion," Laser Physics 13(1), 65–69 (2003).
50. E. I. Galanzha, V. V. Tuchin, A. V. Solovieva, T. V. Stepanova, Q. Luo, and H. Cheng, J., "Skin backreflectance and microvascular system functioning at the action of osmotic agents," Phys. D: Appl. Phys. 36, 1739–1746 (2003).
51. V. V. Tuchin, D. M. Zhestkov, A. N. Bashkatov, and E. A. Genina, "Theoretical study of immersion optical clearing of blood in vessels at local hemolysis," Optics Express 12(13), 2966-2971 (2004).
52. E. A. Genina, A. N. Bashkatov, V. I. Kochubey, and V. V. Tuchin, "Optical clearing of human dura mater," Optics and Spectroscopy 98(3), 470-476 (2005).
53. A. N. Bashkatov, D. M. Zhestkov, E. A. Genina, and V. V. Tuchin, "Immersion clearing of human blood in the visible and near-infrared spectral regions," Optics and Spectroscopy 98(4), 638-646 (2005).
54. V. V. Tuchin, "Optical clearing of tissues and blood using the immersion method," J. Phys. D: Appl. Phys. 38, 2497–2518 (2005).
55. V. V. Tuchin, "Optical immersion as a new tool for controlling the optical properties of tissues and blood," Laser Phys. 15, 1109–1136 (2005).
56. E. A. Genina, A. N. Bashkatov, A. A. Korobko, E. A. Zubkova, V. V. Tuchin, I. V. Yaroslavsky, and G. B. Altshuler, "Optical clearing of human skin: comparative study of permeability and dehydration of intact and photothermally perforated skin," J. Biomed. Opt. 13, 021102 (2008).
57. E. A. Genina, A. N. Bashkatov, and V. V. Tuchin. "Optical clearing of cranial bone," Advanced Optical Technologies 267867 (2008).
58. E. A. Genina, A. N. Bashkatov, K. V. Larin, and V. V. Tuchin, "Light-tissue interaction at optical clearing," Chap. 7 in Laser Imaging and Manipulation in Cell Biology, F. S. Pavone, Ed., pp. 115-164, Wiley-VCH Verlag GmbH & Co. KGaA, Weinheim (2010).
59. I. V. Larina, E. F. Carbajal, V. V. Tuchin, M. E. Dickinson, and K. V. Larin, "Enhanced OCT imaging of embryonic tissue with optical clearing," Laser Phys. Lett. 5, 476–479 (2008).
60. S. G. Proskurin, and I. V. Meglinski, "Optical coherence tomography imaging depth enhancement by superficial skin optical clearing," Laser Phys. Lett. 4, 824–826 (2007).
61. M. Bonesi, S. G. Proskurin, and I. V. Meglinski, "Imaging of subcutaneous blood vessels and flow velocity profiles by optical coherence tomography," Laser Phys. 20, 891–899 (2010).
62. G. Vargas, E. K. Chan, J. K. Barton, H. G. Rylander, and A. J. Welch, "Use of an agent to reduce scattering in skin," Lasers Surg. Med. 24(2), 133–141 (1999).
63. G. Vargas, "Reduction of light scattering in biological tissue: implications for optical diagnostics and therapeutics," PhD Thesis, The University of Texas, USA (2001).
64. G. Vargas, K. F. Chan, S. L. Thomsen, and A. J. Welch, "Use of osmotically active agents to alter optical properties of tissue: effects on the detected fluorescence signal measured through skin," Lasers Surg. Med. 29(3), 213-220 (2001).
65. G. Vargas, A. Readinger, S. S. Dosier, and A. J. Welch, "Morphological changes in blood vessels produced by hyperosmotic agents and measured by optical coherence tomography," Photochem. Photobiol. 77, 541–549 (2003).

66. R. K. Wang, X. Xu, V. V. Tuchin, and J. B. Elder, "Concurrent enhancement of imaging depth and contrast for optical coherence tomography by hyperosmotic agents," J. Opt. Soc. Am. B 18, 948–953 (2001).
67. X. Xu, and R. K. Wang, "The role of water desorption on optical clearing of biotissue: studied with near infrared reflectance spectroscopy," Med. Phys. 30, 1246–1253 (2003).
68. Y. He, R. K. Wang, and D. Xing, "Enhanced sensitivity and spatial resolution for in vivo imaging with low-level light-emitting probes by use of biocompatible chemical agents," Opt. Lett. 28, 2076–2078 (2003).
69. Y. He, and R. K. Wang, "Dynamic optical clearing effect of tissue impregnated with hyperosmotic agents and studied with optical coherence tomography," J. Biomed. Opt. 9, 200–206 (2004).
70. M. H. Khan, B. Choi, S. Chess, K. M. Kelly, J. McCullough, and J. S. Nelson, "Optical clearing of in vivo human skin: implications for light-based diagnostic imaging and therapeutics," Lasers Surg. Med. 34, 83–85 (2004).
71. H. Cheng, Q. Luo, S. Zeng, S. Chen,W. Luo, and H. Gong, "Hyperosmotic chemical agent's effect on *in vivo* cerebral blood flow revealed by laser speckle," Appl. Opt. 43, 5772–5777 (2004).
72. R. LaComb, O. Nadiarnykh, S. Carey, and P. J. Campagnola, "Quantitative second harmonic generation imaging and modeling of the optical clearing mechanism in striated muscle and tendon," J. Biomed. Opt. 13, 021109 (2008).
73. O. Nadiarnykh, and P. J. Campagnola, "Retention of polarization signatures in SHG microscopy of scattering tissues through optical clearing," Opt. Exp. 17, 5794–5806 (2009).
74. D. Zhu, Q. Luo, and J. Cen, "Effects of dehydration on the optical properties of in vitro porcine liver," Lasers Surg. Med. 33, 226-231 (2003).
75. D. Zhu, J. Zhang, H. Cui, Z. Mao, P. Li, and Q. Luo, "Short-term and long-term effects of optical clearing agents on blood vessels in chick chorioallantoic membrane," J. Biomed. Opt. 13(2), 021106 (2008).
76. X. Wen, Z. Mao, Z. Han, V. V. Tuchin, and D. Zhu, "*In vivo* skin optical clearing by glycerol solutions: mechanism," J. Biophotonics 3(1-2), 44-52 (2010).
77. J. Wang, D. Zhu, M. Chen, and X. Liu, "Assessment of optical clearing induced improvement of laser speckle contrast imaging," J. Innovat. Opt. Health Sci. 3, 159–167 (2010).
78. T. Yu, X. Wen, V. V. Tuchin, Q. Luo, and D. Zhu, "Quantitative analysis of dehydration in porcine skin for assessing mechanism of optical clearing," J. Biomed. Opt. 16(9), 095002 (2011).
79. J. Wang, Y. Zhang, T. Xu, Q. Luo, and D. Zhu, "An innovative transparent cranial window based on skull optical clearing," Laser Phys. Lett. 9, 469–473 (2012).
80. X. Wen, S. L. Jacques, V. V. Tuchin, and D. Zhu, "Enhanced optical clearing of skin *in vivo* and optical coherence tomography in-depth imaging," J. Biomed. Opt. 17, 066022 (2012).
81. J. Wang, Y. Zhang, P. Li, Q. Luo, and D. Zhu, "Review: tissue optical clearing window for blood flow monitoring," IEEE J. Sel. Topics in Quantum Electron. 20(2), 6801112 (2014).
82. M. Kinnunen, R. Myllylä, and S. Vainio, "Detecting glucose-induced changes in *in vitro* and *in vivo* experiments with optical coherence tomography," J. Biomed. Opt. 13, 021111 (2008).
83. R. Dickie, R. M. Bachoo, M. A. Rupnick, S. M. Dallabrida, G. M. DeLoid, J. Lai, R. A. DePinho, and R. A. Rogers, "Three-dimensional visualization of microvessel architecture of whole-mount tissue by confocal microscopy," Microvasc. Res. 72, 20–26 (2006).
84. V. Hovhannisyan, P.-S. Hu, S.-J. Chen, C.-S. Kim, and C.-Y. Dong, "Elucidation of the mechanisms of optical clearing in collagen tissue with multiphoton imaging," J. Biomed. Opt. 18(4), 046004 (2013).
85. H. Hama, H. Kurokawa, H. Kawano, R. Ando, T. Shimogori, H. Noda, K. Fukami, A. Sakaue-Sawano, and A. Miyawaki, "Sca*l*e: a chemical approach for fluorescence imaging and reconstruction of transparent mouse brain," Nature Neurosci. 14, 1481–1488 (2011).
86. H. U. Dodt, U. Leischner, A. Schierloh, N. Jährling, C. P. Mauch, K. Deininger, J. M. Deussing, M. Eder, W. Zieglgnsberger, and K. Becker, "Ultramicroscopy: three-dimensional visualization of neuronal networks in the whole mouse brain," Nature Methods 4(4), 331–336 (2007).
87. A. Ertürk, C. P. Mauch, F. Hellal, F. Förstner, T. Keck, K. Becker, N. Jährling, H. Steffens, M. Richter, M. Hübener, E. Kramer, F. Kirchhoff, H. U. Dodt, and F. Bradke, "Three-dimensional imaging of the unsectioned adult spinal cord to assess axon regeneration and glial responses after injury," Nature Med. 18, 166–171 (2012).
88. A. N. Bashkatov, E. A. Genina, Yu. P. Sinichkin, V. I. Kochubey, N. A. Lakodina, and V. V. Tuchin, "Glucose and mannitol diffusion in human *dura mater*," Biophys. J. 85(5), 3310-3318 (2003).
89. M. G. Ghosn, V. V. Tuchin, and K. V. Larin, "Depth-resolved monitoring of glucose diffusion in tissues by using optical coherence tomography," Opt. Lett. 31, 2314–2316 (2006).
90. A. N. Bashkatov, E. A. Genina, and V. V. Tuchin, "Measurement of glucose diffusion coefficients in human tissues," Chap. 19 in Handbook of Optical Sensing of Glucose in Biological Fluids and Tissues, V. V. Tuchin, Ed., pp. 587-621, Taylor & Francis Group LLC, CRC Press (2009).
91. A. N. Bashkatov, E. A. Genina, Yu. P. Sinichkin, V. I. Kochubei, N. A. Lakodina, and V. V. Tuchin, "Estimation of the glucose diffusion coefficient in human eye sclera," Biophysics 48(2), 292-296 (2003).

92. E. A. Genina, A. N. Bashkatov, E. A. Zubkova, T. G. Kamenskikh, and V. V. Tuchin, "Measurements of Retinalamin diffusion coefficient in human sclera by optical spectroscopy," Optics and Lasers in Engineering 46, 915-920 (2008).
93. E. A. Genina, A. N. Bashkatov, V. V. Tuchin, M. G. Ghosn, K. V. Larin, and T. G. Kamenskikh, "Cortexin diffusion in human eye sclera," Quantum Electronics 41(5), 407-413 (2011).
94. E. A. Zubkina, E. A. Genina, A. N. Bashkatov, and V. V. Tuchin, "Optical clearing of eye tissues," Proceedings of the Samara Scientific Center of the Russian Academy of Sciences 13(4(2)), 588-594 (2011) (in Russia).
95. M. G. Ghosn, V. V. Tuchin, and K. V. Larin, "Nondestructive quantification of analyte diffusion in cornea and sclera using optical coherence tomography," Invest. Ophthal. Visual Sci. 48, 2726–2733 (2007).
96. M. G. Ghosn, E. F. Carbajal, N. Befrui, V. V. Tuchin, and K. V. Larin, "Differential permeability rate and percent clearing of glucose in different regions in rabbit sclera," J. Biomed. Opt. 13, 021110 (2008).
97. M. G. Ghosn, N. Sudheendran, M. Wendt, A. Glasser, V. V. Tuchin, and K. V. Larin, "Monitoring of glucose permeability in monkey skin *in vivo* using optical coherence tomography," J. Biophotonics 3, 25–33 (2010).
98. X. Guo, Z. Guo, H. Wei, H. Yang, Y. He, S. Xie, G. Wu, X. Deng, Q. Zhao, and L. Li, "*In vivo* comparison of the optical clearing efficacy of optical clearing agents in human skin by quantifying permeability using optical coherence tomography," Photochem. Photobiol. 87, 734–740 (2011).
99. K. V. Larin, M. G. Ghosn, S. N. Ivers, A. Tellez, and J. F. Granada, "Quantification of glucose diffusion in arterial tissues by using optical coherence tomography," Laser Physics Letters 4(4), 312-317 (2007).
100. X. Guo, G. Wu, H. Wei, X. Deng, H. Yang, Y. Ji, Y. He, Z. Guo, S. Xie, H. Zhong, Q. Zhao, and Z. Zhu, "Quantification of glucose diffusion in human lung tissues by using Fourier domain optical coherence tomography," Photochem. Photobiol. 88, 311–316 (2012).
101. S. Tanev, V. V. Tuchin, and P. Paddon, "Cell membrane and gold nanoparticles effects on optical immersion experiments with noncancerous and cancerous cells: finite-difference time-domain modeling," J. Biomed. Opt. 11, 064037 (2006).
102. M. G. Ghosn, E. F. Carbajal, N. A. Befrui, A. Tellez, J. F. Granada, and K. V. Larin, "Permeability of hyperosmotic agent in normal and atherosclerotic vascular tissues," J. Biomed. Opt. 13, 010505 (2008).
103. H. Q. Zhong, Z. Y. Guo, H. J. Wei, C. C. Zeng, H. L. Xiong, Y. H. He, and S. H. Liu, "Quantification of glycerol diffusion in human normal and cancer breast tissues *in vitro* with optical coherence tomography," Laser Phys. Lett. 7, 315–320 (2010).
104. Q. L. Zhao, J. L. Si, Z. Y. Guo, H. J. Wei, H. Q. Yang, G. Y. Wu, S. S. Xie, X. Y. Li, X. Guo, H. Q. Zhong, and L. Q. Li, "Quantifying glucose permeability and enhanced light penetration in *ex vivo* human normal and cancerous esophagus tissues with optical coherence tomography," Laser Phys. Lett. 8, 71–77 (2011).
105. Z. Zhu, G. Wu, H. Wei, H. Yang, Y. He, S. Xie, Q. Zhao, and X. Guo, "Investigation of the permeability and optical clearing ability of different analytes in human normal and cancerous breast tissues by spectral domain OCT," J. Biophoton. 5, 1–8 (2012).
106. B. Choi, L. Tsu, E. Chen, T. S. Ishak, S. M. Iskandar, S. Chess, and J. S. Nelson, "Determination of chemical agent optical clearing potential using in vitro human skin," Lasers Surg. Med. 36, 72–75 (2005).
107. Z. Mao, D. Zhu, Y. Hu, X. Wen, and Z. Han, "Influence of alcohols on the optical clearing effect of skin *in vitro*," J. Biomed. Opt. 13, 021104 (2008).
108. E. A. Genina, A. N. Bashkatov, Yu. P. Sinichkin, and V. V. Tuchin, "Optical clearing of skin under action of glycerol: ex vivo and in vivo investigations," Optics and Spectroscopy 109(2), 225-231 (2010).
109. J. Hirshburg, B. Choi, J. S. Nelson, and A. T. Yeh, "Correlation between collagen solubility and skin optical clearing using sugars," Lasers Surg. Med. 39, 140-144 (2007).
110. J. M. Hirshburg, K. M. Ravikumar, W. Hwang, and A. T. Yeh, "Molecular basis for optical clearing of collagenous tissues," J. Biomed. Opt. 15(5), 055002 (2010).
111. J. Wang, N. Ma, R. Shi, Y. Zhang, T. Yu, and D. Zhu, "Sugar-induced skin optical clearing: from molecular dynamics simulation to experimental demonstration," IEEE J. Selected Topics in Quantum Electronics 20(2), 7101007 (2014).
112. A. T. Yeh, and J. Hirshburg, "Molecular interactions of exogenous chemical agents with collagen-implications for tissue optical clearing," J. Biomed. Opt. 11(1), 014003 (2006).
113. Y. Ding, J. Wang, Z. Fan, D. Wei, R. Shi, Q. Luo, D. Zhu, and X. Wei, "Signal and depth enhancement for *in vivo* flow cytometer measurement of ear skin by optical clearing agents," Biomed. Opt. Exp. 4(11), 2518-2526 (2013).
114. J. Jiang, and R. K. Wang, "Comparing the synergistic effects of oleic acid and dimethyl sulfoxide as vehicles for optical clearing of skin tissue *in vitro*," Phys. Med. Biol. 49, 5283–5294 (2004).
115. Y. Liu, X. Yang, D. Zhu, and Q. Luo, "Optical clearing agents improve photoacoustic imaging in the optical diffusive regime," Optics Letters 38(20), 4236-4239 (2013).

116. X. Xu, and R. K. Wang, "Synergistic effect of hyperosmotic agents of dimethyl sulfoxide and glycerol on optical clearing of gastric tissue studied with near infrared spectroscopy," Phys. Med. Biol. 49, 457–468 (2004).
117. J. Jiang, M. Boese, P. Turner, and R. K. Wang, "Penetration kinetics of dimethyl sulphoxide and glycerol in dynamic optical clearing of porcine skin tissue *in vitro* studied by Fourier transform infrared spectroscopic imaging," J. Biomed. Opt. 13(2), 021105 (2008).
118. E. A. Genina, A. N. Bashkatov, E. A. Kolesnikova, M. V. Basco, G. S. Terentyuk, and V. V. Tuchin, "Optical coherence tomography monitoring of enhanced skin optical clearing in rats *in vivo*," J. Biomed. Opt. 19(2), 021109 (2014).
119. A. N. Bashkatov, A. N. Korolevich, V. V. Tuchin, Y. P. Sinichkin, E. A. Genina, M. M. Stolnitz, N. S. Dubina, S. I. Vecherinski, and M. S. Belsley, "*In vivo* investigation of human skin optical clearing and blood microcirculation under the action of glucose solution," Asian J. Physics 15(1), 1–14 (2006).
120. E. A. Genina, A. N. Bashkatov, and V. V. Tuchin, "Glucose-induced optical clearing effects in tissues and blood," Chap. 21 in Handbook of Optical Sensing of Glucose in Biological Fluids and Tissues, V. V. Tuchin, Ed., pp. 657-692, Taylor & Francis Group LLC, CRC Press (2009).
121. A. T. Yeh, B. Choi, J. S. Nelson, and B. J. Tromberg, "Reversible dissociation of collagen in tissues," J. Invest. Dermatol. 121, 1332–1335 (2003).
122. J. Hirshburg, B. Choi, J. S. Nelson, and A. T. Yeh, "Collagen solubility correlates with skin optical clearing," J. Biomed. Opt. 11, 040501 (2006).
123. J. W. Wiechers, J. C. Dederen, and A. V. Rawlings, "Moisturization mechanisms: internal occlusion by orthorhombic lipid phase stabilizers - a novel mechanism of action of skin moisturization," Chap. 9 in Skin Moisturization, 2nd ed., A. V. Rawlings and J. J. Leyden, Eds., pp. 309–321, Informa Healthcare, Taylor & Francis Group, New York (2009).
124. A. V. Papaev, G. V. Simonenko, V. V. Tuchin, and T. P. Denisova, "Optical anisotropy of a biological tissue under conditions of immersion clearing and without them," Optics and Spectroscopy 101(1), 46-53 (2006).
125. A. Roggan, M. Friebel, K. Dorschel, A. Hahn, and G. Mueller, "Optical properties of circulating human blood in the wavelength range 400–2500 nm," J. Biomed. Opt. 4, 36–46 (1999).
126. M. Friebel, J. Helfmann, and M. Meinke, "Influence of osmolarity on the optical properties of human erythrocytes," J. Biomed. Opt. 15(5), 055005 (2010).
127. I. Fine, B. Fikhte, and L. D. Shvartsman, "RBC aggregation assisted light transmission through blood and occlusion oximetry," Proc. SPIE 4162, 130–139 (2000).
128. V. V. Tuchin, X. Xu, and R. K. Wang, "Dynamic optical coherence tomography in studies of optical clearing, sedimentation, and aggregation of immersed blood," Appl. Opt. 41(1), 258–271 (2002).
129. H. Schaefer, and T. E. Redelmeier, Skin Barrier, Karger, Basel (1996).
130. C. Liu, Z. Zhi, V. V. Tuchin, Q. Luo, and D. Zhu, "Enhancement of skin optical clearing efficacy using photo-irradiation," Lasers Surg. Med. 42, 132–140 (2010).
131. V. V. Tuchin, G. B. Altshuler, A. A. Gavrilova, A. B. Pravdin, D. Tabatadze, J. Childs, and I. V. Yaroslavsky, "Optical clearing of skin using flashlamp-induced enhancement of epidermal permeability," Lasers Surg. Med. 38, 824–836 (2006).
132. E. A. Kolesnikova, A. S. Kolesnikov, E. A. Genina, L. E. Dolotov, D. K. Tuchina, A. N. Bashkatov, and V. V. Tuchin, "Use of fractional laser microablation of skin for improvement of its immersion clearing," Proc. SPIE 8699, 86990B (2013).
133. E. A. Genina, A. N. Bashkatov, V. V. Tuchin, G. B. Altshuler, and I. V. Yaroslavski, "Possibility of increasing the efficiency of laser-induced tattoo removal by optical skin clearing," Quantum Electronics 38(6), 580-587 (2008).
134. X. Xu, Q. Zhu, and C. Sun, "Assessment of the effects of ultrasound-mediated alcohols on skin optical clearing," J. Biomed. Opt. 14, 034042 (2009).
135. H. Zhong, Z. Guo, H. Wei, C. Zeng, H. Xiong, Y. He, and S. Liu, "*In vitro* study of ultrasound and different-concentration glycerol-induced changes in human skin optical attenuation assessed with optical coherence tomography," J. Biomed. Opt. 15, 036012 (2010).
136. O. Stumpp, B. Chen, and B. Welch, "Using sandpaper for noninvasive transepidermal optical skin clearing agent delivery," J. Biomed. Opt. 11, 041118 (2006).
137. J. Yoon, T. Son, E. Choi, B. Choi, J. S. Nelson, and B. Jung, "Enhancement of optical clearing efficacy using a microneedle roller," J. Biomed. Opt. 13(2), 021103 (2008).
138. J. Yoon, D. Park, T. Son, J. Seo, J. S. Nelson, and B. Jung, "A physical method to enhance transdermal delivery of a tissue optical clearing agent: combination of microneedling and sonophoresis," Lasers Surg. Med. 42, 412-417 (2010).
139. M. A. Fox, D. G. Diven, K. Sra, A. Boretsky, T. Poonawalla, A. Readinger, M. Motamedi, and R. J. Nichols, "Dermal scatter reduction in human skin: a method using controlled application of glycerol," Lasers Surg. Med. 41, 251-255 (2009).

140. C. G. Rylander, T. E. Milner, S. A. Baranov, and J. S. Nelson, "Mechanical tissue optical clearing devices: enhancement of light penetration in ex vivo porcine skin and adipose tissue," Lasers Surg. Med. 40, 688-694 (2008).
141. X. Xu, and Q. Zhu, "Evaluation of skin optical clearing enhancement with Azone as a penetration enhancer," Optics Communications 279, 223-228 (2007).
142. J. Jiang, and R. K. Wang, "How different molarities of oleic acid as enhancer exert its effect on optical clearing of skin tissue *in vitro,"* Journal of X-Ray Science and Technology, 13, 149-159 (2005).
143. J. Jiang, M. Boese, P. Turner, and R. K. Wang, "Penetration kinetics of dimethyl sulphoxide and glycerol in dynamic optical clearing of porcine skin tissue *in vitro* studied by Fourier transform infrared spectroscopic imaging," J. Biomed. Opt. 13(2), 021105 (2008).
144. A. K. Bui, R. A. McClure, J. Chang, C. Stoianovici, J. Hirshburg, A. T. Yeh, and B. Choi, "Revisiting optical clearing with dimethyl sulfoxide (DMSO)," Lasers Surg. Med. 41, 142-148 (2009).
145. M. Zimmerley, R. A. McClure, B. Choi, and E. O. Potma, "Following dimethyl sulfoxide skin optical clearing dynamics with quantitative nonlinear multimodal microscopy," Appl. Opt. 48(10), D79-D87 (2009).
146. S. Karma, J. Homan, C. Stoianovic, and B. Choi, "Enhanced fluorescence imaging with DMSO-mediated optical clearing," Journal of Innovative Optical Health Sciences 3(3), 153-158 (2010).
147. Z. Zhi, Z. Han, Q. Luo, and D. Zhu, "Improve optical clearing of skin in vitro with propylene glycol as a penetration enhancer," Journal of Innovative Optical Health Sciences 2(3), 269-278 (2009).
148. X. Xu, Q. Zhu, and C. Sun, "Combined effect of ultrasound-SLS on skin optical clearing," IEEE Photonic Technol. Lett. 20(24), 2117–2119 (2008).
149. H. Zhong, Z. Guo, H. Wei, L. Guo, C. Wang, Y. He, H. Xiong, and S. Liu, "Synergistic effect of ultrasound and thiazone–PEG 400 on human skin optical clearing *in vivo*," Photochem. Photobiol. 86(3), 732–737 (2010).
150. T. Kurihara-Bergstrom, K. Knutson, L. J. de Noble, and C. Y. Goates, "Percutaneous absorption enhancement of an ionic molecule by ethanol–water system in human skin," Pharm. Res. 7, 762–766 (1990).
151. A. C. Williams, and B. W. Barry, "Penetration enhancers," Adv. Drug Deliv. Rev. 56, 603–618 (2004).
152. J.-M. Andanson, K. L. A. Chan, and S. G. Kazarian, "High-throughput spectroscopic imaging applied to permeation through the skin," Appl. Spectrosc. 63(5), 512–517 (2009).
153. A. P. Funke, R. Schiller, H. W. Motzkus, C. Gunther, R. H. Muller, and R. Lipp, "Transdermal delivery of highly lipophilic drugs: in vitro fluxes of antiestrogens, permeation enhancers, and solvents from liquid formulations," Pharm. Res. 19(5), 661–668 (2002).
154. A. Pagnoni, A. Knuettel, P. Welker, M. Rist, T. Stoudemayer, L. Kolbe, I. Sadiq, and A. M. Kligman, "Optical coherence tomography in dermatology," Skin Res. Technol. 5(2), 83–87 (1999).
155. R. Samatham, K. G. Phillips, and S. L. Jacques, "Assessment of optical clearing agents using reflectance-mode confocal scanning laser microscopy," J. Innovative Opt. Health Sci. 3(3), 183–188 (2010).
156. P. Liu, Y. Huang, Z. Guo, J. Wang, Z. Zhuang, and S. Liu, "Discrimination of dimethyl sulphoxide diffusion coefficient in the process of optical clearing by confocal micro-Raman spectroscopy," J. Biomed. Opt. 18(2), 020507 (2013).
157. G. Terentyuk, E. Panfilova, V. Khanadeev, D. Chumakov, E. Genina, A. Bashkatov, V. Tuchin, N. Khlebtsov, and B. Khlebtsov, "Gold nanorods with hematoporphyrin-loaded silica shell for dual-modality photodynamic and photothermal treatment of tumors *in vivo*," NanoResearch 7(3), 325–337 (2014).
158. O. Stumpp, A. J. Welch, and J. Neev, "Enhancement of transdermal skin clearing agent delivery using a 980 nm diode laser," Lasers Surg. Med. 37, 278–285 (2005).
159. A. Tezel, and S. Mitragotri, "Interaction of inertial cavitation bubbles with stratum corneum lipid bilayers during low frequency sonophoresis," Biophys. J. 85, 3502–3512 (2003).
160. A. K. Nugroho, G. L. Li, M. Danhof, and J. A. Bouwstra, "Transdermal iontophoresis of rotigotine across human stratum corneum *in vitro*: influence of pH and NaCl concentration," Pharm. Res. 21(5), 844–850 (2004).
161. O. Stumpp, and A. J. Welch, "Injection of glycerol into porcine skin for optical skin clearing with needle-free injection gun and determination of agent distribution using OCT and fluorescence microscopy," Proc. SPIE 4949, 44–50 (2003).
162. H.-J. Weigmann, J. Lademann, S. Schanzer, U. Lindemann, R. von Pelchrzim, H. Schaefer, W. Sterry, and V. Shah, "Correlation of the local distribution of topically applied substances inside the stratum corneum determined by tape stripping to differences in bioavailability," Skin Pharmacol. Appl. Skin Physiol. 14, 93–103 (2001).
163. W. R. Lee, R. Y. Tsai, C. L. Fang, C. J. Liu, C. H. Hu, and J. Y. Fang, "Microdermabrasion as a novel tool to enhance drug delivery via the skin: an animal study," J. Dermatol. Surg. 32, 1013–1022 (2006).
164. A. N. Bashkatov, E. A. Genina, V. V. Tuchin, and G. B. Altshuler, "Skin optical clearing for improvement of laser tattoo removal," Laser Physics 19(6), 1312-1322 (2009).
165. X. Xu, and Q. Zhu, "Feasibility of sonophoretic delivery for effective skin optical clearing," IEEE Trans. Biomed. Eng. 55(4), 1432–1437 (2008).

166. X. Xu, and Q. Zhu, "Sonophoretic delivery for contrast and depth improvement in skin optical coherence tomography," IEEE J. Sel. Top. Quantum Electron. 14(1), 56–61 (2008).
167. I. Lavon, N. Grossman, J. Kost, E. Kimmel, and G. Enden, "Bubble growth within the skin by rectified diffusion might play a significant role in sonophoresis," J. Controlled Release 117(2), 246–255 (2007).
168. X. Xu, and C. Sun, "Ultrasound enhanced skin optical clearing: microstructural changes," J. Innovative Opt. Health Sci. 3(3), 189–194 (2010).
169. A. K. Nugroho, O. Della Pasqua, M. Danhof, and J. A. Bouwstra, "Compartmental modeling of transdermal iontophoretic transport: I. in vitro model derivation and application," Pharmaceutical Research 21(11), 1974-1984 (2004).
170. J. Wang, X. Zhou, S. Duan, Z. Chen, and D. Zhu, "Improvement of in vivo rat skin optical clearing with chemical penetration enhancers," Proc. SPIE 7883, 78830Y (2011).
171. Yu. P. Sinichkin, and S. R. Utz, In vivo reflectance and fluorescence spectroscopy of human skin, Saratov: Saratov University Press (2001).
172. Yu. P. Sinichkin, N. Kollias, G. Zonios, S. R. Utz, and V. V. Tuchin, "Back reflectance and fluorescence spectroscopy of the human skin in vivo," in Handbook on Optical Biomedical Diagnostics and Imaging, V. V. Tuchin, Ed., pp. 725-785, Bellingham, SPIE Press (2002).
173. G. A. Askar'yan, "Enhancement of transmission of laser and other radiation by soft turbid physical and biological media," Sov. J. Quantum Electron. 12(7), 877-880 (1982).
174. E. K. Chan, B. Sorg, D. Protsenko, M. O'Neil, M. Motamedi, and A. J. Welch, "Effects of compression on soft tissue optical properties," IEEE J. Sel. Topics in Quantum Electr. 2(4), 943–950 (1996).
175. H. Shangguan, S. A. Prahl, S. L. Jacques, and L. W. Casperson, "Pressure effects on soft tissues monitored by changes in tissue optical properties," Proc. SPIE 3254, 366–371 (1998).
176. Yu. P. Sinichkin, S. R. Uts, and E. A. Pilipenko, "Spectroscopy of human skin in vivo: 1. Reflection spectra," Optics and Spectroscopy 80(2). C. 228-234 (1996).
177. B. W. Murphy, R. J. Webster, B. A. Turlach, C. J. Quirk, C. D. Clay, P. J. Heenan, and D. D. Sampson, "Toward the discrimination of early melanoma from common and dysplastic nevus using fiber optic diffuse reflectance spectroscopy," J Biomed. Opt. 10(6), 064020 (2005).
178. W. Chen, R. Liu, K. Xu, and R. K. Wang, "Influence of contact state on NIR diffuse reflectance spectroscopy in vivo," J. Phys. D: Appl. Phys. 38, 2691-2695 (2005).
179. L. L. Randeberg, Diagnostic applications of diffuse reflectance spectroscopy, PhD thesis, Norwegian University of Science and Technology, Trondheim, Norway (2005).
180. S. A. Carp, T. Kauffman, Q. Fang, E. Rafferty, R. Moore, D. Kopans, and D. Boas, "Compression-induced changes in the physiological state of the breast as observed through frequency domain photon migration measurements," J. Biomed. Opt. 11(6), 064016 (2006).
181. R. Reif, M. S. Amorosino, K. W. Calabro, O. A'Amar, S. K. Singh, and I. J. Bigio, "Analysis of changes in reflectance measurements on biological tissues subjected to different probe pressures," J. Biomed. Opt. 13(1), 010502 (2008).
182. Y. Ti, and W. C. Lin, "Effects of probe contact pressure on in vivo optical spectroscopy," Opt. Express 16(6), 4250-4262 (2008).
183. A. Cerussi, S. Siavoshi, A. Durkin, C. Chen, W. Tanamai, D. Hsiang, and B. J. Tromberg, "Effect of contact force on breast tissue optical property measurements using a broadband diffuse optical spectroscopy handheld probe," Appl. Opt. 48, 4270-4277 (2009).
184. J. A. Delgado Atencio, E. E. Orozco Guillén, S. Vázquezy Montiel, M. Cunill Rodríguez, J. Castro Ramos, J. L. Gutiérrez, and F. Martínez, "Influence of probe pressure on human skin diffuse reflectance spectroscopy measurements," Optical Memory & Neural Networks (Information Optics) 18(1), 6-14 (2009).
185. L. Lim, B. Nichols, N. Rajaram, and J. W. Tunnell, "Probe pressure effects on human skin diffuse reflectance and fluorescence spectroscopy measurements," J. Biomed. Opt. 16(1), 011012 (2011).
186. S. Ruderman, A. J. Gomes, V. Stoyneva, J. D. Rogers, A. J. Fought, B. D. Jovanovic, and V. Backman, "Analysis of pressure, angle and temporal effects on tissue optical properties from polarization-gated spectroscopic probe measurements," Biomedical Optics Express 1(2), 489-499 (2010).
187. Yu. P. Sinichkin, S. R. Uts, I. V. Meglinskii, and E. A. Pilipenko, "Spectroscopy of human skin in vivo: II. Fluorescence spectra," Optics and Spectroscopy 80(3). C. 383-389 (1996).
188. A. Nath, K. Rivoire, S. Chang, D. Cox, E. N. Atkinson, M. Follen, and R. Richards-Kortum, "Effect of probe pressure on cervical fluorescence spectroscopy measurements," J. Biomed. Opt. 9(3), 523-533 (2004).
189. K. Rivoire, A. Nath, D. Cox, E. N. Atkinson, R. Richards-Kortum, and M. Follen, "The effects of repeated spectroscopic pressure measurements on fluorescence intensity in the cervix," Am. J. Obstet. Gynecol. 191(5), 1606-1617 (2004).
190. A. Izquierdo-Roman, W. C. Vogt, L. Hyacinth, and C. G. Rylander, "Mechanical tissue optical clearing technique increases imaging resolution and contrast through ex vivo porcine skin," Lasers Surg. Med. 43, 814–823 (2011).

191. V. V. Sapozhnikova, R. V. Kuranov, I. Cicenaite, R. O. Esenaliev, and D. S. Prough, "Effect on blood glucose monitoring of skin pressure exerted by an optical coherence tomography probe," J. Biomed. Opt. 13(2), 021112 (2008).
192. M. Y. Kirillin, P. D. Agrba, and V. A. Kamensky, "In vivo study of the effect of mechanical compression on formation of OCT images of human skin," J. Biophotonics 3(12), 752–758 (2010).
193. A. A. Gurjarpadhye, W. C. Vogt, Y. Liu, and C. G. Rylander, "Effect of localized mechanical indentation on skin water content evaluated using OCT," Int. J. Biomed. Imag. 2011, 817250 (2011).
194. M. H. Khan, B. Choi, S. Chess, K. M. Kelly, J. McCullought, and J. S. Nelson, "Optical clearing of in vivo human skin: Implications for light-based diagnostic imaging and therapeutics," Lasers Surg. Med. 34(2), 83-85 (2004).
195. H. Kang, T. Son, J. Yoon, K. Kwon, J. S. Nelson, and B. Jung, "Evaluation of laser beam profile in soft tissue due to compression, glycerol, and micro-needling," Laser Surg. Med. 40(8), 570-575 (2008).
196. C. G. Rylander, T. E. Milner, S. A. Baranov, and J. S. Nelson, "Mechanical tissue optical clearing devices: enhancement of light penetration in ex vivo porcine skin and adipose tissue," Lasers Surg. Med. 40(10), 688-694 (2008).
197. I. V. Ermakov, and W. Gellermann, "Dermal carotenoid measurements via pressure mediated reflection spectroscopy," J. Biophotonics 5(7), 559-570 (2012).
198. L. E. Dolotov, and Yu. P. Sinichkin, "Features of applying fiber-optic sensors in spectral measurements of biological tissues," Optics and Spectroscopy 115(2), 187-192 (2013).
199. C. Li, J. Jiang, and K. Xu, "The variations of water in human tissue under certain compression: studied with diffuse reflectance spectroscopy," J. Innov. Opt. Health Sci. 6(1), 1350005 (2013).
200. K. A. Martin, Direct measurement of moisture in skin by NIR spectroscopy," J. Soc. Cosm. Chem. 44, 249-261 (1993).
201. C. W. J. Oomens, D. H. Vancampen, and H. J. Grootenboer, "A mixture approach to the mechanics of skin," J. Biomech. 20(9), 877-885 (1987).
202. A. Hidenobu, and E. Mariko, "Non-contact skin moisture measurement based on near-infrared spectroscopy," Appl. Spectrosc. 58, 1439-1446 (2004).
203. A. N. Bashkatov, E. A. Genina, and V. V. Tuchin, "Optical properties of skin, subcutaneous and muscle tissues, a review," J. Innovative Opt. Health Sci. 14(1), 9-38 (2011).
204. T. L. Troy, and S. N. Thennadil, "Optical properties of human skin in the NIR wavelength range of 1000-2200 nm," J. Biomed. Opt. 6, 167-176 (2001).
205. I. Yu. Yanina, G. V. Simonenko, and V. V. Tuchin, "Destructive fat tissue engineering using photodynamic and selective photothermal effects," Proc SPIE 7179, 71790C (2009).
206. V. A. Doubrovsky, I. Yu. Yanina, and V. V. Tuchin, "Inhomogeneity of photo-induced fat cell lipolysis," Proc. SPIE 7999, 79990M (2011).
207. Yu. A. Vladimirov, and A. Ya. Potapenko, Physico-chemical basis of photobiological processes, Moscow: Dropha (2006).
208. M. Wanner, M. Avram, D. Gagnon, M. C. Mihm Jr., D. Zurakowski, K. Watanabe, Z. Tannous, R. R. Anderson, and D. Manstein, "Effects of noninvasive, 1210 nm laser exposure on adipose tissue: results of a human pilot study," Lasers Surg. Med. 41, 401–407 (2009).
209. W. R. Chen, R. L. Adams, S. Heaton, D. T. Dickey, K. E. Bartels, and R. E. Nordquist, "Chromophore-enhanced laser-tumor tissue photothermal interaction using an 808-nm diode laser," Cancer Lett. 88, 15-19 (1995).
210. W. R. Chen, R. L. Adams, A. K. Higgins, K. E. Bartels, and R. E. Nordquist, "Photothermal effects on murine mammary tumors using indocyanine green and an 808-nm diode laser: an in vivo efficacy," Cancer Lett. 98, 169-173 (1996).
211. S. Fickweiler, R. M. Szeimies, W. Baumler, P. Steinbach, S. Karrer, A. E. Goetz, C. Abels, F. Hofstadter, and M. Landthaler, "Indocyanine green: intracellular uptake and phototherapeutic effects in vitro," J. Photochem. Photobiol. B 38, 178-183 (1997).
212. V. V. Tuchin, E. A. Genina, A. N. Bashkatov, G. V. Simonenko, O. D. Odoevskaya, and G. B. Altshuler, "A pilot study of ICG laser therapy of *acne vulgaris*: photodynamic and photothermolysis treatment," Lasers Surg. Med. 33(5), 296-310 (2003).
213. E. A. Genina, A. N. Bashkatov, G. V. Simonenko, O. D. Odoevskaya, V. V. Tuchin, and G. B. Altshuler, "Low-intensity Indocyanine green - laser phototherapy of acne vulgaris: Pilot study," J. Biomed. Opt. 9(4), 828-834 (2004).
214. V. I. Kochubey, T. V. Kulyabina, V. V. Tuchin, and G. B. Altshuler, "Spectral characteristics of indocyanine green upon its interaction with biological tissues," Optics and Spectroscopy 99(4), 560-566 (2005).
215. E. A. Genina, A. N. Bashkatov, Yu. P. Sinichkin, V. I. Kochubey, N. A. Lakodina, G. B. Altshuler, and V. V. Tuchin, "In vitro and in vivo study of dye diffusion into the human skin and hair follicles," J. Biomed. Opt. 7(3), 471–477 (2002).

216. E. Engel, R. Schraml, T. Maisch, K. Kobuch, B. König, R.-M. Szeimies, J. Hillenkamp, W. Bäumler, and R. Vasold, "Light-induced decomposition of indocyanine green," Invest. Ophthalmol. Vis. Sci. 49, 1777–1783 (2008).
217. M. Sznitowska, "The influence of ethanol on permeation behavior of the porous pathway in the stratum corneum," Int. J. Pharmacol. 137, 137-140 (1996).
218. A. K. Levang, K. Zhao, and J. Singh, "Effect of ethanol/propylene glycol on the in vitro percutaneous absorption of aspirin, biophysical changes and macroscopic barrier properties of the skin," Int. J. Pharm. 181, 255-263 (1999).
219. C. A. Squier, M. J. Kremer, and P. W. Wertz, "Effect of ethanol on lipid metabolism and epidermal permeability barrier of skin and oral mucosa in the rat," J. Oral Pathol. Med. 32, 595-599 (2003).
220. V. A. Dubrovskii, B. A. Dvorkin, I. Yu. Yanina, and V. V. Tuchin, "Photoaction upon adipose tissue cells in vitro," Cell and Tissue Biology 5(5), 520-529 (2011).
221. B. Alberts, D. Bray, J. Lewis, M. Raff, K. Roberts, and J. D. Watson, Molecular Biology of the Cell, 2nd edition, Vol. 1, Garland Publishing. Inc. New York London (1989).
222. A. L. Lehninger, Principles of Biochemistry, Vol. 2, Worth Publisher, Inc. (1982).
223. L. Stryer, Biochemistry, W. H. Freeman and Company, San Francisco (1981).
224. I. Yu. Yanina, N. A. Trunina, and V. V. Tuchin, "Photoinduced cell morphology alterations quantified within adipose tissues by spectral optical coherence tomography," J. Biomed. Opt. 18(11), 111407 (2013).
225. R. K. Wang, and V. V. Tuchin, "Enhance light penetration in tissue for high resolution optical imaging techniques by the use of biocompatible chemical agents," J. X-Ray Science and Technol. 10, 167-176 (2002).
226. R. K. Wang, and J. B. Elder, "Propylene glycol as a contrasting agent for optical coherence tomography to image gastrointestinal tissues," Lasers Surg. Med. 30(3), 201-208 (2002).
227. H. Xiong, Z. Guo, C. Zeng, L. Wang, Y. He, and S. Liu, "Application of hyperosmotic agent to determine gastric cancer with optical coherence tomography *ex vivo* in mice," J. Biomed. Opt. 14(2), 024029 (2009).
228. H. Q. Zhong, Z. Y. Guo, H. J. Wei, J. L. Si, L. Guo, Q. L. Zhao, C. C. Zeng, H. L. Xiong, Y. H. He, and S. H. Liu, "Enhancement of permeability of glycerol with ultrasound in human normal and cancer breast tissues *in vitro* using optical coherence tomography," Laser Physics Letters 7(5), 388-395 (2010).
229. Z. Zhu, H. Wei, G. Wu, H. Yang, Y. He, and S. Xie, "Synergistic effect of hyperosmotic agents and sonophoresis on breast tissue optical properties and permeability studied with spectral domain optical coherence tomography," J. Biomed. Opt. 17(8), 086002 (2012).
230. D. J. Faber, F. J. van der Meer, M. C. G. Aalders, and T. G. van Leeuwen, "Quantitative measurement of attenuation coefficients of weakly scattering media using optical coherence tomography," Optics Express 12(19), 4353-4365 (2004).
231. P. Lee, W. Gao, and X. Zhang, "Performance of single-scattering model versus multiple-scattering model in the determination of optical properties of biological tissue with optical coherence tomography," Appl. Opt. 49(18), 3538-3544 (2010).
232. K. V. Larin, and V. V. Tuchin, "Monitoring of glucose diffusion in epithelial tissues with optical coherence tomography," Chap. 20 in Handbook of Optical Sensing of Glucose in Biological Fluids and Tissues, V. V. Tuchin, Ed., pp. 635-668, Taylor & Francis Group LLC, CRC Press (2009).
233. T. Yamaguchi, N. Omatsu, E. Morimoto, H. Nakashima, K. Ueno, T. Tanaka, K. Satouchi, F. Hirose, and T. Osumi, "CGI-58 facilitates lipolysis on lipid droplets but is not involved in the vesiculation of lipid droplets caused by hormonal stimulation," J. Lipid Res. 48(5), 1078-1089 (2007).
234. J. Sharpe, "Optical projection tomography," Annual Review of Biomedical Engineering 6, 209–228 (2004).
235. J. Sharpe, U. Ahlgren, P. Perry, B. Hill, A. Ross, J. Hesksher-Sorensen, R. Baldock, and D. Davidson, "Optical projection tomography as a tool for 3D microscopy and gene expression studies," Science 296, 541–545 (2002).
236. T. Alanentalo, A. Asayesh, H. Morrison, C. E. Loren, D. Holmberg, J. Sharpe, and U. Ahlgren, "Tomographic molecular imaging and 3D quantification within adult mouse organs," Nature Methods 4(1), 31–33 (2007).
237. T. Alanentalo, C. E. Loren, A. Larefalk, J. Sharpe, D. Holmberg, and U. Ahlgren, "High-resolution three-dimensional imaging of isletinfiltrate interactions based on optical projection tomography assessments of the intact adult mouse pancreas," J. Biomed. Opt. 13(5), 054070 (2008).
238. H. Schneckenburger, R. Steiner, W. S. L. Strauss, K. Stock, and R. Sailer, "Fluorescence Technologies in Biomedical Diagnostics," Chap. 15 in Handbook of Optical Biomedical Diagnostics, V. V. Tuchin (Ed.), pp. 825-874, SPIE Press, PM107, Bellingham (2002).
239. H. Ashkenazi, Z. Malik, Y. Harth, and Y. Nitzan, "Eradication of *Propionibacterium acnes* by its endogenic porphyrins after illumination with high intensity blue light," FEMS Immunol. and Med. Microbiol. 35, 17-24 (2003).
240. Y. Kotoku, J. Kato, G. Akashi, Y. Hirai, and K. Ishihara, "Bactericidal effect of a 405-nm diode laser on *Porphyromonas gingivalis*," Laser Physics Letters 6(5), 388-392 (2009).

241. K. König, G. Flemming, and R. Hibst, "Laser-induced autofluorescence spectroscopy of dental caries lesion," Cell. Mol. Biol. 44, 1293-1300 (1998).
242. E. G. Borisova, T. T. Uzunov, and L. A. Avramov, "Early differentiation between caries and tooth demineralization using laser-induced autofluorescence spectroscopy," Lasers Surg. Med. 34, 249-253 (2004).
243. E. Borisova, T. Uzunov, and L. Avramov, "Laser-induced autofluorescence study of caries model in vitro," Lasers Med. Sci. 21(1), 34-41 (2006).
244. R. R. Alfano, W. Lam, H. J. Zarrabi, M. A. Alfano, J. Cordero, D. B. Tata, and C. E. Swenberg, "Human teeth with and without caries studied by laser scattering, fluorescence, and absorption spectroscopy," IEEE J. Quantum Electronics QE-20(12), 1512-1516 (1984).
245. K. Konig, H. Schneckenburger, and R. Hibst, "Time-gated in vivo autofluorescence imaging of dental caries," Cell. Mol. Biol. 45, 233-239 (1999).
246. E. Borisova, P. Troyanova, P. Pavlova, and L. Avramov, "Diagnostics of pigmented skin tumors based on laser-induced autofluorescence and diffuse reflectance spectroscopy," Quantum Electronics 38(6), 597-605 (2008).
247. E. Borisova, E. Carstea, L. Cristescu, E. Pavlova, N. Hadjiolov, P. Troyanova, and L. Avramov, "Light-induced fluorescence spectroscopy and optical coherence tomography of basal cell carcinoma," Journal of Innovative Optical Health Sciences 2(3), 261-268 (2009).
248. S. K. Chang, Y. N. Mirabal, E. N. Atkinson, D. Cox, A. Malpica, M. Follen, and R. R. Richards-Kortum, "Combined reflectance and fluorescence spectroscopy for *in vivo* detection of cervical pre-cancer," J. Biomed. Opt. 10(2), 024031 (2005).
249. A. Alimova, A. Katz, V. Sriramoju, Y. Budansky, A. A. Bykov, R. Zeylikovich, and R. R. Alfano, "Hybrid phosphorescence and fluorescence native spectroscopy for breast cancer detection," J. Biomed. Opt. 12(1), 014004 (2007).
250. A. Gerger, S. Koller, T. Kern, C. Massone, K. Steiger, E. Richtig, H. Kerl, and J. Smolle, "Diagnostic applicability of *in vivo* confocal laser scanning microscopy in melanocytic skin tumors," J. Invest. Dermatol. 124, 493–498 (2005).
251. S.-J. Tseng, Y.-H. Lee, Z.-H. Chen, H.-H. Lin, C.-Y. Lin, and S.-C. Tang, "Integration of optical clearing and optical sectioning microscopy for three-dimensional imaging of natural biomaterial scaffolds in thin sections," J. Biomed. Opt. 14(4), 044004 (2009).
252. Y.-Y. Fu, C.-W. Lin, G. Enikolopov, E. Sibley, A.-S. Chiang, and S.-C. Tang, "Microtome-free 3-dimensional confocal imaging method for visualization of mouse intestine with subcellular-level resolution," Gastroenterology 137(2), 453–465 (2009).
253. Y.-Y. Fu, and S.-C. Tang, "Optical clearing facilitates integrated 3D visualization of mouse ileal microstructure and vascular network with high definition," Microvascular Res. 80, 512-521 (2010).
254. Y.-A. Liu, Y. Chen, A.-S. Chiang, S.-J. Peng, P. J. Pasricha, and S.-C. Tang, "Optical clearing improves the imaging depth and signal-to-noise ratio for digital analysis and three-dimensional projection of the human enteric nervous system," Neurogastroenterology & Motility 23, e446-e457 (2011).
255. Y.-Y. Fu, C.-H. Lu, C.-W. Lin, J.-H. Juang, G. Enikolopov, E. Sibley, A.-S. Chiang, and S.-C. Tang, "Three-dimensional optical method for integrated visualization of mouse islet microstructure and vascular network with subcellular-level resolution," J. Biomed. Opt. 15(4), 046018 (2010).
256. A.-S. Chiang, Y.-C. Liu, S.-L. Chiu, S.-H. Hu, C.-Y. Huang, and C.-H. Hsieh, "Three dimensional mapping of brain neuropils in the cockroach *Diploptera punctata*," J. Comp. Neurol. 440, 1–11 (2001).
257. A. S. Chiang, "Aqueous tissue clearing solution," US Patent, US6472216 (2002).
258. J. Huisken, and D. Y. R. Stainier, "Selective plane illumination microscopy techniques in developmental biology," Development 136, 1963–1975 (2009).
259. K. Becker, N. Jährling, E. R. Kramer, F. Schnorrer, and H.-U. Dodt, "Ultramicroscopy: 3D reconstruction of large microscopical specimens," J. Biophotonics 1, 36–42 (2008).
260. K. Becker, N. Jährling, S. Saghafi, R. Weiler, and H. U. Dodt, "Chemical clearing and dehydration of GFP expressing mouse brains," PLOS One 7(3), e33916 (2012).
261. O. I. Efimova, and K. V. Anokhin, "Increase of optical permeability of isolated adult mouse brain structures," Bull. Exp. Biol. Med. 147(1), 4–7 (2009).
262. A. Ertürk, K. Becker, N. Jährling, C. P. Mauch, C. D. Hojer, J. G. Egen, F. Hellal, F. Bradke, M. Sheng, and H. U. Dodt, "Three-dimensional imaging of solvent-cleared organs using 3DISCO," Nature Protocols 7(11), 1983–1995 (2012).
263. R. G. M. Kolkman, E. Hondebrink, W. Steenbergen, and F. F. M. de Mul, "*In vivo* photoacoustic imaging of blood vessels using an extreme-narrow aperture sensor," IEEE J. Sel. Top. Quantum Electron. 9, 343–346 (2003).
264. R. G. M. Kolkman, J. H. G. M. Klaessens, E. Hondebrink, J. C. W. Hopman, F. F. M. de Mul, W. Steenbergen, J. M. Thijssen, and T. G. van Leeuwen, "Photoacoustic determination of blood vessel diameter," Phys. Med. Biol. 49, 4745–4756 (2004).

265. K. Maslov, G. Stoica, and L. H. Wang, "In vivo dark-field reflection-mode photoacoustic microscopy," Opt. Lett. 30(6), 625-627 (2005).
266. A. A. Oraevsky, A. A. Karabutov, S. V. Solomatin, E. V. Savateeva, V. A. Andreev, Z. Gatalica, H. Singh, and R. D. Fleming, "Laser optoacoustic imaging of breast cancer *in vivo*," Proc. SPIE 4256, 6–15 (2001).
267. H. F. Zhang, K. Maslov, and L. H. Wang, "*In vivo* imaging of subcutaneous structures using functional photoacoustic microscopy," Nature Protocols 2(4), 797-804 (2007).
268. R. O. Esenaliev, I. V. Larina, K. V. Larin, D. J. Deyo, M. Motamedi, and D. S. Prough, "Optoacoustic technique for noninvasive monitoring of blood oxygenation: a feasibility study," Appl. Opt. 41, 4722–4731 (2002).
269. C. C. Harland, J. C. Bamber, B. A. Gusterson, and P. S. Mortime, "High frequency, high resolution B-scan ultrasound in the assessment of skin tumours," Br. J. Dermatol. 128, 525-532 (1993).
270. Y. Zhou, J. J. Yao, and L. H. Wang, "Optical clearing-aided photoacoustic microscopy with enhanced resolution and imaging depth," Opt. Lett. 38(14), 2592-2595 (2013).
271. K. M. Quan, G. B. Christison, H. A. MacKenzie, and P. Hodgson, "Glucose determination by a pulsed photoacoustic technique: an experimental study using a gelatin-based tissue phantom," Phys. Med. Biol. 38, 1911–1922 (1993).
272. M. Kinnunen, and R. Myllyla, "Application of optical coherence tomography, pulsed photoacoustic technique, and time-of-flight technique to detect changes in the scattering properties of a tissue-simulating phantom," J. Biomed. Opt. 13(2), 024005 (2008).
273. H. A. MacKenzie, H. S. Ashton, S. Spiers, Y. Shen, S. S. Freeborn, J. Hannigan, J. Lindberg, and P. Rae, "Advances in photoacoustic noninvasive glucose testing," Clin. Chem. 45, 1587–1595 (1999).
274. O. S. Khalil, "Non-invasive glucose measurement technologies: an update from 1999 to the dawn of the new millennium," Diabetes Technol. Ther. 6, 660–697 (2004).
275. R. Cicchi, S. Sestini, V. De Giorgi, D. Massi, T. Lotti, and F. S. Pavone, "Nonlinear laser imaging of skin lesions," J. Biophotonics 1(1), 62–73 (2008).
276. P. J. Campagnola, H. A. Clark, W. A. Mohler, A. Lewis, and L. M. Loew, "Second-harmonic imaging microscopy of living cells," J. Biomed. Opt. 6(3), 277-286 (2001).
277. P. J. Campagnola, A. C. Millard, M. Terasaki, P. E. Hoppe, C. J. Malone, and W. A. Mohler, "Three-dimensional high-resolution second-harmonic generation imaging of endogenous structural proteins in biological tissues," Biophys. J. 82, 493–508 (2002).
278. P. Bianchini, and A. Diaspro, "Three-dimensional (3D) backward and forward second harmonic generation (SHG) microscopy of biological tissues," J. Biophotonics 1(6), 443-450 (2008).
279. V. Ajeti, O. Nadiarnykh, S. M. Ponik, P. J. Keely, K. W. Eliceiri, and P. J. Campagnola, "Structural changes in mixed Col I/Col V collagen gels probed by SHG microscopy: implications for probing stromal alterations in human breast cancer," Biomedical Optics Express 2(8), 2307-2316 (2011).
280. T. Yasui, Y. Tohno, and T. Araki, "Characterization of collagen orientation in human dermis by two-dimensional second-harmonic-generation polarimetry," J. Biomed. Opt. 9(2), 259–264 (2004).
281. H. G. Breunig, M. Weinigel, R. Buckle, M. Kellner-Hofer, J. Lademann, M. E. Darvin, W. Sterry, and K. Konig, "Clinical coherent anti-Stokes Raman scattering and multiphoton tomography of human skin with a femtosecond laser and photonic crystal fiber," Laser Physics Letters 10, 025604 (2013).
282. G. Deka, W.-W. Wu, and F.-J. Kao, "In vivo wound healing diagnosis with second harmonic and fluorescence lifetime imaging," J. Biomed. Opt. 18(6), 061222 (2013).
283. A. Ghazaryan, H. F. Tsai, G. Hayrapetyan, W.-L. Chen, Y.-F. Chen, M. Y. Jeong, C.-S. Kim, S.-J. Chen, and C.-Y. Dong, "Analysis of collagen fiber domain organization by Fourier second harmonic generation microscopy," J. Biomed. Opt. 18(3), 031105 (2013).
284. R. Cicchi, L. Sacconi, and F. Pavone "Nonlinear Imaging of Tissues," Chap. 20 in Handbook of Photonics for Biomedical Science, V. V. Tuchin (Ed.), pp. 509-545, CRC Press, Taylor & Francis Group, Boca Raton (2010).
285. M. Muller, J. A. Squier, T. Wilson, and G. Brakenhoff, "3D microscopy of transparent objects using third-harmonic generation," J. Microsc. 191, 266–272 (1998).
286. G. Hall, K. W. Eliceiri, and P. J. Campagnola, "Simultaneous determination of the second-harmonic generation emission directionality and reduced scattering coefficient from three-dimensional imaging of thick tissues," J. Biomed. Opt. 18(1), 116008 (2013).
287. M. Zimmerley, R. A. McClure, B. Choi, and E. O. Potma, "Following dimethyl sulfoxide skin optical clearing dynamics with quantitative nonlinear multimodal microscopy," Appl. Opt. 48(10), D79–D87 (2009).
288. M. V. Schulmerich, J. H. Cole, K. A. Dooley, M. D. Morris, J. M. Kreider, and S. A. Goldstein, "Optical clearing in transcutaneous Raman spectroscopy of murine cortical bone tissue," J. Biomed. Opt. 13(2), 021108 (2008).
289. D. Huang, W. Zhang, H. Zhong, H. Xiong, X. Guo, and Z. Guo, "Optical clearing of porcine skin tissue in vitro studied by Raman microspectroscopy," J. Biomed. Opt. 17(1), 015004 (2012).

290. P. J. Caspers, A. C. Williams, E. A. Carter, H. G. M. Edwards, B. W. Barry, H. A. Bruining, and G. J. Puppels, "Monitoring the penetration enhancer dimethyl sulfoxide in human stratum corneum in vivo by confocal Raman spectroscopy," Pharm. Res. 19(10), 1577–1580 (2002).
291. A. A. Angeluts, A. V. Balakin, M. G. Evdokimov, M. N. Esaulkov, M. M. Nazarov, I. A. Ozheredov, D. A. Sapozhnikov, P. M. Solyankin, O. P. Cherkasova, and A. P. Shkurinov, "Characteristic responses of biological and nanoscale systems in the terahertz frequency range," Quantum Electronics 44(7), 614-632 (2014).
292. M. Nazarov, A. Shkurinov, V. V. Tuchin, and X.-C. Zhang, "Terahertz tissue spectroscopy and imaging," Chapter 17 in Handbook of Photonics for Biomedical Science, V. V. Tuchin, Ed., pp. 592–617, CRC Press, London, Taylor & Francis Group (2010).
293. M. M. Nazarov, A. P. Shkurinov, E. A. Kuleshov, and V. V. Tuchin, "Terahertz time-domain spectroscopy of biological tissues," Quantum Electronics 38(7), 647–654 (2008).
294. G. M. Png, J. W. Choi, B. W.-H. Ng, S. P. Mickan, D. Abbott, and X.-C. Zhang, "The impact of hydration changes in fresh bio-tissue on THz spectroscopic measurements," Phys. Med. Biol. 53, 3501–3517 (2008).
295. A. V. Borodin, V. Ya. Gayvoronsky, O. D. Kachkovsky, Ya. A. Prostota, A. V. Kargovskii, M. M. Nazarov, D. A. Sapozhnikov, Yu. L. Slominskii, I. N. Smirnova, and A. P. Shkurinov, "Structure sensitive changes in the terahertz absorption spectra of merocyanine dye derivatives," Optics and Spectroscopy 107(4), 505-514 (2009).
296. C. S. Joseph, R. Patel, V. A. Neel, R. H. Giles, and A. N. Yaroslavsky, "Imaging of ex vivo nonmelanoma skin cancers in the optical and terahertz spectral regions," J. Biophotonics 7(5), 295-303 (2014).
297. S. J. Oh, J. Kang, I. Maeng, J.-S. Suh, Y.-M. Huh, S. Haam, and J.-H. SonMarch, "Nanoparticle-enabled terahertz imaging for cancer diagnosis," Opt. Express 17(5), 3469–3475 (2009).
298. T. Yu, X. Wen, V. V. Tuchin, Q. Luo, and D. Zhu, "Quantitative analysis of dehydration in porcine skin for assessing mechanism of optical clearing," J. Biomed. Opt. 16, 095002 (2011).
299. A. S. Kolesnikov, E. A. Kolesnikova, A. P. Popov, M. M. Nazarov, A. P. Shkurinov, and V. V. Tuchin, "*In vitro* terahertz monitoring of muscle tissue dehydration under the action of hyperosmotic agents," Quantum Electronics 44(7), 633-640 (2014).
300. R. E. Beck, and J. S. Schultz, "Hindrance of solute diffusion within membranes as measured with microporous membranes of known pore geometry," Biochem. Biophys. Acta 255, 272-303 (1972).
301. A. Kotyk, and K. Janacek, Membrane Transport: An Interdisciplinary Approach, Plenum Press, New York (1977).
302. I. H. Blank, J. Moloney, A. G. Emslie, and I. Apt, "The diffusion of water across the stratum corneum as a function of its water content," J. Invest. Dermatol. 82, 188-194 (1984).
303. B. Sennhenn, K. Giese, K. Plamann, N. Harendt, and K. Kolmel, "In vivo evaluation of the penetration of topically applied drugs into human skin by spectroscopic methods," Skin Pharmacol. 6, 152-160 (1993).
304. K. D. Peck, A.-H. Ghanem, and W. I. Higuchi, "Hindered diffusion of polar molecules through and effective pore radii estimates of intact and ethanol treated human epidermal membrane," Pharmaceutical Research 11(9), 1306-1314 (1994).
305. T. Inamori, A.-H. Ghanem, W. I. Higuchi, and V. Srinivasan, "Macromolecule transport in and effective pore size of ethanol pretreated human epidermal membrane," Int. J. Pharmaceutics 105, 113-123 (1994).
306. R. Bertram, and M. Pernarowski, "Glucose diffusion in pancreatic islets of Langerhans," Biophys. J. 74, 1722-1731 (1998).
307. P. Gribbon, and T. E. Hardingham, "Macromolecular diffusion of biological polymers measured by confocal fluorescence recovery after photobleaching," Biophys. J. 75, 1032-1039 (1998).
308. A. N. Yaroslavskaya, I. V. Yaroslavsky, C. Otto, G. J. Puppels, H. Guindam, G. F. J. M. Vrensen, J. Greve, and V. V. Tuchin, "Water exchange in human eye lens monitored by confocal Raman microspectroscopy," Biophysics 43(1), 109-114 (1998).
309. E. E. Alanis, G. G. Romero, and C. C. Martinez, "Interferometric measurement of diffusion coefficients through a scanning laser beam," Opt. Eng. 39(3), 744-750 (2000).
310. S. Papadopoulos, K. D. Jurgens, and G. Gros, "Protein diffusion in living skeletal muscle fibers: dependence on protein size, fiber type, and contraction," Biophys. J. 79, 2084-2094 (2000).
311. A. E. Kamholz, E. A. Schilling, and P. Yager, "Optical measurement of transverse molecular diffusion in a microchannel," Biophys. J. 80, 1967-1972 (2001).
312. S. S. Olmsted, J. L. Padgett, A. I. Yudin, K. J. Whaley, T. R. Moench, and R. A. Cone, "Diffusion of macromolecules and virus-like particles in human cervical mucus," Biophys. J. 81, 1930-1937 (2001).
313. J. Kusba, L. Li, I. Gryczynski, G. Piszczek, M. Johnson, and J. R. Lakowicz, "Lateral diffusion coefficients in membranes measured by resonance energy transfer and a new algorithm for diffusion in two dimensions," Biophys. J. 82, 1358-1372 (2002).
314. W. Heller, "Remarks on refractive index mixture rules," J. Phys. Chem. 69(4), 1123–1129 (1965).

315. J. S. Maier, S. A. Walker, S. Fantini, M. A. Franceschini, and E. Gratton, "Possible correlation between blood glucose concentration and the reduced scattering coefficient of tissues in the near infrared," Opt. Lett. 19(24), 2062-2064 (1994).
316. M. Kohl, M. Esseupreis, and M. Cope, "The influence of glucose concentration upon the transport of light in tissue-simulating phantoms," Phys. Med. Biol. 40, 1267-1287 (1995).
317. J. M. Schmitt, and G. Kumar, "Optical scattering properties of soft tissue: a discrete particle model," Appl. Opt. 37(13), 2788-2797 (1998).
318. W. H. Press, S. A. Tuekolsky, W. T. Vettering, and B. P. Flannery, Numerical recipes in C: the art of scientific computing, Cambridge: Cambridge University Press (1992).
319. I. S. Grigoriev, and E. Z. Meylikhov (Eds.), Physical Values: Handbook, Moscow: EnergoAtomIzdat (1991).

Contents

1 Introduction: fundamentals of optical clearing of tissues and cells
2 Immersion clearing
3 Compression clearing
4 Photochemical and photothermal clearing
5 Applications of optical clearing
  5.1 Optical coherence tomography
  5.2 Optical projection tomography
  5.3 Fluorescence imaging
  5.4 Photoacoustic imaging
  5.5 Nonlinear and Raman microscopy
  5.6 Terahertz spectroscopy
  5.7 Determination of diffusion coefficients of clearing agents and drugs in tissues
6 Conclusion

1 Introduction: fundamentals of optical clearing of tissues and cells

During the last 25 years the interest to the development and application of optical methods in clinical functional imaging of physiological conditions, diagnostics and therapy of cancer, and other diseases is permanently growing [1-3]. It is caused by the unique informativity, relative simplicity, safety, and sufficiently low cost of optical instruments, as compared, e.g., to X-ray computer tomography or magnetic resonance tomography (MRT). However, the main limitation of optical diagnostic methods, including the optical diffusion tomography, optical coherence tomography (OCT), confocal microscopy, reflection spectroscopy, etc., is the strong scattering of light in biological tissues and blood that reduces the contrast, spatial resolution, and probing depth [3-5].

The scattering coefficient (μ_s) and the scattering anisotropy factor (g) mainly depend upon the refractive index mismatch between the components of the cells that form the tissue, such as the plasma membrane of the cell, mitochondria, nucleus, other organelles, cytoplasm, and extracellular fluid. In fibrous tissues (stroma of eye sclera and cornea, dermis, *dura mater*, connective tissue of vascular walls, fibrous components of muscle tissue and mammary gland, cartilage, tendon, etc.) the scattering is caused by the refractive index difference between the interstitial fluid or cytoplasm and the extensive chains of scleroproteins (collagen, elastin, and reticulin fibrils) [3, 6]. The refractive index values for nuclei and cytoplasm organelles of animal cells, containing nearly the same amount of proteins and nucleic acids, lie within the relatively narrow interval from 1.38 to 1.41 [7]. In particular, for the nucleus the refractive index is n_{nc} = 1.39 [8], and for the cytoplasm n_0 = 1.35–1.37 [3]. The scattering particles (organelles, protein fibrils, membranes, and globules) have greater density of proteins and lipids and, hence, higher refractive index (n_s = 1.39–1.47) in comparison with the base substance of the cytoplasm [6]. The refractive index values of the connective tissue fibrils lie in the range 1.41-1.53 and depend upon the degree of hydration of their major component, the collagen [9]. The refractive index of the interstitial fluid and the blood plasma amounts to nearly 1.33-1.35 depending on the wavelength [3, 10]. The main scatterers in the blood are the red blood cells (erythrocytes), which are acaryocytes, containing 70% of water, 25% of haemoglobin, and 5% of lipids, sugars, salts, enzymes, and proteins [11]. The refractive index values of dehydrated erythrocytes at the wavelength of 550 nm fall within the range 1.61-1.66 [12]. The refractive index of the haemoglobin solution with the concentration of 32 g/dL, which is a typical concentration of haemoglobin in the erythrocyte, amounts to nearly 1.42 [13]. For the human blood the refractive index is 1.36-1.40 depending on the wavelength [3].

Numerous methods have been developed to increase the tissue probing depth [14]. For example, during a long time the limit probing depth in multiphoton microscopy did not exceed 100 μm [15], however, the combination of multiphoton excitation of fluorescence with very high efficiency of light collection increased the imaging depth in a scattering medium to 2 mm [16, 17]. The OCT allows the study of internal structure of tissues to the depth up to 3 mm with the spatial resolution 5-20 μm without disturbing the tissue integrity [18]. The probing depth up to a few centimetres is provided by the multimodal imaging method, combining the light absorption with acoustic detection (referred to as photoacoustic tomography) [19].

One of simple and efficient methods of solving the problem of increasing the depth and quality of intratissular structure imaging, as well as of increasing

the precision of spectroscopic information from the deep tissue layers and the blood, is the temporary reduction of the tissue light scattering [20-22]. In nonlinear spectroscopy and imaging, as well as in high-precision laser surgery (particularly, in cell nanosurgery), the reduction of scattering in the tissue facilitates the decrease of the strongly focused laser beam divergence and provides its precise focusing onto the object, which essentially improves the efficiency of the procedure and allows the reduction of the radiation energy, necessary for successful visualisation or photo-induced effect [21-27].

According to Web of Science, PubMed and other sources, the interest to the optical clearing methods is permanently growing, which is caused by the progress of optical and laser technologies for application in biology and medicine (see Fig. 1).

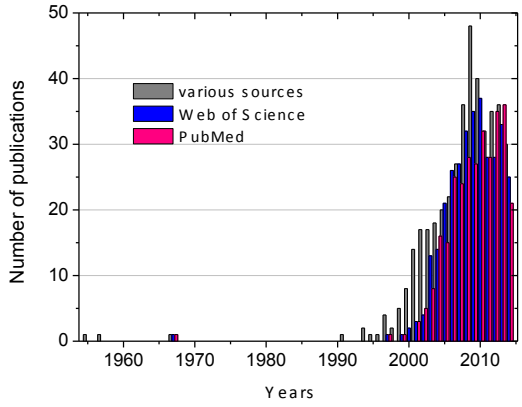


Fig. 1 Approximate evaluation of the number of publications related to the optical clearing of tissues from 1955 to August 2014. The dependences are plotted using the databases Web of Science, PubMed, and other available sources.

Numerous examples of physical and chemical impacts that allow one to control the scattering properties of tissues are reported. They include compression [28, 29], stretching [30], dehydration [31, 32], coagulation [33], immersion with biocompatible chemical agents [20-27, 34-36], as well as photochemical [37, 38] and photothermal [38] clearing.

The majority of methods reducing the tissue scattering are based on the matching of the refractive indices of the tissue components, either due to replacing the interstitial fluid with the immersion agent, possessing a higher refractive index, or due to increasing the concentration of proteins and mucopolysaccharides in the interstitial fluid as a result of water diffusion from the tissue caused by the osmose, making the refractive index of the interstitial fluid closer to that of the fibrils. In addition, the optical homogeneity can increase due to the compaction of scattering centres (e.g., collagen fibres) due to both pressing out the interstitial fluid from the affected volume and the dehydration at the expense of the agent impact or water evaporation. [22, 25, 26, 28-32, 39]. The particular mechanisms of optical clearing depend on the tissue type and the method used.

In the present review we discuss the physical and molecular mechanisms of immersion, compression, and photodynamic/photothermal methods of optical clearing of some fibrous and cellular tissues, as well as the application of these methods for increasing the probing depth and resolution power of optical diagnostic methods, such as optical coherence, projection, and photoacoustic tomography, fluorescence imaging, nonlinear and Raman microscopy, and terahertz imaging. This review is different from earlier published and cited ones (for example, Refs. [36, 39]) extended bibliography due to addition of new references and sections. In particular, the mechanisms and features of compression and photodynamic/photothermal clearing are described in details; sections on methods of OCA diffusion coefficient evaluation and applications of optical clearing technique (THz spectroscopy, projection and photoacoustic tomography etc.) are extended significantly.

2 Immersion clearing

Following the development of immersion refractometry applied to cells, in 1955 Barer et al. [40] have first proposed the optical clearing of cell suspension by means of the protein solution having the same refractive index as the cell cytoplasm. In early 1990s the method of immersion optical clearing was first applied to the eye sclera and cornea [41].

After the appearance of the tissue optical clearing idea many research teams joined the intense studies of the specific features and mechanisms of this phenomenon and demonstrated the capabilities of the method in increasing the probing depth or contrasting the image of optical inhomogeneities inside a scattering medium [39, 42-88].

New original results obtained using the combination of optical clearing with the known optical visualisation methods, such as laser speckle-contrast imaging [34, 71, 75, 77, 79], OCT [20, 29, 35, 59-61, 65, 69, 80, 82], microscopic imaging [23, 24, 83, 84], ultra-microscopy [85-87], etc., demonstrated high potentiality of their mutual use not only for getting high-resolution structure and functional tissue images *in vitro* [72, 73, 83-87], but also for optical imaging and diagnostics *in vivo* [25, 34, 45, 50, 59, 61, 65, 68, 70, 71, 75-77, 79-81]. Table 1 shows the increase of the light penetration depth, caused by clearing agents in some diagnostic methods.

The studies of tissue scattering kinetics under the penetration of immersion agents allowed the development of techniques for assessing the diffusion coefficients and permeability [35, 43, 47, 88-94]. Using these techniques, the diffusion rates of glucose and other medicinal preparations and immersion fluids were determined for the tissues of eye [91-96], skin [45, 97, 98], *dura mater* [88], and other tissues [99, 100]. The monitoring of optical clearing agent diffusion with high resolution in time and depth allows differentiation

between healthy and pathologically modified biotissues [101-105].

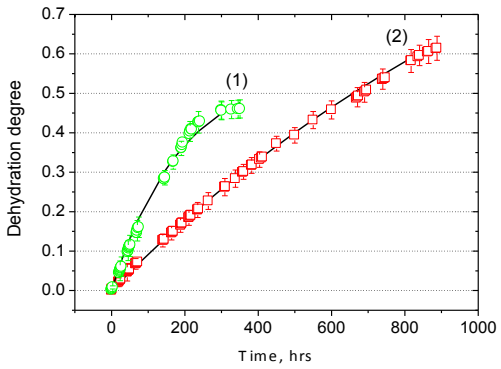
The optical immersion clearing, as already mentioned above, is based on the impregnation (immersion) of the tissue with a biocompatible chemical agent, possessing sufficiently high refractive index to match the refractive indices of the scatterers and the surrounding medium, penetrating into the interstitial liquid of the tissue. Commonly, the optical clearing agent (OCA) has hyperosmotic properties [21, 22]. Many chemical substances used in cosmetology in the composition of different preparations satisfy these conditions. These agents can be roughly divided into polyatomic alcohols (glycerol, polyethylene glycol (PEG), polypropylene glycol, combined mixtures on the base of polypropylene glycols and polyethylene glycols, mannitol, sorbitol, xylitol) [56, 57, 76, 84, 88, 103, 105-108], sugars (glucose, dextrose, fructose, ribose, saccharose) [82, 88-91, 94, 96, 97, 99, 100, 104, 109-111], organic acids (oleic and linoleic acid) [105, 113, 114], other organic solvents (dimethyl sulphoxide (DMSO)) [105, 114-117], and X-ray contrast agents (verografin, trasograph) [6, 42-44].

At present several physical and chemical mechanisms of the light scattering reduction under the action of OCA are proposed and thoroughly described [29, 31, 32, 39, 43, 46, 47, 55, 56, 58, 63, 67, 72, 76, 78, 84, 88, 106-112, 118-122]: dehydration of tissue components, partial replacement of interstitial fluid with the immersion agent, and structure modification or dissociation of collagen. The first mechanism is related to the hyperosmotic properties of the OCA [31, 36, 39, 56, 120]. The contact of hyperosmotic OCA with the tissue surface causes the water diffusion from the tissue. These processes produce fast and considerable clearing effect, since, first, the concentration of salts and proteins dissolved in the interstitial fluid increases and, therefore, the refractive index of the interstitial fluid becomes closer to that of the scattering fibrils, and, second, the weight and the thickness of the tissue decrease, the tissue becomes denser, and the ordering of scattering components increases [36, 39].

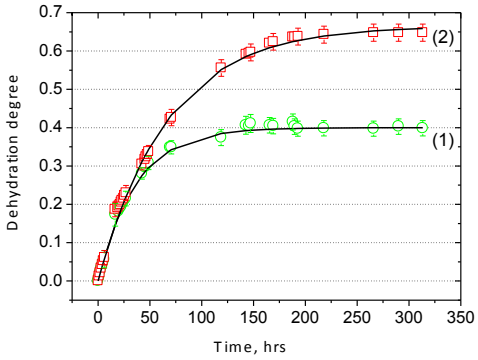
Rylander et al. [31] compared the optical transmission of the rat skin under the application of DMSO and glycerol with that under dehydration. It was shown that in the course of natural water evaporation the light transmission through the skin sample increased in the same way as under dehydration caused by the OCA effect, but during a longer time.

In order to analyse the water loss in the process of tissue optical clearing quantitatively, the authors of Ref. [67] used the optical spectroscopy in the near IR range. Measuring the skin reflection coefficient at the wavelengths λ_1 = 1100 and λ_2 = 1936 nm (the water absorption band), Xu and Wang used the double-wave analysis to assess the water content in the skin. The authors demonstrated that the change of the water content in the skin correlated with the optical clearing effect during the first minutes, namely, under the impact of 80% solutions of glycerol and propylene glycol the water content at first rapidly decreases, and then the dehydration process becomes slower.

The kinetics of skin dehydration degree under the action of 88% aqueous solution of glycerol and air, studied by Genina et al. [56] basing on the weight measurements of human skin samples (see Fig. 2a), allowed the assessment of the characteristic time τ of the process, i.e., the time, during which the dehydration degree increases by e times. Under the action of OCA τ amounts to 193.4 ± 12.3 hours, while under the conditions of natural evaporation of interstitial water this parameter equals 1408.9 ± 36.3 hours.



a



b

Fig. 2 Dehydration kinetics of human skin samples with intact (a) and perforated (b) epidermis under the action of 88% glycerol solution (1) and in the course of interstitial water evaporation in air (2). The symbols correspond to the averaged experimental data; the curves show the result of approximation. The vertical lines present the standard deviation (from the data of Ref. [56]).

At the same time, it is seen from the Fig. 2 that, in contrast to the natural drying in air, under the action of the OCA no full dehydration occurs, since a part of the OCA penetrates into the interstitial space and is mixed with the interstitial fluid. It is known, that most of the OCAs are hygroscopic and in the humid environment they adsorb water molecules till the saturation is achieved. Thus, for glycerol the saturation level

amounts to 55 and for propylene glycol 32 percent in volume [123]. Therefore, OCAs inhibit complete dehydration by keeping a part of water in the tissue.

For fibrous tissues, such as sclera, *dura mater*, dermis, etc., both processes, namely, the water loss and the diffusion of the hyperosmotic agent into the skin, occur simultaneously, but the mechanism of the interstitial fluid replacement with the OCA solution is prevailing for all the agents used, since their molecular size is much smaller than the mean separation between the fibrils [3, 43].

In the case of transepidermal delivery of hydrophilic OCAs into the skin the diffusion is inhibited by the existence of the epidermis lipid barrier. The human skin dehydration at the delivery of the hyperosmotic OCA through the perforated *stratum corneum* (the perforation may be implemented, e.g., by fractional microablation) is presented in Fig. 2,b. The epidermis permeability improvement resulted in the accelerated diffusion of both water and 88% glycerol solution. Fig. 2 shows that when the samples with intact and perforated horny layer are dried under the identical conditions, their final dehydration degree should be practically similar. However, from the analysis of the dehydration characteristic time (for the perforated sample τ amounts to 71.2±1.9 hours) it follows that the dehydration process in this case occurs by more than 20 folds faster than in the intact epidermis (τ = 1408.9±36.3 hours). The value of τ for the sample with perforated epidermis under the action of the OCA was only 36.4 ± 0.7 hours, which is almost by 5.5 folds smaller than for the intact sample (τ = 193.4±12.3 hours) [56].

In Fig. 2,b it is well seen that with the epidermis damaged the maximal value of dehydration degree under the evaporation of water from the tissue is essentially higher than under its osmotic removal. At the same time the skin dehydration rate due to evaporation is by nearly two times smaller than under osmotic water removal.

The study of water evaporation process allowed the separation of the dehydration mechanism of optical clearing from other mechanisms (i.e., the matching of refractive indices due to the penetration of OCA into the tissue and the collagen structure modification). The fact that attracts attention in the dehydration under the action of glycerol is that the degree of dehydration in the samples with perforated *stratum corneum* is smaller than that in the intact samples. As mention above, in both cases there are two counterpropagating fluxes, one of them is the water diffusion from lower layers of epidermis and from dermis into the surrounding solution, and the other one is the diffusion of the OCA from the surrounding solution into the tissue. Apparently, in the non-perforated sample the rate difference between these fluxes is greater than in the perforated one, since in the absence of the epidermis damage the drainage of water from the tissue considerably exceeds the glycerol delivery into the tissue. From the practical point of view, the topical injection of OCA into the skin through the channels in the epidermis hampers the formation of strong concentration gradient between the interstitial fluid and the OCA solution, which reduces the tissue dehydration and can be considered as a positive factor for optical clearing of skin *in vivo*.

Mao et al. [107] focused their attention on the study of the efficiency of six polyatomic alcohols with hydroxyl groups (1-butanol, 1,4-butanediol, 1,3-propanediol, PEG-200, PEG-400, and glycerol) with molecular weights from 74 to 420 Da, and the refractive index values from 1.40 to 1.47, affecting the degree of skin optical clearing. For better *in vitro* modelling of the topical OCA application to the skin *in vivo*, the agents were applied to the pig skin epidermis, while the dermis was moistened with saline. The relative transmission of the samples, measured using the integrating sphere, was used to assess the efficiency of optical clearing [107]. The authors found that the glycerol, which is a triatomic alcohol, caused the maximal clearing effect, the monoatomic alcohol 1-butanol caused the smallest effect, and four diatomic alcohols caused intermediate clearing effect. After checking the interrelation between the optical clearing efficiency and the refractive indices or molecular weight of the OCAs under study, the authors concluded that the clearing effect, caused by alcohols, should be related to the number of hydroxyl groups rather than to the refractive index or the molecular weight value of the OCA.

In fibrous tissues the optical clearing process can also incorporate the variations in the molecular structure of the basic component of these tissues, the collagen fibres, including the reversible solvability of collagen in sugars and polyatomic alcohols. The OCA-induced destabilisation of collagen structure can lead to the additional reduction of optical scattering in a tissue due to the decrease of the basic scatterer size. [121].

The collagen fibres have complex self-organising structure and are the main scattering centres in tissues [112]. They are widely presented in different tissues, particularly, in fibrous ones, such as skin dermis and eye sclera. It is established that the hydrogen bond is the main bonding force between the triple collagen helices. The OCAs with multiple hydroxyl groups possess a greater negative charge that destabilises the highly-ordered collagen structure till its dissociation. Since the hydrogen bonds in the triple collagen helices belong to non-covalent interactions, the OCA-induced effect on the collagen dissociation can be easily reversed. Yeh et al. [109, 112, 121, 122] observed the dissociation of collagen fibres in the tissue *in vitro*, merged in glycerol. The subsequent replacement of glycerol with phosphate-buffer solution provided the restoration of the collagen structure.

Hirshburg et al. [110] performed mathematical modelling of molecular dynamics in order to clarify the formation of hydrogen bonds between the alcohol (glycerol, xylitol, and sorbitol) and collagen molecules. They divided the hydrogen bond bridges into different types depending on the position of hydroxyl groups, involved in the interaction, with respect to carbon

atoms. They associated the type number with the number of carbon atoms in the hydrogen bond bridge. It was found that the bridges with large number, built in between the collagen molecules in the helix, can break the collagen-collagen and collagen-hydroxyl bonds more efficiently than the bridges with smaller numbers. Thus, the alcohols having pairs of hydroxyl groups with longer carbon chain between them should be more efficient in optical clearing that the alcohols having adjacent hydroxyl groups. The results of the modelling explain the fact that 1,3-propanediol demonstrated the optical clearing potential twice as great as that of 1,2-propanediol, although both possessed similar molecular weight (76.10 Da), close values of the refractive index (1.44 and 1.43), and osmolality (8.3 and 8.7 Osm/kg). The reason is that 1,2-propanediol can form only the bridges of the type I, while 1,3-propanediol forms the bridges of the type II [110]. Since the modelling of molecular dynamics can clarify the specific features of interaction between the OCA and the structural elements of the tissue at the microscopic (molecular) level, it can be a powerful tool in the study of optical clearing mechanisms, particularly, for choosing new high-efficiency OCAs.

Of great practical interest is the optical clearing of hard tissues, such as bone, cartilage and tendon. The reduction of scattering in these tissues offers the possibility to develop minimally invasive methods of laser diagnostics and therapy of brain and other deeply located tissues. The possibility of studying brain blood circulation without damaging the scull bone was demonstrated by Wang et al. [81]. The experiments with laboratory mice *in vivo* have shown that the minimal microvascular diameter resolved in the observation through the bone tissue, preliminarily processed with the specially developed optical clearing solution, amounts to 14.4±0.8 μm. The optical clearing of the human skull bone *in vitro* was studied by Genina et al. [57]. The authors have shown that the exposure of the ~5 mm thick skull bone sample to glycerol reduces the value of the transport scattering coefficients by 25% in the spectral range 1400-2000 nm. In the present case the main role in the clearing process is played by the replacement of water in the interstitial space with OCA due to the specific structure of the bone tissue that possesses higher porosity than soft tissues.

The transparency increase was studied in the samples of cartilage tissue of the human nasal septum and knee joint *in vitro* under the impact of trasograph [124] and in the rodent tail cartilage *ex vivo* under the impact of glycerol [112, 121]. The authors demonstrate the increase of the contrast in the image of the tissue by 2 – 2.5 folds during 1 minute for the transverse section and by 1.6 folds during 8 minutes for the longitudinal one [124] and the reversible disorganisation of collagen fibrils under the action of OCA [112, 121].

Optical clearing of the mouse tail tendon *in vitro* exposed to the glycerol solutions with different concentration was demonstrated in the papers by LaComb et al. [72], Nadiarnykh and Campagnola [73], and Rylander et al. [31]. The authors managed to increase the probing depth in the second harmonic generation microscopy up to 450 μm at the expense of considerable reduction of the scattering coefficient (up to 130 folds at the wavelength 890 nm during 5 hours) and increasing the packaging density of fibrils (according to the data of electron microscopy, the volume fraction of fibrils increased from 0.65 to 0.9) [31].

Blood vessels and capillaries transpierce practically all tissues, and the blood is a strongly scattering medium, so that its optical clearing is a serious problem for successful application of optical technologies both in diagnostics and in therapy/surgery. The difference between the refractive indices of the erythrocyte cytoplasm and the blood plasma, as well as the specific size and structure of blood corpuscles explain the blood scattering properties [3, 10, 11]. The refractive index of the erythrocyte cytoplasm is determined mainly by the haemoglobin concentration [11, 13, 125]. The volume and the shape of an individual erythrocyte are determined by the osmolality of the blood plasma [125, 126]. The blood scattering is also dependent on the ability of the red blood cells to aggregate or disaggregate [127].

When an OCA is injected into blood, the refractive index of the blood plasma increases and becomes comparable with the refractive index of the red blood cells. For example, the total attenuation coefficient of whole blood, diluted by two folds with saline, under the addition of 6.5% glycerol solution decreased from 4.2 to 2.0 mm^{-1}, and, correspondingly, the optical probing depth at the wavelength 820 nm increased by 117%. For other OCAs tested (glucose, dextran, propylene glycol, and trasograph) the increase of the probing depth was from 20 to 150% [22, 128]. It was also shown that the introduction of chemical agents is able to change the size and aggregation properties of erythrocytes, which allows the control of the blood optical properties, too [128].

Bashkatov et al. [53] have shown that the minimal light scattering is observed at the concentration of glucose in blood equal to 0.65 g/ml. In this case the blood appears to be completely immersed, but due to the difference in spectral dependence of refractive indices of the glucose solution and erythrocytes the residual scattering is still present. Obviously, such high concentration of glucose can be applied only topically and during a short period of time to prevent the destruction of blood and vascular wall cells. Nevertheless, the use of endoscopic optical imaging systems (OCT or confocal microscopy) and the controlled injection of small glucose volumes into the vascular lumen near the region of imaging may essentially facilitate obtaining a high-contrast image of an atherosclerosis plaque through the layer of blood.

The same group of authors showed the possibility of using a small volume of haemoglobin as an OCA. This haemoglobin can be obtained as a result of local haemolysis of erythrocytes in a blood vessel near the

site of optical endoscopic probe [51]. The blood scattering coefficient reduction by 30-40% was demonstrated theoretically in the spectral region 400-1000 nm under the increase of the local haemolysis by up to 20% in the immediate proximity of the optical probe.

Impregnation of blood-saturated tissues, such as the liver, with solutions having different osmolality also leads to the matching of refractive indices and scattering coefficient reduction, but the effect is not as prolonged as in fibrous tissues [22].

The optical clearing of tissues *in vivo* is, generally, more complex, since in this case a significant role begins to be played by the additional factors, on the one hand, the physiological temperature that accelerates the diffusion of OCA, and, on the other hand, the metabolic reaction of the living tissue, washing the OCA out. These factors can essentially modify the kinetic characteristics and the magnitude of the clearing effect [25, 34, 45, 59, 61, 68, 70, 76, 77, 79, 80, 82, 97, 98, 108, 113, 118, 119]. In living tissues the refractive index is a function of the physiological or pathological condition of the tissue. Depending on the specific features of the tissue condition, the refractive index of scatterers and/or the base substance can change (increase or decrease), and correspondingly the light scattering will change [3, 22]. In addition, the introduction of some OCAs, in particular, glycerol and glucose, into a tissue affects the condition of microcirculation in the tissue, causing a transient stasis of the microvessels [50, 65, 71, 77, 108].

One of the most important problems in optical diagnostics and treatment is the reduction of skin scattering aimed at visualising the inhomogeneities hidden inside the skin or under it. However, it is rather difficult to obtain the optical clearing of skin using noninvasive or minimally-invasive means, since the *stratum corneum* of the skin epidermis is a natural barrier that impedes the OCA penetration into the dermis [129]. For *in vivo* applications of the optical clearing method one has to use direct exposure of the skin dermis, or intradermal OCA injection. However, at low concentrations OCAs do not provide sufficient optical clearing, while at high concentrations they can induce edema, chemical burn, partial necrosis and scarring [45, 65, 108]. To develop an efficient and safe way of breaking the integrity of the epidermis *stratum corneum* and accelerating the penetration of OCA into the dermis, various physical methods [56, 118, 130-140], chemical enhancers of permeability [114, 118, 141-147], and their combinations [118, 148, 149] have been proposed.

Chemical OCA diffusion enhancement is implemented using the agents that serve for increasing the tissue permeability in medicine and cosmetology [36, 39]. In particular, it is shown that Azone [141], oleic acid [142], DMSO [118, 143-146], ethanol [150], propylene glycol [147, 151], Thiazone [149] enhance the tissue permeability for OCAs and increase the efficiency of optical clearing.

The possible mechanism of diffusion enhancement using Azone may consist in increasing the fluidity of hydrophobic regions of the *stratum corneum* and the corresponding reduction of resistance to the penetration of agents [141]. For example, after 60 minutes exposure of *in vitr*o skin to the mixture of 40% glycerol-Azone the absorption of light at the wavelength 1276 nm increased by 41.1%, and the diffuse reflection at the wavelength 1066 nm decreased by 29.3%, which considerably exceeded the values of these parameters under the application of more concentrated 80% aqueous solution of glycerol [141].

The oleic acid is a monounsaturated fatty acid that is widely used as a safe transdermal enhancer for drug delivery. In the region of skin clearing the synergetic effect of oleic acid as a promoter of OCA skin penetration was studied [142].

DMSO is a well-known agent widely used for improving the transdermal delivery of drugs. It is a polar aprotic solvent of *stratum corneum* lipids [143]. DMSO enhances the permeability of the *stratum corneum* for both hydrophilic and lipophilic agents [152, 153]. In addition, it possesses high refractive index and may serve as an OCA as well [144]. It also interacts with the highly organised structure of collagen fibres, changing the interfibrillar space at the sub-micrometre scale [145], which is of great importance for the skin optical clearing. However, the results on the DMSO optical clearing potential and safety are rather contradictory [106, 144, 154, 155]. In Ref. [106] it is shown that the optical clearing potential of DMSO is smaller than that of glycerol, propylene glycol, ethylene glycol, and some other OCAs. The application of high-concentration DMSO to the skin surface causes irritation, accompanied with epidermal spongiosis [154]. On the other hand, it was noticed that DMSO is a high-efficiency OCA of topical application, and no side effects under the 20-minute exposure of the rat skin surface *in vivo* were reported [144]. In spite of the controversial evaluation of the DMSO efficiency and safety, this substance is widely used for optical clearing in the mixtures with different OCAs [64, 118, 143-146, 152, 153, 156].

Ethanol is also a solvent that modifies the skin barrier properties. Under sufficiently high concentration (~40%) ethanol facilitates the formation of pores and essentially increases the transport of agents through them due to increasing the size and/or the density of pores in the epidermal membrane [150].

The mechanism of enhancing the permeability of the epidermis *stratum corneum* under the action of propylene glycol is the solvation of keratin in the process of water replacement in the binding hydrogen groups and the inclusion of propylene glycol into the polar heads of the lipid bilayer [151]. It was shown that the mixtures of different OCAs with propylene glycol increase the efficiency of the optical clearing effect, however, the clearing effect induced by propylene glycol itself is weaker than for these mixed OCAs [147].

The last of the diffusion enhancers mentioned above,

Thiazone, is an innovative agent that increases the skin permeability nearly three folds stronger than Azon [36]. It is also more efficient as compared to propylene glycol [36, 147].

To increase the tissue permeability for OCAs one can use combinations of the abovementioned agents. For example, in Ref. [157] for the optical clearing of skin the combined OCA was used, including glycerol, PEG-300, ethanol and DMSO.

Beside the chemical agents, a number of physical methods of surmounting the skin barrier are proposed to enhance the diffusion, including low- and high-intensity irradiation [130, 158], fractional lamp [131, 133] and laser [132] microablation, mechanical microperforation [137, 138], ultrasonic (US) irradiation [134, 135, 159], electrophoresis [160], needleless injection [161], mechanical removal of the surface layer by means of abrasive paper [136], epidermal stripping [162], and microdermabrasion [163].

Different radiation sources (e.g., CO_2 and Nd:YAG lasers, operating at the wavelengths 532 and 1064 nm, respectively, broad-band sources of intense pulsed light, operating in the ranges 650–1200, 525–1200, and 470–1400 нм) have been used to irradiate the skin *in vivo* before the OCA application with different doses and regimes of exposure. The measurements of reflection spectra before and after the exposure have shown that the radiation of Nd:YAG laser in the modes of Q-modulation and long pulses can induce the improvement of transepidermal penetration of OCA by 8-9 folds as compared to the intact skin [130]. In the other study Stumpp et al. [158] used a diode laser, operating at the wavelength 980 nm for the rodent skin irradiation using artificially absorbing substrates on the surface. The laser radiation provided heating of the *stratum corneum* and caused the failure of the protective barrier function. After the removal of absorbing substrates the skin surface was subjected to glycerol application. The OCT study of skin in the exposed regions has shown the increase of the light penetration depth by up to 42%.

The similar principle was used to create regions of microablation under the action of a broad-band flash lamp. The transparent mask with a set of absorbing carbon centres was applied to the skin surface in order to create the regions of epidermis microdefects under the light absorption [131, 133]. Increasing the skin transparency and image clearness of the tattoo, located under the skin at the depth of 300-400 μm, was demonstrated by Genina et al. [133] and Bashkatov et al. [164]. Fig. 3 presents the tattooed skin images before and after the action of the epidermis fractional thermal ablation and 88% glycerol solution.

Fractional laser microablation of skin surface by means of the erbium laser (2940 nm) with the pulse energy from 0.5 to 3.0 J is also an efficient tool of overcoming the barrier for hydrophilic and hydrophobic OCAs [132].

The integrity of the epidermis *stratum corneum* can be disturbed mechanically using a roller with multiple needles. Yoon et al. [137] used this device, applied in cosmetology, to create transdermal microchannels in samples of porcine skin *ex vivo* with the aim of improving the glycerol penetration into the depth of the skin. The combination of multiple needle perforation with low-frequency ultrasonic effect allowed the increase of the diffusion rate of the 70% glycerol solution into the skin by 2.3 folds in comparison with using the multiple-needle roller solely [138].

The low-frequency US effect (sonophoresis) is one of the noninvasive methods of improving the clearing effect for many OCAs, increasing the depth and rate of their delivery into tissues [134, 135, 165-168]. The combined use of OCA and US provided considerable increase of the depth and contrast of the OCT images of porcine skin *in vitro* and human skin *in vivo* [166]. Xu et al. [134] used the ultrasound with the frequency 1 MHz to enhance the penetration of 60% glycerol solution and 60% PEG-200 solution into the porcine skin *in vitro*. The OCT study has shown the increase of the imaging depth by 40% and 93%, respectively, as compared to using OCA without US.

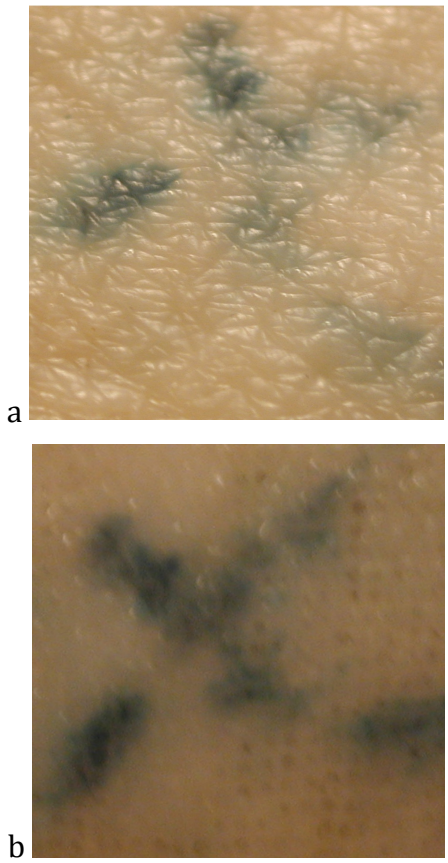


Fig. 3 Images of tattooed skin surface: a) the tattooed sample before the glycerol action; b) the tattooed sample after the surface microperforation and glycerol impact during 24 hours [133].

Cavitation is the main mechanism of the sonophoresis that explains the tissue permeability increase [159, 167]. The theoretical analysis of surface interaction of the cavitation bubbles with lipid bilayers of the epidermal *stratum corneum* considers three

interaction modes, namely, the shock wave propagation, the penetration of microflux into the *stratum corneum*, and the impact of the microflux on the *stratum corneum* [159]. In the process of growth the bubbles can merge, forming larger bubbles that continue growing creating channels. The channels formed in the *stratum corneum* become larger with time in the direction towards the boundaries, which finally leads to the appearance of inner transport ways [167]. These processes induce disorder in the lipid bilayers of the epidermal *stratum corneum*, weaken the barrier function, and enhance the OCA penetration into the inner layers of skin [168].

The transdermal electrophoresis is a well-known and widely used method of controlled delivery of drugs through the skin aided by low-intensity electric current. The specific features of this method are the following: 1) the transport can be significantly intensified as compared to the passive diffusion; 2) the delivery rate may be actively controlled by modulating the electric current density, which allows individual dosage [169].

The electrophoresis can be applied not only with polar electrically charged agents. The dependence of electroosmotic diffusion upon pH of the solution and the content of NaCl ions in it was studied in Ref. [160]. In the experiments the solution containing 0.07M of NaCl and 0.13M of D-mannitol in 5мM of citric-acid buffer with pH = 6 was used. Compared to the passive diffusion, the volume flux of the agent gradually increased approximately by 20 folds after switching the current on, approaching a constant value. After switching the current off, the volume flux slowly decreased to the values, exceeding those before the beginning of the electrophoresis [160].

Stumpp et al. [161] proposed to use a pistol for needleless injection of glycerol with concentrations of 100, 50, and 25% into the porcine skin *ex vivo*.

The removal of the skin surface layer by slight rubbing with an abrasive paper also helps to enhance the OCA penetration through the epidermis *stratum corneum* and to improve the optical clearing effect. The abrasive paper with the gritness 220 was used by Stumpp et al. [136] for smooth rubbing of glycerol or dextrose solution into the depilated hamster skin *in vivo*. After 2-4 min of rubbing in, excluding any visible damage, the skin gradually became more transparent, allowing the observation of subcutaneous blood vessels. The quantitative analysis of the OCT signals has shown that the light penetration depth increased by 36-43%.

The mechanical removal of outer cell layers of the epidermis can be also implemented via a sequence of surface epidermal strips. The procedure of gluing strips of adhesive tape to the skin surface and tearing them off repeated up to 30 times increases the permeability of skin without its essential damage [162]. In Ref. [139] the authors used slides with cyanoacrylate applied to the skin with moderate pressure, kept nearly 3 minutes, and then were left for 2 minutes more. When tearing the slide off the outer layer of the epidermis was removed. The procedure was repeated 3-6 times till the skin became shining. Then the OCA was applied to the processed surface under slight pressure that also improved the agent penetration into the skin.

The combined use of chemical and physical OCA diffusion enhancers facilitates further increase of the optical clearing efficiency [118, 148, 149]. Thus, Xu et al. [148] showed that the sodium lauryl sulphate, a surface-active agent often used as an enhancer of penetration of pharmaceutic and cosmetic products into skin, in combination with the US demonstrates a synergetic enhancing effect on the penetration of 60% glycerol solution into the skin. As a result the optical transmission and OCT probing depth increased and the time of reaching the maximal clearing decreased in comparison with the US used solely.

The US processing was also used in combination with Thiazone to improve the penetration of PEG-400 into the skin [149]. It was shown that after the complex processing with Thiazone, PEG-400, and US the diffuse reflection coefficient decreased by 33.7 folds as compared to the control measurements (without clearing). Using only PEG-400 or PEG-400 with Thiazone the reduction of the reflection coefficient was by 2.7 and 3.3 folds, respectively. The probing depth increased by 41.3% in comparison with the control samples.

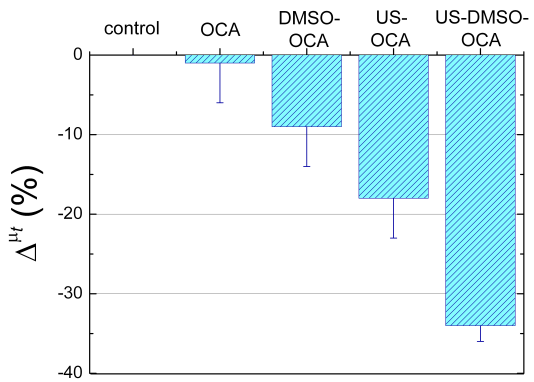


Fig. 4 The difference between the averaged coefficients of total light attenuation by the intact rat skin *in vivo*, calculated from the OCT data. The column "control" corresponds to the data, obtained before the OCA action. "OCA" – 20-minute topical action of OCA (glycerol-PEG-400 mixture in equal proportions); "DMSO-OCA" – 20-minute action of DMSO-OCA mixture; "US-OCA" – 4-minute action of low-frequency ultrasound and OCA; "US-DMSO-OCA" – combined 4-minute action of ultrasound and the DMSO-OCA (from the data of Ref. [118]).

The comparison of the coefficients of total light attenuation by the rat skin *in vivo* using physical and chemical penetration enhancers separately and in combinations was carried out in Ref. [118]. Fig. 4 presents the result of calculating the value

$$\Delta^{\mu_t} = \frac{\mu_{t(treated)} - \mu_{t(control)}}{\mu_{t(control)}} \times 100\%$$

of the relative attenuation coefficient change as a result of the multimodal skin processing with respect to the control measurements. In this case the control group consisted of animals not subjected to the treatment. For this group $\Delta^{\mu_t} = 0$. The results allow the assessment of the efficiency of different OCA diffusion enhancers (the OCA was a mixture of equal parts of glycerol and PEG-400). It is seen that the OCA column has the minimal height, which means the minimal efficiency of the 20-minute OCA action on the surface of intact skin (the optical clearing is absent). The 20-minute application of 9% DMSO solution in OCA appeared to be less efficient than the 4-minute ultrasonophoresis. However, the maximal efficiency of optical clearing was observed under the combined use of US-DMSO-OCA during 4 minutes.

The combined use of surface epidermis stripping with chemical enhancers of diffusion, such as Thiazone, Azon and propylene glycol, was studied in the rat skin *in vivo* [170]. After tape strips from the skin surface the mixture of the enhancer with PEG-400 was applied to the prepared region. As a result the skin diffuse reflection coefficient was reduced, the greatest change being observed when using Thiazone-OCA, then, in descending order, Azon-OCA, propylene glycol-OCA and OCA without adding the permeability enhancer. These results differ from the data of *in vitro* studies of porcine skin, for which the optimal combination of OCA and enhancer was propylene glycol-OCA, and the minimal reduction of the reflection coefficient was demonstrated by Azon-OCA [147].

The influence of microdermabrasion on the skin permeability for hydrophilic and lipophilic agents was studied in Ref. [163]. Microdermabrasion is a partial ablation and homogenisation of the epidermal *stratum corneum* under the action of high-pressure flow of microparticles. Depending on the pressure (15-25 centimetres of mercury) and the time of exposure the skin permeability for hydrophilic agents increased by 8-24 folds, as compared to the intact skin. This method can be used for enhancing the OCA diffusion as well.

3 Compression clearing

The influence of external mechanical compression on the optical properties of biological tissues *in vivo* is interesting for several reasons. First, the specific features of light propagation in the tissue vary depending on its morphologic, biochemical, and physiological characteristics, therefore, the spectral composition of light, outgoing from the tissue, carries information on its morphologic and functional condition [171, 172]. Second, as a result of local mechanical compression, produced, e.g., by the end of a fibre-optical probe (the area of the force application about a few square millimetres) at the compression site a gradient of the refractive index is induced, and this volume of the tissue plays the role of a lens for the probing radiation, propagating through the tissue. When the mechanical compression is applied to a relatively large area of the tissue surface (of the order of a few cm^2), the lens effects are absent, but the compaction of the medium can manifest itself in the change of its optical characteristics due to the variation of the packing density of the scatterers.

Since the external mechanical compression can essentially change the optical and structural properties of the tissue, this method can be considered as an alternative to the widely used immersion method of controlling the tissue optical parameters, based on the influence of chemical agents. As discussed above, the main mechanisms of the immersion clearing are the transport of water from the tissue and the partial replacement of intercellular or intracellular water with a chemical agent, as a result of which the difference of refractive indices of the scatterers and the interstitial fluid becomes smaller, reducing the scattering. Analogous processes partially occur under the compression, since the removal of water from the intercellular space and the increase of protein concentration in it as a result of applying the external compression should also lead to the reduction of scattering.

The effect of increasing the depth of laser radiation penetration into a biological tissue under the application of the external local mechanical pressure was demonstrated more than 30 years ago [173]. From that time a considerable number of publications appeared, related to using the influence of external mechanical compression of tissues on their optical properties (absorption and scattering).

The first studies [174, 175] were carried out with the tissue samples *ex vivo*. The authors noticed that the external compression changed the optical properties of the tissue samples, which manifested itself in the change of diffuse reflection and transmission of light by the samples of tissues. Thus, in Ref. [174] the studies of compression of soft tissue samples demonstrated the growth of the transmission coefficient and the reduction of the diffuse reflection coefficient in the spectral region from 400 to 1800 nm. It was concluded that the compression increases the coefficients of absorption and scattering of the tissue, and the possible mechanisms of the "clearing" are the reduction of the sample thickness and its dehydration. Similar results were also obtained by the authors of Ref. [175]. The studies of the compression effect on the samples of porcine skin have shown that the mechanical compression causes the increase of the light transmission through the samples, and the effect is inertial.

The mechanical compression also changes the optical properties of tissues *in vivo*, which is accompanied by the spectral changes both in the diffuse reflection [176-186] and in the fluorescence [185, 187-189]. The authors of [176, 187] were one of the first researchers who noticed the influence of the compression on the spectra of diffuse reflection and autofluorescence of human skin *in vivo*. It was reported that the pressure exerted on the skin reduces the depth of the dip in the green region of the spectrum that indicates the presence of blood in the tissue, as a result

of which the reflection coefficient of skin in this region increases, while in the red and yellow region it decreases. In the reflection spectrum an isobestic point was found, for which the reflection coefficient does not change in the presence or in the absence of compression [176]. The external compression also caused the increase of the skin autofluorescence intensity in the short-wave region of the visible spectrum [187].

The reduction of diffuse reflection in the region 1100 – 1700 nm was reported [178] in human skin *in vivo*. It was shown that under the increase of the pressure of the fibre-optical probe on the skin surface the diffuse reflection is decreased. The authors related such behaviour with the change of the internal structure of the skin tissue. A similar fact was also noticed in the visible region of the spectrum [184].

In Ref. [185] the influence of short-time (smaller than 2 seconds) and long-time (greater than 30 seconds) mechanical action upon the diffuse reflection and autofluorescence spectra of human skin *in vivo* was studied. It was shown that at high pressure the significant spectral changes occur both for short-time and long-time compression, the probe pressure affecting not only the optical, but also the physiological parameters of the skin.

The influence of external compression on the physiological parameters of breast was studied by the authors of Ref. [180]. Under the compression of the tissue the light scattering was reduced, also decreased was the total blood content and the saturation of the tissue with oxygen. After the compression removal the effect of hyperaemia was observed. The changes in the blood circulation system (compression of blood vessels and reduction of blood oxygenation), to the opinion of the authors of Ref. [181], can enhance the sensitivity and specificity of early diagnostics of cancer.

At present the external mechanical compression is used as a method that allows the increase of image resolution and contrast in optical coherence tomography (OCT) and microscopy [28, 190-193].

The method of compression optical clearing of tissues is implemented instrumentally (tissue optical clearing device, TOCD) [29, 31, 194-196].

Finally, the mechanical compression of skin allows the assessment of the content of chromophores in it, whose absorption under the normal conditions is masked by the absorption by other chromophores. Thus, the extrusion of blood from the region of compression makes it possible to evaluation the content of carotenoids in the skin by the spectra of diffuse reflection [197], and the content of melanin in skin by the spectra of fluorescence [171, 172].

Although the amount of publications related to the mechanical compression of tissues is relatively large, the results are often somewhat controversial, which is mainly due to the difference in the conditions of the force application (local or distributed) and the detection of the reflected light (fibre-optical or open detecting system) [198]. Besides, it is necessary to take the inertial character of the tissue response to the external action into account.

The compression method of controlling optical parameters has a number of potential advantages in comparison with the immersion method. For example, moderate mechanical compression saves the barrier functions of the *stratum corneum* and the epidermis as a whole.

In the visible region the absorption coefficient of water is insignificant as compared to the near IR region, where the absorption peaks caused by the combinations and overtones of fundamental vibrations are located. In the skin the absorption spectral bands of water bound with the proteins of interstitial matrix are shifted with respect to the bands of free water towards the long-wave region of the spectrum. Thus, the manifestations of bands in the reflection spectrum of skin at 1160 nm and 1220 nm were reported [199], attributed by the authors to the absorption bands of free and bound water. The absorption bands at 1879 nm and 1890 nm were attributed [200] to the absorption of free water, and the bands at 1909 nm and 1927 nm to the bound water.

The effect of water transport was studied by Rylander et al. [196]. In the skin the natural gradient of water content depending on the depth exists. In the *stratum corneum* the water content depends upon the air humidity and can be at the level 15%. The water content grows with depth, reaching 70% in dermis. A considerable part of this amount is free water, the molecules of which due to their high permeability percolate from the region of external compression into the adjacent regions. The water migration from the skin regions subject to compression leads to the matching of the refractive indices of the tissue components [31], which reduces the scattering coefficient.

The water transport in the skin tissue can be analysed on the base of two-phase nonlinear mixture [201], according to which the skin is presented as a solid elastic matrix, formed mainly by elastic fibrils and cells and filled with water. This model is sufficient to present the composition and mechanical properties of the skin well enough [196, 201]. Basing on this model the authors of Ref. [193] studied the influence of mechanical compression on the optical properties of the skin. The samples of porcine skin *ex vivo* and human skin *in vivo* were studied using OCT at the wavelength λ = 1310 nm. It was found that for the porcine skin samples *ex vivo* the compression reduces the water fraction in the tissue by more than three folds (from 0.66 to 0.2).

The detailed analysis of possible mechanisms affecting the skin optical properties was carried out in Ref. [199] where the influence of human skin compression on the variation of its scattering properties and the free and bound water content were studied. The changes in the diffuse reflection spectra were correlated with the effects of tissue deformation within the framework of two-phase nonlinear mixture model. The optical properties of the skin were considered basing on the three-layer medium (epidermis, dermis, subcutaneous fat), and the scattering properties of the

tissue were determined as the combination of scattering by large (Mie scattering) and small (Rayleigh scattering) particles. The expressions for the scattering coefficients of each of the skin layers were taken from Refs. [202, 203], and the skin absorption in the near IR region was determined as the superposition of absorption by water and lipids. The water contribution into the absorption amounted to 20% for epidermis, 70% for dermis, and 60% for subcutaneous tissue (fat and muscle) [203, 204].

Experimental diffuse reflection spectra were analysed for two absorption lines of water in the near IR region, 1160 nm and 1220 nm, attributed by the authors to the absorption of free and bound water, respectively, basing on the comparative analysis of the reflection spectra of skin and pure water.

The measurement of water content in the skin *in vitro* has shown that under compression the intensity of the band at 1220 nm significantly grows, while the intensity of the band at 1160 nm decreases. When the pressure is increased to 376 kPa, the absorption peak at 1160 nm almost vanishes. This indicates the fact that under the compression of skin the free water leaves the compressed region, while the bound water that forms complexes with proteins stays. When the pressure achieves 400 kPa, the volume of free water decreases to 30% of its initial value. This is the main cause of the tissue deformation. Under the long-time compression the absorption peak of free water decreases with time, and the peak of bound water increases. At the early stages of the deformation due to the large stress in the tissue the free water leaves the compressed region with sufficiently high rate. As the stress relaxes, the deformation of the tissue and the rate of free water migration gradually decrease. After nearly 6 minutes the tissue deformation and the water transport stop. The duration of this process is also related to the compression magnitude.

Thus, for the analysis of the structural and optical changes occurring in the skin *in vivo* under the conditions of external compression the above model of the tissue can be considered, according to which the skin consists of a solid matrix formed by the collagen fibres and the interstitial fluid, the major part of which is water. When the skin is compressed, the solid matrix is deformed and the interstitial fluid leaves the region subject to compression with the rate determined by the density of packing of the matrix fibres and the viscosity of the fluid. This hypothesis is in good agreement with the experimental data. The relation of skin deformation and relaxation time under the conditions of compression depends upon the elastic properties of the fibrils and the density of their packing, as well as upon the amount and viscosity of the fluid in the tissue. Since the bound water is integrated in the tissue solid matrix, the measurements of free and bound water content variations can reflect the deformation of the solid matrix and the transport of free water in the tissue under the conditions of compression.

4 Photochemical and photothermal clearing

For a number of applications, particularly, in the case of laser therapeutic or surgical interventions, one can control the optical properties of the tissues by means of photochemical or photothermal action. The heating and coagulation of a tissue change its optical properties, and this should be taken into account in the calculation of the radiation doze in the process of treatment [3, 22]. The method of controlling optical properties of fat tissue, which is usually a strongly scattering tissue, was proposed in [205, 206]. The method is based on the combined photochemical and photothermal effect [2, 207] induced in the fat tissue cells.

The selective photothermal action on the fat tissue can be implemented by the laser radiation wavelength choice using the absorption by the endogenous (own) tissue chromophores, in the present case the lipids contained in the fat drop of adipocytes, under the exposure to light with the wavelength 1210 nm [208]. However, with exogenous chromophores, e.g., the indocyanine green (ICG), the efficiency of light interaction with tissue may be essentially higher and more selective [209-213]. The intensity and position of ICG absorption peaks depend upon the solvents used [214-216]. The solutions with complex compositions, e.g., such as water-alcohol-glycerol, stabilise the ICG absorption peaks [215]. Besides that, the alcohol component of the solution makes the cell membrane permeable for the dye [217-219]. The next step of the interaction between the dye and the cell is related to the light action. The light causes photochemical reactions; for ICG they simultaneously follow two scenarios: 1) photodynamic reactions; 2) reactions yielding toxic products [216]. Depending on the intensity, the biological response of the cell may lead to reversible of irreversible injury of the cell membrane. Reversible membrane injury consists in the creation of new pores or enlargement of the already existing ones, which facilitates efficient exchange between the cell content and the environment. In fat cells the presence of pores increases the lipolysis, as a result of which the intercellular space becomes filled with the cell content and decay products (triglycerides, fatty acids, water and glycerol) [37, 220-223]. The appearance of such immersion fluid in the intercellular space facilitates the process of optical clearing of the adipose tissue [37].

The probability of triglyceride leaving the cell through the membrane pores is rather small due to the relation between the pore diameter (0.1 – 2 nm) and the triglyceride molecule size (nearly 1-2 nm) [221-223]. The hydrolysis of triglycerides occurs in two stages. At the first stage the hydrolysis of external complex ether bonds occurs; this process is catalysed by the lipase enzyme. The hydrolysis of triglycerides is referred to as lipolysis. The monoglyceride produced at the first stage of the triglyceride decay, is further hydrolysed by the nonspecific esterase, producing glycerol and three molecules of higher fatty acids [221-223]. The

hydrolysis products can easily leave the cell through the pores, since their molecular size is small compared to the pore size. In this process the refractive index of the intercellular fluid (n_M = 1.36) [45] approaches the refractive index inside the adipose cell itself (n_B = 1.44), the medium becomes more optically homogeneous and, as a result, more transparent [22].

In Refs. [37, 220] the photodynamic effect in adipose cells *in vitro* sensitised with brilliant green (BG) was studied. The result was also the cell lipolysis. The hypothesis of pore formation is in good agreement with the experimental results [37, 206, 220, 224].

Fig. 5 presents the transmitted light images of the subcutaneous fatty tissue sample, stained with BG, before (a) and after (b-e) the irradiation with a dental diode lamp Ultra Lume Led5 with the wavelengths 442 and 597 nm and the total power density 75 mW/cm^2 during 15 minutes at the constant temperature 33°C. The cell lipolysis is seen to stimulate the leakage of a part of intracellular fluid into the intercellular space and the tissue gradually undergoes immersion clearing.

5 Applications of optical clearing

5.1 Optical coherence tomography

OCT is a noninvasive method of visualising the internal structure of optically inhomogeneous objects that allows the study of tissue internal microstructure with high resolution and without disturbing its integrity [18]. However, the multiple scattering essentially worsens the OCT imaging characteristics, namely, the image resolution, probing depth, and the precision of localisation [21]. In this connection the progress of optical clearing techniques is of huge potentiality for noninvasive OCT medical diagnostics [28, 29, 35, 36, 39, 190, 192, 196].

The efficiency of mechanical compression for better differentiation of chronic inflammation and carcinoma in the OCT images was studied by Agrba et al. [28]. They also determined the threshold impact that allows the detection of difference between these cases. Using the endoscopic probe of unique construction that allowed the control of the compression force applied to the tissue, the possibility of differentiating the pathologic changes of rectum *ex vivo* with inflammation and carcinoma was demonstrated.

The same research team has shown that the application of compression to human skin causes various changes of the optical properties of skin layers depending on their elasticity. These changes increase the contrast of the OCT-imaged boundaries between the layers [192].

The efficiency of the mechanical device for biotissue optical clearing, designed by Rylander et al. [196] was determined using OCT [29]. The authors have shown that the depth of light penetration into the human skin *in vivo* at the OCT wavelengths 850 and 1310 nm increase by 3 folds in the area of compression. The contrast of the OCT image of the epidermis-dermis boundary was also increased. OCT allowed the specification of compression clearing mechanism. Thus, the OCT M-scans recorded during the pressure application have shown that the optical penetration depth monotonically increases, undergoing a jump at the initial time period (5-10 s), during which the water content in the tissue abruptly decreases and the group refractive index increases in the local area of pressure application.

The authors of Ref. [191] proposed to use OCT with compression for continuous noninvasive monitoring of blood glucose content. The results of *in vivo* skin studies at different pressures have shown that the pressure of the OCT probe on the skin reduces the artefacts related to the object motion, but may shift the OCT signal slope that allows the blood glucose monitoring. Thus, the controlled external pressure < 1 kPa significantly improved the precision and reproducibility of the glucose OCT monitoring.

The potentialities of immersion optical clearing are mainly related to the fact that OCT allows the imaging of relatively thin layers of tissues that can be rapidly impregnated with OCA applied to the surface. In Refs. [21, 22] it was demonstrated that the internal tissues, such as the walls of blood vessels, oesophagus, ventricle, large intestine, and other organs can be imaged to the depth of 1-2 mm. The application of immersion liquids increases the probing depth nearly by 3.5 folds and significantly improves the image contrast of the internal inhomogeneities [225, 226]. The possibility of malignant melanoma diagnostics, observation of subepidermal cavity, and control of the skin scattering properties under the application of glycerol and propylene glycol to its surface was shown by the example of OCT visualisation of human skin *in vitro* and *in vivo* [22]. Moreover, the variation rate of the OCT A-scan slope in the course of the optical clearing allows additional differentiation of the healthy and tumour tissue of the human oesophagus and mammary gland [103-105, 227, 228].

Optical coherence tomography offers a unique possibility to assess the variation of the tissue light scattering coefficient with sufficient depth resolution. The total light attenuation coefficient μ_t of the tissue local volume, which is a sum of the absorption coefficient μ_a and the scattering coefficient μ_s, may be found by fitting the parameters of the approximating curve, calculated within the framework of the appropriate model, using the local A-scan slope of the OCT signal [18, 118, 230-232].

The single scattering model is based on the assumption that only the light undergoing singe scattering (ballistic photons) preserves the coherence properties and contributes to the OCT signal. In this case the OCT signal $i(z)$ is determined as [18, 230, 231]: $\left(\left\langle i^2(z)\right\rangle\right)^{1/2} \approx \left(\left\langle i^2\right\rangle_0\right)^{1/2} \left(\exp(-2\mu_t z)\right)^{1/2}$, where z is the depth, from which the reflected signal comes.

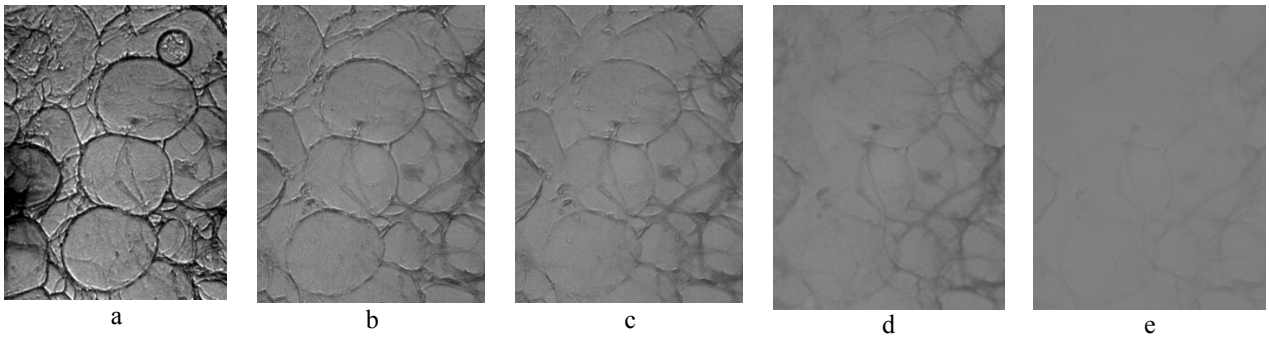


Fig. 5 Transmitted light images of a subcutaneous fatty tissue sample stained with brilliant green before (a) and after (b-e) light exposure during 15 min. The time interval between the image recording and the end of exposure is 8 min (b), 19 min (c), 39 min (d), 120 min (e). The sample temperature is 33°C. Diode lamp, 442 and 597 nm, the total power density 75 mW/cm^2.

It is known that the result of OCT is the measurement of the reflected signal intensity from the studied tissue, $R(z) \propto \left(\left\langle i^2(z) \right\rangle \right)^{1/2}$, upon the depth z. The OCT signal intensity depends upon the reflectance $\alpha(z)$ of the tissue at the given depth and the total attenuation coefficient $\mu_t = \mu_a + \mu_s$ of the tissue. In accordance with the singe scattering model that is valid both for weakly scattering tissues and for the surface layers of strongly scattering tissues [231], the reflected power in proportional to $\exp(-\mu_t z)$ [18], i.e., can be approximated with the expression [118]: $R(z) = A\exp(-\mu_t z) + B$, where A is the coefficient equal to $P_0\alpha(z)$, with P_0 being the optical power of the beam, incident on the tissue surface, $\alpha(z)$ being determined by the local capability of the tissue to scatter the light in the backward direction (to reflect), which is largely dependent upon the local value of the refractive index, and B being the background signal.

Since the absorption coefficient is essentially smaller than the scattering coefficient for many tissues in the near IR spectral range, the exponential decay of the ballistic photons is mainly determined by the scattering coefficient [18]. The scattering coefficient depends on the difference of refractive indices in the tissue volume, so that the increase of the refractive index of the interstitial fluid and the corresponding reduction of scattering is recorded as the change (decrease) of the slope of the OCT signal amplitude as a function of the probing depth [18, 35, 89, 90, 93, 95-100].

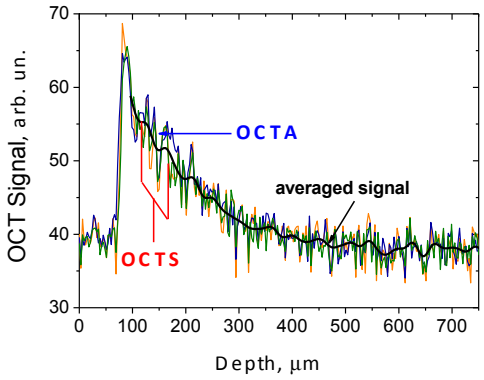
This method allows the measurement of the permeability coefficient of tissues both for OCAs and for the medicinal preparations, possessing the properties of OCA, using two approaches: measuring the OCT signal slope (OCTS) and the OCT signal amplitude (OCTA) (Fig. 6a) [35, 95, 232]. In the OCTS approach, analysing the variation of the OCT signal slope due to the OCA diffusion, one can calculate the mean permeability coefficient of a certain region in the tissue. In this case two-dimensional OCT images are averaged over the lateral coordinate (x axis) to get a one-dimensional depth distribution of the OCT signal intensity. In the tissue it is necessary to choose the region, for which the signal is linear and its fluctuations are minimal, where the tissue thickness (z_{region}) must be measured. Then the monitoring of the agent diffusion in the chosen region is performed and the time of diffusion (t_{region}) is recorded. The mean permeability coefficient $\left(\bar{P}\right)$ can be calculated as the thickness of the region divided by the time, during which the diffusion of the agent through the chosen region occurs $\left(\bar{P} = \frac{z_{region}}{t_{region}} \right)$ [232].

The OCTA approach can be used to calculate the permeability coefficient at a definite depth in the tissue: $P(z) = z_i / t_{z_i}$, where z_i is the measurement depth and t_{z_i} is the time of agent diffusion to the given depth. The value of t_{z_i} should be calculated from the time of the agent application to the time of the beginning of the OCT signal amplitude variation, caused by the OCA [232].

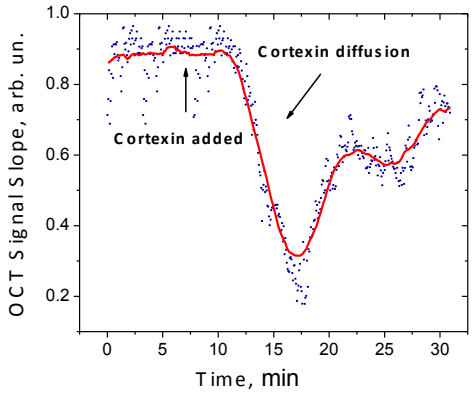
These approaches allowed the assessment of the following permeability coefficients: rabbit cornea for mannitol $(8.99 \pm 1.43) \times 10^{-6}$ cm/s [95], rabbit sclera for mannitol and 20% glucose solution $(6.18 \pm 1.08) \times 10^{-6}$ and $(8.64 \pm 1.12) \times 10^{-6}$ cm/s, respectively, [95], human sclera for cortexin $(2.40 \pm 0.32) \times 10^{-5}$ cm/s (Fig. 6b) [93], porcine aorta for 20% glucose solution $(1.43 \pm 0.24) \times 10^{-5}$ cm/s [99], epidermis and dermis for 40% glucose solution $(6.01 \pm 0.37) \times 10^{-6}$ cm/s and $(2.84 \pm 0.68) \times 10^{-5}$ cm/s, respectively, [97], lung tissue for 30% glucose solution $(1.35 \pm 0.13) \times 10^{-5}$ cm/s (the norm) [100], and lung tissue for 30% glucose solution in the case of different malignant neoplasms [100].

The depth-resolved analysis of the tissue optical properties using OCT allows the reconstruction of two-dimensional diffusion maps. The visual representation of the molecular diffusion front was first demonstrated by Ghosn et al. [97] in the course of noninvasive determination of the penetration rate of 20% glucose

solution into the rhesus macaque skin *in vivo*.



a



b

Fig. 6 The region and the depth, indicated in the averaged OCT signal, used in OCTS and OCTA approaches (a), and the time dependence of the OCT signal slope in the process of interaction of the sclera with the cortexin solution (b) (from the data of [93]).

Using the OCT methods one can reveal the variations of the effective refractive index of the adipose tissue as a result of the light photodynamic action, which arise both directly after the exposure, and in the process of the system biological response [38, 224]. The observed changes of effective refractive index can be interpreted as the reduction of the relative refractive index of the scatterers, which can be related to the immersion optical clearing.

Fig. 7 shows the series of OCT images of adipose tissue stained with BG before (a) and after (b-d) the irradiation with the light of a diode lamp during 15 minutes and under the heating of the samples to the physiological temperature. Fig. 7,b shows the image of the adipose tissue immediately after the irradiation, while the OCT images in Figs. 7,c and 7,d correspond to relatively long observation time (60 and 120 min., respectively). The mean thickness of the samples amounted to 237±10 μm.

The visual comparison of the OCT tomograms of the adipose tissue shows that after the irradiation the tissue structure considerably varies in time. One can easily see the changes of the outer layer of the cellular structure that becomes more homogeneous, which can be associated with partial destruction of cells and formation of immersion layer consisting of intracellular content and the products of the adipose component hydrolysis. In Fig. 7(b-d) this layer is as thick as 80-90 μm. The mean size of adipocytes in the tissue amounts to 60-70 μm.

Provided that the geometric thickness of the studied layer is known, the effective refractive index n is calculated as $n = z/l$, where l is the geometric path length (the true sample thickness in μm), and z is the layer thickness observed in the OCT image, i.e., the optical path length in μm. The geometric thickness was measured using a micrometre gauge. The optical path length was found from the OCT signal as the difference between the depths of two peaks, corresponding to the sample boundaries (see Fig. 7). For better determination of the boundaries the A-scans were averaged over the lateral region of 2 mm. This operation smooths out the stochastic noise and the disordered cell structure of the tissue, while the peaks, corresponding to the sample boundaries, become more distinct. The calculation of the refractive index showed its monotonic decrease with the growth of observation time.

The observed changes in the OCT images can be interpreted as the result of lipolysis and cell destruction at the surface of the sample due to the photochemical effect. The intracellular fluid leaks from the cells and fills the intercellular space, as a rule, containing the intercellular fluid, thus producing the cleared (more homogeneous) outer layer and giving rise to optical clearing inside the tissue by matching the refractive indices of cells and intercellular medium.

In Ref. [233] the chemically induced lipolysis activity was assayed by measuring the amount of glycerol released from the cells into the surrounding medium. Besides, using frame-by-frame CARS (coherent anti-Stokes Raman spectroscopy) processing of a single living cell, the authors could control the morphological changes of lipid droplets in the cells. They found that the microscopic lipid droplets appeared gradually in the course of the experiment, achieving the size of nearly 1 μm in 60 min after the impact. All these observations allow the assumption that analogous processes may occur in the case of light-induced lipolysis.

The results of OCT measurements of the refractive index of adipose tissue after the exposure to light can be explained basing on the idea of forming two layers with the course of time. One of these layers is cleared (the released intracellular fluid) and the other one is scattering (cells). The refractive index m of the scattering medium can be expressed as [128]

$$m \equiv n_0 + \Delta m = \bar{n} + \frac{\overline{n^2} - \bar{n}^2}{\bar{n}} Q(\lambda / l), \qquad (1)$$

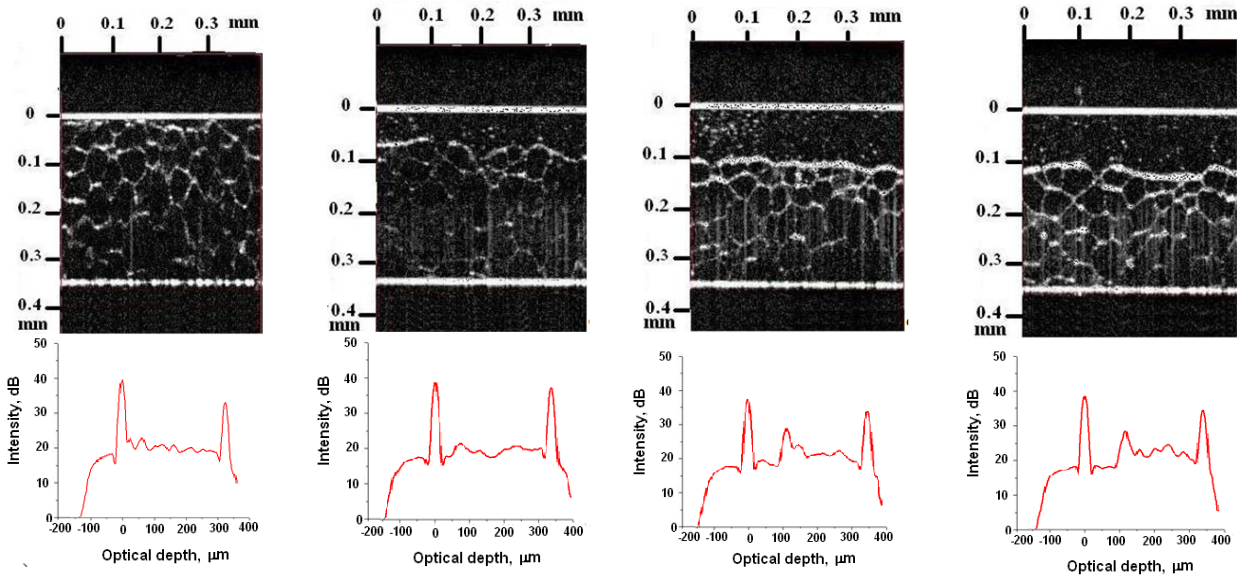


Fig. 7 OCT images of adipose tissue stained with BG before the irradiation (a), immediately after 15-minute irradiation (b), in 60 min (c), and in 120 min (d) after the irradiation. The source was the dental diode lamp Ultra Lume Led5 (442 and 597 nm, 75 mW/cm^2). The dye concentration is 6 mg/ml. The sample temperature is 37 ºC. The curves correspond to A-scans of the OCT image, averaged over the whole B-scan region [224].

where

$$\bar{n} = n_0\left[1+\left(\frac{n}{n_0}-1\right)\frac{V_s}{V_0}\right], \qquad (2)$$

V_s is the total volume of scattering particles, V_0 is the volume of the scattering medium, $\overline{n^2}$ is the mean square value of the refractive index fluctuations, $Q(\lambda/l)$ depends upon the shape and aggregation of scatterers, and l is the correlation length of randomly distributed fluctuations of the refractive index. Q = 1.17 for the limit case of large correlation length, $l >> \lambda$ (large particles). In the process of the adipose tissue degradation the two-phase system appears, consisting of cytoplasm of the adipose cells (the cleared outer layer in Fig. 7,b) and the adipose cells themselves. Each phase of the medium has its own thickness and refractive index. Denoting the time-dependent thickness of the layer of adipose cells as $H(t)$, and the thickness of the outer layer of transparent cytoplasm as $[L - H(t)]$, the mean refractive index of the layer with the thickness L, containing two layer with different refractive indices, can be written as

$$m_T = \frac{\left[L-H(t)\right]}{L}\bar{n} + \frac{H(t)}{L}m, \qquad (3)$$

where m and $\bar{n}$ are defined by Eqs. (1) and (2). Since m is always greater than $\bar{n}$ due to the effect of scattering and tissue degradation, this leads to the decrease of $H(t)$, and the summary refractive index should decrease with time.

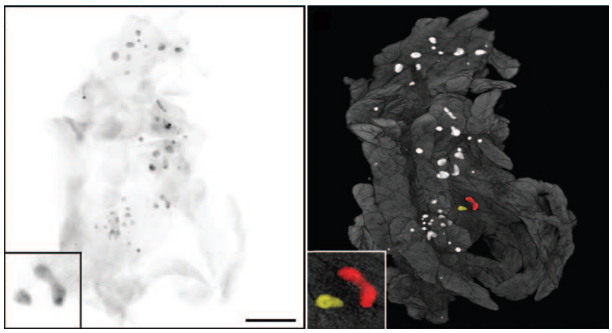
In the process of adipose tissue degradation and formation of greater amount of lipolysis products the conditions of refractive index matching can be implemented, which will lead to further reduction of light scattering, i.e., the part of the refractive index m, depending on these processes. Both these mechanisms, the tissue degradation and the refractive index matching, explain the experimentally observed reduction of the mean refractive index of the sample layer, i.e., the reduction of its scattering capability, in the course of time.

5.2 Optical projection tomography

Optical projection tomography (OPT) is a new approach to three-dimensional visualisation of small biological objects. It fills the gap between the MRT and confocal microscopy (CM), being the most suitable for studying the objects with the size from 1 to 10 mm [234]. The possibility to analyse the organisation of a biological tissue in three dimensions is inestimable for understanding the embryonal development, a complex process in which the tissues undergo a complex sequence of transformations with respect to each other [235]. Since the OPT allows the registration of both the absorption and emission profiles, this method offers an opportunity to use different staining techniques, developed to observe the spatial distribution of gene activity [234, 235]. Other important applications of the OPT help in the analysis of normal and abnormal morphology and in determining the position of labelled cells in the tissue [235].

The most widely used approach to the OPT imaging implies the suspension of the object in the immersion liquid in order to reduce the surface light scattering and

to decrease the refractive index nonuniformity all over the sample. This means that the light passes through the sample along nearly straight trajectories (ballistic photons), and the standard algorithm of back projection can generate images with high resolution [234]. Alanentalo et al. [236, 237] have shown that the OPT allows successful construction of three-dimensional images of specially labelled structures inside the cleared organs of a mouse (see, Fig. 8).



a b

Fig. 8 Single image from the OPT scan datasets with the selected regions of interest (inset) (a) and volume reconstruction of the pancreas based on the background autofluorescence (dark gray) and the signal from insulin-specific antibodies (white-islets) with the regions of interest (inset) (b) [237].

The role of OCA was played by «Murray's clear» (1 part of benzyl alcohol and 2 parts of benzyl benzoate (BABB)) with the refractive index 1.55.

5.3 Fluorescence imaging

The methods of fluorescence spectroscopy and microscopy belong to noninvasive methods of biomedical diagnostics. Fluorescence spectra often provide detailed information about the fluorescent molecules, their conformations, sites of bonding and interaction with cells and tissues [238]. Under the excitation with ultraviolet light ($\lambda \leq 300$ нм) one can observe the autofluorescence of both the proteins and the nucleic acids. The porphyrin molecules are also endogenic phosphors, the content of which in cells considerably increases under some pathologic conditions. Besides, some bacteria, causing, e.g., the inflammation diseases of skin [239] and gums [240], inhabiting the caries tooth lesions [241], can accumulate considerable amounts of porphyrins. Combining the measured autofluorescence spectra with those of reflection and absorption, OCT and other optical methods allows the diagnostics of caries and tooth tissue demineralisation [241-245], skin cancer [246, 247], and pre-cancer changes of cervical tissue [248], mammary gland [249], and other diseases.

Thanks to the growing number of fluorescent dyes, specifically staining the biological molecules (nucleic acids, proteins) or cell organelles, the methods of fluorescence microscopy acquire greater and greater significance [238].

At present in different biomedical studies the confocal microscopy (CM) is widely used, which allows visualisation of internal structure of biological tissues at the cellular and subcellular level [250, 251]. A confocal microscope illuminates a small volume inside the object and detects the scattered light of fluorescence signal from the same small volume. The main CM advantage as compared to the methods of common microscopy is the capability to obtain the optical cross-sections of thick samples [251]. This method allows the creation of high-quality (with micron spatial resolution) images of cell layers. The high contrast and spatial resolution of CM images are due to probing a small volume of the medium, limited by the size of the central focal spot formed by the focusing optical system. The main limitation of CM in the skin studies is the considerable scattering that spoils the quality of cell imaging. The increase of the transparency of the outer layers of skin may improve the light penetration depth, the contrast and the spatial resolution of the CM.

In the publications by Meglinsky at al. [48, 49] basing on the Monte-Carlo modelling the possibility of increasing the human skin probing depth was considered theoretically for the first time using the method of reflectance CM with the reduction of spatial fluctuations of the refractive index of the outer skin layers by optical clearing. Later in the paper by Dickie et al. [83] the experimental method was described that allowed visualisation of microvessels of different mouse tissues using the CM at the depth up to 1500 μm below the sample surface due to the optical clearing of thick slices of the tissue. The OCA for CM in Refs. [252-256] was the commercially available multicomponent agent FocusClear™ [257], especially developed for using in fluorescence and non-fluorescence light microscopy. FocusClear™ does not give rise to the tissue dehydration and allows the improvement of the obtained image quality. The refractive index of this agent is 1.46.

FocusClear™ was successfully used for confocal imaging of murine rectum and ileum [252, 253], the wall of the human ileum [254], the murine pancreas [255], and the brain of the insect (*Diploptera punctata*) [256] *in vitro*. The optical clearing facilitated the identification of spatial and temporal changes of crypt morphology of the murine large intestine with colitis, as well as the detection of transgene fluorescent proteins, expressed in large intestine and ileum [252]. The increase of resolution and visualisation depth of the microstructure and vascular system of ileum was observed under the combined use of blood vessel staining and optical clearing [253]. The authors of Ref. [255] declare that by using OCA the thickness of the studied samples can be increased by 80 folds, which allows better reproduction of the structure and the vascular system of the tissue (see Fig. 9). The use of OCA allowed three-dimensional reconstruction of microvascular architecture of the insect brain with sub-micron resolution to the depth of 1500 μm [256].

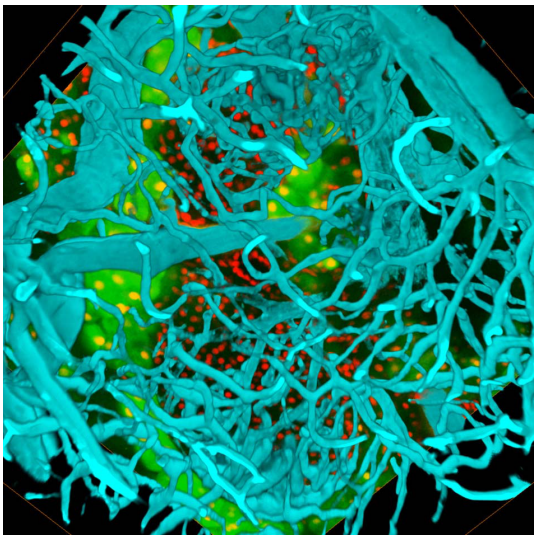


Fig. 9 Fly-through presentation of the islet vasculature using multiple projection angles and magnifications. Dimensions of the scanned volume: 521 μm (*x*)×521 μm (*y*)×333 μm (*z*, depth). Two islets reside in the scanned volume [255].

However, the visualisation depth of 500-1500 μm is not sufficient for three-dimensional reconstruction of neuron networks of the murine brain as a whole. Hama et al. [85] developed an OCA, called Sca*l*e, which not only increases the transparency of a biological sample, but also does not reduce the intensity of fluorescence signals from the cleared structures.

Dodt et al. [86] used the idea of illuminating the object with so called light sheet, which allows observation of macroscopic objects, such as the brain as a whole, with micrometre resolution. The sample is illuminated from two sides with the laser radiation in the blue part of the spectrum, forming a thin planar light beam. The fluorescence signal is, therefore, emitted only from a thin optical section and is collected by the objective lenses. The declined light is blocked by a filter, and the image is projected through a cylindrical lens onto the screen of a digital camera. Since all sample parts below or above the light sheet are not illuminated, the emission is not excited beyond the limits of the focus and, therefore, is not to be eliminated from the useful signal. This approach is referred to as ultra-microscopy (UM). In comparison with CM or two-photon microscopy, UM can rapidly create optical sectioning of macroscopic samples, since the objectives with small focal power and small numerical aperture can provide a large field of view. However, the use of UM is completely dependent upon the optical transparency of biological objects, so that the improvement of optical clearing efficiency, including that due to the development of new OCAs, remains to be an urgent problem [86, 87, 258-262]. In Ref. [258] it was shown that the use of optical clearing allowed cellular resolution in sectioning the fixed mouse brain and detecting individual neurons, labelled with green fluorescent protein, in the removed murine hippocampus. In the isolated hippocampus the three-dimensional images of dendrite structures and processes of neuron populations were obtained. The use of UM includes the imaging of cleared murine organs and total embryo specimens, adult insects *Drosophila,* and other fixed tissues with the size of a few millimetres [259].

Ertürk et al. [87] found that tetrahydrofurane (THF) in combination with BABB can completely clear the spinal cord, preserving its fluorescence. Recently Ertürk et al. [262] developed a new protocol of optical clearing using the dibenzyl ether instead of BABB in combination with THF to get three-dimensional images of neurons of the whole mouse brain using the UM. This method was called three-dimensional imaging of solvent-cleared organs (3DISCO). In this study the clearing of the tissue took only three hours, and the visualisation was performed during 45 minutes.

5.4 Photoacoustic imaging

Optothermal effects occur in a tissue due to its interaction with pulsed or intensity-modulated optical radiation. Such interaction gives rise to a number of thermoelastic effects in the tissue, in particular, the generation of acoustic waves. Detection of the acoustic waves is the base of the optoacoustic (or photoacoustic) methods [1, 3]. The main applications of the photoacoustic (PA) method are in the field of visualisation of strongly absorbing objects, such as blood vessels [263-265] and tumours [266]. This method can be also used for imaging of subcutaneous structures [267] and measuring the blood oxygenation [268]. The quality of the PA signal depends upon the penetration depth of the optical signal and the damping of the acoustic signal.

The optical clearing technologies allow the increase of the tissue transparency, which facilitates the reduction of optical radiation scattering and increases the depth of the detected inhomogeneities. On the other hand, the flow of OCA into the tissue and of water out of the tissue changes the composition and structure of the skin, thus changing the acoustic impedance and absorption and, therefore, the acoustic wave damping [269]. Recently it was demonstrated that the optical resolution of PA microscopy can be significantly increased using the aqueous solutions of glycerol as OCA [270]. Liu et al. [115] studied several OCAs *in vitro* and *in vivo*, and showed that PEG-400 in combination with Thiazon improves the visualisation of deep blood vessels of skin, while glycerol is better for imaging small branching blood vessels. In this case the immersion time should be controlled to prevent the reduction of the signal amplification.

Based on the amplification of PA signal at the expense of reduction of scattering, this method can be also efficiently used for noninvasive monitoring of glucose content in blood and tissues, which was demonstrated both in phantoms [271, 272], and in the *in vitro* and *in vivo* studies [273].

By means of PA spectroscopy the influence of glucose can be detected measuring the interval between the peaks of the pressure waves induced by the laser

radiation [272]. The studies demonstrated the applicability of PA spectroscopy to measuring the concentration of glucose [272]. The maximal relative change in the PA response was observed in the region of the second C-H overtone at the wavelength 1126 nm with the additional peak in the region of the second O-H overtone at the wavelength 939 nm [273]. Besides, the analysis of the generated pulsed temporal profile of the PA signal allows the determination of the glucose influence on the tissue scattering, which decreases with the growth of glucose concentration [22, 274].

5.5 Nonlinear and Raman microscopy

Multiphoton excitation of molecules is a nonlinear process, involving the absorption of two or more photons, the total energy of which is sufficient to induce a transition of the molecule to the excited state. Two-photon technique uses the photons with the wavelength of the second harmonic of the incident radiation, coming exactly from the focal region of the incident beam [2, 3]. The unique advantage of the multiphoton microscopy consists in the possibility to study three-dimensional distributions of chromophores, excited by the ultraviolet radiation in thick samples. Such investigation becomes possible because the chromophores can be excited by the radiation of the second harmonic (e.g., at the wavelength of 350 nm), providing high quantum yield under the irradiation of the tissue, e.g., with the laser light having the wavelength near 700 nm, where the tissues possess high transparency. In this case the long-wave radiation can reach deeper layers with less tissue damage [3].

The use of OCA can appear particularly important for improving the two-photon microscopy [23], since it was shown that the light scattering effect strongly reduces the light penetration depth to values, smaller that the depth of the single-photon fluorescence, whereas the resolution remains generally unchanged [251]. This happens mainly because of the exciting beam defocusing in the scattering medium. On the other hand, this method is useful for better understanding of molecular mechanisms of the optical clearing of the tissue under the immersion and dehydration [23].

The improvement of the deep-tissue two-photon signal by means of optical immersion method using hyperosmotic agents, such as glycerol and propylene glycol in the dehydrated form, and the glucose solution, was first demonstrated by Cicchi et al. [23] in the experiments with human skin *ex vivo*. The optical clearing of deeper layers of the tissue occurs mainly at the expense of the cumulative effect of reducing the scattering in the near-surface layers of the tissue sample, which provides smaller damping of the incident and detected radiation of fluorescence. Better focusing (smaller distortion of the focused beam) is achieved in a medium with weaker scattering [23].

Tseng et al. [251] have shown that the combined confocal/two-photon microscopy provides a noninvasive method of microscopic studying of the scaffold structure, which can be a valuable tool for complex investigation of biomaterials and their interaction with the molecules/cells of interest inside the scaffold. The integration of optical clearing with FocusClear, confocal/two-photon microscopy, and three-dimensional presentation is an efficient approach to the microscopic study of the scaffold structure.

Additional morphological information is provided by combining the second harmonic generation (SHG) microscopy with the microscopy based on two-photon excitation [275].

At present SHG is one of the new high-resolution nonlinear-optical imaging methods for the study of intact tissues and cell structures [276-284]. Similar to multiphoton fluorimetry, the SHG method has a few important advantages compared to the methods of linear spectroscopy and imaging, since the exciting near infrared light is weakly scattered by the tissue, while the second harmonic generation occurs already inside the tissue, in the small focal region of the focused laser beam. This provides high spatial resolution, acceptable probing depth, and decoupling of exciting and detected signals. Strongly focused laser beams with high power density and very short pulse duration of tens and hundreds of femtoseconds allow the harmonic generation in a living tissue practically without any damage, because of small interaction time and the total energy, too small for molecular ionisation [284].

SHG is a nonlinear optical process of the second order that can occur only in the media, possessing no central symmetry. The method can be used for imaging highly-ordered structure proteins without any exogenous labels, as well as for probing biological membranes with high specificity to the membrane type [277]. In turn, the third harmonic generation is very sensitive to the refractive index variations and can be used to visualise interphase regions in cells and tissues [285].

Due to its coherent nature, the wave of the second harmonic is mainly radiated in the forward direction. For thicker and strongly scattering samples a part of the SHG signal is scattered. The major part of the SHG radiation still propagates in the forward direction. A great part of structural information encoded in the forward signal is lost in the backward signal due to multiple scattering events. Nevertheless, the mode of SHG backscattering allows the study of upper layers of intact skin or whole animals that could not be implemented in the transmission mode [24, 278, 284, 286].

The SHG in skin is provided, mainly, by the dermis due to its major component, the collagen that possesses considerable nonlinear susceptibility [280-283]. Obviously, the reduction of scattering due to optical clearing for the incident long-wave light and, particularly, for the short-wave second-harmonic detected light can improve the SG images of the collagen structures of the dermis in the forward direction and worsen the signal in the reflection mode.

Wen et al. [76] injected glycerol solutions into the rat skin *in vivo*, and after 10 minutes the samples were

cut for SHG imaging. With the solution having the concentration 75% the dehydration (diameter reduction) of dermis collagen fibres was observed.

Fig. 10 illustrates the change of packing density of the dermis collagen fibres under its interaction with 50% PEG-400 solution. The images were obtained using the SHG microscopy.

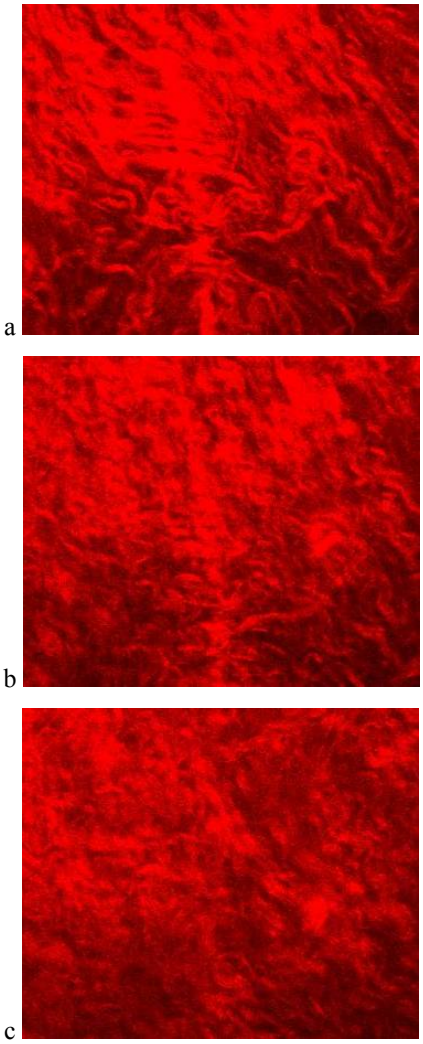


Fig. 10 The packing density change of collagen fibres in the rat skin *ex vivo* under the action of 50% aqueous solution of PEG-400: the initial state (a); immediately after the OCA application (b), and in 15 minutes after the application of OCA (c). The images were obtained by means of SHG microscopy. The incident light wavelength was 790 nm, the detected wavelength 395 nm.

Yeh et al. [121] and Wen et al. [76] demonstrated that for the collagen-based connective tissues (samples of tendon and model tissues) the optical clearing process using the high-concentration glycerol (13 M) manifested itself in considerable reduction of the backscattered signal intensity and the increase of the transmitted signal.

For deeper probing of the murine skeletal muscle and tendon samples using three-dimensional SHG microscopy in the transmission mode the authors of Ref. [24] used the 50% solution of glycerol. They obtained the increase of SHG imaging depth by 2.5 times in the muscle tissue. The amplification of the signal was also due to better packing of the fibrils. It was also shown that the axial attenuation of the direct SHG signal is reduced with the increase of the glycerol concentration (25, 50, and 75%) [72]. The backward SHG signal considerably decreased in the process of optical clearing due to the scattering reduction and the change of the local density of dipoles, producing the second harmonic [72].

The Raman nonlinear spectroscopy also finds its application in studying the mechanisms of optical clearing. Thus, e.g., in Ref [287] the signal of coherent anti-Stokes Raman scattering (CARS) served as the reference in the study of DMSO impact on the collagen structure and, therefore, the loss of SHG signal and the reduction of light scattering by human skin. Hirshburg et al. [110] found the correlation between the rate of the water loss by the rodent skin *ex vivo* under the effect of different OCAs and the potential of optical clearing, which was determined by the slope of the line μ_s' (before clearing)/ μ_s' (after clearing).

Raman spectroscopy is a potential noninvasive method for studying the bone development and for diagnostics of bone diseases [288]. Essential amplification of commonly undetectable Raman signals from internal tissues can be implemented by means of optical clearing of near-surface layers of the tissue that shade the object of study [288, 289]. In this way the transcutaneous spectroscopy of the rat tibial bone *in vivo* was performed under the skin optical clearing with glycerol [288]. The process of porcine skin optical clearing was studied *in vitro* by means of Raman microspectroscopy [289]. The intensity of Raman peaks at the depth of 400 μm was increased by 2-4 times. Besides, the shifts of the peaks in the Raman spectrum of skin at different concentrations of glycerol were observed [289].

The confocal Raman spectroscopy can also be used for *in vivo* monitoring of penetration of clearing agents and permeability enhancers (particularly, DMSO) into the skin *stratum corneum* [290].

5.6 Terahertz spectroscopy

The terahertz (THz) frequency range is intermediate between the IR and microwave frequency ranges (the frequency ν = 1 THz corresponds to the free-space wavelength λ = 300 μm). Recent progress in generating and detecting the THz radiation and its usage offer its promising applications in biology and medicine [291]. Since the energy of THz photons is too small to ionise molecules in biological systems, the THz spectroscopy is expected to be a promising method of study in biology and medicine. Many vibrational transitions of biomolecules lie just in this frequency range, and the light scattering is not so strong as in the visible and near infrared spectral region, so that the excitation by ultrashort pulses can allow the study of a wide

frequency range in a single measurement with high temporal resolution [3, 292-294]. Terahertz spectroscopy allows the determination of the medium complex refractive index in a single measurement, which is important for creating a functional THz tomograph with high sensitivity to the change of metabolite concentrations and precise mapping of the pathologic process boundaries [3]. At the same time, due to the difficulties associated with the specific features of such objects, the biomedical applications are considered as medium-term and long-term goals of THz studies [291].

Keeping in mind that the frequencies of the THz range mainly coincide with the frequencies of rotational and vibrational transitions of the organic molecules, the study of this range may be used for spectral identification of molecules [295]. This circumstance allows the use of THz technologies in addition to the spectroscopic techniques, based on using electromagnetic waves of other frequency ranges. In this connection the development of spectroscopic methods of studying biological tissues in the THz region, providing the detection and visualisation of metabolic and pathologic processes, attracts great interest in recent years, especially as an additional channel of getting information in multimodal systems, in combination with optical methods [296, 297]. In such applications the immersion clearing of the tissue solves many problems of applying optical methods at the expense of reversible reduction of light scattering, and the accompanying dehydration of the tissue facilitates greater permeability for THz radiation due to the reduction, also reversible, of absorption by water contained in the tissue. Direct *in vitro* measurements of the effect of porcine muscle tissue dehydration under the immersion of the sample in glycerol during 30 minutes have shown essential reduction of THz radiation absorption in the region 0.1–1.5 THz, measured using the method of frustrated total internal reflection [292]. The loss of the sample mass amounted to 10% of its initial mass, and the transmission in the visible wavelength range increased upon the average by 5%. This experiment also demonstrated the high sensitivity of the THz range to the concentration of water in tissues, which apparently can serve as one of the criteria for pathology recognition [296].

The influence of dehydration by freezing (lyophilisation) of tissue samples of different rat organs (kidney, diaphragm, liver, rectum, stomach) on the THz spectra in the range 0.4–2.2 THz was studied in Ref. [294]. Among the drawbacks of this method it is worth mentioning the impossibility of *in vivo* studies. Moreover, deep and long freezing of the tissue leads to essential changes of its structure. The dehydration of a tissue can be also implemented by the thermal impact (e.g., using a fan), i.e., by mere drying [298]. However, this method suffers from the same drawbacks as the one presented above.

Obviously, the implementation of *in vivo* dehydration requires temporary and reversible changes in the tissues under study. In Ref. [299] it is proposed to perform the dehydration of muscle tissue using the hyperosmotic agents. As clearing agents the authors used PEG-600, dehydrated glycerol, and propylene glycol. The possibility of reducing the absorption of radiation in the range 0.25 – 1.6 THz under its propagation through the tissue by applying OCA has been unambiguously proved, which offers a possibility of essential increase of the probing depth of a tissue with such radiation. Depending on the frequency of radiation within the studied range, the absorption coefficient reduction approached 60%, and the necessary application time was 8 – 10 minutes, which is acceptable for using this technology in medical practice [299].

5.7 Determination of diffusion coefficients for clearing agents and drugs in tissues

In spite of multiple studies related to the control of optical properties of tissues, the problem of determining diffusion coefficients for hyperosmotic fluids in tissues still remains insufficiently studied. Due to the complex multicomponent structure of tissues and nonlinear character of diffusion processes the measurement of diffusion coefficient of hyperosmotic fluids in tissues is a rather difficult scientific problem. According to the present-day conceptions, the diffusion of different substances in tissues occurs in several stages. At the first stage the penetration of diffusing agents into the intercellular and interfibrillar space and their interaction with cell membranes and interstitial matrix of tissues occurs. At the next stage the transmembrane diffusion of the agent into cells probably occurs, accompanied by the change of the intracellular osmotic pressure. One should not exclude also the possibility of transformation of the membranes themselves, related to the change of the intercellular fluid properties. Under the sufficient saturation of interfibrillar space of a connective tissue with the clearing agent its interaction with the tissue fibrils will obviously take place.

However, the use of sufficiently simple optical and diffusion models allows the solution of the present problem without significant loss of accuracy, and the natural dispersion of optical and structural properties of tissues makes this simplification acceptable. The resulting values of diffusion coefficients can be successfully used in mathematical models, describing the processes of interaction between the hyperosmotic immersion fluids and the tissues, which, in particular is rather urgent in the study of processes, related to transcutaneous delivery of medicinal preparations and metabolic agents.

At present a number of biophysical methods and techniques for determining the diffusion coefficients of different agents exist [300-313], but, unfortunately, only a small part of the methods can be successfully applied to assess the diffusion coefficients in tissues. The available methods are mainly based on using the fluorescence measurement techniques or radioactive

Table 1 Light penetration depth increase by optical clearing agents in different diagnostic methods.

Diagnostic method	Tissue	OCA, refractive index	Spectral range	Light penetration depth increase	Reference
Confocal microscopy	Dehydrated murine adipose tissue, muscle tissue, myocardium, brain	Murray's Clear, 1.55	334 – 799.3 nm	~35 folds	[250]
Two-photon microscopy	Human skin *ex vivo*	Dehydrated glycerol, 1.47	Excitation – 700-1000 nm, detection – 370-670 нм	2 folds	[23]
Confocal/two-photon microscopy	Cellulose membrane	FocusClear, 1.46	Excitation – 820 nm, detection – 390-465 nm	2 folds	[251]
3-D second-harmonic microscopy (direct wave mode)	Muscle tissue of a mouse	50% glycerol solution, 1.395	Excitation – 890 nm, detection – 445 nm	2.5 folds	[24]
Raman microspectroscopy	Porcine skin in vitro	80% glycerol solution, 1.46	785 nm	4 folds	[289]
THz spectroscopy	Bovine muscle tissue	Dehydrated glycerol, 1.47	0.25-1.6 THz	45%	[299]
OCT	Mouse embryo	50% glycerol solution, 1.395	1310 nm	4.5 folds	[59]
	Human skin *in vivo*	Pre-polymer mixture on the base of propylene glycol and polyethylene glycol, 1.47	1305 nm	1.2 folds	[70]
	Whole blood, diluted by two times with saline	6.5% glycerol solution, 1.34	820 nm	2.4 folds	[128]

labels for recording the flow of diffusing substance. The use of fluorescence measurement technique is impossible for the assessment of diffusion coefficients of non-fluorescent substances (e.g., aqueous solutions of glucose or glycerol), and the use of radioactive substances can be undesirable in the case of *in vivo* measurements. Moreover, the high sensitivity of fluorescence and radioactive measurements makes their use difficult also because of the natural metabolic activity of the organism, which introduces additional errors into the measurement process. The method that allows the assessment of diffusion coefficients of non-fluorescent hyperosmotic fluids in tissues was proposed in 1997 [43] and later developed in Refs. [47, 90]. This method is based on measuring the time dependence of the tissue scattering characteristics under the action of hyperosmotic fluids and can be successfully used for both *in vitro* and *in vivo* measurements.

The process of immersion fluid transport in fibrous tissues can be described using the free diffusion model. In this case the following assumptions related to the transport process are commonly made: 1) only the concentration diffusion takes place, i.e., the exchange flux of the immersion fluid or drug into the tissue and of water from the tissue at a given point is proportional to the gradient of concentration of the clearing agent at this point; 2) the diffusion coefficient is constant at all points in the studied tissue sample.

Geometrically the tissue sample is presented as a plane-parallel plate of final thickness. Since the area of the upper and lower surfaces of this plate is much larger than the side area, it is possible to neglect the edge effects and solve the one-dimensional diffusion problem described by the equation

$$\frac{\partial C(x,t)}{\partial t} = D\frac{\partial^2 C(x,t)}{\partial x^2}, \qquad (4)$$

presenting the second Fick law, where $C(x,t)$ is the concentration of the immersion agent (e.g., glucose) in the skin (g/ml); D is the diffusion coefficient (cm^2/s); t is the time, during which the diffusion process occurs (s); x is the spatial coordinate along the sample thickness direction (cm). Since in the experiments the volume of the immersion fluid, as a rule, significantly exceeds the volume of the tissue sample, the appropriate boundary conditions have the form

$$C\left(0,t\right)=C_0 \qquad \text{and} \qquad \frac{\partial C\left(l,t\right)}{\partial x}=0\,, \tag{5}$$

where C_0 is the glucose concentration in the solution (f/ml); l is the tissue sample thickness (cm). The second boundary condition reflects the fact that the diffusion of the immersion fluid into the skin sample occurs only from one side of the sample, i.e., from the dermis side. In the case, when the immersion agent diffuses from both sides of the tissue sample (such situation arises, e.g., in experiments with sclera or dura mater in vitro), the boundary conditions have the form:

$$C\left(0,t\right)=C_0 \qquad \text{and} \qquad C\left(l,t\right)=C_0\,. \tag{5*}$$

The initial conditions express the absence of the immersion agent in all internal points of the sample before its incubation into the solution, i.e.,

$$C\left(x,0\right)=0\,. \tag{6}$$

The solution of the diffusion equation (4) with the initial (6) and boundary (5) conditions taken into account has the form:

$$C\left(x,t\right)=C_0\left(1-\sum_{i=0}^{\infty}\frac{4}{\pi\left(2i+1\right)}\sin\left(\frac{\left(2i+1\right)\pi x}{2l}\right)\times\right.$$
$$\left.\times\exp\left(-\frac{\left(2i+1\right)^2 D\pi^2 t}{4l^2}\right)\right).$$

The mean concentration of the immersion solution in the tissue sample $C(t)$ as a function of time is determined by the expression

$$C\left(t\right)=C_0\left(1-\frac{8}{\pi^2}\sum_{i=0}^{\infty}\frac{1}{\left(2i+1\right)^2}\times\right.$$
$$\left.\times\exp\left(-\left(2i+1\right)^2 t\frac{\pi^2}{4}D\Big/l^2\right)\right). \tag{7}$$

In the case of double-side diffusion the solution of the diffusion equation (4) with the initial (6) and boundary (5*) conditions has the form

$$C\left(x,t\right)=C_0\left(1-\sum_{i=0}^{\infty}\frac{4}{\pi\left(2i+1\right)}\sin\left(\frac{\left(2i+1\right)\pi x}{l}\right)\times\right.$$
$$\left.\times\exp\left(-\frac{\left(2i+1\right)^2 D\pi^2 t}{l^2}\right)\right).$$

In this case the mean concentration of the immersion solution in the tissue sample $C(t)$ as a function of time is determined by the expression

$$C\left(t\right)=C_0\left(1-\frac{8}{\pi^2}\sum_{i=0}^{\infty}\frac{1}{\left(2i+1\right)^2}\times\right.$$
$$\left.\times\exp\left(-\left(2i+1\right)^2 t\pi^2 D\Big/l^2\right)\right). \tag{7*}$$

In the first approximation Eq. (7) can be rewritten as

$$C\left(t\right)\approx C_0\left(1-\exp\left(-t\pi D\Big/l^2\right)\right), \tag{8}$$

and Eq. (7*) as

$$C\left(t\right)\approx C_0\left(1-\exp\left(-t\pi^2 D\Big/l^2\right)\right). \tag{8*}$$

Note, that Eqs. (8) and (8*) correspond to the equation describing the diffusion through a thin penetrable membrane.

As the immersion agent penetrates into the tissue, the increase of the refractive index of the interstitial fluid will be observed. The assessment of the refractive index of the interstitial fluid depending on the diffusion time can be performed basin on the Gladstone-Dale law, according to which the refractive index of a mixture of non-interacting liquids is a sum of the refractive indices of individual components multiplied by the volume fractions of these components [314]. Mathematically the Gladstone-Dale law is written as

$$n_\Sigma=\sum_i n_i C_i\,,\ \text{where}\ \sum_i C_i=1\,. \tag{9}$$

Here n_Σ is the refractive index of the multicomponent mixture of non-interacting liquids; n_i and C_i are the refractive indices and volume fractions of each component. In the case of two-component solutions (in our case the components are the interstitial fluid and the solution of the immersion agent) the Gladstone-Dale law has the form

$$n_l\left(t\right)=\left(1-C\left(t\right)\right)n_{base}+C\left(t\right)n_{osm}\,, \tag{10}$$

where n_{base} is the refractive index of the interstitial fluid at the initial moment of time, and n_{osm} is the refractive index of the hyperosmotic immersion fluid (e.g., glucose or glycerol solution). For the aqueous solution of glucose the value of the refractive index $\left(n_{gl}\right)$ can be found from the expression [315]

$$n_{gl}\left(\lambda\right)=n_{H_2O}\left(\lambda\right)+0.1515\times C_{gl}\,, \tag{11}$$

where $n_{H_2O}(\lambda)$ is the spectrally dependent refractive index of water ($[\lambda] = \text{nm}$), and C_{gl} is the glucose concentration in the solution(g/ml). The spectral dependence of the water refractive index has the form [316]:

$$n_{H_2O}(\lambda) = 1.3199 + \frac{6.878\times10^3}{\lambda^2} - \frac{1.132\times10^9}{\lambda^4} + \frac{1.11\times10^{14}}{\lambda^6}. \quad (12)$$

The optical characteristics of skin are determined by the optical properties of dermis (since its thickness is dominating with respect to the thickness of other skin layers). Hence, the optical model of the tissue can be presented as a layer having the thickness l, containing the scatterers in the form of infinitely long thin dielectric cylinders, parallel to the sample surface. In the first approximation one can assume that in the process of interaction of the tissue with the immersion fluid the scatterer size does not change. For densely packed tissues, i.e., the tissues with sufficiently large volume fraction of scatterers, to which the skin belongs, it is important to allow for the interference effects that arise because each scatterer is located in the near-field zone of radiation, scattered by the other scatterers, described by introducing the packing factor [3, 317]. For a system of thin dielectric cylinders, arranged parallel to each other, the packing factor has the form $(1-\varphi)^3/(1+\varphi)$ [317], where φ is the volume fraction of the scatterers. Thus, the expression describing the tissue scattering coefficient can be written in the form [90]:

$$\mu_s = \frac{\varphi}{a}\frac{\pi x^3}{8}\left(m^2-1\right)^2\left(1+\frac{2}{\left(m^2+1\right)^2}\right)\frac{(1-\varphi)^3}{1+\varphi}. \quad (13)$$

The time dependence of the collimated transmission coefficient of the tissue sample immersed in the solution of a hyperosmotic liquid or medicinal preparation has the form:

$$T_c(t) \approx \exp\left(-\left(\mu_a + \mu_s(t)\right)\times l\right), \quad (14)$$

where μ_a is the absorption coefficient of the tissue sample.

Equations (4)-(13) determine the dependence of the collimated transmission coefficient upon the concentration of the immersion fluid solution (e.g., the solution of glucose or glycerol) in the sample of the tissue, i.e., formulate the direct problem. The inverse problem is to reconstruct the values of the diffusion coefficient from the time dependence of the collimated transmission. This problem is solved by minimisation of the target functional

$$f(D) = \sum_{i=1}^{N_t}\left(T_c(D,t_i) - T_c^*(t_i)\right)^2, \quad (15)$$

where N_t is the total number of experimental points, obtained by recording the time dependence of collimated transmission at the fixed wavelength: $T_c(D,t)$ is the value of the transmission coefficient, calculated using the formula (14) at the time moment t for the given values of D; $T_c^*(t)$ is the experimentally measured value of the transmission coefficient at the time moment t.

The flowchart of the program implementing the present algorithm is shown in Fig. 11. The main steps of the algorithm include:

1) Specification of the initial parameters for the chosen wavelength (the absorption coefficient μ_a, the refractive index of the interstitial fluid n_s, the refractive index of the glucose solution or a drug n_l, the thickness of the tissue sample l) obtained either from independent measurements, or from literature data.

2) Specification of the initial value of the diffusion coefficient D. The initial value of D can be obtained from the analysis of variation of the sample collimated transmission basing on the equation

$$\tau = -\frac{\sum_{j=1}^{n} t_j^2}{\sum_{j=1}^{n}\left(t_j \ln y_j\right)},$$

where t_j is the time moment of measuring each value of T_c, T_c is the collimated transmission coefficient, $y = 1 - T_c/A$; A is the maximal value of the collimated transmission coefficient; τ is the diffusion time constant (s); $\tau = \frac{l^2}{\pi D}$ in the case of single-side diffusion and $\tau = \frac{l^2}{\pi^2 D}$ in the case of double-side diffusion.

3) Calculation of the kinetics of collimated transmission versus time for given D and t_j using the Bouguer's law (Eq. (14)).

4) Comparison of the calculated and measured values of collimated transmission coefficients. If the difference does not exceed the prescribed error, the value of D is found and the process is terminated, otherwise the value of D is changed using the minimisation simplex method [318], and the procedure is repeated till the prescribed accuracy is achieved.

As an example, Table 2 presents the values of diffusion coefficients of glucose aqueous solutions in tissues, measured using the above method at the room temperature (about 20°C). However, for medical applications the most interesting are the diffusion coefficient values measured at the physiological temperature (nearly 37°C). Since the direct measurement of the diffusion coefficients at the physiological temperature requires thermostating of the

Table 2 Glucose diffusion coefficients in biotissues [47].

Tissue	Immersion fluid	Diffusion coefficient, $\times 10^{-6}$, cm^2/s, measured at 20°C	Diffusion coefficient, $\times 10^{-6}$, cm^2/s, at the temperature 37°C
Eye sclera	Aqueous solution of glucose, 0.2 g/ml	0.57 ± 0.09	0.91 ± 0.09
Eye sclera	Aqueous solution of glucose, 0.3 g/ml	1.47 ± 0.36	2.34 ± 0.36
Eye sclera	Aqueous solution of glucose, 0.4 g/ml	1.52 ± 0.05	2.42 ± 0.05
Pachymeninx	Aqueous solution of glucose, 0.2 g/ml	1.63 ± 0.29	2.59 ± 0.29
Skin	Aqueous solution of glucose, 0.4 g/ml	1.10 ± 0.16	1.75 ± 0.16
Skin (*in vivo*)	Aqueous solution of glucose, 0.4 g/ml		2.56 ± 0.13

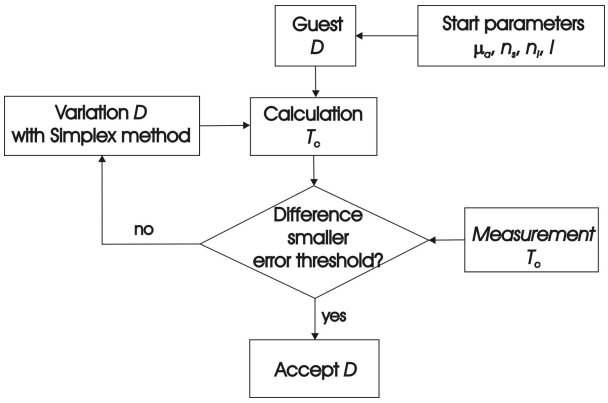


Fig. 11 Flowchart of the program for calculating the diffusion coefficients of glucose and drugs basing on the kinetics of collimated transmission of tissue samples.

tissue sample that essentially complicates the experimental setup and measurement technique, one can determine the diffusion coefficient at the physiological temperature theoretically, using the following dependence of the diffusion coefficient upon the temperature [319]:

$$D(T_2) = D(T_1)\frac{T_2}{T_1}\frac{\eta(T_1)}{\eta(T_2)},$$

where $\eta(T)$ is the viscosity of the medium where the diffusion occurs (e.g., water) at the given temperature T. In our case $T_1 = 20^{\circ}C$ and $T_2 = 37^{\circ}C$. In Table 2 (4-th column) the values of the diffusion coefficients calculated for the temperature 37°C are presented.

From Table 2 it is well seen that the temperature increase from room to physiological, i.e., by 17°C, causes the increase of the diffusion coefficient nearly by 1.5 times.

6 Conclusion

A review of specific features and methods of optical clearing and related interaction of light with biological tissues is presented. The impact of the OCA on a tissue allows efficient control of the optical properties, particularly, the reduction of tissue scattering coefficient, which facilitates the efficiency increase in different methods of optical imaging (optical biopsy) in medical applications. Both immersion and compression techniques of optical clearing possess considerable potential for many diagnostic, therapeutic, and surgical methods, in which the laser impact on the target site hidden in the tissue is used.

The work was supported by Russian Presidential grant NSh-703.2014.2, the Government of the Russian Federation grant 14.Z50.31.0004 (EAG, ANB, IYuY, and VVT), RFBR grant 14-02-20101 (VVT), and The Tomsk State University Academic D.I. Mendeleev Fund Program (EAG, ANB, YuPS, and VVT).

The authors wish to thank Prof. Dan Zhu (HUST, China) and her PhD students for their help in the obtaining of the SHG-images.

Change of optical properties of hair cells during malignant tumour development

V.S. Maryakhina[1*], L.S. Scheglova[1], K.A. Anenkova[2]
[1] Orenburg state university, 13 Pobedy st., Orenburg, 460018, Russia
[2] M. V. Lomonosov Moscow state university, 1 Leninskiye Gory, Moscow, 119991, Russia

* **e-mail:** v.s.maryakhina@gmail.com

Abstract. The results of experimental investigations on the differences of wool microstructure and its biophysical properties of healthy mice and mice with malignant tumour are represented in the paper. It is shown that destruction of wool structure as well as biochemical composition change of wool cells is during pathology development. Difference is seen even when tumour is small. We have shown that the general regularity of spectral measurements for mammary and hair cells is conserved at health state and pathology present. Taking into account this, the represented data about wool structure can be used to improve the optical techniques for non-invasive diagnostics of cancer diseases at different stages of pathology. © 2015 Samara State Aerospace University (SSAU).

Keywords: breast cancer; hair; optical biomedical diagnostics; dynamic light scattering; fluorescence.

Paper #1868 received 2014.11.29; revised manuscript received 2015.01.13; accepted for publication 2015.01.16; published online 2015.03.28.

References

1. V. V. Tuchin, "Light scattering study of tissues," Phys. Usp. 40, 495 - 515 (1997).
2. V. S. Maryakhina, and V. V. Gun'kov, "Fluorescent probe immobilization into enzyme molecules", Computer research and modeling 5, 201-208 (2013).
3. S. N. Letuta, V. S. Maryakhina, and R. R. Rakhmatullin, "Optical diagnostics of biological tissue cells during their cultivation in polymers," Quantum electronics 41, 314-317 (2011).
4. Th. Schlake, "Determination of wool structure and shape," Seminars in Cell & Developmental Biology 18, 267–273 (2007).
5. S. B. Park, S. W. Choi, and A. Y. Nam, "Wool Tissue Mineral Analysis and Metabolic Syndrome," Biol Trace Elem Res 130, 218-228 (2009).
6. V. S. Maryakhina, L. S. Scheglova, and K. A. Anenkova, "Features of structure of external layer of murine hair at different stages of malignant tumour development," Journal of Innovative Optical Health Sciences 8, 1541001 (2015).
7. G. Z. Kammins, and E. R. Paik, Photon Correlation and Light Beating Spectroscopy. New York: Plenum (1974).
8. R. Pecora, Dynamic Light Scattering from Macromolecules, Stanford: Stanford Univ. (1984).
9. K. A. Anenkova, G. P. Petrova, V. V. Gibizova, L. A. Osminkina, and K. P. Tamarov, "Optical properties of serum albumin water solutions, containing mesoporous silicon particles," Optics and Spectroscopy 115, 166-170, (2013).
10. G. E. Dobretsov, Fluorescent Probes in the Studies of Cells, Membranes, and Lipoproteins, Moscow: Nauka (1989).
11. L. S. Scheglova, L. L. Abramova, and V. S. Maryakhina, "Optical diagnostics of tumour cells at different stages of pathology development," Quantum electronics 43, 1088-1090 (2013).
12. N. M. Emanuel, R. E. Kavetskiy, B. N. Tarusov, and E. P. Sidorik, Biophysics of cancer, Kiev: Science (1976).

13. S. N. Letuta, and V. S. Maryakhina, "The delayed fluorescence kinetics as a method of biological tissue diagnostics," Proc. SPIE 7999, 799907 (2011).
14. V. James, J. Kearsley, T. Irving, Y. Amemiya, and D. Cookson, "Using wool to screen for breast cancer," Nature 398, 33-34 (1999).
15. F. Briki, B. Busson, B. Salicru, F. Estève, and J. Doucet, "Breast-cancer diagnosis using wool," Nature 400, 226 (1999).
16. M. Hart, "Using wool to screen for breast cancer," Synchrotron Rad. News 12, 31-37 (1999).
17. Q. Pasha, S. A. Malik, N. Shaheen, and M. H. Shah, "Investigation of trace metals in the blood plasma and scalp wool of gastrointestinal cancer patients in comparison with controls," Clinica Chimica Acta 411, 531-539 (2010).
18. E. L. Abel, J. M. Angel, K. Kiguchi, and J. DiGiovanni, "Multi-stage chemical carcinogenesis in mouse skin: Fundamentals and applications," Nature Protocols 4, 1350-1362 (2009).
19. V. S. Maryakhina, and S. N. Letuta, "Pathology development stage and its influence to the delayed fluorescence kinetics of molecular probes," Laser physics 23, 025604 (2013).

1 Introduction

The optical techniques of biomedical diagnostics are used for detection of biotissue pathological states due to their non-invasiveness and high sensitivity to pathology. However, sensitivity of all these techniques is not enough for early diagnostics of cancer diseases. According to that it is essential to raise the accuracy of the optical methods. Parameter, which significant different for health and tumour cells, should be found. It can be carried out by either device improving or research object change.

Biotissues and somatic cells are widespread objects for the optical biomedical diagnostics but their significant heterogeneity together with high scattering light [1] significantly complicate obtaining statistically reliable data. That's why new research objects are needed.

In this work we show the possibility of using hair for optical biomedical diagnostics because of difference in their structure in normal and pathological states.

2 Objects and methods of research

2.1 Objects of research

The object of the research was wool of mice (line BYRB) with spontaneous tumours of mammary gland. Wool had been cut from all skin surfaces of healthy mice and mice with malignant tumour(s) of same line. Additionally, we had also carried out experiments with wool from skin located above tumour only. Diameter of tumour capsule was from 1 to 3 cm. The wool aliquot was previously cleared twice in medical alcohol. To obtain reliable results not less than 15 female mice were used for each type of samples.

2.2 Optical microscopy

The cleared wool was placed on the slide. Wool structure was investigated by the optical inverted microscope Altami invert 3 with video camera working in phase contrast mode (magnification x400).

2.3 Spectrofluorimetry

The cleared wool aliquots were placed into collagenase solution (0.5 mg/ml) dissolved in phosphate buffer (pH=7.4) and were incubated at 37 ^{0}C for 40 minutes for stirring. The obtained suspension (collagenase with dissolved cells and peptides) was investigated by spectrofluorimetry. A few microliters of rhodamine 6G was added to the suspension and was incubated during 10-15 minutes for diffusion equilibrium establishment [2]. The colored suspension was placed to slide for full drying up. Fluorescence spectra were measured on the optical device (fig.1) containing xenon lamp XBO 150W/1 (light source) **1** and monochromator MDR-206 **2**. The monochromatic light was focused by the lens **3** and was routed to sample surface **5** by the swivel mirror **4**. Emission of the samples was focused by the lens **6** to the entrance slit of the monochromator MDR-41 **7** and was registered by FEU-100 **8**. Collection, accumulation and processing of the experimental data were performed in an automatic mode by the personal computer and CAMAC crate **9** and computer **10**. The excitation wavelength was 515 nm.

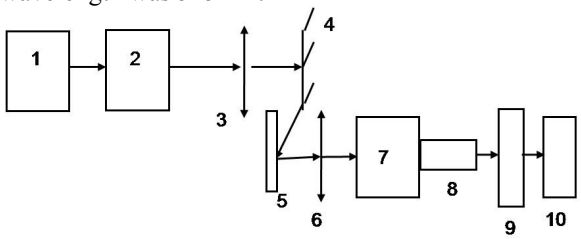


Fig. 1 Scheme of experimental device for fluorescence spectra measurements.

2.4 Phosphorescence kinetics

The obtained cell suspension was cleared twice from collagenase molecules by centrifuging at 6000 rpm for 5 minutes. Aliquot of bengal rose was added to the cell solution and was incubated during 10-15 minutes. The colored cells were placed to the mica for measuring. Phosphorescence kinetics was measured on experimental setup for biomedical investigations. Its

description had been published in detail in our earlier work [3]. The wavelength of excitation was at 532 nm (the second harmonics of Nd:YAG laser). Registration of emission was at 680 nm. All measurements were carried out at atmosphere pressure. The registered signal is result of accumulation of 20 signals from each sample for measurements error decrease.

2.5 Dynamic light scattering

The obtained cell suspension was placed to "Photocor complex" for cells size measuring. Laser wavelength was 647 nm, it power was 25 mW. Each measurement was during 10 min. For statistical adequacy the all represented results are average of ten or more measurements. All used solutions were free-prepared from dry compounds produced by Sigma-aldrich.

3 The results and discussion

It is known [4] that hair of both animals and people has layer structure. External layer is connective tissue cells. Next two internal Henley and Huxley layers consist of keratinized cells with irregular shape. The internal layer is hair shaft. In spite of complex multilayer structure, hair can be as health indicator sometimes [5]. Any changes of metabolic processes lead to change of wool biochemical composition. As a rule, its destruction starts from external layer. Photo samples of the wool of health mice females and females with spontaneous tumour of mammary gland are presented in Figure 2. As you can see, disturbance of hair structure is traceable on sequential stages. Wool of health mouse has dense structure, external layer is pronounced. At the time, wool of mice with tumour is thinner, external and internal layers are destroyed. Difference is even when tumour diameter is small.

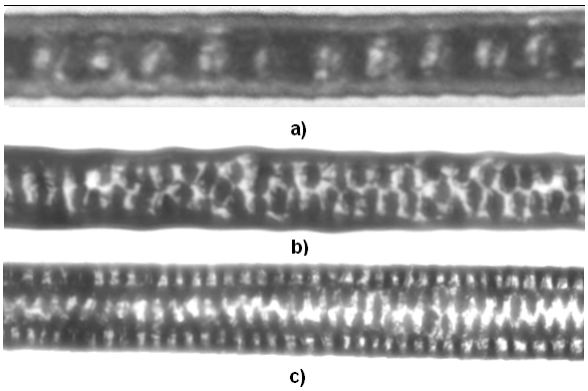


Fig. 2 Wool structure of health mouse (a) and mice with tumour 1 cm (b), 3 cm (c). Magnification x400.

The described changes lead to absorption spectra changes described in our previous work [6]. A serial decrease of supernatant optical density is. At the time, their maxima spectra shift to short-wave region. It is a result of hair structure destruction with pathology development, cells number decreases.

In addition to the decrease of cell quantity in the external layer, its thinning was observed. These data were confirmed by dynamic light scattering method (DLS). The DLS method allows to determine the translation diffusion coefficient of disperse particles in a fluid through the analysis of the characteristic time of fluctuations of the scattered light intensity [7]. The chaotic Brownian motion of dispersed particles causes microscopic fluctuations of their local concentration. These fluctuations, in turn, lead to local inhomogeneities of the refractive index. The passage of a laser beam through the medium means that part of the light is scattered on these inhomogeneities; the fluctuations of the intensity of the scattered light correspond to fluctuations of the dispersed particles' local concentration.

The dynamic information in the particles is derived from autocorrelation of the intensity trace recorded during the experiment. The autocorrelation function describes the relationship between the signal at the delay time τ and $\tau + d\tau$ as follows:

$$G(t) = \langle I(t) \cdot I(t+\tau) \rangle, \quad (1)$$

where τ is the delay time and I is the density.

This technique is named photon correlation spectroscopy and it is also known as quasielastic light scattering [8].

In the case of a mono-dispersed solution, that contains spherical non interacting particles of the same size, it is possible to show that the photocurrent power spectrum has the form of a Lorentzian curve [7] with half width Γ. The normalized intensity correlation function is described by an exponential with relaxation time $\tau_{rel} = 1/\Gamma$ as

$$g_1(\tau) = \exp(-\Gamma t) \quad (2)$$

The decay rate Γ is related to the physical properties of the particles and the experimental conditions by the following expressions:

$$\Gamma = D_t q^2, \quad (3)$$

$$D_t = \frac{kT}{6\pi\eta R}, \quad (4)$$

$$q = k_i - k_s = \left(\frac{4\pi n}{\lambda}\right)\sin\frac{\theta}{2}, \quad (5)$$

where k_i is the wave vector of incident radiation, k_s is the wave vector of scattered radiation, D_t is the translational diffusion coefficient of particles, n is the refractive index of a medium, λ is the scattered light wave length, θ is the scattering angle, T is the absolute temperature of the scattering solution, K is the

Boltzman's constant, η is the solvent viscosity, and R is the hydrodynamic radius of a particle.

In the case of polydisperse solutions with different sizes of particles, the photocurrent spectrum is a continuous set (integral) of Lorentzian curves with different half widths. Therefore, to find the size distribution of particles (diffusion coefficients); it is necessary to solve the inverse spectral problem in the form of anintegral equation with the Lorentzian kernel:

$$g^{(2)}(t) = \left(g^{(1)}(t)\right)^2 + 1 + \zeta(t); \qquad (6)$$

$$g^{(1)}(t) = \int_0^\infty P(\Gamma) \exp(-\Gamma t)\, d\Gamma, \qquad (7)$$

where $g^{(1)}(t)$ is the normalized autocorrelation function of a signal, $g^{(2)}(t)$ is the normalized autocorrelation function of intensity, and $\zeta(t)$ is an error associated with the stochastic nature of the signal itself rather than with the inaccuracy of photocurrent measurement or the noises of a recording channel [7,9].

Equation (7) is known as the Siegert relation, will allow one to calculate $g^{(1)}(t)$ in terms of $g^{(2)}(t)$ accumulated by a correlator in the course of an experiment. Integral equation (3) forms the main principle of data processing in the method of photon correlation spectroscopy.

The results of our experiments were processed using the DYNALS package of programs, in which approximate solution (3).

The results of calculations are presented in table 1. As you can see each sample contains two cell types. These cell types have different size. We assume that it connects on partially separation of Henley layer during collagenase treatment. With pathology process development cells size decrease for both cell types. We note that difference between wool cell size of normal states and small tumour are nearly 36% for two cell types. Consequently, these distinctions are statistically significant. We do not observed difference in the results after investigation of wool cuted from all skin surface and from tumour surface only for all mice types.

Moreover, biochemical composition is also changed during breast cancer development. It is confirmed by fluorimetric measurements with molecular probes. It is known [10] that rhodamine 6G penetrates into cell and connects with mitochondria. Thus, fluorescence spectra of rhodamine can be as an indicator of mitochondria structure changes. In Fig. 3 fluorescence spectra of the probe are depicted. They shift to long wave region with tumour development. This regularity for rhodamine we had also seen for normal and cancer mammary cells. These results had been published in our previous work [11]. Wave lengths are different in two types of experiments because of difference of cells biochemical composition, however, the general regularity is observed.

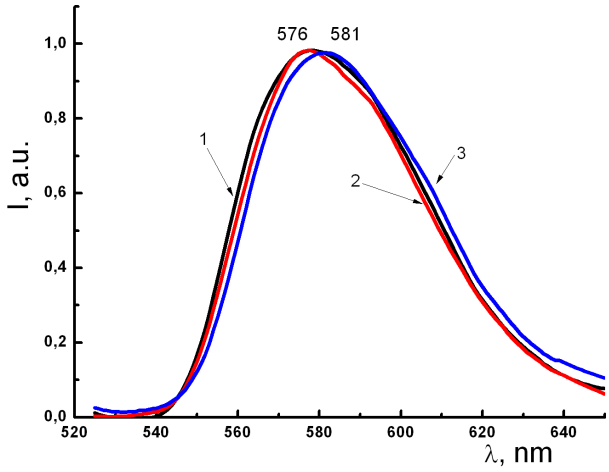


Fig. 3 Fluorescence spectra of rhodamine 6G in hair cells from health mouse (1), from mouse with small (2) and large tumour (3).

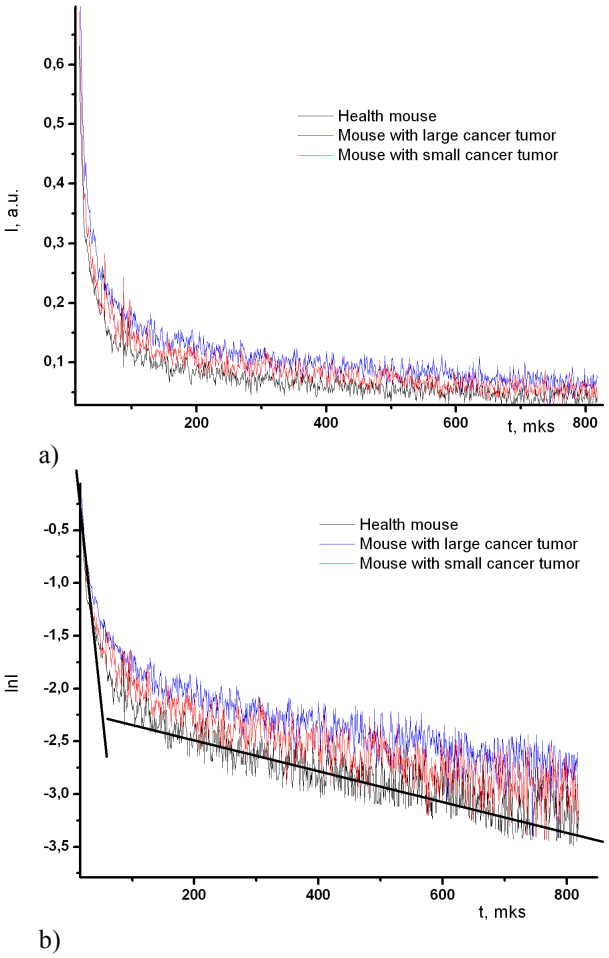


Fig. 4 The phosphorescence kinetics of bengal rose located in wool cells from health mouse (1), from mouse with small (2) and large tumour (3). Curves are carried out in Descartes (a) and semilogarithmic (b) coordinates.

The microviscosity and peptide concentrations of hair cells are also changes with tumour growth. It can be measured by phosphorescence kinetics of bengal rose

(Fig. 4a) which connect with peptides. The kinetics has a two-exponential type. It is distinctly seen if these curves are carried out in semilogarithmic coordinates (Fig. 4b).

These curves of Fig. 4a are approximated by the following function

$$I_{ph}(t) = A_1 \exp(-t/\tau_1) + A_2 \exp(-t/\tau_2). \quad (8)$$

Value τ_1 and τ_2 are represented in table 2. As you can see from approximation results, τ_1 decreases with tumour growth. It can be results of increases of annihilation processes rate with triplet states of the probe. At the time τ_2 rises with pathology development. It can be connected with peptide concentration increases [12] and immobilization of the probe into peptide molecules. We note that similar regularity had been seen for fluorescent probes located in normal and cancer mammary cells [13].

4 Conclusion

Although biomedical diagnostics methods are present, search of method of the earlier diagnostics of cancer diseases is. For example, earlier [14] the method of breast cancer diagnostics based on wool structure investigation by X-rays was proposed. Later investigations [15,16] had not confirmed these data. Nonetheless, research of wool structure for diagnostics applications are carrying on (see, for example, [17]).

The biological tissue cells are objects with specific very inhomogeneous structure. Effectivity of photoprocesses happening inside the cells depends on composition of intracellular structures, composition of cell membrane etc. In its turn, the physical-chemical composition of the cells received from pathogenic tissues depends on the stage of pathological process development [18]. It leads to change spectral-luminescent properties of cells obtained from tumour at different stages of pathology as well as photosensitizers located within it [11,19]. In the paper we have shown that the general regularity of spectral measurements for mammary and hair cells is conserved at health state and pathology present. Taking into account this, the represented data about wool structure can be used to improve the optical techniques for non-invasive diagnostics of cancer diseases at different stages of pathology.

The work was partially supported by grant of Ministry of science and education of Russian Federation № 450 from 01.02.2014

Table 1 Cells radius of external wool layer and their diffusion coefficients.

Normal wool		**d_{tumour} = 1 cm**		**d_{tumour} = 3 cm**	
R, nm	**$D_t \cdot 10^{-8}$, cm^2/s**	**R, nm**	**$D_t \cdot 10^{-8}$, cm^2/s**	**R, nm**	**$D_t \cdot 10^{-8}$, cm^2/s**
776±146	0,28±0,06	495±83	0,44±0,07	368±74	0,59±0,13
199±36	1,1±0,2	126±13	1,7±0,2	99.4±13	2,7±0,4

Table 2 The result of approximation of bengal rose phosphorescence curves by function (8).

Curves	**τ_1, μs**	**τ_2, μs**
Health mouse	19.3±0.5	657±11.5
Mouse with small tumour	16.8±0.4	673±13.1
Mouse with large tumour	16.1±0.3	727±14.1

Line optical traps formed by LC SLM

A. Korobtsov[1], S. Kotova[1,2*], N. Losevsky[1], A. Mayorova[1,2], S. Samagin[1]
[1] Lebedev Physical Institute, 221 Novo-Sadovaya Str., Samara, 443011, Russia
[2] Samara State Aerospace University (SSAU), 34 Moskovskoye shosse, Samara, 443086, Russia

* **e-mail:** kotova@fian.smr.ru

Abstract. The methods for generation of optical traps in the form of line segments by means of liquid crystal modulators of two types are addressed in the paper, they are a multi-pixel modulator HOLOEYE HEO 1080P and a tunable liquid crystal focusing device (4-channel modulator) developed by the authors. The numerical and experimental assessment of the capture forces of the generated optical trap is fulfilled. The description of manipulation experiments with microobjects, including biological ones, carried out by the optical traps with the intensity distribution in the form of segments is offered. © 2015 Samara State Aerospace University (SSAU).

Keywords: optical manipulation; liquid crystal modulators; biological microobjects; light segment.

Paper #1893 received 2014.12.04; revised manuscript received 2015.01.22; accepted for publication 2015.02.01; published online 2015.03.28.

References

1. H. Zhang, and K-K. Liu, "Optical tweezers for single cells," J. R. Soc. Interface 5, 671-690 (2008).
2. A. Banerjee, S. Chowdhary, W. Losert, and S. K. Gupta, "Survey on indirect optical manipulation of cells, nucleic acids, and motor proteins," J. Biomedical Optics 16, 051302 (2011).
3. K. Svoboda, and S. Block, "Biological applications of optical forces," Ann. Rev. Biophys. Biomol. Struct. 23, 247-285 (1994).
4. R. Skidanov, M. Rykov, G. Iannacchione, and S. Krivoshlykov, "The modification of laser beam for optimization of optical trap force characteristic," Computer optics 36**,** 377-386 (2012).
5. M. Rykov, and R. Skidanov, "Modifying the laser beam intensity distribution for obtaining improved strength characteristics of optical trap," Applied Optics 53(2), 156-164 (2014).
6. A. Korobtsov, S. Kotova, N. Losevsky, A. Mayorova, and S. Samagin, "Formation of contour optical traps with a four-channel liquid crystal focusator," Quantum Electronics 44(12), 1157-1164 (2014).
7. F. Cheong, C. Sow, A. Wee, P. Shao, A. Bettiol, J. van Kan, and F. Watt, "Optical travelator: transport and dynamic sorting of colloidal microspheres with an asymmetrical line optical tweezers," Applied Physics, 83, 121-125 (2006).
8. R. W. Applegate Jr, J. Squier, T. Vestad, J. Oakey, and D. W. M. Marr, "Fiber-focused diode bar optical trapping for microfluidic flow manipulation," Applied Physics Letter 92(1), 01394 (2008).
9. R. W. Applegate Jr, D. W. M. Marr, J. Squier, and S.W. Graves, "Particle size limits when using optical trapping and deflection of particles for sorting using diode laser bars," Optic Express 17, 16731 (2009).
10. R. Skidanov, and A. Porfir'ev, "Optical micromanipulation with using binary focusator," Computer optics 34, 214-218 (2010).
11. E. Spyratou, M. Makropoulou, and A. Serafetinides, "Red blood cell micromanipulation with elliptical laser beam profile optical tweezers in different osmolarity conditions," Proc. of SPIE-OSA Biomedical Optics, 8092, 80920T (2011).
12. R. Dasgupta, S.K. Mohanty, and P.K. Gupta, "Controlled rotation of biological microscopic objects using optical line tweezers," Biotechnol. Lett. 25(19), 1625-1628 (2003).
13. R. Applegate Jr., J. Squier, T. Vestad, J. Oakey, and D. Marr, "Optical trapping, manipulation, and sorting of cells and colloids in microfluidic systems with diode laser bars," Optics Express 12(19), 4390-4398 (2004).
14. R. Applegate Jr., J. Squier, T. Vestad, J. Oakey, D. Marr, P. Bado, M. A. Dugan, A. A. Said, "Microfluidic sorting system based on optical waveguide integration and diode laser bar trapping," Lab. Chip. 6(3), 422-6 (2006).

15. S. P. Kotova, V. V. Patlan, and S. A. Samagin, "Tunable liquid-crystal focusing device. I. Theory," Quantum Electron. 41(1), 58-64 (2011).
16. S. P. Kotova, V. V. Patlan, and S.A. Samagin, "Tunable liquid-crystal focusing device. II. Experiment," Quantum Electron. 41(1), 65-70 (2011).
17. S. P. Kotova, V. V. Patlan, and S.A. Samagin, "Focusing light into a line segment of arbitrary orientation using a four-channel liquid crystal light modulator," Journal of Optics 15(3), 035706 (2013).
18. M. Capitanio, G. Romano, R. Ballerini, M. Giuntini, F.S. Pavone, D. Dunlap, and L. Finzi, "Calibration of optical tweezers with differential interference contrast signals," Review of Scientific Instruments 73(4), 1687-1696 (2002).
19. A. Korobtsov, S. Kotova, N. Losevsky, A. Mayorova, V. Patlan, and S. Samagin, "Optical trap formation with a four-channel liquid crystal light modulator," Journal of Optics 16, 035704 (2014).

1 Introduction

Probable causes for the interest in the optical tweezers applications for the problems of biology and medicine (see reviews [1-3]) can be the unique capabilities of this toolkit, i.e. the possibility of contactless impact on the objects being studied, resulting in a high sterility, the possibility submicrometer precision of displacement control of the biological objects, etc. The sizes of objects that can be effectively trapped by the optical tweezers, range from a few nanometers to hundreds micrometers, and these very sizes are typical of the most biological cells and their organelles. The order of the applied forces, from 10^{-12} to 10^{-9} N, is sufficient for the effective capture and manipulation of biological objects. In view of the diversity of sizes and shapes of biological objects, as well as a wide range of biomedical problems solvable by means of specified tools, the capture and manipulation of biological objects is fulfilled with the aid of not only the point optical traps representing sharply focused Gaussian beams, but also the traps of other configurations. It is important to search the optimal form and parameters of the trap to solve a specific biomedical problem. Thus the traps with the intensity distribution in the form of Crescent are proposed by the authors of [4, 5] for the manipulation of biological microobjects. Such traps can effectively capture objects while acting on their periphery, not the center. This property is important for the maintenance of the functional state of the cells. The corresponding intensity distributions can be formed either through modification of the Gaussian beam or superposition of vortex beams with the use of stationary diffractive optical elements. The contour optical traps (in the form of rings, ellipses and C-shaped) formed with the LC focusing device [6] can also be used to minimize the radiation effects. The advantage of this method for the traps formation is the possibility of real-time control of their shape and size.

The optical traps with the intensity distribution in the form of line segments allow to capture simultaneously several objects, locate them in the required position, sort them by size and refractive index [7-9], move them along the trap [10] and align the elongated objects along the trap [11]. It is obvious that all these capabilities are of interest for biomedical applications. The techniques of generation of traps in the form of a line segment with the use of the LC modulators, in particular multi-pixel modulator HOLOEYE HEO 1080P and a tunable liquid crystal focusing device (4-channel modulator) developed by the authors are discussed in the article. A comparative analysis of the forces occurring in the point trap and the trap in the form of a segment was carried out. The results of experiments on manipulations of microscopic objects with formed traps are set forth below.

2 Methods for the line optical traps generation

The most simple, effective and inexpensive technique of the line optical trap (LOT) generation is that based on the use of a cylindrical lens placed in the path of the beam forming the trap. For the first time this method was proposed by R. Dasgupta et al. in 2003 [12]. The authors realized the rotation of the trapped objects (in particular the bacteria *E.coli*) by means of the lens rotation. Two cylindrical lenses were used for the formation of the LOT with asymmetrical (non-uniform) intensity profile by the authors of [7]. The generated LOT capabilities for the transportation and sorting of colloidal microspheres were demonstrated. As the advantages of the proposed optical tweezers scheme, the simplicity of its implementation and low cost were pointed out. The scheme for the formation of the optical trap in the form of a line segment with the use of two cylindrical lenses was also described in [11]. The LOT dimensions were 1 X 20 μm and it was used for the simultaneous capture of several RBCs and their orientation along the line segment.

The methods for such traps formation through the use of binary diffractive optical elements (DOE) are known [10]. First the corresponding DOE was computed so that the phase changed linearly along the line segment and then it was obtained with the aid of the photolithographic technique on the glass substrate. The authors described the experiments on the polystyrene microspheres (individual and multiple) capture and their further relocation along the generated line segment.

A large number of studies is devoted to the formation of LOTs by means of the laser diode bars [8, 9, 13, 14]. The optical trap in the shape of a line segment was realized with the use of the 1 μm-wide

linear single laser emitters that ranged in length from 25 μm to 1 mm. The authors noticed the technique simplicity, its low cost, possibilities for creating of a long linear trapping area for micromanipulation and easy embedding of diode bars into flowing microfluidic systems. The microparticles sorting in a fluid flow and also the capture of large particles (up to 200 μm-size) were realized with the generated optical trap.

Not only the generation of the light line segment but also its dynamic control can be achieved with the use of spatial light modulators. The typical scheme of the experimental setup for the generation of the dynamical optical traps is presented in Fig.1.

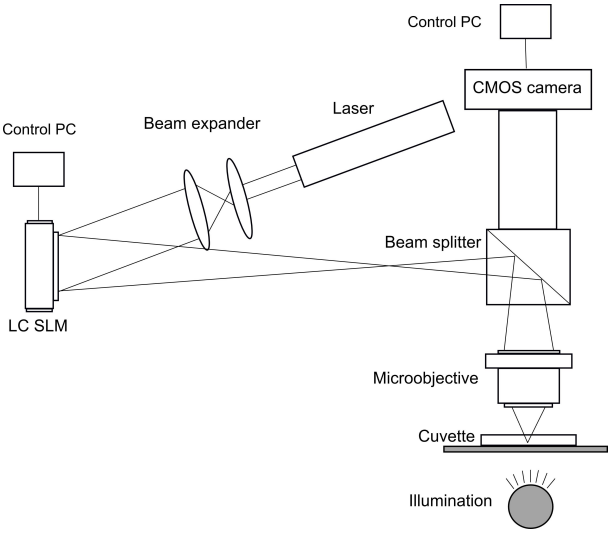


Fig.1 Scheme of optical tweezers with the implemented SLM.

We used a multi-pixel LC SLM HOLOEYE HEO 1080P for the intensity distribution generation in the form of a line segment. The used modulator had 1920 × 1080 addressable pixels and allowed to specify 256 phase gradation of the phase within the range from 0 to 2π. The line segment in the microscope working plane was obtained as a result of the formation of an astigmatic Fresnel lens by the transparency. The segment length could be controlled by the change of the astigmatism value. The transparency was illuminated with a uniform plane wave.

The four-channel LC focusing device can be used for the generation of dynamically controlled line optical traps as an alternative to multi-pixel liquid crystal modulators. In this case the optical scheme presented in Fig.1 can be used. However, the peculiar feature of the LC focusing device is its ability to operate in the transmission regime (note that the reflection regime is also possible if necessary), thus simplifying structurally the scheme of its integration into the manipulator. The principle of the LC focusing device operation was described in detail in [15-17]. The modulator under consideration is the device constructed on the basis of crossed substrates of the cylindrical modal LC lenses joint into the integrated structure. The device had four control contact electrodes and allowed to focus illumination into a point or segment. To focus the light into a segment, it was necessary to determine the voltage distribution with the equipotential lines in the shape of parallel lines. In this case the profiles of the phase delay in the form of the cylindrical lenses surface could be created. The optical transparency with such phase transmission will focus plane wave into light segment which position and orientation can be controlled by means of change of amplitude and/or phase of voltage applied to contacts [17]. The dimension of the generated line segment was determined by the focusing device aperture and parameters of the optical system, providing the input beam entry into the microscope.

It is clear that the LC modulators method for the line optical trap generating is significantly higher in price than the techniques based on the use of cylindrical lenses or laser diode bars. However, the use of the LC modulators widens the scope of opportunities for the formation and dynamic control of optical traps of different types. Besides, the precise mechanical movements of the active element are not required. It should be noted that the use of the 4-channel LC focusing device is considerably low-price as compared with the commercial multi-pixel liquid crystal modulators because of its significantly simpler design and control system. The device is characterized by quite a high energy efficiency and a wide working spectrum range, simplicity of its integration into the manipulator scheme due to the mode of transmission, and also by the ability to form a smooth continuous profile of the phase delay and to smoothly control it. The last-named ability is attainable due to the use of solid electrodes.

The results of the microscopic objects (including biological ones) manipulation experiments, carried out with the use of the generated optical trap are given in Section 4.

3 Analysis of the line optical trap capture force

The optical trap force was estimated experimentally with the use of the so-called drag-force method [18], which was for the first time presented in [3]. The optical trap force can be estimated by the viscous force determined by the formula:

$$F = V \times \beta, \tag{1}$$

where V is the velocity of particle motion in the liquid, β – the coefficient of viscosity. For a spherical particle of the radius r located close to the bottom of the cell, subject to the distance h between the particle center and the cell bottom, β is defined by the Faxen's formula:

$$\beta = \frac{6\pi\eta r}{1 - \frac{9}{16}(\frac{r}{h}) + \frac{1}{8}(\frac{r}{h})^3 - \frac{4}{256}(\frac{r}{h})^4 - \frac{1}{16}(\frac{r}{h})^5},$$

where η is the fluid viscosity.

Thus by measuring the microobjects escape velocity, it is possible to estimate the maximum or escape force of optical trap (the capture force). In our experiments the microobjects relocation in the liquid was attained by means of the microscope stage motion while the particle was held with the optical trap. For this purpose the microscope stage was equipped with stepper motors (SY 35ST26-0284A) and the corresponding actuators with the movement step of 0.15 μm, operated from the computer. The developed software (graphical user interface) allows to control the operation of the stepper motors in real-time from the screen monitor that displays the working field of the microscope. In particular, the system enables to place the cell in its original position for the initial capture of the micro-object and move the stage with the cuvette of samples with a given initial velocity and constant acceleration. Then the image of the operating field and the parameters of the cell moving are recorded in real time in the video file. The subsequent processing of the recorded data allows get the information about the optical trap force.

The experimental dependences of the escape velocity and capture force of the microoobjects on their radius for the line optical trap are shown in Fig. 2 and Fig. 3 respectively. The received dependences are compared with those for the point optical trap. The latex spheres of a certain size were used in these experiments as microobjects. The beam waist radius for the focused point beam and the half-width of the formed line segment in the manipulation plane were 1 μm. The radiation power in the trap was 10 mW.

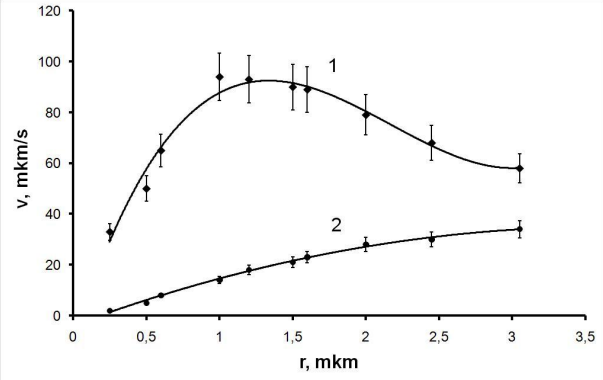


Fig. 2 The dependences of the escape velocity on the microsphere size for the point trap (1) and the LOT (2).

As mentioned above, the traps in the form of light segments are successfully used for the microparticles sorting [7, 9, 13]. The received dependences justify this possibility. Indeed, the analysis of the calculated graphs shows that the trap in the form of a segment allows a wider-range sorting of microparticles and a higher sensitivity to the microparticles size than the point trap. This fact can be explained as follows. The placed in a viscous fluid microbjects are trapped by the LOT. The objects motion in the liquid results in the viscous force appearance. The particles detachment from the trap occurs at the moment when maximal force of the optical trap is equal to the viscous force. Thus the value of the escape velocity is determined by the equilibrium between the optical trap force and the viscous force. The viscous force is increased linearly with the increasing particle size, leading to the velocity decrease. And the behavior of the dependences of the optical trap forces on the particle size differs for the point optical trap and line optical trap as it is seen from Fig. 3. The difference is explained by the fact that in case of the LOT the amount of the light flux intercepted by the particle continuously grows with the increasing of the particle size. And for the point trap the growth of the intercepted light flow is stopped when the particles size becomes equal to the trap size, and consequently the growth of escape velocity is also stopped. Thus for the case of point traps, the extremum appears in the dependence of the escape velocity. So for the case of the point trap, as you can see from Fig. 2, the escaped velocity can be equal for microspheres of different radius. There is no extremum observed in the dependence of the velocity on the particle size in case of line optical trap.

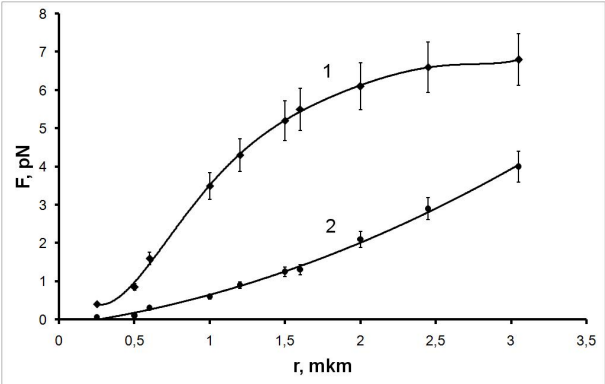


Fig. 3 The dependences of the capture force on the microsphere size for the point trap (1) and the LOT (2).

At the same time, the line-shaped trap provides a higher sensitivity of the capture force to the particle size. This fact is confirmed by both theoretically and experimentally obtained values of the capture forces for the traps in the form of a segment. Note that the calculations are performed in the framework of geometric optics subject to the geometry of the light beam in its waist. The simulations are based on the idea of an impulse flow transferred by the light wave, and the Fresnel formulas for the coefficients of reflection and refraction of light at the interface of two media. The initial field is defined in the plane perpendicular to the beam axis and tangent to the top point of the particles. Its intensity and phase are determined by the evolution of a Gaussian beam during propagation. Further the ray paths are set by the laws of geometrical optics. The diffraction of the laser beam on the microobjects as well as wave interference inside the microparticles are not taken into account during the simulation.

Both the simulated and experimental results for the capture force of the LOT for two values of the particle radius are presented in Table 1. The difference of the

calculated and experimental results is not exceeding 20%.

Table 1. The capture force for the LOT.

r, μm	F, pN (simulated)	F, pN (experimental)
0.6	0.30±0.03	0.24±0.04
1.6	1.30±0.13	1.25±0.18

As you can see from the table the strong dependence of the capture force on the particles size is observed for the LOT. The capture force for the 1.6 μm radius particles by 4-5 times exceeds the capture force for 0.6 μm-radius particles. The obtained results were compared with those for the point optical trap. As shown by simulations, for the case of the point traps the force values are higher, they are 1.6 pN and 5.5 pN for particles with the radius of 0.6 μm and 1.6 μm respectively for the same value of the radiation power in the trap. However, their ratio is less and is about 3.4.

Thus, the optical trap in the form of a segment can effectively capture micro-objects. And our simulations confirm that the sensitivity of the capture forces to the particles size for LOT is somewhat higher than for the point trap. So there is good reason to assert that the line optical traps can be more efficiently used for the micro-objects sorting by their size as compared to the spot traps.

4 The experiments on the microobjects manipulation

4.1 Experiments with the use of SLM HOLOEYE HEO 1080P

The experiments on the LOT-aided manipulation have been carried out by means of the experimental setup presented in Fig.1 with the SLM HOLOEYE HEO 1080P as the LC modulator. A solid-state diode-pumped laser with the emission wavelength of 0.53 μm and maximal output power of 500 mW was used to form the optical traps. The laser beam was directed through an interface collimator onto the LC SLM HOLOEYE HEO 1080P. Then the beam was introduced into the 100x objective of an upgraded microscope XSP-104 and the result was a reduced intensity distribution reproduced in the manipulation plane. In order to visualize the working area of the experiment, an illuminator was placed under the cell with the microscopic objects. The imaging of the experimental procedure was made with the computer-operated ocular digital camera DCM-130. As the microobjects of various diameters (0.9 ÷ 3.2 μm), the latex spheres suspended in water were used. The velocity of the microscope stage relocation was about 5 μm/sec. The particles captured into the beam are held there under the impact of gradient force of light pressure. Since the light segment was placed at the 45^0-angle to the direction of the stage movement, the particles moved along the beam generated and escaped at its edge. Thus, the area "covered" by the light line segment remained free from any particles. The optical force was not sufficient to capture the particles of different size and these particles passed through the optical trap without deflection.

The usability of the LOT as the optical shield for the formation of a pure area in the fluid flow is illustrated by Fig. 4. The 1.2 μm-latex spheres were used for this experiment. The LOT geometry was 18 μm X 1 μm. The black arrows indicate the direction of the particle motion along the line segment (short arrow) and the direction of the LOT movement due to the microscope stage motion (long arrow).

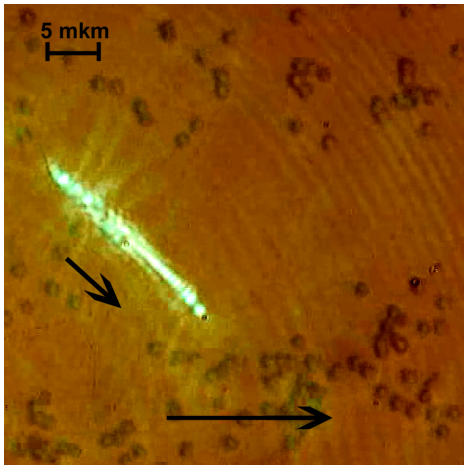


Fig. 4 LOT used as the optical shield for formation of a pure area.

4.2 Experiments with the use of the 4-channel LC focusing device

As already mentioned, the formation of the optical traps with the LC modulators allows to generate the defined intensity distributions and also dynamically control them. This functional property of the trap in the form of a line segment was obtained with the use of the LC focusing device. The solid-state diode-pumped laser and XSP-104-microscope described in paragraph 4.1 were used. The aperture of the focusing device was 1×1 mm^2. The applied voltages changed within the range from 3 to 8 V. The laser beam was directed through the interface collimator onto the LC focusing device where the required light field distribution in the specified plane was formed. Then the beam was introduced into the 100x-objective of the microscope and as a result the reduced intensity distribution was reproduced in the manipulation plane. The line segment in the plane of manipulation in our experiments had the following parameters: 7 μm-length and ~ 0.7 μm-width. The line segment planar orientation was achieved by the proper choice of the amplitude and phase of voltages applied to the focusing device contacts. The voltage generator used in the experiments allowed setting of the voltage amplitude accurate within 0.1 V, and phase – within 6 degrees. Under these conditions the discreteness of specifying the trap rotation angle was 15 degrees. A

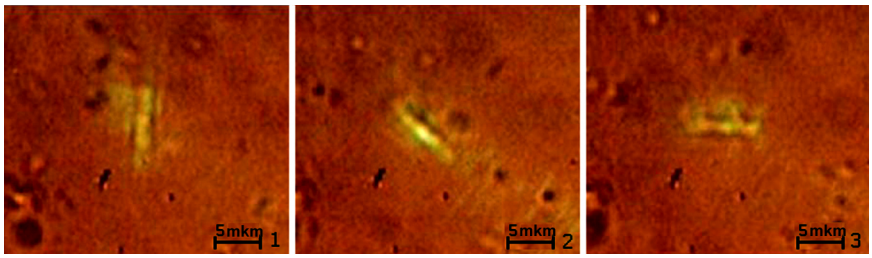


Fig. 5 LOT-aided capture, alignment and the rotation of the *E.coli* bacterium.

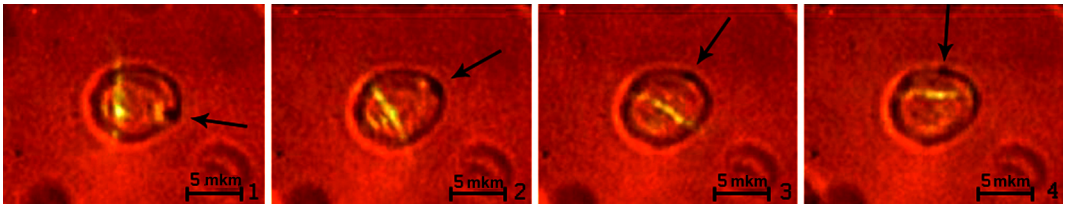


Fig. 6 LOT-aided capture, alignment and rotation of yeast cell.

more detailed description of the LC focusing device operation in this mode can be found in [17, 19].

The experiments with biological microobjects, in particular *E.coli*-bacteria and yeast *Saccharomy cescerevisiae* have been carried out. The yeast cells were previously held at 24^0 C for 13 hours in water. And the process of the *E.coli* preparation was as follows: the *Colibacterin siccum* was suspended in physiological solution, after that the glucose was added to the solution and the obtained mixture was additionally held for 12 hours at 36^0 C. The constant temperature was maintained with the aid of a thermostat.

The frames from the video presented in Fig. 5 and Fig. 6 illustrate the manipulation experiments for the *E.coli* and yeast *Saccharomy cescerevisiae* respectively. In both cases the microobjects were trapped with the LOT and kept in the trap during its rotation. The colibacillus (dark stripe in Fig. 5) having the form of a rod was aligned along the light segment.

The yeast cell size significantly exceeds the width of the light segment. However the rotation of the cell with the trap was obtained. A slight heterogeneity in the cell is marked with a black arrow in Fig. 6. And it is seen that the rotation of the LOT led to the cell rotation.

5 Conclusion

The techniques of the LOT generation with the use of the LC SLM are discussed. The capabilities and advantages of the optical traps of this shape in manipulation experiments have been studied both experimentally and numerically. The experimentally proved capabilities for the formation of a pure area in the fluid flow as well as for the alignment and rotation of biological microobjects afford a basis to talk about the prospects of the LC focusing device use in optical manipulation, including, biomedical applications.

This work was supported by the Ministry of Education and Science of the Russian Federation.

Lung neoplasm diagnostics using Raman spectroscopy and autofluorescence analysis

V.P. Zakharov[1*], I.A. Bratchenko[1], D.N. Artemyev[1], O.O. Myakinin[1], D.V. Kornilin[1], S.V. Kozlov[2], A.A. Moryatov[2]

[1] Laser and biotechnical systems department, Samara State Aerospace University, 34 Moskovskoe Shosse, Samara, 443086, Russia

[2] Oncology Department, Samara State Medical University, 89 Chapaevskaya str., Samara, 443099, Russia

* **e-mail:** zakharov@ssau.ru

Abstract. A method of lung neoplasm diagnostics is proposed based on the combined analysis of Raman and autofluorescence spectra excited by laser beam with the wavelength 785 nm. Such approach allows fast selection of the pathology region followed by differentiation of the neoplasm type. The developed method demonstrated the sensitivity of 90.9% and the specificity of 71.4% in the differentiation of squamous cell carcinoma and adenocarcinoma cases. © 2015 Samara State Aerospace University (SSAU).

Keywords: Raman spectroscopy; autofluorescence; optical diagnostics for medicine; spectroscopy; biological tissue; lung cancer.

Paper #1988 received 2014.12.11; revised manuscript received 2015.01.20; accepted for publication 2015.01.20; published online 2015.03.28.

References

1. P. Boyle, World Cancer Report 2008, International Agency for Research on Cancer, Lyon (2008).
2. C. D. Mathers, and D. Loncar, "Projections of global mortality and burden of disease from 2002 to 2030," PLoS Med 3. e442 (2006).
3. R. J. Friedman, "The diagnostic performance of expert dermatoscopics vs a computer-vision system on small diameters melanomas," Arch Dermatol. 144(4), 476-482 (2008).
4. J. Zhao, H. Lui, D.I. McLean, and H. Zeng, "Real-time Raman spectroscopy for noninvasive in vivo skin analysis and diagnosis," New developments in biomedical engineering 24, 455-474 (2010).
5. Z. Huang, A. McWilliams, H. Lui, D. I. McLean, S. Lam, and H. Zeng, "Near-infrared Raman spectroscopy for optical diagnosis of lung cancer," Int J Cancer. 107(6), 1047-1052 (2003).
6. J. Surmacki, J. Musial, R. Kordek, and H. Abramczyk, "Raman imaging at biological interfaces: Applications in breast cancer diagnosis," Molecular Cancer, 12(1), 48 (2013).
7. P. C. Ashok, B. B. Praveen, N. Bellini, A. Riches, K. Dholakia, and C. S. Herrington, "Multi-modal approach using Raman spectroscopy and optical coherence tomography for the discrimination of colonic adenocarcinoma from normal colon," Biomedical Optics Express 4(10), 2179-2186 (2013).
8. A. Pavićević, S. Glumac, J. Sopta, A. Popović-Bijelić, M. Mojović, and Goran Bačić, "Raman microspectroscopy as a biomarking tool for in vitro diagnosis of cancer: a feasibility study," Croat Med J. 53, 551-557 (2012).
9. J. Zhao, H. Lui, D. I. McLean, and H. Zeng, "Real-time Raman spectroscopy for in vivo skin cancer diagnosis," Cancer Res. 72(10), 2491-2500 (2012).
10. N. Bulgakova, V. Sokolov, L. Telegina, K. Vereshchagin, G. Frank, and V. Chissov, "Study of laser-induced autofluorescence emission spectra from normal and malignant bronchial epithelium," Photonics and Lasers in Medicine 2(2), 93-99 (2013).
11. H. Pahlevaninezhad, A. M. D. Lee, S. Lam, C. MacAulay, and P. M. Lane, "Coregistered autofluorescence-optical coherence tomography imaging of human lung sections," Journal of Biomedical Optics, 19(3), 036022 (2014).

12. M. E. Darvin, N. N. Brandt, and J. Lademann, "Photobleaching as a method of increasing the accuracy in measuring carotenoid concentration in human skin by Raman spectroscopy," Optics and Spectroscopy (English translation of Optika i Spektroskopiya), 109(2), 205-210 (2010).
13. R. O. Duda, P. E. Hart, and D. G. Stork, Pattern Classification, 2nd Edition, Wiley (2000).
14. O. Yusuke, S. Hideyuki, T. Tatsuji, F. Chie, and S. Hidetoshi, "A Discrimination analysis of human lung cancer cells associated with histological type and malignancy using Raman spectroscopy," Journal of Biomedical Optics 15(1), 017009 (2010).
15. J. L. Castro, M. R. Lopez Ramirez, J. F. Arenas, and J. C. Otero, "Vibrational spectra of 3-phenylpropionic acid and L-phenylalanine," Journal of Molecular Structure 887, 744–747 (2005).
16. C. De Silva, K. Czarnecki, and M.D. Ryan, "Visible and resonance Raman spectra of low valent iron porphyrins," Inorganica Chimica Acta 287, 21-26 (1999).
17. C.-H. Chuang, and Y.-T. Chen, "Raman scattering of L-tryptophan enhanced by surface plasmon of silver nanoparticles: vibrational assignment and structural determination," J. Raman Spectrosc. 40, 150–156 (2009).
18. C. Magnon, S. J. Hall, J. Lin, X. Xue, L. Gerber, S. J. Freedland, and P.S. Frenette, "Autonomic Nerve Development Contributes to Prostate Cancer Progression," Science 341(6142), 1236361 (2013).
19. A. F. D'Adamo Jr., and F. M. Yatsu, "Acetate metabolism in the nervous system," Journal of Neurochemistry 13(10), 961–965 (1966).
20. A. Barth, "The infrared absorption of amino acid side chains," Progress in Biophysics & Molecular Biology. 74, 141–173 (2000).
21. P. Kupser, K. Pagel, J. Oomens, N. Polfer, B. Koksch, G. Meijer, and G. von Helden, "Amide-I and -II Vibrations of the Cyclic β-Sheet Model," J. Am. Chem. Soc. 132(6), 2085–2093 (2010).
22. M. Keller, E. M. Kanter, and A. Mahadevan-Jansen, "Raman spectroscopy for cancer diagnosis" Spectroscopy 21(11), 33-41 (2006).
23. I. J. Bigio, and J. R. Mourant, "Optical Biopsy," Encyclopedia of Optical Engineering, 1577-1593 (2003).
24. Y. Freund, and R.E. Schapire, "A Decision-Theoretic Generalization of On-Line Learning and an Application to Boosting," Journal of Computer and System Sciences 55(1), 119-139 (1997).
25. N. Otsu, "A threshold selection method from gray-level histograms," IEEE Trans. Sys. Man. Cyber. 9, 62-66 (1979).

1 Introduction

In recent 20—25 years the number of newly-revealed malignant and benign neoplasms of skin, lung, intestine, and internals significantly increased [1]. According to the prognosis of medical experts, the number of oncological patients will steadily increase [2]. The efficiency indicators in the early diagnostics of malignant neoplasms by general practitioners, in general, remain unsatisfactory, which is due to the complexity of interpreting the clinical differential features of neoplasms at the early stage [3]. The low level of early diagnostics of cancer diseases favours the neoplasm development and, finally, increases the risks of fatal outcome. In order to improve the efficiency of diagnostics, it is necessary to use instrumental methods and means.

One of the convenient methods of noninvasive analysis of neoplasms is Raman spectroscopy (RS). The use of this method for diagnostics of cancer neoplasms was demonstrated by a number of authors in *ex vivo* and *in vivo* studies of skin [4], lung [5], breast [6], intestine [7] and other tissues. Thus, e.g., the authors of Ref. [5] demonstrated high efficiency of Raman scattering method in lung cancer diagnostics; the achieved sensitivity was 94 % and the specificity 92%. However, in the case of mass screening the sensitivity and the specificity of the method are essentially lower, in particular, in the lung studies [8] the accuracy of Raman analysis of neoplasms was only 77%. Similar trend is seen in the studies of other biological tissues, e.g., the skin. In Ref. [9] the achieved sensitivity and specificity are at the level of 91% and 75%, respectively. The low specificity is related to the high variance of Raman scattering intensity peaks depending on the concentration of the tissue biochemical components in different samples and the use of absolute criteria in the methods, proposed in the papers considered above.

To overcome these difficulties, in this paper we propose to complete the method of Raman spectroscopy with the analysis of autofluorescence that inevitably arises under the illumination of the studied tissue with the probing laser radiation. To reduce the effect of spectral characteristics variance in the studies of various biological objects it is reasonable to use the comparative analysis of the autofluorescence and Raman scattering intensity from the tumor and from the adjacent healthy tissue.

Autofluorescence (AF) spectroscopy can be used to detect lung pathologies [10, 11]. It is known that the biological tissues contain fluorescent chromophores: elastin, collagen, and NADH, which contribute to the autofluorescence spectrum, as well as purely absorbing chromophores, such as haemoglobin. As a rule, for AF diagnostics the lasers of UV spectral range (300-400 nm), or those of the visible spectral range (400-650 nm) are used. The choice of these ranges is determined by the position of the basic emission spectra of the tissue chromophores. In this paper we report the analysis of

the possibility to diagnose lung neoplasms using the intrinsic fluorescence, excited by the laser radiation with the wavelength 785 nm.

Simultaneous application of two spectral methods provides the increase of informative features and, therefore, is expected to reduce the number of diagnostic errors, while the comparative spectral analysis will help to allow for the personal specificity of the chemical composition of the tissue under study. Besides that, the analysis of autofluorescence allows the selection of spectral anomaly regions and the fast determination of the neoplasm boundaries.

2 Materials and methods

2.1 Experimental setup

In the present work we used the experimental setup schematically presented in Fig. 1. The main elements of the setup are the following: the thermally stabilised semiconductor laser 1 (LML-785.0RB-04), the optical Raman unit 2 (PBL 785), the spectrograph 3 (Sharmrock SR-303i) with the integrated digital camera (ANDOR DV-420A-OE), and the computer 4. The probing laser radiation with the wavelength 785 nm via the band-pass filter BPF is directed by the mirror M and dichroic reflector DM, and focused by the lens L_2 onto the studied sample. The filter BPF serves to filtering the incident radiation from the Raman components that might be generated in the transmitting fibre. The scattered and autofluorescence radiation is collected by the lens L_2 and directed into the spectrometer 3 via the long-pass filter LPF, aimed at eliminating the laser radiation from the recorded signal. The lenses L_1 and L_2 are used for matching the optical unit 2 with the supplying and the signal optical fibres.

Raman and AF spectra were registered simultaneously with one optical unit 2. The optical unit 2 was located directly above the studied region at the distance of 6-7 mm. The diameter of the laser probing beam was 1 mm. Series of spectra were registered from the neoplasm and the healthy tissue. The obtained data was analysed by comparing with the results of the histologic study. The time of examination of each sample did not exceed 3-5 min. Time of signal registration was chosen to match the AF decrease conditions. Irradiation of tissue samples with exposure times about 2-3 minutes leads to the decreasing in AF level. The decrease in the intensity of AF associated with the effect of tissues photobleaching [12]. At this regard it is important to say that the intensity of tissues Raman bands remains unchanged. Thus such an approach helps to increase signal-to-noise ratio and precisely register a Raman signal.

Selection of the autofluorescence and Raman scattering signals was carried out using the method of polynomial approximation with additional filtration of random noise effects and automatic determination of the polynomial power for the given spectral interval. The polynomial fitting function corresponding to the AF was subtracted from raw acquired spectrum to separate Raman spectrum. The registered signal, which consists of Raman and AF signals, was recorded the spectral interval 800-920 nm (250-1800 cm^{-1}) with the resolution 0.05 nm (1 cm^{-1}) at low level of intrinsic noises. The Raman signal was analysed in the spectral interval 1200-1800 cm^{-1}. The AF signal was analysed in the spectral interval 250-1800 cm^{-1}.

2.2 Tissue samples

In the series of *ex vivo* experiments the spectra were recorded from 46 samples (23 adenocarcinomas, 18 squamous cell carcinomas, and 5 carcinoids). The detailed information about the studied samples, including the information about the patients and the localisation of lung lesions, is presented in Table 1. All samples were obtained after surgical resection in Samara Regional Clinical Oncology Dispensary (SRCOD). The tissue samples were kept in sterile boxes at +4 ± 2 °C and were tested not later than in four hours after the resection. Each tumor examination was accompanied by histologic analysis that determined the final diagnosis.

All patients (12 women and 34 men, all Europeans) that took part in the examination were more than 18 years old, passed the preliminary examination and were prepared for the surgical treatment in the departments of SRCOD. All human tissue samples were studied in correspondence with the protocol affirmed by the Bioethics Committee of Samara State Medical University. The participation in the study was voluntary and accompanied with informed consent.

2.3 Separation of classes in the phase plane

To separate the classes in the phase space formed by the values of the Raman spectral peak intensities the canonical discriminant analysis (DA) was used. The quality of the approach was characterised by its sensitivity and specificity. The DA is capable of flexible change of priority in favour of the sensitivity or, on the contrary, in favour of the specificity. The DA is implemented in most of the widely used mathematical software packages.

In the present paper we use the method of quadratic discriminant analysis (QDA) [13]. In fact, the QDA determines the hyperquadric, the form of which depends upon the degree of dispersion of the experimental results and the centres of gravity of the separated classes. By varying the class priorities one can shift the dividing curve to achieve the required proportion between the sensitivity and specificity.

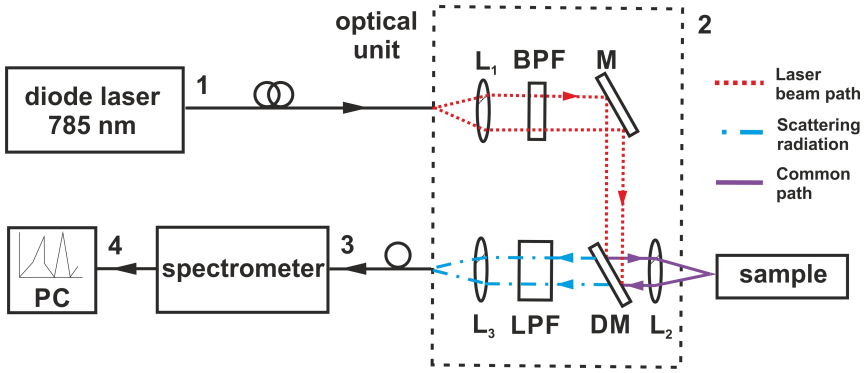


Fig. 1 Optical schematic diagram of the experimental setup.

Table 1 Summary of patients and lesions.

Subjects						Location	
Final lesion diagnosis	Mean age, y (range)	Mean diameter, cm (range)	Male	Female	Number of lesions	Right lung	Left lung
SCC	64 (55–72)	4.5 (2.5–8)	18	-	18	10	8
ADC	63 (42–79)	2,4 (0.2–6)	13	10	23	9	14
Carcinoid	60 (57- 66)	2,1 (0,5-4)	3	2	5	3	2

3 Results and discussion

3.1 Analysis of Raman spectra of lung neoplasms

The characteristic normalised Raman spectra of neoplasms and healthy lung tissue are presented in Fig. 2. The maximum of the Raman spectrum corresponds to the frequency shift by 1450 cm^{-1}. This is the frequency of bending mode (deformation vibration) of the bonds CH_2/CH_3 that occurs in phospholipids and proteins, such as collagen. Alongside with this band, other bands are also confidently recorded, namely, the band at 1210 cm^{1} (stretching vibrations C-C_6H_5 in tryptophan and phenylalanine), 1230 cm^{-1} (stretching asymmetric vibrations of PO_2- in nucleic acids), 1265 cm^{-1} (stretching vibrations of CN, bending vibrations of NH in amid III, α-spirals, collagen, and tryptophan), 1300 cm^{-1} (twisting and wagging CH_2 vibrations in collagen and phospholipids), 1335 cm^{-1} (wagging vibrations of CH_3CH_2 in collagen and nucleic acids), 1520, 1550, 1580 cm^{-1} (stretching vibrations C=C in carotenoids, tryptophan and porphyrin, and phenylalanine, respectively), 1620 cm^{-1} (stretching vibrations C=C in tryptophan and porphyrin), 1660 cm^{-1} (stretching vibrations C=O in amid I, α-spirals and proteins, such as collagen and elastin, stretching vibrations C=C in fats), 1700, 1750 and 1780 cm^{-1} (stretching vibrations C=O in phospholipids) [5, 14-17].

In the *ex vivo* spectra of healthy lung tissue and neoplasms 6 strongest Raman bands were chosen, namely, 1200-1240, 1300-1340, 1440-1460, 1540-1580, 1650-1670, and 1750-1790 cm^{-1}. The normalisation of the spectra was performed using the peak value at 1450 cm^{-1}, having the maximal intensity among the recorded peaks. The band 1750-1790 cm^{-1} has the smallest intensity, and the relative intensity of this peak for the healthy tissue slightly differs from the analogous value in the region of tumor both for adenocarcinoma and for squamous cell carcinoma.

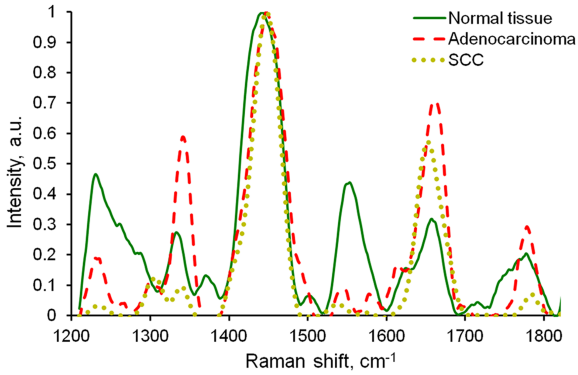


Fig. 2 Normalised *ex vivo* Raman spectra of healthy lung tissue, adenocarcinoma, and squamous cell carcinoma in the region 1200-1800 cm^{-1}.

For the bands 1200-1240 and 1540-1580 cm^{-1} a higher level of intensity is characteristic for healthy tissue in comparison with the adenocarcinoma and squamous cell carcinoma. The intensity value for these bands in healthy tissue can vary from sample to sample, however, its value is always higher than the corresponding spectral intensity of Raman scattering, obtained for a tumor. It is particularly clearly seen for the squamous cell carcinoma, where the signal level only slightly exceeds the level of noise effects. In these bands the vibrations in the following substances are responsible for the appearance of the peak: tryptophan

(1208, 1552, and 1618 cm^{-1}), phenylalanine (1207 and 1606 cm^{-1}), and porphyrin (1552 and 1618 cm^{-1}) [5, 11-14.], which, in turn, is a manifestation of higher content of these substances in healthy tissue as compared to a tumor. This assumption does not agree with the conclusions of Ref. [5] that assume the inverse relative content of the substances in the tumor and in the healthy tissue. The results of recent studies [18] show that the active growth of cancer tumors occurs in the presence of accumulated nerve cells. Particular role in stimulating the growth of cancer neoplasms is played by some receptors of the sympathetic nervous system [18]. Since the functioning of lung is controlled by the vegetative nervous system (the sympathetic nervous system is a part of the vegetative one), the healthy lung tissues adjacent to the tumor region should contain nervous fibres. The nerve cells of the sympathetic system contain such substances as asparagine and glutamine acids that play the role of neuromediators [19]. The Raman spectral bands of asparagine and glutamine acids are located at 1570 cm^{-1} [20] and can be shifted by +60/-40 cm^{-1}. Therefore, the presence of a strong peak at 1550 cm^{-1} in the normal lung tissue may be caused by accumulation of nerve cells near the pathologic region.

The band 1300-1340 cm^{-1} is formed by two RS peaks at 1300 cm^{-1} and 1335 cm^{-1} that arise due to the vibrational links in collagen, phospholipids, and nucleic acids. The signal level for this band essentially decreases when moving from healthy tissue to the region of squamous cell carcinoma, and for adenocarcinoma the signal remains practically unchanged. In the case of adenocarcinoma the relative fraction of this band in the Raman spectrum is greater due to the "transfer" of some part of the signal to the region of the peak at 1365 cm^{-1} (deformation vibrations of COH and OH in polysaccharides) [21]. Waging vibrations of CH_2 and bending vibrations of CH in tryptophan also contribute to this peak [17, 21]. The intensity of the peak at 1335 cm^{-1} for adenocarcinoma increases due to higher concentration of nucleic acids in the tumor [5].

In the lung tissue the vibrations of amid I bonds in proteins having spiral conformation are responsible for the peak at 1650-1670 cm^{-1}. The relative increase of the peak for the tumor tissues can be related to the increase of relative concentrations of protein molecules with β-folded conformations and conformations of random spirals (statistical balls) [5, 21].

Thus, the specific feature of Raman spectrum and the differences in the intensities of individual bands for the tumor as compared to the healthy lung tissue reflect molecular and cellular changes related to the malignant transformation of the tissue. The essential difference of Raman peak intensity in the bands 1300-1340 and 1650-1670 cm^{-1} of the studied samples of tumor and healthy tissue allows the differentiation of the tissue types by means of the Raman spectroscopy. For the determination of the type of the studied tissue the method of phase analysis of intensities in the Raman spectrum of lung tissues is proposed.

3.2 Double-stage phase method of neoplasm diagnostics

Most of the known methods of neoplasm Raman spectra analysis [7, 8, 22] are based on the introduction of threshold characteristics of the peak intensities at 1300-1340, 1640-1680 и 1440-1460 cm^{-1}. The sensitivity and specificity of the methods based on the absolute threshold characteristics rarely exceed 80%.

Our studies allow the formulation and proposal of a different method of neoplasm Raman spectra analysis, the method of calculating phase criteria of assessing malignant neoplasms with respect to other types of biological tissues.

The initially recorded Raman spectra are analysed in two stages. At the first stage two phase characteristics are introduced, namely, the ratio of the scattered intensity I_{1320} in the band 1300-1340 cm^{-1} and I_{1660} in the band 1640-1680 cm^{-1} with respect to the Raman intensity in the band 1440-1460 cm^{-1}. Then each measurement can be presented as a point in the phase plane I_{1320} - I_{1660} (Fig. 3a). Using the histologic study as an etalon, each experimental point in the phase plane can be attributed to a particular type of tumor or healthy tissue. This makes it possible to introduce a method of successful selection of malignant neoplasms in comparison with the spectra of healthy tissue.

At the second stage of diagnostics the changes of Raman scattering intensities in the neoplasm area were considered with respect to the surrounding healthy tissue in the bands k = 1320, 1450, and 1660 cm^{-1}. For this aim the relative values (indices) of the intensity change were introduced as

$$\Delta I_k = \frac{\left| I_k^{(m)} - I_k^{(h)} \right|}{I_k^{(m)} + I_k^{(h)}},$$

where the superscripts m and h correspond to the intensity values in the malignant area and in the healthy tissue. These three indices compose a phase space, in which every point corresponds to one measurement that can be identified basing on the histological study. The projections on three phase planes (the first with axes ΔI_{1320} and ΔI_{1450} , the second with axes ΔI_{1320} and ΔI_{1660}, and the third with axes ΔI_{1450} and ΔI_{1660}) can be directly obtained by the experimental data processing. In *ex vivo* studies of lung neoplasms the analysis of the phase plane with the coordinates ΔI_{1450} and ΔI_{1660} was most informative, which allows the separation of the plane into regions, corresponding to different types of neoplasms (Fig. 3b).

The tracing of changes in Raman spectra of neoplasms in comparison with the spectra of healthy tissue in one patient allows precise evaluation of quantitative changes of the concentration of definite substances (markers) in the neoplasm cells. Such assessment, in turn, makes it possible to divide the studied neoplasms into groups with respect to the concentration of the chosen substances. In analogy with

the first stage, this division is most easily presented in the phase plane.

Figure 3 illustrates the results of the performed studies. To separate the classes in the phase plane, the QDA classifier was used. It is seen that the classes of healthy tissue and those of tumors (adenocarcinoma and squamous cell carcinoma) are well localisable, in spite of some dispersion of the experimental data.

The analysis of Fig. 3a shows that with the use of QDA classifier the sensitivity of lung malignant tumor identification at the first stage amounted to 89.2%, the specificity being equal to 72.9%. However, the first stage of the Raman spectra analysis does not allow the differentiation between the cases of squamous cell carcinoma and adenocarcinoma. In fact, what occurs at the first stage is the separation of malignant neoplasms from benign ones. The second stage (Fig. 3b) allows the separation of the adenocarcinoma cases from those of squamous cell carcinoma and provides the sensitivity value of 90.9% with the specificity of 71.4%.

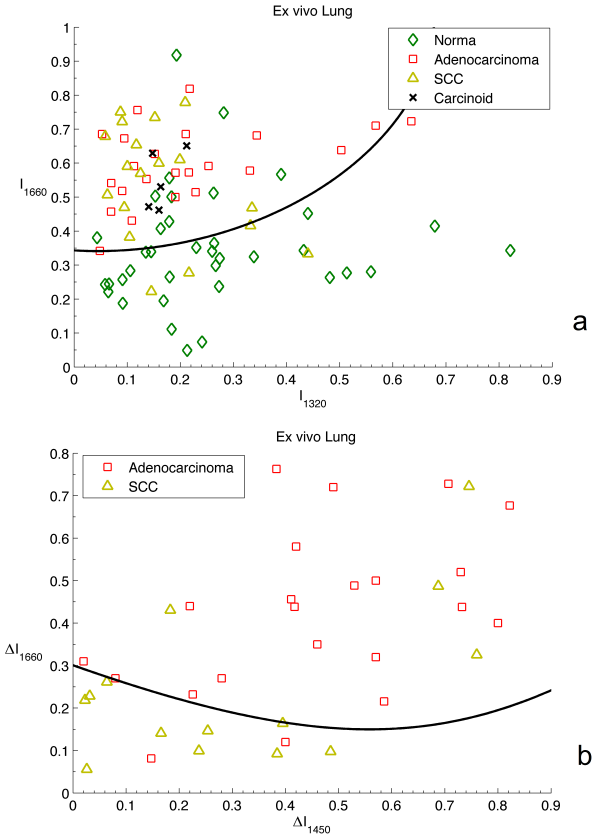


Fig. 3 Classification of lung neoplasm using the double-stage phase method *ex vivo*: a – differentiation of normal and pathological tissue, b – differentiation of adenocarcinoma and squamous cell carcinoma.

It is worth noting, that in Fig. 3a the data for carcinoid cancer of lung are additionally shown. The position in the phase plane allows the definite conclusion that the studied type of a tissue is a malignant neoplasm. However, using only the data of Raman spectral analysis it is impossible to assess its type unambiguously even at the second stage. Probably, the latter is due to the small number of studied carcinoid samples.

One of the ways of further improvement of the diagnostics precision is the use of autofluorescence analysis. The registration of the autofluorescence signal is possible with the times much smaller than those required for the recording the Raman spectra. This fact allows the use of autofluorescence analysis for rapid location of the tumor area by the spectral anomaly of the signal.

3.3 Autofluorescence analysis

In the chosen range the shape of the autofluorescence spectrum is affected by nucleic acids, fats, haemoglobin, and such proteins as elastin, collagen and keratin. [23]. Characteristic autofluorescence spectra of lung neoplasm and normal tissue are presented in Fig. 4. It is seen that the AF spectrum of the lung tissue demonstrates a nonlinear, exponentially decreasing dependence upon the wavelength.

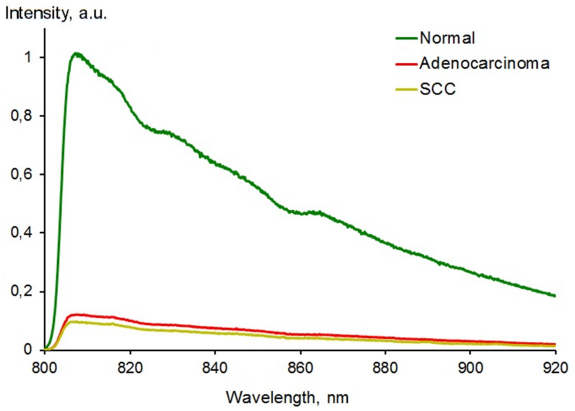


Fig. 4 Typical normalised autofluorescence spectra of lung healthy tissue and neoplasms *ex vivo*.

By the AF intensity the neoplasms are well differentiated from the healthy lung tissue. The AF level in healthy tissue exceeds the intensity of the signal from adenocarcinoma and squamous cell carcinoma by almost an order of magnitude.

Fig. 5 presents the typical averaged AF spectra of squamous cell carcinoma and normal tissue, plotted with the confidence interval. In this figure one can easily select two non-intersecting regions, located far from each other and corresponding to possible intensity values of the spectra of normal and pathological tissues. The maximal spread of the AF intensity produced by a healthy lung is equal to 20%. The spread increase in the intensity values is due to the steady lowering of the AF signal with time under the continuous exposure of the tissue sample to laser radiation. The longer is the exposure of the sample, the weaker becomes the autofluorescence of the tissue corresponding to tissue photobleaching [12].

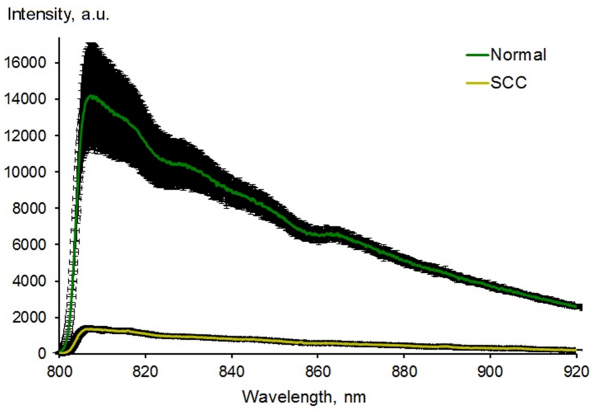


Fig. 5 Typical autofluorescence spectrum of squamous cell carcinoma in comparison with the spectrum of healthy lung tissue.

The AF spectra of four studied carcinoids were by two times smaller in intensity than the mean values of the spectra of adenocarcinoma and squamous cell carcinoma. The AF spectrum intensity of one of the studied samples of carcinoids exceeded the AF value for the normal skin by two times. These data allow the conclusion that using AF analysis one can rapidly reveal the region of spectral anomaly of the tissue, corresponding to the lung oncologic pathology, but without specifying the particular type of the neoplasm.

The characteristic differences in the AF spectra of normal skin and pathologies allow the conclusion that the precision of AF diagnostics of the neoplasm type is smaller than that of Raman spectral analysis. Therefore, using the AF analysis in the IR spectral range solely, it is rather difficult to determine the tumor type reliably. However, the possibility exists to use the AF as an additional method of analysing neoplasms within the complex method of neoplasm type determination together with the analysis of Raman spectrum.

In Ref. [24] it was proved that having N diagnostic methods (classifiers, weak hypotheses) w_i, it is possible to construct the method $w_{N+1}=S$ (strong hypothesis), the efficiency of which will exceed those of the methods w_i. The only necessary condition is that the probability of success for every w_i should exceed 0.5, i.e., should be at least a little better than for random choice from two classes.

One of the autofluorescence analysis application fields can be the fast (the mean acquisition time of AF signal in our experiments was a few tenths of a second) location of tumor boundaries without determination of the neoplasm type. Fig. 6 presents a map of AF from the sample with squamous cell carcinoma of lung, in which the values of the AF intensity are presented at the points, located along the tumor section at the distance 2.5 mm from each other. The calculation of the threshold value in the AF map is performed using the Otsu method [25]. The points 1-5 correspond to the tumor and the points 6-8 to the healthy lung tissue.

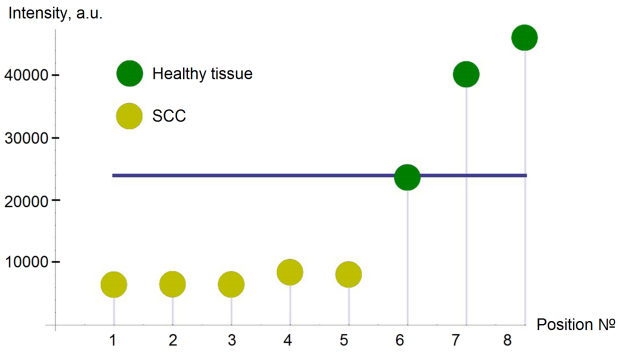


Fig. 6 The AF map of squamous cell carcinoma (SCC) in the healthy lung tissue.

4 Conclusion

The first results of the combined use of Raman spectroscopy and autofluorescence analysis demonstrate high efficiency of the proposed method for the differential diagnostics of lung malignant neoplasms The high sensitivity and speed of performing the study indicate the high potential capabilities of the method.

The efficiency of the proposed double-stage method of Raman diagnostics of lung neoplasms is, upon the average, by 5—10% higher in comparison with other methods of diagnostics [5, 8], based on the analysis of Raman scattering. The method allows not only the detection of the pathology, but also the determination of the particular neoplasm type. It is important that the individual characteristics of the Raman spectrum obtained for the neoplasm and the healthy tissue, are compared in each patient (the second stage of the study). This approach allows individualisation of the neoplasm analysis method. High sensitivity indicators are particularly important in the organisation of mass screening of neoplasms during the preventive examinations, because in this case the method yields no false negative results, and the probability of missing the disease is essentially reduced.

The method of Raman spectroscopy has an advantage in sensitivity and specificity of determination of the particular type of neoplasm, but yields to the AF method in the speed of the signal procession (in our experiments the acquisition of signal during 2-3 minutes at each measurement point was required to reduce the noise effect). The combined use of AF and RS spectroscopy allows fast detection of the pathology presence using the AF determination of its boundary, and the analysis of the neoplasm type can be performed already inside the selected area, using the RS method.

Acknowledgments

This research was supported by the Ministry of Education and Science of the Russian Federation.

OCT/LCT monitoring the drug effect on the human cornea structure *in vivo*

E.A. Genina[1,2]*, A.N. Bashkatov[1,2], I.D. Kamenskikh[3], I.O. Kolbenev[3], T.G. Kamenskikh[3], V.V. Tuchin[1,2,4]

[1] N.G. Chernyshevsky Saratov State University, 83 Astrakhanskaya Str., Saratov, 410012, Russia
[2] Tomsk State University, 36 Prosp. Lenina, Tomsk, 634050, Russia
[3] V.I. Razumovsky Saratov State Medical University, 112 Bolshaya Kazachya Str., Saratov, 410012, Russia
[4] Institute of Precision Mechanics and Control, Russian Academy of Sciences, 24 Rabochaya Str., Saratov, 410028, Russia

* **e-mail:** eagenina@yandex.ru

Abstract. The effect of anti-glaucoma drugs on the structure components of human eye cornea are studied. The eye drops Timolol-AKOS 0.5% and Kosopt were used as the object of study. 10 voluntary patients of the Eye Disease Clinic aged from 70 to 75 suffering from glaucoma took part in the studies. The study of cornea *in vivo* was carried out using the methods of laser scanning confocal tomography (LCT) and optical coherence tomography (OCT) before the application of drugs and at different time moments after the application. The eye cornea thickness values measured using the OCT are presented. From the LCT data the mean diameter of the cornea epithelial cells was calculated. As a result of the complex studies carried out, it was shown that the Timolol-AKOS medication causes the swelling of the cornea within the limits of 5%. Under the use of Kosopt medication the cornea dehydration was observed. © 2015 Samara State Aerospace University (SSAU).

Keywords: glaucoma; cornea; optical coherence tomography; confocal microscopy.

Paper #1989 received 2014.12.17; revised manuscript received 2015.01.21; accepted for publication 2015.01.21; published online 2015.03.28.

References

1. Y. L. Kim, J. T. Walsh Jr., T. K. Goldstick, and M. R. Glucksberg, "Variation of corneal refractive index with hydration," Phys. Med. Biol. 49, 859-868 (2004).
2. K. V. Larin, and M. G. Ghosn, "Optical coherent tomography measurements of the diffusion rate of water and drugs in an isolated and whole cornea," Quantum Electronics 36(12), 1083-1088 (2006).
3. Y. Wu, D. Clarke, A. Mathew, I. Nicoud, and X. Li, "Noninvasive optical coherence tomography monitoring of structure and hydration changes of human corneas in different preservation media," J. Biomed. Opt. 16(2), 026015 (2011).
4. M. G. Ghosn, V. V. Tuchin, and K. V. Larin, "Nondestructive quantification of analyte diffusion in cornea and sclera using optical coherence tomography," Invest. Ophthalmol. & Vis. Sci. 48(6), 2726-2733 (2007).
5. M. Bohnke, and B. R. Masters, "Confocal microscopy of the cornea," Progress in Retinal and Eye Research 18(5), 553-628 (1999).
6. S. E. Avetisov, G. B. Egorova, A. A. Fedorov, and N. V. Bobrovskikh, "Confocal microscopy of cornea. Communication 1. The features of normal morphology pattern," Vestnik oftalmologii 3, 3-5 (2008) (in Russian).
7. I. G. Smetankin, and D. I. Agarkova, "Confocal microscopy and optical coherence tomography in the assessment of anatomy and functional condition of a cornea wound (in vivo) after the phacoemulsification of cataract," Sovremennye tekhnologii v medistine 3, 89-92 (2012) (in Russian).
8. Y. Zhou, K. K. H. Chan, T. Lai, and S. Tang, "Characterizing refractive index and thickness of biological tissues using combined multiphoton microscopy and optical coherence tomography," Biomedical Optics Express 4(1), 38-50 (2013).

9. D. E. Freund, R. L. McCally, and R. A. Farrell, "Effects of fibril orientations on light scattering in the cornea," J. Opt. Soc. Am. A. 3, 1970-1982 (1986).
10. R. A. Farrell, D. E. Freund, and R. L. McCally, "Research on corneal structure," Johns Hopkins Appl. Physics Lab. Techn. Digest. 11(1,2) 191-199 (1990).
11. A. S. Orlova, A. N. Bashkatov, E. A. Genina, I. O. Kolbenev, I. D. Kamenskikh, T. G. Kamenskikh, and V. V. Tuchin, "Influence of 40%-glucose solution on a human corneal structure," Izvestiya Saratov. Universiteta. New ser. Ser. Physics 14(1), 11-19 (2014).

1 Introduction

It is well known that at present glaucoma is one on the main causes of vision loss. The traditional definition of the glaucoma notion incorporates a large group of eye diseases, characterised by permanent or periodic increase of intraocular pressure caused by the disturbed afflux of the aqueous fluid from the eye. The pressure increase results in the development of visual dysfunction, typical for glaucoma, and atrophy with the visual nerve excavation.

The permanent improvement of medicinal preparations and methods of affecting the biological tissue greatly contributes to the struggle for the patients' health, particularly in ophthalmology, and the use of modern optical methods for diagnostics and monitoring the eye disease treatment is now a standard procedure already available in the majority of medical institutions. At the same time, in spite of apparent progress in pharmacology, additional studies of the medication effect on the eye tissue structural elements remain to be an urgent scientific problem, aimed at reducing the possible side effects and increasing the efficiency of the medical treatment procedures.

Optical coherence tomography and confocal microscopy are widely used methods of noninvasive control of the cornea thickness and refractive index, of studying its structural features, and of monitoring the diffusion of drugs into a tissue [1-6]. Combining several visualisation methods allows wider capabilities of diagnosing the structural and optical cornea parameters [7, 8].

The goal of the present paper is to study the short-term effect of anti-glaucoma drugs Timolol-AKOS and Kosopt on the structural components of the human eye cornea at their single topical application.

2 Human eye cornea structure

The cornea plays the key role in the optical system of the eye, provided that it is transparent. The cornea has a multilayer structure. From the outer side it is coated with epithelium, consisting of six cellular layers with the thickness of ~ 40 μm. The basic cornea substance (~90%) consists of transparent connective stroma and squamous cells (keratocytes) occupying 3-5% of the cornea volume. The stroma thickness amounts to ~ 500 μm. From the front and from the behind the stroma is adjacent to two terminal plates. The front plate or the Bowman's layer (~ 10 μm thick) is a derivative of the corneal base substance. It is separated from the outer epithelium by the ~ 0.05 μm thick membrane. The back plate, or the Descemet's membrane, is a derivative of the endothelium that coats the back surface of the cornea and the anterior chamber of the eye. Together with the endothelium, the thickness of the Descemet's membrane amounts to ~ 10 μm [9, 10]. Fig. 1 shows sagittal histological section for light microscopy of normal human cornea.

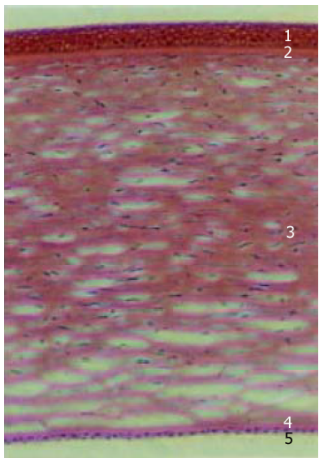


Fig. 1 Sagittal histological section for light microscopy of normal human cornea: 1 is the epithelium layer; 2 is the Bowman's layer; 3 is the stroma; 4 is the Descemet's membrane; 5 is the endothelium layer. Total corneal thickness is 540 μm [5].

3 Materials and methods of the study

The study was carried out in the Clinic of Eye Diseases, V.I. Razumovsky Saratov State Medical University.

The eye drops Timolol-AKOS 0.5% (Sintez, Russia) and Kosopt (MSD, USA and Canada) were used as the studied drugs.

The eye drops Timolol-AKOS 0.5% (1 ml contains 6.8 mg of the active substance timolol maleate and adjuvants, namely, disodium phosphate dodecahydrate, sodium dihydrophosphate monohydrate, disodium edetate dihydrate, sodium chloride, benzalconium chloride, sodium hydroxide, purified water) are an anti-glaucoma drug, a nonselective beta-adrenoblocker. Being topically applied, Timolol reduces the intraocular pressure at the expense of decreasing the aqueous fluid formation and minor increase of its drainage. The pH value of the preparation measured using the universal indicator paper (Likont, Perm) amounted to ~7.

The eye drops Kosopt (1 ml contains the active substances, 22.26 mg of dorzolamide hydrochloride and

6.83 mg of timolol maleate, and the adjuvants, namely, benzalconium chloride, sodium citrate, mannitol, hydroxyethyl cellulose, sodium hydroxide, water for injections) are used to treat the increased intraocular pressure in the cases of open-angle glaucoma and pseudoexfoliative glaucoma. The combined action of active substances leads to more expressed reduction of intraocular pressure at the expense of reducing the secretion of intraocular fluid, probably due to the decreased production of bicarbonate ions, which, in turn, causes the deceleration of sodium and fluid transport. The pH value of the preparation amounts to ~5.

The refractive index values of the medicinal preparations under study, measured using the Abbe refractometer at the wavelength 589 nm, were close to the refractive index of saline (0.09% NaCl) ~1.335.

The study of cornea *in vivo* was carried by means of laser scanning confocal tomography (LCT) using the confocal tomograph Heidelberg Retina Tomograph (HRT-II) with the cornea module Rostok Cornea Module (RCM) (Heidelberg Engineering GmbH, Germany) that allowed layer-specific imaging of the cornea, limb and conjunctive, as well as the epithelium cells counting and intracorneal pachymetry. Optical coherence tomography (OCT) was carried out using the OCT tomograph Topcon 3D OCT-1000 (Topcon, Japan).

The light source used in the LCT system was a diode laser with the wavelength 670 nm. The studied area was 400×400 μm, the image size was 384×384 pixels, the axial resolution was 4 μm and the lateral one was 2 μm. The image recording rate was 30 frames per second. The examination procedure included the topical anaesthesia and the exposure of the contact gel that was applied to the water immersion objective. We used the manual examination regime, and the measurement of cell diameters was semiautomatic. Fig. 2 presents the image of the human eye corneal epithelium, obtained using the confocal retinal tomograph.

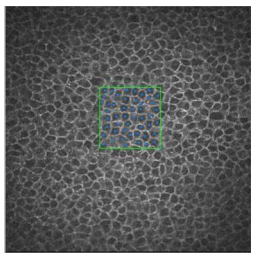


Fig. 2 Image of human eye cornea epithelium obtained by means of confocal microscopy. In the image centre the area in which the cells are counted is selected.

In the OCT tomograph the light source was a superluminescent diode with the wavelength 840 nm. The optical power at the cornea surface was 650 μW with the frequency 6.5 Hz, the axial resolution 6 μm, and the lateral resolution 20 μm.

Ten volunteers of the Clinic of Eye Diseases aged from 70 to 75 suffering from glaucoma took part in the investigations. The patients were randomly divided into two groups 5 persons in each. One of the groups was treated with Timolol-AKOS and the other one with Kosopt. The drugs were dropped into both eyes.

The OCT/LCT studies were performed before the application of the drugs and in 30-40 minutes after the application. After each measurement the mean diameter of the cornea epithelial cells were calculated from the LCT data. (Fig. 2). From the OCT data the mean cornea thickness was calculated for every group (Fig. 3). The mean diameter of the cornea epithelial cells and the mean cornea thickness were measured with built-in software of the used devices.

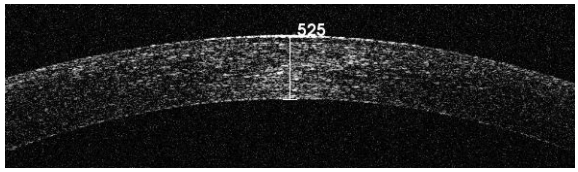


Fig. 3 Image of the human eye cornea cross section obtained by means of the optical coherence tomography. The figures indicate the cornea thickness in μm.

The comparison was carried out using the Student's test between the initial value of the studied parameter averaged over the group and its posterior values at the moment of registration also averaged over the group. The differences were considered to be statistically significant in the case when the value of the parameter p was smaller than 0.05.

4 Results and discussion

Fig. 4 shows the values of the cornea thickness at the initial moment and at different periods after the application of the studied preparations. It is well seen that Timolol-AKOS causes short-time swelling of the tissue; the cornea thickness has first grown by 3% upon the average during 20 minutes of observation and then began to decrease. Kosopt causes the reduction of the cornea thickness by 5% upon the average during 30 minutes of observation.

Fig. 5 presents the effect of the studied drugs on the size of cornea epithelium cells. Both Timolol-AKOS and Kosopt increase the cell diameter by 5% (in 40 min) and 1% (in 30 min), respectively.

The statistical analysis of the studied parameters has shown that the increase of the mean cornea thickness in 20 minutes after the application of Timolol-AKOS in comparison with the initial values is statistically significant. The increase of the epithelial cells diameter during the same period of time is statistically significant as well.

The comparison of the mean cornea thickness at the initial moment of time and in 30 minutes after the application of Kosopt has demonstrated statistical significance of the difference. However, the variations of the epithelial cell diameter appeared to be insignificant, so that it is possible to conclude that this

preparation does not essentially affect the cornea epithelial cells.

From the experimental data presented above it is seen that the anti-glaucoma preparations Timolol-AKOS and Kosopt, executing their main function of reducing the intraocular pressure by decreasing the amount of the produced intraocular fluid, affect the eye cornea in a slightly different way. Thus, Timolol-AKOS causes the cornea swelling, while after the use of Kosopt the cornea thickness decreases. Besides the different composition of the drugs (side effect of timolol maleate is edema of the corneal epithelium), this effect may be explained by the different pH values of the solutions. The experiments with the rabbit cornea *in vitro* described earlier in Ref. [11] demonstrated that the hydration degree of the cornea decreases and reaches its minimum in 20 minutes after putting the tissue sample into the buffer solution with pH = 5. From Fig. 4 it is seen that Kosopt having pH ~5, causes the reduction of the cornea thickness, while Timolol-AKOS having pH ~7 causes the tissue swelling.

5 Conclusion

As a result of the performed complex studies of the effect of anti-glaucoma drugs on the condition of the cornea using the optical coherence tomography and laser confocal tomography it was shown that the preparation Timolol-AKOS 0.5% causes the cornea swelling within the limits of 5%, which also affects the increase of the epithelial cells diameter. On the contrary, the use of Kosopt leads to the observable cornea dehydration.

The work was carried out within the frameworks of the Programme for Increasing the Competitive Ability of Tomsk State University and under the partial support from the President of Russia, grant “Leading Scientific Schools” No. 1177.2012.2.

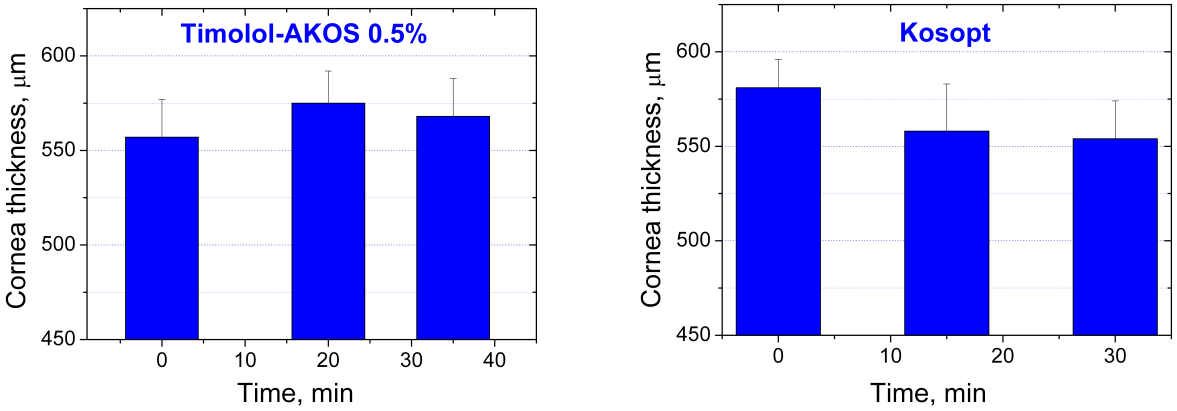


Fig. 4 Human eye cornea thickness *in vivo* at different time moments under the action of the studied drugs.

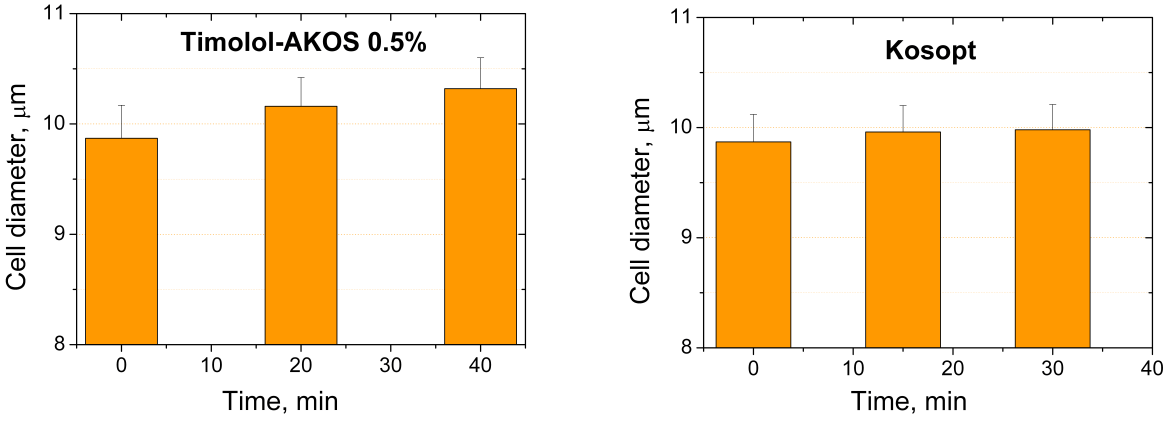


Fig. 5 Human eye cornea epithelium cell diameter *in vivo* in different periods of the action of the studied drugs.

A pulsed photoacoustic technique for studying red blood cell sedimentation

M. Kinnunen
Optoelectronics and Measurement Techniques Laboratory, University of Oulu, Erkki Koiso-Kanttilan katu 3, P.O. BOX 4500, 90014, Finland

e-mail: matti.kinnunen@ee.oulu.fi

Abstract. This study shows the capability of a pulsed photoacoustic (PA) technique to measure red blood cell sedimentation and aggregation processes in vitro. Red blood cells are the main source of absorption in blood. The PA signal is proportional to the sample's optical absorption coefficient, and hence, dynamic changes in the sample can be monitored by analyzing the PA pulse amplitude and pulse arrival time. Optical coherence tomography (OCT) is used as a parallel method for comparison. Diluted whole blood and different concentrations of washed red blood cells were used as samples. The pulsed PA technique is suitable for monitoring changes in sedimentation velocity when dextran is added to the sample. When the measurement section with the fastest sedimentation rate was selected for analysis, a more than 10-fold increase in the sedimentation rate, induced by dextran, was found with both the PA and OCT techniques. The PA pulse delay was found to be a more reliable measure of changes in the sample than the PA signal amplitude. © 2015 Samara State Aerospace University (SSAU).

Keywords: blood sedimentation; red blood cell aggregation; dextran; pulsed photoacoustic technique; optical coherence tomography.

Paper #1990 received 2014.11.22; revised manuscript received 2015.01.20; accepted for publication 2015.01.20; published online 2015.03.28.

References

1. S. E. Bedell, and B. T. Bush, "Erythrocyte sedimentation rate. From folklore to facts," Am. J. Med. 78, 1001-1009 (1985).
2. T. L. Fabry, "Mechanism of erythrocyte aggregation and sedimentation," Blood 70(5), 1572-1576 (1987).
3. A. V. Priezzhev, N. F. Nikolai, and J. Lademann, "Light backscattering diagnostics of red blood cell aggregation in whole blood samples," Chapter 11 in Handbook of optical biomedical diagnostics, Tuchin V. V. Ed., SPIE Press, Bellingham (2002).
4. B. Neu, R. Wendy, and H. J. Meiselman, "Effects of dextran molecular weight on red blood cell aggregation," Biophys. J. 95, 3059-3065 (2008).
5. A. Westergren, "Studies of the suspension stability of the blood in pulmonary tuberculosis," Acta Medica Scandinavica 54, 247–282 (1921).
6. L. E. Böttiger, and C. A. Svedberg, "Normal erythrocyte sedimentation rate and age," Brit. Med. J. 2, 85-87 (1967).
7. M. L. Bridgen, "Clinical utility of the erythrocyte sedimentation rate," Am. Fam. Physician 60(5), 1443-1450 (1999).
8. J. M. Jou, S. M. Lewis, C. Briggs, S.-H. Lee, B. de la Salle, and S. McFadden, "ICSH review of the measurement of the erythrocyte sedimentation rate," Int. Jnl. Lab. Hem. 33, 125-132 (2011).
9. A. V. Priezzhev, O. M. Ryaboshapka, N. N. Firsov, and I. V. Sirko, "Aggregation and disaggregation of erythrocytes in whole blood: study by backscattering technique," J. Biomed. Opt. 4(1), 76-84 (1999).
10. C. V. L. Pop, and S. Neamtu, "Aggregation of red blood cells in suspension: study by light-scattering technique at small angles," J. Biomed. Opt. 13(4), 041308 (2008).

11. X. Xu, L. Yu, and Z. Chen, "Velocity variation assessment of red blood cell aggregation with spectral domain Doppler optical coherence tomography," Ann. Biomed. Eng. 38, 3210-3217 (2010).
12. F. T. H. Yu, and G. Cloutier, "Experimental ultrasound characterization of red blood cell aggregation using the structure factor size estimator (SFSE)," J. Acoust. Soc. Am. 122, 645-656 (2007).
13. E. Franceschini, F. T. H. Yu, F. Destrempes, and G. Cloutier, "Ultrasound characterization of red blood cell aggregation with interventing attenuation tissue mimicking phantoms using structure factor size and attenuation estimator," J. Acoustic Soc. Am. 127, 1104-1115 (2010).
14. S. J. Lee, H. Ha, and K.-H. Nam, "Measurement of red blood cell aggregation using X-ray phase contrast imaging," Opt. Express 18, 26052-26061 (2010).
15. Z. Zhao, X. Wang, and J. F. Stoltz, "Comparision of three optical methods to study erythrocyte aggregation," Clinical Hemorheology and Microcirculation 21, 297-302 (1999).
16. M. R. Hardeman, J. G. G. Dobbe, and C. Ince, "The laser-assisted optical rotational cell analyzer (LORCA) as red blood cell aggregometer," Clinical Hemorheology and Microcirculation 25, 1-11 (2001).
17. I. Y. Kuo, and K. K. Shung, "High frequency ultrasonic backscatter from erythrocyte suspension," IEEE Trans. Biomed. Eng. 41(1), 29-34 (1994).
18. M. S. van der Heiden, M. G. M. de Kroon, N. Bom, and C. Borst, "Ultrasound backscatter at 30 MHz from human blood: influence of rouleau size affected by blood modification and shear rate," Ultrasound in Med. & Biol. 21(6), 817-826 (1995).
19. A. A. Oraevsky, S. L. Jacques, F. K. Tittel, "Measurement of tissue optical properties by time-resolved detection of laser-induced transient stress," Appl. Opt. 36, 402-415 (1997).
20. J. S. Antoniow, J. Egèe, M. Chirtoc, C. Bissieux, and G. Potron, "Real time analysis of erythrocyte sedimentation by photothermal methods," Journal de Physique IV, CT-469 – C7-472 (1994).
21. A. Landa, and J. J. Alvarado-Gil, "Photoacoustic monitoring of real time blood and hemolymph sedimentation," Rev. Sci. Instrum. 74(1), 377-379 (2003).
22. P. Helander, and I. Lundström, "Whole blood – a sedimenting sample studied by photoacoustic spectroscopy," J. Photoacoust. 1(2), 203-215 (1982).
23. S. Oka, "A physical theory of erythrocyte sedimentation," Biorheology 22, 315-321 (1985).
24. E. I. Galanzha, and V. P. Zharov, "In vivo photoacoustic and photothermal cytometry for monitoring multiple blood rheology parameters," Cytometry Part A 79 A, 746-757 (2011).
25. H. Schmid-Schönbein, H. Malotta, and F. Striesow, "Erythrocyte aggregation: causes, consequence and methods of assessment," J. Netherlands Soc. Clin. Chem. 15, 88-97 (1990).
26. J. K. Armstrong, R. B. Wendy, H. J. Meiselman, and T. C. Fisher, "The hydrodynamic radii of macromolecules and their effect on red blood cell aggregation," Biophys. J. 87, 4259-4270 (2004).
27. X. Xu, R. K. Wang, J. B. Elder, and V. V. Tuchin, "Effect of dextran-induced changes in refractive index and aggregation on optical properties of whole blood," Phys. Med. Biol. 48, 1205-1221 (2003).
28. V. V. Tuchin, X. Xu, and R. K. Wang, "Dynamic optical coherence tomography in studies of optical clearing, sedimentation, and aggregation of immersed blood," Appl. Opt. 41(1), 258-271 (2002).
29. V. V. Tuchin, R. K. Wang, E. I. Galanzha, J. B. Elder, and D. M. Zhestkov, "Monitoring of glycated hemoglobin by OCT measurements of refractive index," Proc. SPIE 5316, 66-77 (2004).
30. X. Xu, V. V. Tuchin, and R. K. Wang, "Immersion technique as a tool for in depth OCT imaging trough human blood and body's interior tissues," Proc. SPIE 4251, 89-96 (2001).
31. V. V. Tuchin, R. K. Wang, and X. Xu, "Whole blood and RBC sedimentation and aggregation study using OCT," Proc. SPIE 4263, 143-149 (2001).
32. X. Xu, L. Yu, and Z. Chen, "Effect of erythrocyte aggregation on hematocrit measurement using spectral-domain optical coherence tomography," IEEE Trans. Biomed. Eng. 55(12), 2753-2758 (2008).
33. V. V. Tuchin, Optical clearing of tissues and blood, SPIE press, Washington, Bellingham, USA, 2006.
34. M. Yu Kirillin, A. V. Priezzhev, V. V. Tuchin, R. K. Wang, and R. Myllylä, "Effect of red blood cell aggregation and sedimentation on optical coherence tomography signals from blood samples," J. Phys. D: Appl. Phys. 38, 2582-2589 (2005).
35. V. V. Tuchin, D. M. Zhestkov, A. N. Bashkatov, and E. A. Genina, "Theoretical study of immersion optical clearing of blood in vessels at local hemolysis," Opt. Express 12(13), 2966-2971 (2004).
36. C. Li, and L. V. Wang, "Photoacoustic tomography and sensing in biomedicine," Phys. Med. Biol. 54, R59-R97 (2009).
37. J. Laufer, C. Elwell, D. Delpy, and P. Beard, "In vitro measurements of absolute blood oxygen saturation using pulsed near-infrared photoacoustic spectroscopy: accuracy and resolution," Phys. Med. Biol. 50, 4409-4428 (2005).
38. J. Laufer, D. Delpy, C. Elwell, and P. Beard, "Quantitative spatially resolved measurement of tissue chromophore concentrations using photoacoustic spectroscopy: application to the measurement of blood oxygenation and haemoglobin concentration," Phys. Med. Biol. 52, 141-168 (2007).

39. R. K. Saha, and M. C. Kolios, "A simulation study on photoacoustic signals from red blood cells," J. Acoust. Soc. Am. 129(5), 2935-2943 (2011).
40. E. Hysi, R. K. Saha and M. C. Kolios, "On the potential of using photoacoustic spectroscopy to monitor red blood cell aggregation," Proc. SPIE 8222, 82220Q (2012).
41. G. Barshtein, I. Tamir, and S. Yedgar, "Red blood cell rouleaux formation in dextran solution: dependence on polymer conformation," Eur. Biophys. J. 27, 177-181 (1998).
42. M. Kinnunen, and R. Myllylä, "Application of optical coherence tomography, pulsed photoacoustic technique and time-of-flight technique to detect changes in the scattering properties of a tissue-simulating phantom," J. Biomed. Opt. 13(2), 024005 (2008).
43. G. J. Diebold, and T. Sun, "Properties of photoacoustic waves in one, two, and three dimensions," Acustica 80, 339-351 (1994).
44. M. Kinnunen, "Monitoring the effect of dextran on blood sedimentation using a pulsed photoacoustic technique," Proc. SPIE 8222, 82221E (2012).
45. F. A. Duck, Physical properties of tissue: a comprehensive reference book, Academic Press Inc., San Diego (1990).
46. M. Meinke, G. Müller, J. Helfmann, and M. Friebel, "Optical properties of platelets and blood plasma and their influence on the optical behavior of whole blood in the visible to near infrared wavelength range," J. Biomed. Opt. 12(1), 014024 (2007).
47. A. B. Karpiouk, S. R. Aglyamov, S. Mallidi, J. Shah, W. G. Scott, J. M. Rubin, and S. Y. Emelianov, "Combined ultrasound and photoacoustic imaging to detect and stage deep vein thrombosis: phantom and ex vivo studies," J. Biomed. Opt. 13(5), 054061 (2008).
48. R. D. Eastham, "The erythrocyte sedimentation rate and the plasma viscosity," J. Clin. Path. 7, 164-167 (1954).
49. S. Kim, S. Yang, and D. Lim, "Effect of dextran on rheological properties of rat blood," J. Mech. Sci. Technol. 23, 868-873 (2009).
50. M. Kinnunen, Z. Zhao, and R. Myllylä, "Glucose-induced changes in the optical properties of Intralipid," Opt. Spectrosc. 101(1), 54-59 (2006).
51. B. E. Treeby, E. Z. Zhang, A. S. Thomas, and B. T. Cox, "Measurement of the ultrasound attenuation and dispersion in whole human blood and its components from 0-70 MHz," Ultrasound in Med. & Biol. 37(2), 289-300 (2011).
52. H.-J. Lim, Y.-J. Lee, J.-H. Nam, S. Chung, and S. Shin, "Temperature-dependent threshold shear stress of red blood cell aggregation," J. Biomech. 43, 546-550 (2010).
53. D. J. Faber, F. J. van der Meer, M. C. G. Aalders, and T. G. van Leeuwen, "Quantitative measurement of attenuation coefficients of weakly scattering media using optical coherence tomography," Opt. Express 12(19), 4353-4365 (2004).
54. Z. Zhao, S. Nissilä, O. Ahola, and R. Myllylä, "Production and detection theory of pulsed photoacoustic wave with maximum amplitude and minimum distortion in absorbing liquid," IEEE Trans. Instrum. Meas. 47(2), 578-583 (1998).

1 Introduction

Red blood cell sedimentation velocity, also called erythrocyte sedimentation rate (ESR), is an indicator in clinical diagnosis and an auxiliary method for indicating possible underlying disease [1-4]. The initial method for measuring ESR in test tubes was described by Westergren [5]. The analysis of the results is not very straightforward. There are variations in the ESR values of healthy controls [6] and the ESR value may be affected by several factors in different diseases [7]. However, ESR measurement is still used as a test to screen and monitor disease processes that affect plasma proteins and the ESR value [8]. The RBC aggregation process can be altered in the case of a disease compared with healthy controls [9], which also affects the ESR value.

In vitro methods of diagnosing red blood cell aggregation include both optical and acoustical techniques, namely, backscattering optical radiation [9], small-angle light scattering [10], optical coherence tomography (OCT) [11], and ultrasonic backscattering [12,13]. Also other methods can be found in literature, e.g. X-ray phase contrast imaging [14]. Optical methods are based on light scattering and detection of changes in the scattered signals. Both backscattering and transmitted light can be measured [15,16]. They are also sensitive to changes in the refractive index. Commercial instruments facilitate laboratory analysis [15]. In the ultrasound method [12], measurement of backscattered power is dependent on the scatterer concentration. This scatterer density is high in blood, and therefore it makes ultrasonic blood characterization difficult. A nonlinear relationship has been found between backscattering power and scatterer concentration in an extremely dense medium (such as blood) [17]. Backscattering is dependent on an acoustic impedance mismatch between the tissue and cell components [12]. In blood, this means the acoustic impedance difference between RBCs and the surrounding medium. More specifically, it is

related to hemoglobin concentration inside and outside of RBCs [18].

Illuminating a sample with short laser pulses can result in generation of acoustic waves that travel through the examined medium. The sample's optical absorption at a certain wavelength will affect the strength of the acoustic signal. Other parameters affecting the signal are the volume expansion coefficient and specific heat capacity. The PA signal generation principle differs from the ultrasonic backscattering technique, and different problems are associated with that technique than with the ultrasonic technique [19]. Earlier papers on monitoring blood sedimentation with photoacoustic and photothermal methods have used chopped light and phase-sensitive detection [20-22]. Both amplitude and phase have been analyzed. These parameters tell about the sample's properties during the sedimentation process [20-22]. Helander et al. [22] found that a lower initial RBC concentration gave a higher final amplitude value, probably due to the more closely packed structure of the RBCs at the bottom of the cuvette at the end of the experiment. Different theoretical models have been developed to understand the physics behind the sedimentation process [2,20,23]. Earlier PA studies on blood sedimentation were focused on understanding the dynamics of sedimentation and modeling the process [20-23]. On the other hand, blood rheology *in vivo* can be studied, e.g. by photoacoustic flow cytometry (PAFC), where rheological processes can be monitored at a single RBC level [24]. Several blood parameters, such as blood viscosity, hematocrit, and RBC aggregation affect kinetic and flow properties *in vivo* [24].

Non-specific adsorption of aggregating plasma proteins on the surfaces of RBCs will induce RBC aggregation [9,25,26]. RBC aggregation can also be induced with dextrans [4,26]. The OCT technique for characterizing blood sedimentation has been studied extensively during the last ten years. In addition, different biocompatible agents, such as dextrans, have been used to study optical clearing to enhance OCT imaging depth and light penetration [27-33]. Also, theoretical models have been developed to understand optical methods in more detail [34], as well as blood optical clearing induced by local hemolysis [35].

Recent increased utilization of the PA technique in imaging and sensing applications [19,36-38] has also raised interest towards *in vitro* diagnostics of blood aggregation properties with the PA method [39,40]. Saha *et al.* performed Monte Carlo simulations to study the effect of RBC aggregation on the PA signal [39], whereas Hysi *et al.* used a pulsed laser to induce PA waves in the sample and used the acoustic frequency spectrum to analyze RBC aggregation [40]. Galanzha and Zharov have done valuable work in the field of PAFC and blood diagnostics *in vitro* and *in vivo* [24].

The aim of this work was to explore the capability of the pulsed photoacoustic (PA) technique to monitor dextran-induced changes in the sedimentation rate in diluted whole blood as well as washed RBC samples with different hematocrit values. Here it is shown that it is possible to monitor the sedimentation process with PA pulse delays generated by absorbing optical pulses in the moving blood layer. OCT is used as a parallel method to enhance understanding of the changes in the RBC samples during the experiments. The results are discussed in relation to data found in literature which have been obtained with optical methods.

2 Materials and Methods

2.1 Sample preparation

Blood samples were taken from a healthy volunteer (male, 33 years). EDTA was used to prevent coagulation. Table 1 presents the ingredients of the different samples. Samples 1–4 were prepared by diluting whole blood with PBS (Thermo Scientific, HyClone Laboratories, Inc., Utah, USA). Samples 5–8 were prepared by diluting RBC mass with the same PBS. RBCs were separated from the whole blood with a centrifuge and washed with PBS (two times 10 min at 2000 rpm). Dextran T500 (Pharmacia Fine Chemicals AB, Uppsala, Sweden, molecular weight ~500000) was used in the experiments to induce RBC aggregation. When washed RBCs were used, also bovine serum albumin (Sigma Chemicals CO., St. Louis, MO, USA) with a concentration of 1.0 g/dl (1 % albumin concentration was taken from Ref. 41) was used. The experiments were repeated on two separate days with two different sets of samples (denoted as sample (1–8)_1 and sample (1–8)_2).

Table 1 Samples with different analytes.

No.	Sample	Dextran (g/dl)	Albumin (g/dl)	Hct (%)
1	diluted blood	0	0	31
2	diluted blood	0.5	0	31
3	diluted blood	0	0	21
4	diluted blood	0.5	0	21
5	washed RBCs	0	0	27
6	washed RBCs	0.5	1.0	27
7	washed RBCs	0	0	18
8	washed RBCs	0.5	1.0	18

2.2. Measurement setup

Fig. 1 shows a schematic diagram of a measurement setup. A diode-pumped solid state Nd:YAG laser with a passive Q-switched crystal (model LCS-DTL-324QT) at a wavelength of 1064 nm was used in the measurements. The pulse repetition rate of the laser was 500 Hz and the pulse length was < 10 ns. The pulse energy was ≈ 106 μJ before entering the optical fiber. The optical pulse was slightly focused on the sample surface after the fiber to form a spot with a diameter of

~2 mm. A photoacoustic transducer with a center frequency of 1 MHz (Panametrics V103) was used to detect acoustic signals. The signals were amplified with a preamplifier (Olympus 5662) and the data were collected with a data acquisition card (National Instruments, PCI-5124). A sampling frequency of 20 MHz was used and the signals were averaged 500 times. A cuvette was made of grey PVC (polyvinyl chloride) plastic material. The cuvette dimensions were: thickness 5 mm, width 25 mm, length 40 mm, the total volume being 5 ml. The acoustic transducer was placed under the cuvette at a 5 mm distance from the sample. A 1-mm-thick glass plate was used on the upper side of the cuvette.

Optical coherence tomography was used to monitor blood sedimentation simultaneously with the PA experiment. A commercial OCT device (manufactured by the Institute of Applied Physics, Nizhny Novgorod, Russia) was used. The wavelength of the light source was 910 nm, axial resolution in air < 10 μm, and spatial resolution < 10 μm for 1-x magnification. The details of the device are described elsewhere [42].

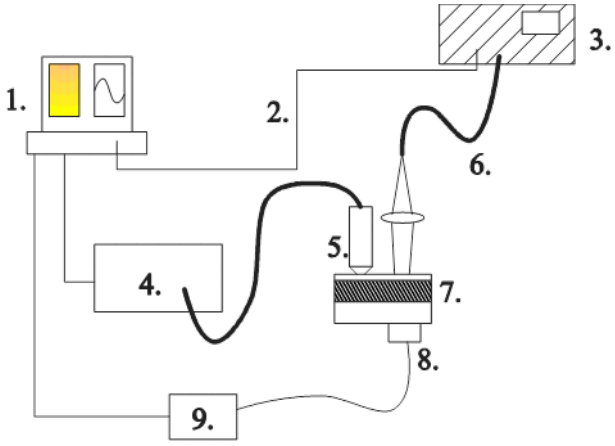


Fig. 1 Measurement setup. 1. Computer with data acquisition card and software, 2. Cable for triggering, 3. Laser source, 4. OCT device, 5. OCT probe, 6. Optical fiber illumination with laser pulses, 7. Cuvette with sample, 8. Pietzoelectric transducer, 9. Preamplifier.

2.3 Measurement protocol

Samples were prepared right before the measurements. The samples were prepared and the measurements were taken at room temperature. Blood and washed red blood cells were diluted to the final concentration and the sample was carefully mixed. The samples were loaded onto the cuvette and the PA and OCT measurements were started immediately. The PA signal waveform was saved on the computer at time points 0, 2, 4, 6, 8, 10, 15, 20, 25, and 30 minutes. In four cases out of 16 measurements the experiment was stopped earlier than at 30 min due to the fast sedimentation process. The time delay of the pulse peak as well as the pulse amplitude values were extracted from the wave shapes. The OCT signal was recorded during the same period for further analysis. To visualize the sedimentation process, only a-scans were registered from a single point as a function of time (see Fig. 3). Fifty a-scans were averaged for samples without dextran and five a-scans for samples with dextran. Different averaging was used because sedimentation kinetics varied considerably between the different samples. The image dimensions were 2500 x 500 pixels, corresponding to 550 μm x 1931 μm.

2.4. Signal analysis

The amplitude of the PA signal is proportional to the optical absorption coefficient μ_a and the Grüneisen parameter Γ, which is defined by $\beta v^2/C_P$. Eq. (1) shows this relation:

$$\Delta P = \rho v^2 \cdot \beta \Delta T = \left(\frac{\beta v^2}{C_P}\right) \cdot \left(\frac{E_a}{V}\right) = \Gamma H_f \mu_a, \qquad (1)$$

where E_a/V is the absorbed optical energy density that equals the product of laser fluence H_f and the sample's optical absorption coefficient μ_a. β is the volume expansion coefficient, C_p is specific heat at constant pressure, and v is the velocity of acoustic waves in the medium [43]. Hence, all these parameters take part in acoustic pulse generation. The photo-induced pressure rise ΔP propagates outside the irradiated volume in the form of an acoustic wave. It is worth noting that Γ is sensitive to temperature, and temperature changes can affect the measurements [19,36].

Fig. 2(a) shows examples of the PA pulse profiles from one experiment. The pulse amplitude generated in the sample (A1), the time delay (Δt), and the amplitude from the bottom of the cuvette (A2) are analyzed in detail. It is clearly seen from Figs. 2(a) and (b) that the pulse amplitude increases and shifts to the earlier times (pulse delay decreases) when blood sedimentation occurs.

Sedimentation velocity can be deduced from curve 2(b) [44], v=s/Δt, where s is the propagation distance of the blood layer during time Δt and is the product of the pulse peak time shift and acoustic velocity. Δt is the period for that time (e.g. 10 min). The pulse peak shift is in the range of microseconds and the value of 1550 m/s is used for acoustic velocity [45].

Relative change in the PA pulse arrival time was calculated to facilitate easier comparison of the sedimentation dynamics between samples. The pulse arrival times of the experiments with different samples were divided by the arrival time of the signal at the beginning of each experiment (at time 0 min). Fig. 4 shows relative values (a.u.), and values smaller than 1 indicate faster arrival of the PA pulse on the detector than at the initial stage of the experiment.

Errors in the sedimentation velocity were estimated by defining the timing error (time to save the PA signal and its deviation from full minutes) and calculating a relative error by dividing this error by the time used in velocity estimation (see Table 2). The effect of possible

temperature variation on acoustic velocity was taken into account by adding an error of ± 1°C (± 2m/s, see text later) in acoustic velocity. Errors were rounded up to get reasonable error estimation together with the extracted result (see Table 2).

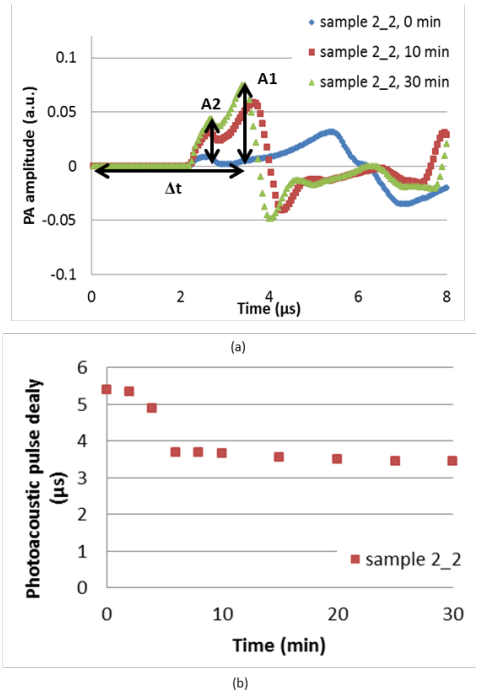


Fig. 2 (a) Photoacoustic signals at different time points of the experiment when measuring sample 2_2 and (b) the time delay of the PA pulse as a function of the measurement time.

The OCT images were analyzed by selecting averaged a-scans from two points in the image and recording the time position of those a-scans (Fig. 3). The velocity estimation range was selected so that maximal velocity could be found. Time dependency of the sedimentation velocity was shown by Antoniow et al. [20]. Then the depth profiles were plotted and the change in the depth of the blood-plasma/PBS layer was calculated. The following values for the refractive index of plasma and PBS were used in the calculations: n_{av}= X*n_{plasma} + Y*n_{pbs}: n_{plasma} = 1.347 [46], and n_{PBS} = 1.333 [46], resulting in the following mean values for the samples' background medium: 1: n_{av}= 1.3414, 2: n_{av}= 1.3414, 3: n_{av}= 1.3386, 4: n_{av}= 1.3386 , 5: n_{av}= 1.333, 6: n_{av}= 1.333, 7: n_{av}= 1.333, and 8: n_{av}= 1.333. In OCT, an error of 2 pixels in reading the image was considered as experimental error in defining sedimentation velocity. The time of an averaged a-scan was calculated from the total measurement time divided by the number of averaged a-scans in the image (2500). Errors were rounded up to get reasonable error estimation together with the extracted result (see Table 2).

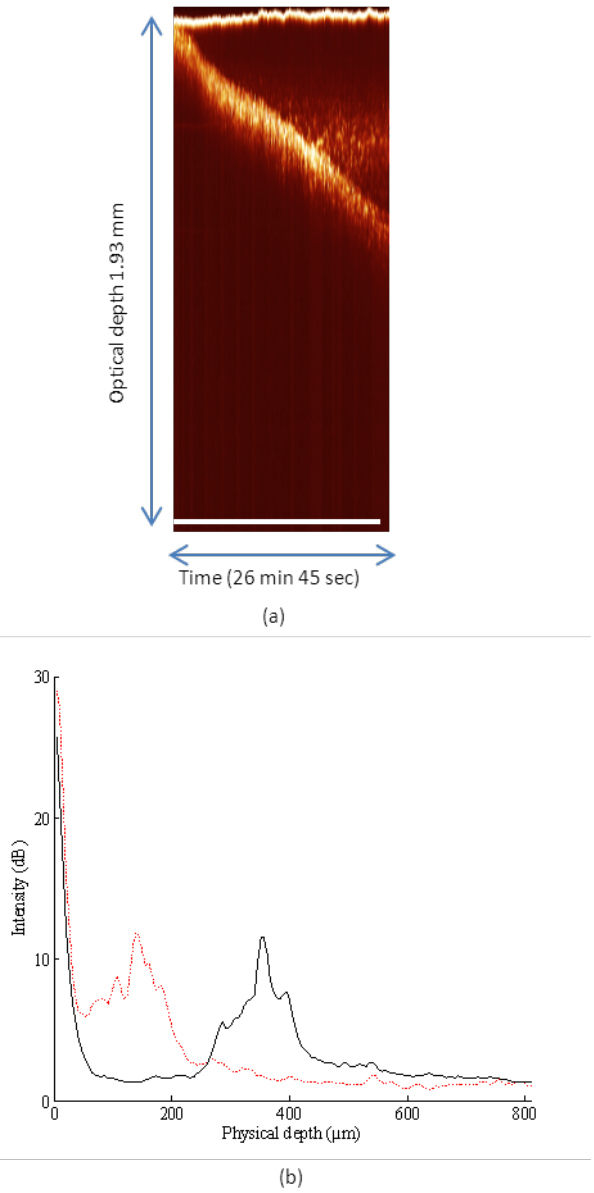


Fig. 3 (a) OCT image from sample 2_1 and (b) OCT signal depth profiles from sample 2_1 (figure (a)) at time points 64 s (dashed line) and 321 s (solid line) from the beginning of the experiments. The profiles are an average of 50 a-scans (modified from Fig. 6, Ref. [44]).

3 Results and discussion

Fig. 2(a) shows the PA pulse profiles from a blood sample with dextran at different time points of the experiments. The PA signal amplitude is proportional to the RBC concentration, i.e. hematocrit, and hence, to optical absorption [47]. The amplitude increases when the RBC concentration in the absorbing layer increases. Also other physical and optical properties of the sample may vary simultaneously. The PA amplitude is sensitive to changes in the contact of the transducer. Therefore, the time delay of the pressure pulse is a more reliable measure and is analyzed in more detail. Fig. 4 (a) shows

relative changes in the PA pulse arrival time in diluted blood samples (1–4) during the sedimentation process, whereas Fig. 4(b) shows the results for washed RBC samples. The dynamics of sedimentation are clearly visible. The same can be seen in Fig. 3(a). These findings support earlier investigations [28]. The sedimentation process has non-linear behavior, which has also been found in some other publications [2,20,23]. It can be seen that dextran makes the sedimentation process faster by inducing RBC aggregation. Another phenomenon slowing down the process is the dextran-induced increase in plasma viscosity [48,49]. Dextran-induced increase in blood viscosity is mostly due to red blood cell aggregation [49].

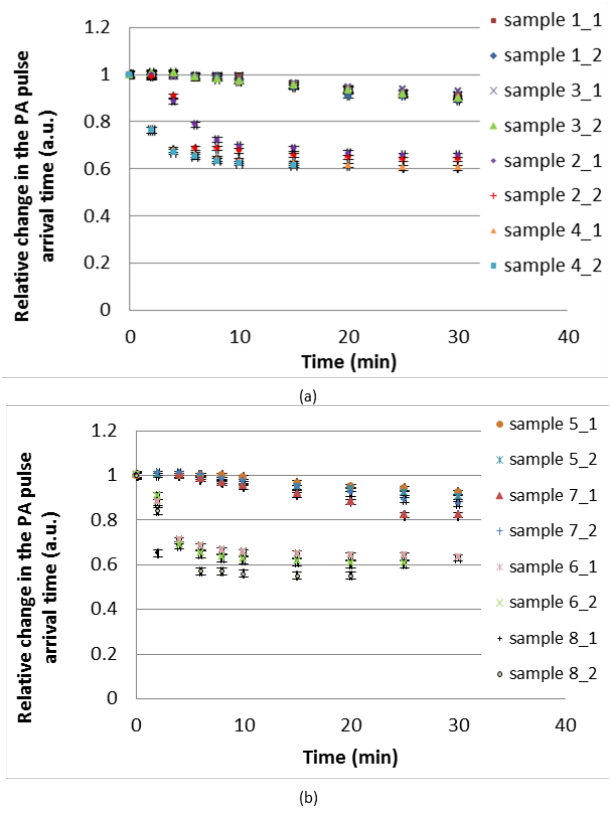


Fig. 4 (a) Relative change in the PA pulse delay as a function of the measurement time for diluted blood samples and (b) relative change in the PA pulse delay as a function of the measurement time for washed RBCs.

It is clearly seen in Fig. 2(a) that blood sedimentation increases light transmittance through the RBC layer. More light hits the cuvette, light is absorbed in the plastic and generates an acoustic wave due to thermoelastic expansion, and the PA signal amplitude (A2) from the bottom of the cuvette increases. The hematocrit of the sample affects the sedimentation rate [2]. It was found (Fig. 4(a)) that the sedimentation process was the fastest with samples 4, where RBC concentration was the lowest.

The same effect can be seen in Fig. 4(b), where dextran increased the sedimentation rate. Due to the limited measurement time (30 min) and slow sedimentation velocity, the PA signal amplitudes from diluted whole blood samples remained almost constant, while dextran greatly increased the amplitude (Fig. 5).

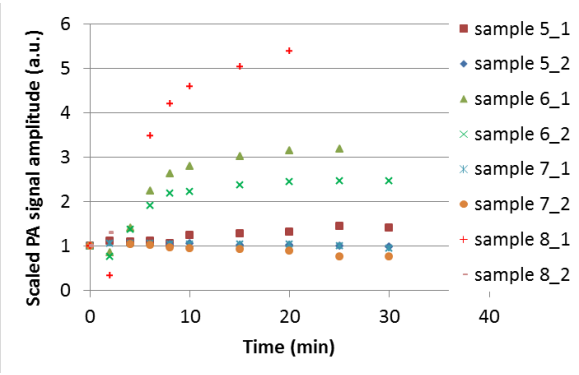


Fig. 5 Scaled PA signal amplitude as a function of the measurement time for different washed RBC samples.

Changes in the acoustic pulse delay tell about changes in the PA pulse generating area, and hence, in the sedimentation of the RBCs. The optical properties of the sample will change during RBC aggregation [28,34]. The anisotropy factor g is larger for aggregates than for single cells. RBC aggregates are larger than single cells, and hence, light scattering will be more forward directed [34]. When blood sedimentation occurs, the layer with RBCs becomes thinner and the multiple scattering properties will change as the cells get closer to each other. It is also worth remembering that dextran will increase the refractive index of the sample, reducing the refractive index mismatch between RBCs and the background medium and reducing scattering (optical clearing) [27,33]. Decreased scattering increases optical energy density in the illuminated sample area [50]. Absorption also increases due to the increased cell density. These effects result in an increased PA amplitude (Fig. 5). This is also seen as increased transmittance in OCT experiments [28,30,31]. The acoustic source is hence moving down and its properties are changing due to the changing optical properties. The earlier findings with OCT [28] are now supported also by PA experiments, as shown in Figs. 4 and 5. It must be pointed out that when the background suspension of the blood sample is changed from plasma to PBS, e.g. from whole blood to washed RBCs, the refractive index of the background medium changes from 1.347 (for plasma) to 1.333 (for 0.9 saline solution or water) [46]. This alters the optical scattering properties of the sample [46]. The highest OCT signal intensity, i.e. the best image contrast, was achieved from samples 1 and 3.

The sedimentation rate varied considerably during the experiments, especially when the aggregation process was enhanced. Hematocrit also affects sound velocity [45], being smaller for diluted concentrations. Acoustic wave velocity is dependent on both the sample's temperature and its blood hematocrit value. Sound velocity for a 1.0 % saline solution of water is 1493.6 m/s at 20°C and 1538.9 m/s at 40°C [45]. For

blood plasma the velocity is 1546 m/s, and for whole blood, 1584.2 m/s (at 37 °C) [45]. It was found that the temperature dependence of the acoustic velocity of blood is – 2m/s / °C. This value was used in error estimation, giving 0.13 % error. Hence, for 20 °C the value is 1550 m/s. Another source gives a value of 1535 m/s for PBS, 1553 m/s for plasma, and 1590 m/s for whole blood at 37 °C [51]. Variation in sound velocity in different samples may induce a small error in the estimated sedimentation values. It is also worth noting that viscous properties are different for plasma and PBS [46]. Viscosity is also dependent on temperature, being higher at room temperature than at 37 °C [52]. Dextran will also increase viscosity [48,49], reducing the sedimentation rate at high dextran concentrations [48]. Hence, the effects of viscosity must be taken into account when analyzing dextran-induced aggregation and enhanced sedimentation rate [48].

Table 2 shows velocity values extracted from both PA signals and OCT images. The velocity estimation range was selected so that maximal velocity could be found from the measured data. The time-dependent change in the sedimentation velocity is found in the work of Antoniov et al. [20]. Dextran accelerated the sedimentation velocity more than 10-fold. In some cases the effect of dextran was found to be higher in samples with lower hematocrit. When the sedimentation rates for diluted blood (with plasma) and RBCs in PBS were compared, the results resembled each other considerably. The values in Table 2 for samples without dextran match well with typical values found in the literature, which are 0–15 mm/h for men and 0–20 mm/h for women [6,28]. The plasma proteins of whole blood induce a certain amount of RBC aggregation also in healthy blood samples, which might affect the variation in sedimentation times between different persons [26].

Sources of error in the experiments are the accuracy of saving the wave shape during the experiments (0.11–6.67 %) and sample preparation accuracy. The wave shape might also be affected by the transducer's bandwidth, which makes the analysis of the pulse shape inaccurate. Time-resolved detection of PA signals with a wide frequency bandwidth transducer will be a part of future research. Figs. 4 (a) and (b) also show that samples 4 and 8 exhibit very rapid sedimentation. Therefore, a reliable value for the sedimentation rate could not be extracted for sample 1_8 (see Table 2). Hence, real-time data acquisition would be better, and the software will be developed in the future.

Sample-to-sample variation in sedimentation kinetics affects repeatability. Velocity differences obtained with OCT and PA methods might be explained by the different depths used in the analysis. In the current measurement procedure, the time point during the measurement can be more accurately determined from OCT images than from PA pulses (error in Table 2). In addition, the OCT signal's focus point in the sample affects signal intensity and image contrast [53]. Low image contrast makes estimation of sedimentation velocity difficult. In the PA experiments the detected signal shape and amplitude might be affected by the laser beam's spot size and the energy density of the PA wave source [54].

The sedimentation process can be analyzed as a two-layer system. The upper layer consists of plasma or PBS and the lower layer of RBCs. The thickness of the upper layer increases as a function of time and the thickness of the lower layer decreases [20,29–31]. Heat and light transfer are complex in such systems [20,21]. The optical signal is converted to an acoustic pulse at the surface of the RBC/plasma layer. It is well known that this surface is not a pure reflecting surface [28,34]. It can be seen from Fig. 3 that the light intensity in the sample has a maximum at a certain depth. However, it must be noted that the optical absorption of red blood cells is almost two orders of magnitude higher than that of blood plasma and platelets [46]. Also, optical scattering is three or more orders of magnitude larger in red blood cells that in plasma and platelets [46] at the wavelength used—1064 nm. Hence, their effect on PA pulse generation is negligible.

Earlier research has demonstrated that the PA amplitude is dependent on the hematocrit [47]. Saha et al. found in simulations that the intensity of the PA signal increases when single RBCs form clusters [39]. The amplitude of the PA signal also increases when the RBC concentration of the illuminated area increases. Hence, those results support the findings in this paper. Aggregation affects scattering [34] and other optical properties. OCT is extensively studied in the context of different optical clearing agents [27–31]. The data in this paper show and support the fact that OCT can be used to monitor the sedimentation kinetics of various blood samples with different hematocrits.

4 Conclusions

The pulsed photoacoustic technique was demonstrated to be capable of detecting blood sedimentation dynamics *in vitro*. Photoacoustic pulse delay was found to be a good indicator for monitoring dextran-accelerated RBC sedimentation, both with diluted blood samples and with washed RBCs. Changes in the optical properties of the sample clearly affected acoustic signal generation in the sample and at the bottom of the cuvette.

5 Acknowledgments

This study was supported by the Academy of Finland (grant **128073**). The author would like to also thank T. Sipola for help in preparation of the cuvette and Prof. A. V. Priezzhev, Dr. A. Bykov and Dr. Z. Zhao for help and fruitful discussions during the experiments. Final thanks are addressed to Oulu University Hospital, which provided their laboratory facilities for taking blood samples.

Table 2 Sedimentation velocities calculated from PA and OCT signals and time intervals for the estimation of the sedimentation velocities.

Sample	sample set 1, velocity estimation range	sample set 1, PA measurement (mm/h)	sample set 2, velocity estimation range	sample set 2, PA measurement (mm/h)	sample set 2, velocity estimation range	sample set 2, OCT measurement (mm/h)
1	0–30 min	1.6 ± 0.1	0–30 min	1.9 ± 0.1	5.3–16.2 min	1.0 ± 0.1
2	2–6 min	26.7 ± 1.0	2–6 min	38.4 ± 0.7	0.1–1.0 min	15.3 ± 0.1
3	0–30 min	1.2 ± 0.1	0–30 min	1.7 ± 0.1	5.0–15.1 min	1.2 ± 0.1
4	0–4 min	39.5 ± 0.8	0–4 min	40.7 ± 2.8	0.2–0.4 min	29.9 ± 0.1
5	0–30 min	1.4 ± 0.1	0–30 min	1.7 ± 0.1	10.5–21.0 min	1.5 ± 0.1
6	0–4 min	39.5 ± 2.1	2–6 min	32.6 ± 0.9	0.2–0.7 min	19.5 ± 0.1
7	0–30 min	3.3 ± 0.1	0–30 min	2.2 ± 0.1	5.6–9.4 min	1.6 ± 0.1
8	-	-	0–6 min	35.7 ± 0.1	0.2–0.5 min	32.6 ± 0.1

Quantification of Mouse Embryonic Eye Development with Optical Coherence Tomography *In Utero*

N. Sudheendran[1], M. Mashiatulla[1], R. Raghunathan[1], S.H. Syed[2], M.E. Dickinson[2], I.V. Larina[2], K.V. Larin[1,2,3*]

[1] Department of Biomedical Engineering, University of Houston, 2028 SERC Building, Houston, TX 77204, USA
[2] Department Molecular Physiology and Biophysics, Baylor College of Medicine, Houston, TX 77030, USA
[3] Institute of Optics and Biophotonics, Saratov State University, Saratov, 410012, Russia

* **e-mail:** klarin@uh.edu

Abstract. Mouse models are commonly used as research tools to understand regulatory pathways affected by human diseases and disorders. Live imaging tools for visualization of mouse embryonic ocular tissues would be beneficial in research associated with developmental ocular defects. In this study, *in utero* quantitative assessment of ocular structures in mouse embryos was performed with a swept-source optical coherence tomography (SSOCT). To define developmental changes in eye morphology in live embryos, the volume of the embryonic eye lens and the globe at different embryonic stages ranging from E13.5 to E18.5 was quantified. It is determined that the major axis diameter of the eye lens and the globe was found to increase from 0.44±0.18 mm to 0.98±0.05 mm and from 0.56±0.22 mm to 1.23±0.14 mm, respectively, as the embryo ages from E13.5 to E18.5. For the same stages, the volume of the eye lens and globe was found to increase from 0.028±0.027 mm^3 to 0.32±0.08 mm^3 and from 0.09±0.08 mm^3 to 0.75±0.27 mm^3, respectively. These results suggest that OCT can accurately assess developmental processes of ocular structures and can be potentially used to assess embryonic ocular growth in mouse mutants with eye abnormalities and to study the effect of toxicological and pharmacological agents. © 2015 Samara State Aerospace University (SSAU).

Keywords: Eye volume; *in utero*; mouse embryo; optical coherence tomography.

Paper #2039 received 2015.01.13; revised manuscript received 2015.02.25; accepted for publication 2015.02.26; published online 2015.03.28.

References

1. J. V. Gross, and B. D. Perkins, "Zebrafish mutants as models for congenital ocular disorders in humans," Mol Reprod Dev 75, 547-555 (2008).
2. N. Goodall, et al., "3-Dimensional modelling of chick embryo eye development and growth using high resolution magnetic resonance imaging," Exp Eye Res 89, 511-521 (2009).
3. Y. Ai, et al., "A mouse model of galactose-induced cataracts," Hum Mol Genet 9, 1821-1827 (2000).
4. M. G. Anderson, et al., "Mutations in genes encoding melanosomal proteins cause pigmentary glaucoma in DBA/2J mice," Nat Genet, 30, 81-85 (2002).
5. J. J. Windle, et al., "Retinoblastoma in transgenic mice," Nature 343, 665-669 (1990).
6. N. A. Syed, et al., "Transgenic mice with pigmented intraocular tumors: tissue of origin and treatment," Invest Ophthalmol Vis Sci. 39, 2800-2805 (1998).
7. P. Parasoglou, et al., "High-resolution MRI of early-stage mouse embryos," NMR Biomed, (2012).
8. S. W. John, et al., "Essential iris atrophy, pigment dispersion, and glaucoma in DBA/2J mice," Investigative ophthalmology & visual science 39, 951-62 (1998).
9. F. S. Foster, et al., "In vivo imaging of embryonic development in the mouse eye by ultrasound biomicroscopy," Investigative ophthalmology & visual science 44, 2361-2366 (2003).

10. A. S. Brown, et al., "Quantitation of hemodynamic function during developmental vascular regression in the mouse eye," Investigative ophthalmology & visual science 46, 2231-7 (2005).
11. D. Huang, et al., "Optical coherence tomography," Science 254, 1178-1181 (1991).
12. I. V. Larina, et al., "Live imaging of blood flow in mammalian embryos using Doppler swept-source optical coherence tomography," J Biomed Opt. 13, 060506 (2008).
13. I. V. Larina, et al., "Hemodynamic measurements from individual blood cells in early mammalian embryos with Doppler swept source OCT," Opt. Lett. 34, 986-988 (2009).
14. N. Sudheendran, et al., "Speckle variance OCT imaging of the vasculature in live mammalian embryos," Laser Phys Lett. 8, 247-252 (2011).
15. I. V. Larina, et al., "Sequential Turning Acquisition and Reconstruction (STAR) method for four-dimensional imaging of cyclically moving structures," Biomed Opt Express 3, 650-660 (2012).
16. S. H. Syed, et al., "Optical coherence tomography for high-resolution imaging of mouse development in utero," Journal of biomedical optics 16, 046004 (2011).
17. I. V. Larina, et al., "Optical coherence tomography for live phenotypic analysis of embryonic ocular structures in mouse models," Journal of biomedical optics 17, 081410 (2012).
18. V. Tuchin, Tissue Optics - Light Scattering Methods and Instruments for Medical Diagnosis, 2nd Edition, SPIE Press, Bellingham, WA (2007).
19. T. Ramaesh, et al., "Corneal abnormalities in Pax6(+/-) small eye mice mimic human aniridia-related keratopathy," Investigative ophthalmology & visual science 44, 1871-1878 (2003).
20. E. Steingrimsson, et al., "Molecular-Basis of Mouse Microphthalmia (Mi) Mutations Helps Explain Their Developmental and Phenotypic Consequences," Nat Genet 8, 256-263 (1994).
21. C. Harch, H. B. Chase and N. I. Gonsalves, "Studies on an Anophthalmic Strain of Mice .6. Lens and Cup Interaction," Dev Biol. 63, 352-357 (1978).

1 Introduction

Embryonic development is an intricate process regulated by both, genetic and environmental factors. Animals such as zebra fish [1], chick, [2] and mice [3] are commonly used as models for human ocular diseases. Mice have been the preferred animal to study mammalian development and human congenital disorders due to easily manipulated genomes. A wide range of mutant models are available for various human diseases, including ocular defects such as cataract [3], glaucoma [4], retinoblastoma, [5] and intraocular tumors [6].

Histological studies have been traditionally used to study ocular defects; however, the lack of 3D information, tissue deformation during fixation and processing, and the inability to perform live studies limits the information that can be gained and precludes longitudinal analysis of a single sample. Imaging tools such as magnetic resonance imaging (MRI) and ultrasound (US) allow performing repeated observations in mouse embryos. These methods are noninvasive and can capture real-time, 3D, structural and dynamic information, however, the spatial resolution of these approaches is a limitation for embryonic ocular research. While *ex vivo* MRI imaging of fixed mouse embryos has previously been performed with up to 20 μm of resolution, *in utero* imaging only allows for resolution of about 100 μm; besides with long imaging times (~ 2h) required to achieve sufficient signal-to-noise ratio (SNR) [7]. High-frequency US is a well-established approach for mouse embryo research. Measurements of the anterior chamber using an ultrasound bio-microscope (UBM) were performed to study the development of glaucoma in mutant mice at different ages ranging from 2 to 30 months [8]. UBM has also been utilized to monitor the development of ocular tissues at different stages of embryonic and postnatal development, for instance to examine the regression of hyaloid vasculature in mice [9, 10]. High frequency ultrasound imaging can achieve axial resolution of up to 30 μm and lateral resolution of about 90 μm, which might not be sufficient to resolve fine details within the developing eye.

Recently we have demonstrated that Optical Coherence Tomography (OCT) technique has clear advantages in resolution and the provides sufficient contrast for structural and functional imaging of mammalian embryos [12-15]. OCT is a noninvasive optical imaging modality which is capable of high speed (MHz A-line rate), high resolution (~2-20 μm), real-time 3-D imaging without requirement for any external contrast agents as it relies on inherent optical contrast [11]. By combining live mouse embryo manipulation approaches with OCT, we developed approaches for live *in vivo* and *in utero* longitudinal mouse embryonic imaging and demonstrated that these methods allow for visualization of ocular structures [16, 17]. In this study, we performed, for the first time to the best of our knowledge, a quantitative assessment of mouse embryonic ocular structures at different stages of development *in utero* with OCT. Acquired measurements were correlated with previously reported values obtained with UBM. While our results correlate with previously reported values, the spatial resolution of OCT gives a potential for more accurate assessment of embryonic development and visualization of structures, which are not accessible with other available methods.

2 Methods

2.1 Imaging system

A swept-source optical OCT (SS-SOCT) system has been employed in this study to visualize embryonic ocular structures [14]. The SS-OCT system comprises of a swept-source laser (Thorlabs SL-1325-P16), with a wavelength range of 1325 ± 50 nm, scan rate of 16 kHz and an output power of 12 mW. The power on the sample arm is 3.6 mW. A beam-splitter splits the laser beam in the ratio of 90% and 10% into the sample and reference arms, respectively. The interference pattern formed from the back-reflected light from the sample and the reference arms is detected by a balanced photodetector (Thorlabs, PDB 140C) and digitized by a 14-bit ADC (AlazarTech). An external Mach-Zehnder interferometer (MZI) clock is used for linear k-space calibration. Fast Fourier transform (FFT) is performed on the calibrated data to obtain 1D depth scan (A-scan). Galvanometer-mounted mirrors are used to perform 2D and 3D imaging by scanning the laser beam on the surface of the sample. The axial and transverse resolutions of the system are measured to be 12 μm (in air) and 15 μm, respectively.

2.2 Mouse manipulations

All animal manipulation procedures described here were approved by the Animal Care and Use Committee of the University of Houston. The animal manipulation protocol is described in details in our previous publication [16]. Briefly, the pregnant CD-1 mice at the desired gestinational stage have been anesthetized using isoflurane by inhalation. The anesthetized mouse was placed on a heating platform maintained at 37° C during the entire procedure. An electrical razor was used to remove the abdominal fur at the incision site. An incision of ~1-2 cm was made on the abdomen to expose the uterine horn for imaging. OCT imaging of the embryonic ocular structure was performed through the uterine wall. From every litter, 2-3 embryos were imaged. Each 3D volume contained 512×512×512 pixels. The lateral scan size depended on the size of the eye. The later pixel resolution was ensured to be at least as much as the transverse resolution (15 μm). The in depth scan range was always 3 mm (in air). The beam in the sample arm was focused on the ocular structures of the embryonic eye. At least five embryos from each stage were analyzed. Each embryo was imaged only once for the purpose of this study. Following the imaging session, the adult mouse was sacrificed. Measurements were made at different stages ranging from embryonic day (E) E13.5 to E18.5.

2.3 Eye volume measurements

To estimate the volume of the eye, we assume the eye to be of oblate spheroid shape [9]. The volume (V) of the oblate spheroid is given by equation (1); [9]:

$$V = \frac{4}{3}\pi a^2 c, \quad (1)$$

where, a is the major axis radius and c is the minor axis radius. The minor axis of the eye is along the optical axis of the eye and the major axes radii are perpendicular to it. Orienting embryos *in utero* for imaging is a challenging task, and the optic axes of the embryo eye can be randomly located within the acquired data set during imaging. To overcome this, a Matlab based application was developed to perform manual 3D rotation of the data set to orient the cross-sectional visualization plane along the optic axis of the eye. The application allows a user to view and manually rotate the eye in three dimensions until the entire major and minor axis radii can be captured in a single 2D frame individually. Since the original scanning distances as well as the rotation angles in three dimensions are known, the distances after 3D rotation can be computed using coordinate transformation. The number of pixels along each direction of the 3D volume was scaled corresponding to the scanning distance so that the 3D voxel is cubic. The refractive index was assumed to be 1.4 [18] and does not change significantly with development. Once the 3D OCT data sets were rotated to correct the alignment, ImageJ software was used to measure the diameters along the major and minor axes.

3 Results

Typical OCT images containing embryonic eyes acquired *in utero* at different stages are presented in Fig. 1. Even at the latest state (E18.5), the imaging depth of OCT is able to capture the entire eye with sufficient contrast. Different embryonic ocular structures including lens and retina are easily identifiable (as labeled). The difference in size and morphology is clearly distinguishable between the developmental stages, as expected.

To orient the OCT data sets along the optic axes of the embryonic eye for measurement, we developed and applied a Matlab based application (as described in the Materials and Methods section). The effect of 3D rotation of the mouse embryo eye data set is demonstrated in Fig. 2. Figs. 2(a, c) show the OCT axial and transverse cross-sections of the eye prior to application of the code, while Figs. 2(b, d) demonstrate corresponding cross-sections after the OCT data set rotation.

The major and minor axes diameters were measured from the oriented 3D data sets using the ImageJ software. To estimate the volume of the eye, the shapes of the eye lens and the eye globe are assumed to be oblate spheroid. An oblate spheroid is circular in its transverse cross-section (in our convention, xy plane) and elliptical in its axial cross-sections (xz or yz plane), with its major axes (x and y axes) along the transverse directions and its minor axis along the axial direction (z axis). Since an oblate spheroid is circular in its

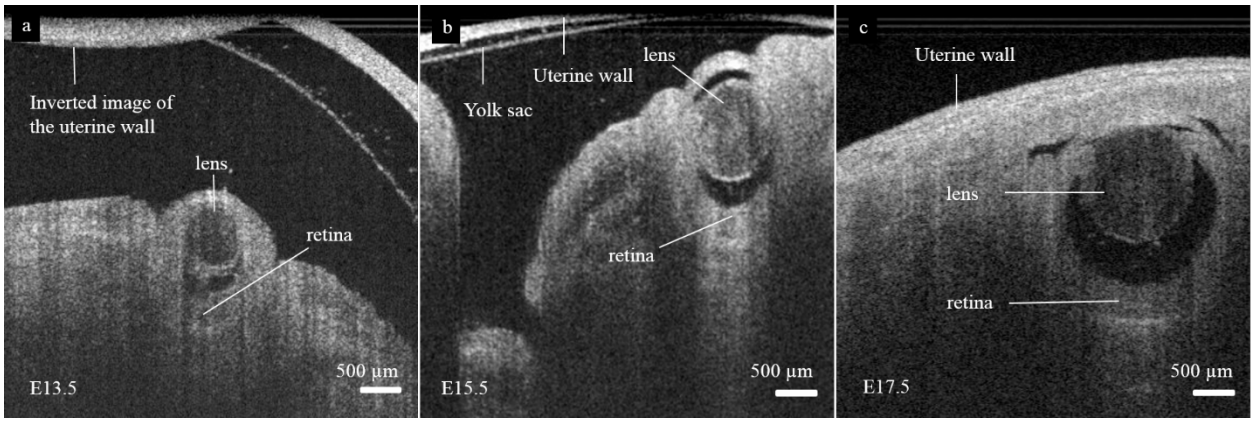


Fig. 1 2D OCT images through the eye *in utero* at different stages of embryonic growth.

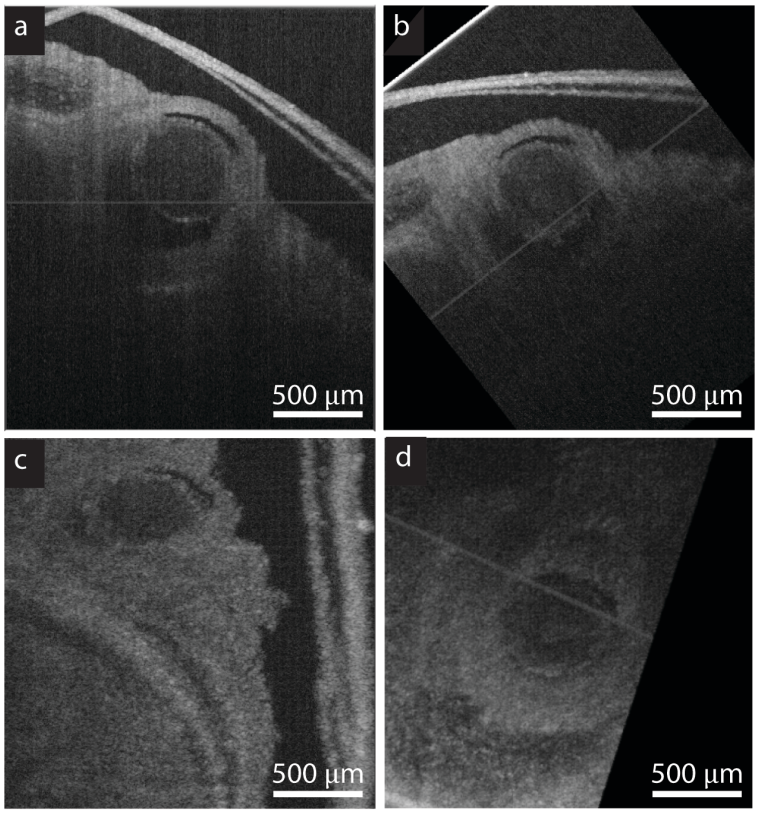


Fig. 2 2D cross-sectional OCT images before and after rotational orientation of the 3D OCT data set. (a) Axial cross-sectional image before 3D rotation. (b) Axial cross-sectional image after 3D rotation. (c) Transverse cross-sectional image before application of the rotational orientation algorithm. (d) Transverse cross-sectional image after the rotational orientation of the 3D data set.

transverse direction, the measurement of the major axis diameters along the x-axis and the y-axis should be the same. It can be observed from Fig. 2b that the axial cross-section of the eye lens and globe is elliptical and the circular nature of the transverse cross-section is apparent in Fig. 2d. To further validate the assumption of oblate spheroid shape, the major axis diameter from both the x-axis and the y-axis (transverse axes) of the eye lens and globe at different growth stages were measured and presented in Figs. 3a and 3b, respectively. The slope of 0.91 with R^2 (coefficient of determination) value of 0.84 for the eye lens and slope of 0.85 with R^2 value of 0.87 for the eye globe implies that the diameters of major axes in the transverse direction are similar, which justifies the assumption that the entire eye lens and eye globe are close to the oblate spheroidal shape [9].

The major axis diameters from different stages of embryonic growth, obtained using OCT, are presented in Fig. 4. It can be noted from Figs. 4a and 4b (green

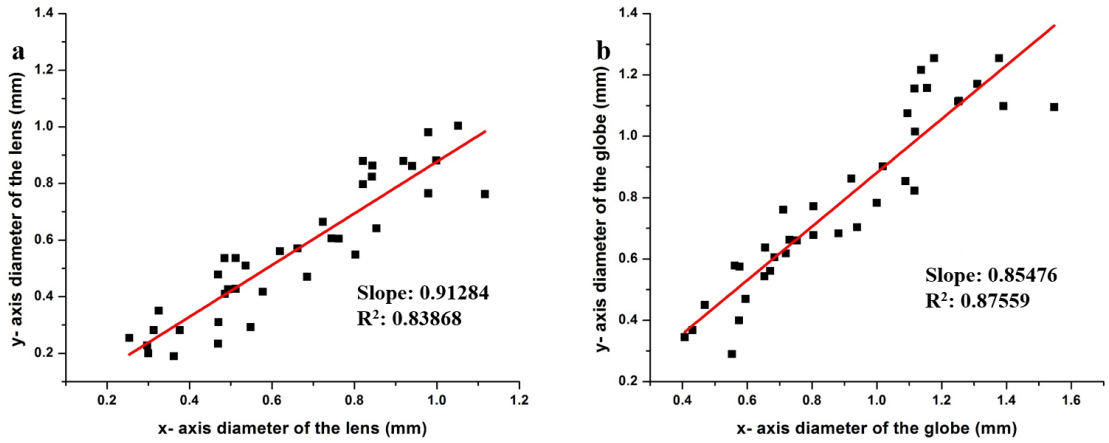


Fig. 3 Plots of major axis diameter measured along the x-axis and y-axis (transverse axes) of the eye (a) lens (b) globe.

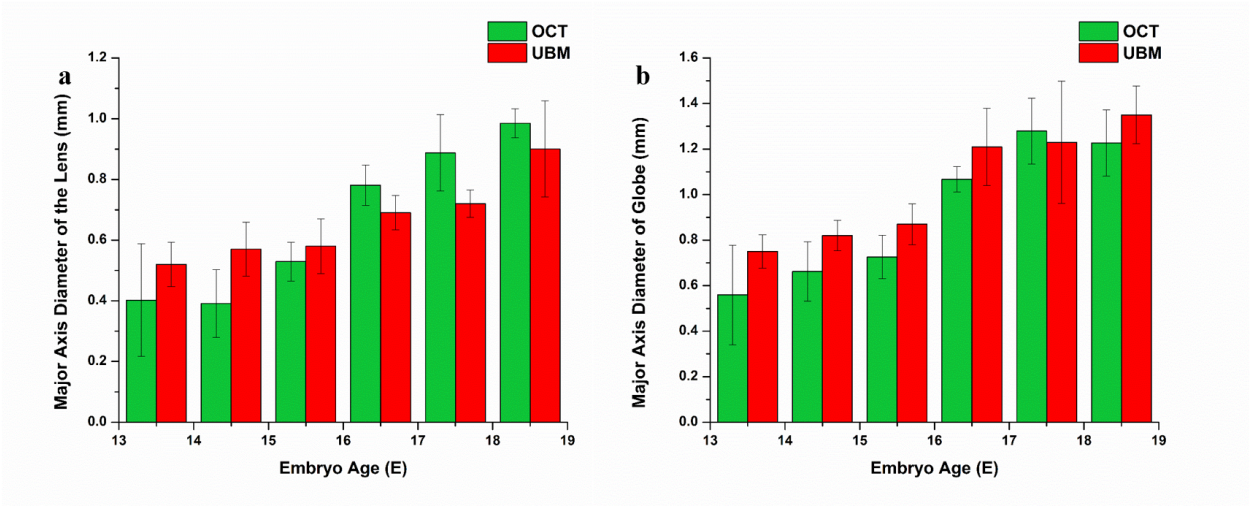


Fig. 4 Major axis diameter measurements of the eye (a) lens (b) globe correlate well with previously reported UBM values (n≥5). The error bars represent SD. The UBM data is obtained from [9].

bars) that there is roughly a 2-fold increase in major axis diameter of the eye lens and a 3-fold increase in major axis diameter of the eye globe from E13.5 to E18.5. Using the measurements of the major and minor axis diameters, the volumes of the eye lens and the globe were computed using Eq. (1). These results correlate well with Foster et.al [9], where the authors measured the major axis diameters and volumes of eye lens and globe using UBM (resolution of 40 µm). The results obtained using UBM (from [9]) are presented in Fig. 4 (red bar). The major axis diameter measurements are within similar range, as compared to OCT measurements, across the different stages of development. Note that the standard deviation values from the UBM measurements are comparatively larger to the ones from OCT measurements, suggesting higher precision with the latter technique. The volume measurements of the eyes are presented in Fig. 5. It was determined that the volume of the eye lens and globe increased from 0.028±0.027 mm^3 to 0.32±0.08 mm^3 and from 0.09±0.08 mm^3 to 0.75±0.27 mm^3, respectively. All the values in Fig. 4 and 5 are reported as average ± SD format, the SD arises due to variability between different embryos.

4 Discussion

As evident from structural images of the embryo eyes, the contrast and resolution offered by OCT enables clear distinction of the embryonic ocular structures *in utero*. The measurements of the major axis diameters of lens and globe using OCT between E13.5 to E18.5 are within similar range as the measurements from previous study using UBM [9]. UBM has an inferior resolution (~40×60 µm) as compared to OCT (~12×15 µm). Moreover, the major and minor axis diameters were measured without any correction for the tilt of the eye. This can result in underestimating the actual diameters. It can also be noted from [9], that the reported values for the volumes of the eye lens and the globe is not

consistent with the respective values of the major axis diameters, as the authors likely used different measurements to obtain the final values.

Although OCT has the advantage of superior resolution and contrast compared to UBM, limited depth penetration in tissues is a significant drawback. This limitation requires the use of surgery to expose the uterus of the pregnant mouse to image the embryos. However, our group has devised protocols to perform *in utero* longitudinal studies of mouse embryos. We have also demonstrated that this methodology does not affect the growth of the embryos [16].

5 Conclusions

In this preliminary study, we have used measurements of eye lens and globe volumes as means to demonstrate ability of OCT to study ocular development in mouse embryos. The volumes of the eye lens and the globe have been shown to increase from 0.028±0.027 mm^3 to 0.32±0.08 mm^3 and from 0.09±0.08 mm^3 to 0.75±0.27 mm^3, respectively, from E13.5 to E18.5. This study suggests that our approach can potentially be used for live quantitative characterization of ocular tissues in a variety of ocular research studies. These include monitoring morphological changes during eye development in mutant mice models for human ocular diseases such as aniridia [19], microphthalmia [20] and anophthalmia [21]. Our future studies will involve an automated algorithm to perform the rotation of the dataset and also longitudinal measurements of various biometrics related to the eye in both normal and mutant mouse embryos.

In conclusion, we have demonstrated that *in utero* OCT embryo imaging approach allows for live quantitative assessment of mouse embryonic ocular growth with higher resolution, than other currently available methods. Potentially, this approach can be used to assess embryonic ocular growth in mouse mutants with eye abnormalities and to study the effect of toxicological and pharmacological agents.

Acknowledgement

This research was supported by NIH HL077187, HL095586, HL120140, T32 HL007676, and AHA 10SDG3830006.

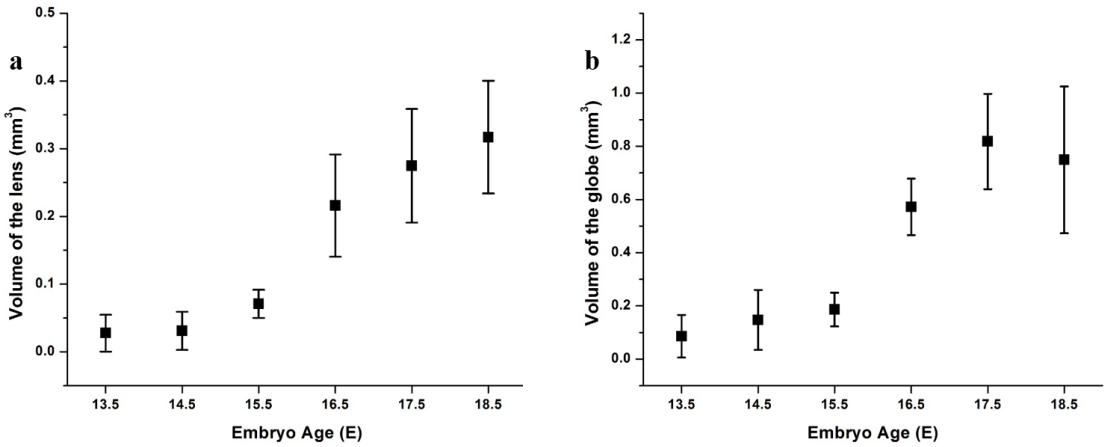


Fig. 5 Plot of volume of the eye (a) lens (b) globe measured using OCT *in utero*. The error bars represent SD (n≥5).